Integrated InP Mach-Zehnder Modulators for 100 Gbit/s Ethernet Applications using QPSK Modulation

vorgelegt von

Diplom-Physiker

Holger Klein

aus Berlin

von der Fakultät II -
Mathematik und Naturwissenschaften
der Technischen Universität Berlin

zur Erlangung des akademischen Grades

Doktor der Naturwissenschaften
- Dr. rer. nat. -

genehmigte Dissertation

Promotionsausschuss:
Vorsitzender: Prof. Dr. E. Schöll
1. Gutachter: Prof. Dr. D. Bimberg
2. Gutachter: Prof. Dr. D. Jäger (Universität Duisburg-Essen)
Tag der wissenschaftlichen Aussprache: 20. September 2010

Berlin 2010

D83

Zusammenfassung

In der vorliegenden Arbeit wird ein monolithisch integrierter doppelt-paralleler IQ-Modulator auf Basis des Halbleiters Indium-Phosphid für die Datenübertragung bis zu 2x50 Gbit/s in optischen Glasfasern bei einer Wellenlänge von 1.55 μm entwickelt und charakterisiert. Beginnend mit einer Diskussion der Struktur der zugrunde liegenden optischen Wellenleiter wird im weiteren Verlauf die Funktionsweise der eingesetzten kapazitiv belasteten Wanderwellenelektrode anhand des einfachen Mach-Zehnder Modulator (MZM) erläutert. Darüber hinaus erfolgt eine Einführung in die physikalischen Effekte, welche sich für die Modulation der optischen Phase in den eingesetzten Multi-Quantum-Well Schichten der optischen Wellenleiter verantwortlich zeigen. Darauf aufbauend werden Optimierungsansätze für die drei charakteristischen Modulator-Parameter Einfügeverluste, Schaltspannung und elektro-optischen Bandbreite entwickelt und hierfür drei unterschiedliche optische Wellenleitertypen evaluiert. Diese sind bezeichnet als stark, halbstark sowie schwach geführte Wellenleiter, welche die Vorteile der beiden zuerst genannten Varianten vereint. Optische Verluste sind ein wesentlicher Parameter der hier beschriebenen IQ-Modulatoren, zu deren Reduzierung optische Modenfeld-Konverter für die drei vorher genannten Wellenleitertypen entwickelt werden. Realisiert wird eine hocheffiziente Faser-Chip-Kopplung, welche trotz der absorbierenden n-dotierten Halbleiterschichten Verluste unter 0.8 dB ermöglicht. Als weitere Möglichkeit zur Reduzierung der Einfügeverluste wird die Änderung des Dotierprofils der p-i-n-Diodenstruktur diskutiert. Diese Option der Verlustreduktion wird für die drei Wellenleitertypen in Bezug auf Dotierkonzentrationsänderung als auch Dotiertiefenänderung untersucht.

Die Reduktion der Schaltspannung ist essentiell, da der IQ-Modulator im Betrieb der Quadratur-Phasenumtastung (QPSK) eine doppelt so hohe Spannung benötigt wie im Standard-Modulationsbetrieb und da eine Reduktion der Treiberspannung mit einer Reduktion der Kosten für den Treiber IC sowie mit einer Reduktion des Energieverbrauchs und der Wärmeentwicklung Hand in Hand geht. Möglichkeiten zur Reduktion der Schaltspannung werden in Bezug auf die

Optimierung des eingesetzten Multi-Quantum-Wells, sowie die bereits erwähnten Wellenleiter-typen und Dotierprofil-Variationen evaluiert. Zur Bestimmung von Abhängigkeiten der elektro-optischen Bandbreite des Mach-Zehnder Modulators von geometrischen und prozesstechnischen Variationen werden elektrische Simulationen mit einem Hochfrequenz-Struktursimulator durchgeführt und mittels eines elektro-optischen Modulator-Modells ausgewertet. Die für eine 3-dB-Bandbreite von 40 GHz in Frage kommenden Geometrien werden anschließend in Bezug auf ihren Einfluss auf optische Einfügeverluste und Schaltspannung bewertet.

Im Anschluss an die Optimierungsbetrachtungen des einfachen Mach-Zehnder-Modulators werden die strukturellen Änderungen aufgezeigt, welche zur Herstellung des doppelt-parallelen IQ-Modulators notwendig sind. Darauf folgt eine kurze Einführung in das angewendete QPSK-Modulationsformat. Zur Berechnung von charakteristischen Großsignal-Modulationseigenschaf-ten wird ein mathematisches Modell des einfachen Mach-Zehnder Modulators sowie des inte-grierten IQ-Modulators entwickelt, welches die nichtlinearen elektro-optischen Effekte berück-sichtigt. Unter Einbeziehung von realen Messdaten wird das mathematische IQ-Modulator Modell zur Berechnung der sogenannten Fehlervektor-Größe (EVM - error vector magnitude) für diverse nicht-optimale Betriebszustände herangezogen. Der Fehlervektor ist eine charak-teristische Größe für höherwertige Quadratur-Amplitudenmodulationsverfahren, welche einen Rückschluss auf die zu erwartende Fehlerrate erlaubt.

Das darauf folgende Kapitel präsentiert ausgewählte Messdaten der DC- und Hochfrequenz-Charakterisierung von Einzel- als auch IQ-Modulatoren. Die Auswertung von Intensitäts-Matrixmessungen zeigt eine sehr gute Korrelation zu den vorher getroffenen theoretischen Betrachtungen für verschiedene Halbleiter-Schichtstrukturen. Die niedrigste Schaltspannung eines Mach-Zehnder Modulators mit 4 mm Elektrodenlänge bei 1550 nm Wellenlänge liegt bei lediglich 1.05 V. Ein im Folgenden vorgestellter DC-Charakterisierungs-Algorithmus dient zur Bestimmung der korrekten Phaseneinstellungen des IQ-Modulator während der Großsig-nalmodulation. Dies führt zu einer erheblichen Reduzierung der benötigten Zeit für die Hochfre-quenzcharakterisierung. Elektro-optische Kleinsignalmessungen von Modulatoren mit verschie-denen Elektrodenlängen zeigen mit 3-dB Bandbreiten jenseits von 40 GHz das Potential für fehlerfreie 2x50 Gbit/s=100 Gbit/s Übertragung. Mit Hilfe von Großsignal-Hochfrequenzmes-sungen im Zeit- und Frequenzbereich wird die Funktion des IQ-Modulators in Quadratur-Pha-senumtastung bei 2x40 Gbit/s=80 Gbit/s erfolgreich demonstriert.

Den Abschluss dieser Arbeit bildet eine Zusammenfassung der geleisteten Arbeit sowie ein Ausblick auf die weiteren Entwicklungsmöglichkeiten, welche sich aus den Ergebnissen der vorliegenden Arbeit ableiten lassen.

Abstract

In this work, a monolithically integrated dual-parallel IQ modulator (IQM) is developed and characterized. It is based on the semiconductor Indium phosphide and is intended for data transmission at 2x50 Gbit/s over optical fiber at a wavelength of 1.55 μm. This thesis begins with a discussion of the fundamental structure of a single Mach-Zehnder modulator (MZM) including the optical waveguides and the implemented capacitively loaded traveling-wave electrodes (TWE). An introduction will be given to the physical effects responsible for the modulation of the optical phase in matter and especially in the semiconductor multi-quantum-well waveguide of the modulator. Based on that knowledge, an optimization approach for the three characteristic modulator parameters insertion loss, switching voltage and electro-optic bandwidth will be developed. Three different waveguide geometries, referred to as 'deep etch', 'shallow etch' and 'median etch' will be analyzed, where the latter combines the advantages of the two former geometries. The optical insertion loss is a key parameter of the InP-based modulator in the competition with other material systems such as lithium niobate. An acceptable optical losses is achieved by the incorporation of an on-chip spot-size converter. A highly efficient fiber-chip coupling with less than 0.8 dB is realized for all three waveguide types mentioned. As another possibility to achieve acceptable low optical insertion losses, a variation of the doping profile of the modulators p-i-n-diode is evaluated. This option is discussed for different doping concentrations as well as a modification of the thickness of the intrinsic space-charge region.

A low drive voltage of the IQ modulator is essential as the applied quadrature-phase-shift-keyed (QPSK) modulation scheme requires a switching voltage of $2V_\pi$ which is twice the value required for on-off keying (OOK) with a standard MZM. Thus, a modulator drive voltage as low as possible reduces the cost for the necessary driver amplifier and lowers power consumption and heat dissipation at the same time. The optimization of the multi quantum well (MQW) structure will be discussed as one possibility to achieve a higher modulation efficiency, and the various waveguide geometries and different doping profiles will be evaluated with respect to

their influence on the drive voltage. To determine the influence of geometrical variations of the traveling-wave electrode and fabrication process tolerances on the electro-optic bandwidth of the Mach-Zehnder modulator, electrical high-frequency simulations are conducted. All electrode designs capable to achieve a 40-GHz 3-dB bandwidth are then compared with respect to their impact on optical insertion loss and drive voltage.

The theoretical considerations for an optimized single Mach-Zehnder modulator design are followed by a discussion of structural modifications needed for realizing the IQ modulator (IQM), and a short introduction to the QPSK modulation format is given as well. To calculate the characteristic large-signal modulation properties of the IQM, a mathematical model of the entire modulator is developed that accounts for the non-linear electro-optic effects in the MQW waveguide. Taking experimental data of the phase- and absorption-voltage-response, the mathematical model is used to predict the so called error vector magnitude (EVM) for various non-ideal drive conditions of the IQM. The EVM is a common measure of the modulation quality for advanced modulations formats which allows to predict the bit error rate.

The next chapter presents selected measurement results of single Mach-Zehnder modulators and IQ modulators. The evaluation of DC intensity matrices of wafers with different doping profiles shows an excellent correlation with theoretical values derived before. The lowest drive voltage for a MZM with 4 mm electrode length measured at 1550 nm is 1.05 V only. A DC characterization algorithm of the IQ modulator is presented, that allows the determination of the correct phase electrode settings for large signal modulation. This leads to a significant reduction of test time under large signal conditions. Electro-optic small-signal response measurements with 3-dB frequencies beyond 40 GHz are presented for different TWE lengths showing the potential for error-free 2x50 Gbit/s=100 Gbit/s data transmission. Time-domain and frequency-domain large signal measurements demonstrate successful IQM operation at a data rate of 2x40 Gbit/s=80 Gbit/s using QPSK modulation.

This work concludes with a summary of the work accomplished and an outlook on the possibilities of future developments based on the presented results.

Contents

List of Figures

List of Tables

Introduction

The demand for internet bandwidth grows as new applications and technologies on the Internet continue to develop. So called Web 2.0 services like voice-over-IP, TV-over-IP, video-on-demand and many others have lead to a massive growth in internet traffic. This steady traffic increase has created pressure to develop higher capacity transport systems. While fiber-optic communication systems have already revolutionized telecommunication infrastructures in the past and today, additional significant research efforts will be required to meet the expected data growth of the fast growing Internet. The discovery of the low attenuation windows of optical fibers around 980 nm, 1310 nm and 1550 nm has enabled the introduction of wavelength division multiplexing (WDM) transmission techniques in the early 1990s. This was an easy way to increase the cumulative data rate of a single optical fiber by transmitting different data streams via different wavelength channels which have a distinct spacing from the next neighboring channel. Today's WDM networks usually have 50 GHz or 100 GHz (cf. Figure 1.1) channel spacing following the ITU-T (International Telecommunication Union) standard and a single channel data rate of 10 Gbit/s. 40 Gbit/s equipment is starting to be deployed these days and the research in the field of 100 Gbit/s optical communication systems, the next generation Ethernet standard, has been augmented in the last 2-3 years. The driving factor for telecommunication companies to upgrade their transmission systems is the inability to cope with the fast increase of internet traffic today. Already deployed WDM equipment, e.g. routers, filters or interleavers, have a limited electrical bandwidth and support channel spacings of 50 GHz or 100 GHz [1]. One challenge arising from the single channel bandwidth growth from 10 Gbit/s to 40 Gbit/s or even 100 Gbit/s is the increasing signal spectral width. Standard NRZ OOK (non-return-to-zero on-off keying) modulation has a spectral efficiency of about 0.4-0.5 bit/s/Hz, depending on bandwidth limitations of the transmitter. This means that a 40 Gbit/s data stream requires 80-100 GHz optical bandwidth, which is the allowed maximum for current WDM systems.
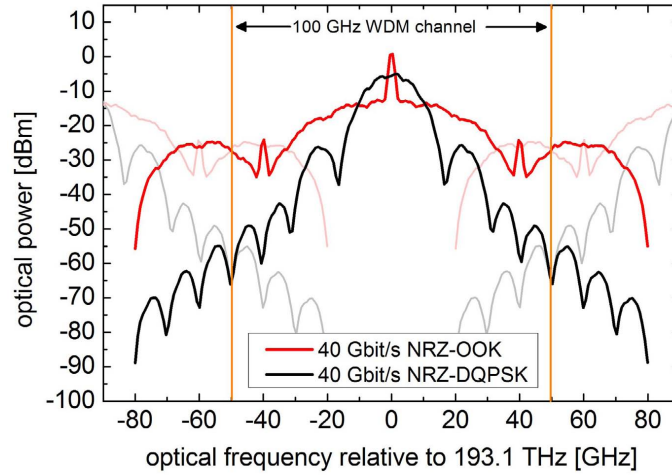
Fig. 1.1: Simulated optical spectra of NRZ-OOK (red) and NRZ-DQPSK (black) modulation formats at 40 Gbit/s for identical launch powers. The 100 GHz WDM channel spacing is indicated by the orange lines.

Higher data rates would cause unacceptable crosstalk between adjacent WDM channels. The only reasonable and cost effective way to upgrade existing transmission systems to higher data rates is to introduce advanced modulation formats with a higher spectral efficiency. Of course, these techniques allow telecommunication companies to use as much as possible of their actual deployed network equipment. Furthermore, there is no need to upgrade all channels at once.

1.1 Motivation

The modulation format which is currently expected to be the next Ethernet standard - following the 10 Gbit/s Ethernet standard first published in 2002 - for long-haul single channel 100 Gbit/s transmission is differential quadrature phase shift keying (DQPSK). DQPSK offers a good balance between single-component performance and overall transmitter and receiver complexity, and it provides sufficient spectral efficiency to enable 100 GHz WDM channels. Compared to standard OOK modulation DQPSK coded data signals have an approximately 25 dB lower channel crosstalk at the same data rate. This is illustrated in Figure 1.1 for 40 Gbit/s data rate. DQPSK modulation can be implemented in various ways. Two parallel Mach-Zehnder modulators (MZM) are the preferred architecture for long-haul chirp free operation. Each MZM is operated in the differential-binary-phase-shift-keyed (DBPSK) mode, and the signals of both single modulators are superimposed with 90° phase difference in order to to generate the four different phase states in the complex plane constellation diagram where each phase state transmits the information of two bits at the same time.

Mach-Zehnder modulators based on indium phosphide (InP) have shown higher electrical

3-dB bandwidths of up to 60 GHz [2] and lower driving voltages V_π of 2.2 V [3] compared to its commercial competitor made out of Lithium Niobate (LiNbO$_3$). This gives InP the unique opportunity to be the material of choice in the development of optical modulators for Next Generation Networks using advanced modulation formats.

1.2 Objectives

The first intention of this thesis is to develop a device model for InP Mach-Zehnder modulators that allows the optimization of the three major performance parameters: switching voltage V_π, optical modulation response bandwidth f_{3dB} and optical insertion loss. The second goal is to successfully develop an integrated InP-based IQ modulator (consisting of two parallel Mach-Zehnder modulators) that is capable of transmitting 2x50 Gbit/s by using quadrature phase shift keying (QPSK) as the modulation format allowing a channel data rate of 100 Gbit/s. The operation conditions regarding optical insertion loss, drive voltage and electrical bandwidth are targeted to meet the specifications required for a successful product. These conditions typically are (i) an optical insertion loss < 10 dB (3 dB optical power is lost in the IQ modulator during operation due to the 90° phase difference between both single MZMs), (ii) a drive voltage $V_\pi \leq 2$ V, and (iii) a f_{3dB}-bandwidth ≥ 40 GHz. Phase-shift-keyed modulation using a Mach-Zehnder modulator requires a driving voltage of two V_π compared to only one V_π for on-off keying (OOK). This makes the reduction of the required π-switching voltage the primary task to achieve compatibility of the modulator with commercially available 50-Gbit/s broadband amplifiers. These amplifiers are offered only by a small number of companies and typically provide a peak-to-peak voltage of $V_{pp} \sim 4$ V and an electrical 3-dB bandwidth of ~ 40 GHz.

Besides these three goals, the main objectives of this thesis are as follows:

- point out performance limiting mechanisms of the InP Mach-Zehnder modulator and investigate their interdependencies

- derive performance-optimization trade-offs for optimum performance of the InP-based MQW-type Mach-Zehnder modulator

- build test structures, standard modulators and IQ modulators to experimentally verify the theoretical performance optimizations

- demonstrate that the product target specifications for V_π, f_{3dB} and optical insertion loss can be met in a single device

- demonstrate error free 2x50 Gbit/s QPSK operation of a packaged IQ modulator

1.3 Thesis structure

Following this introduction, Chapter 2 briefly introduces the optical waveguide structure of the Mach-Zehnder modulator (MZM) and gives an overview of the operation principles from a DC and RF point of view. The second part of Chapter 2 covers the main physical electro-optic effects responsible for the phase of the optical carrier signal being changed in the multi-quantum-well (MQW) waveguide core layer. Chapter 3 introduces the design criteria for the three most important performance parameters optical insertion loss, drive voltage V_π and electro-optical f_{3dB}-bandwidth. It will be shown that the integration of an on-chip optical spot size converter significantly reduces the overall insertion loss of the modulator compared to simple fiber-chip coupling into a simple waveguide. The impact of changing the doping profile of the p-i-n diode waveguide configuration on insertions loss and switching voltage will be highlighted. The discussion hereafter gives an insight to the design criteria of the traveling-wave electrode used for the MZ modulator to achieve an electro-optic bandwidth of 40 GHz. The last section of Chapter 3 is dedicated to the presentation of performance trade-offs for the three relevant parameters which will allow to select optimal device configurations. Chapter 4 addresses the design and development of the dual-parallel IQ modulator (IQM). A mathematical model for the InP-based MZM is developed that allows the precise simulation the DC modulation characteristics arising from non-linear physical effects. This model is enhanced for the dual-parallel IQM and used to predict the large signal modulation performance of the IQM under various drive conditions. The following Chapter 5 is focused on the device characterization metrology and presents selected measurement results in order to prove the theoretical concepts introduced in the previous chapters. A fast and easy DC characterization algorithm for the IQ modulator will be presented, which is of utmost importance, as measurement costs tend to make up a large fraction of production costs of such high performance devices. This algorithm will be verified with measurement results from large signal RF characterization of a packaged IQM. Small signal modulation results will be presented for fabricated single MZMs and dual-parallel IQMs. Measurement results from large signal testing of packaged single MZMs at 40 Gbit/s and 80 Gbit/s will reveal error-free operation. For the first time, successful QPSK modulation of a packaged InP-based dual-parallel IQ modulator will be demonstrated at 80 Gbit/s. This thesis will conclude in Chapter 6 with a summary of the work accomplished and an outlook on possible future developments based on the present work.

Remark

Due to a non disclosure agreement (NDA) between the Fraunhofer Heinrich-Hertz-Institute and Cogo Optronics Inc. no information will be given on the processing technology used to fabricate the high-speed InP-based Mach-Zehnder modulators developed in this thesis. In addition, the specific values of a few design variables which are used in the theoretical design optimization process in Chapter 3 will remain undisclosed (especially in Section 3.5 where theoretical trade-off curves for an optimized MZM design are presented).

Chapter 2

Theoretical background

2.1 Introduction

The purpose of this chapter is to provide a description of the fundamental operation principles of a high-speed InP-based Mach-Zehnder modulator. The advantages of single drive push-pull operation will be explained as well as the physical effects enabling high-speed modulation of the optical phase in the Mach-Zehnder interferometer (MZI). Due to the need of high-speed operation, an introduction will be given to the basic design rules for traveling-wave electrodes with special emphasis to the application of segmented capacitive loads.

2.2 Mach-Zehnder modulator principles

A Mach-Zehnder interferometer (MZI), named after Ludwig Mach and Ludwig Zehnder, who independently developed this interferometer principle in 1891/1892 [4, 5], is a device to measure phase shifts of a sample placed in one arm of the interferometer. In a Mach-Zehnder modulator a phase shift is intentionally introduced to obtain an intensity modulation at the output. For optoelectronic devices used in telecommunication systems the interferometer consists of optical waveguides fabricated from electrooptic active material (e.g. polymers or semiconductors). Typically, three different variants of waveguide structures are used to build Mach-Zehnder interferometric modulators. The simplest structure has a single input waveguide that splits into two arms for a certain distance L and recombines again to a single output waveguide (cf. Figure 2.1a). A more advantageous but also more complex structure integrates a so called 2x2 multi-mode interference coupler (MMI) that connects the two modulator branch waveguides to two output waveguides (cf. Figure 2.1b). The advantage of this approach is that during operation, light can exit the chip on both waveguides and no light is scattered inside the chip which would
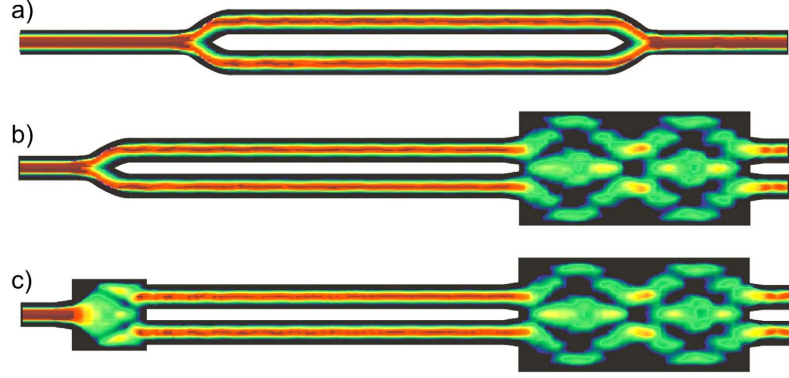
Fig. 2.1: Three types of Mach-Zehnder interferometric structures. a) interferometer with Y-branch splitter and a Y combiner. b) MZI with 2x2 multimode interference coupler (MMI) at the output. c) MZI with 1x2 MMI as power splitter at the input and 2x2 MMI at the output.
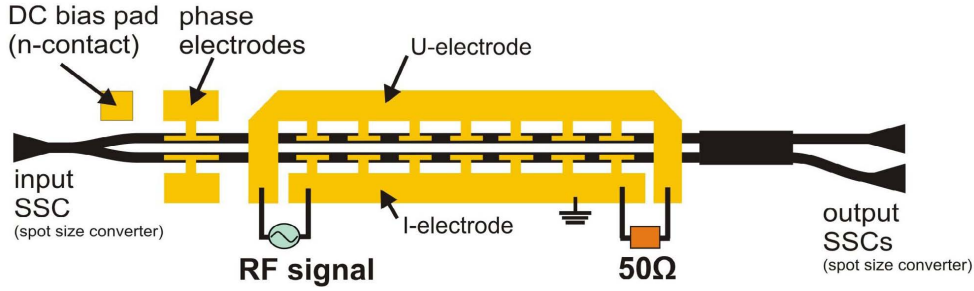
Fig. 2.2: Schematic of Mach-Zehnder modulator optical waveguide and electrical electrode layout.

cause unwanted back reflections and heating of the sample. Figure 2.1c shows an alternative to the Y-branch splitter at the input. In this case, a 1x2 MMI provides a more robust power splitting compared to a conventional Y-branch when fabrication tolerances are taken into account.

The on-off switching behavior of the MZ modulator is achieved by introducing a phase difference between both Mach-Zehnder arms before they recombine. For the MZI configuration with Y-branches at the input and the output, 0° phase difference equals a constructive interference giving the ON state for amplitude modulation. A phase difference of 180° between both arms results in destructive interference with no light being sent to the output (OFF state). The phase-amplitude correlation in an MMI is somewhat more complicated. If both arms of the interferometer have 0° or 180° phase difference, the optical power is equally split between both output ports. When the upper arm of the Mach-Zehnder modulator has +90° phase difference (with the optical field defined as $E(t) = E_0 e^{i\omega t}$) against the lower arm, the total optical power is transferred to the lower output waveguide while a -90° phase difference means that all light is fed to the upper output.
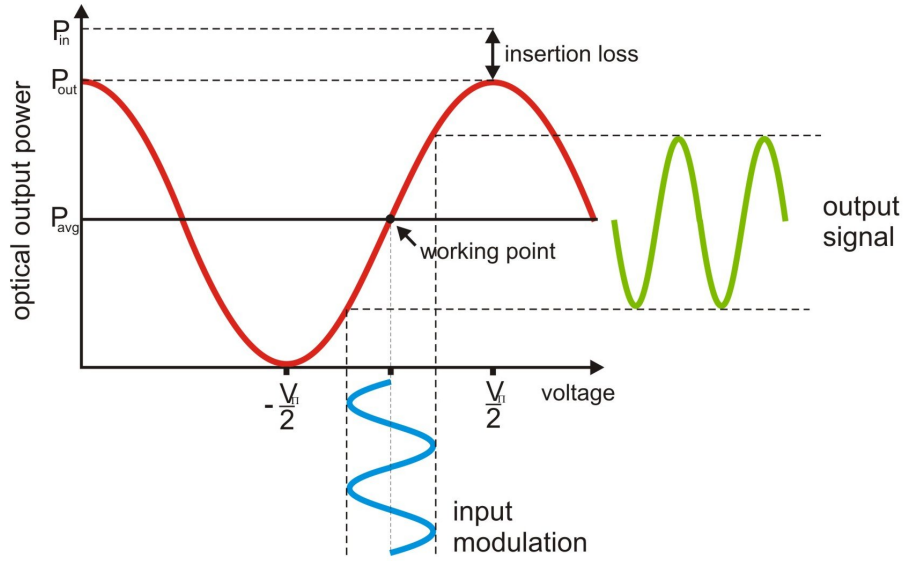
Fig. 2.3: Mach-Zehnder interferometer transfer function for MZI type b) and c) shown in Figure 2.1. The output signal power is a squared cosine function of the modulation voltage (cf. Equation (2.1)). For MZI type a) the ON state would have no applied voltage (0V).

The relation between the phase difference in both interferometer arms and the output power is given by the Mach-Zehnder transfer function. The transmitted optical power of the modulator is a squared cosine function of the applied voltage V and is given by [6]

$$T(V) = cos^2(\frac{\varphi_0}{2} - \frac{\pi V}{2V_\pi}). \tag{2.1}$$

φ_0 is the initial phase difference with no modulation voltage applied and V_π is the half-wave voltage of the modulator describing the required voltage to induce a 180° phase shift. Figure 2.3 shows the Mach-Zehnder transmittance as a function of an applied modulation voltage V. When reverse voltages are applied simultaneously to the upper U-electrode and the lower I-electrode (cf. Figure 2.2) of the Mach-Zehnder interferometer the so called output intensity matrix is obtained by measuring the optical power at one output of the MZM. A 2D and 3D representation of this intensity matrix is shown in Figure 2.4. The working point of the MZM is indicated by the yellow dot. The working point can be varied along the red dashed line by applying a variable DC bias voltage. During modulation between the on-state and the off-state the output power follows the black line in the 2D contour in Figure 2.4. This RF switching curve is given by the MZI transfer function plotted in Figure 2.3.
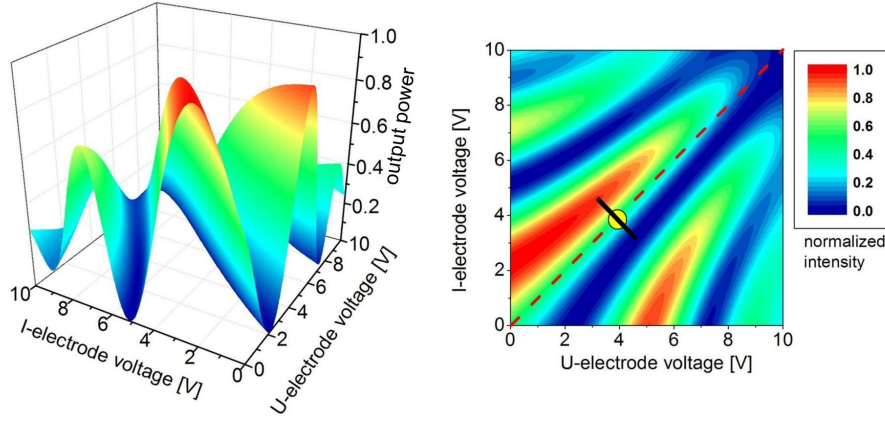
Fig. 2.4: Simulated Mach-Zehnder output intensity matrix in 3D and as a 2D contour plot. The output power is varied by applying different reverse voltages to the U- and the I-electrode (cf. Figure 2.2). The dashed red line presents possible working points. The yellow dot is the working point for 4V DC bias and the black line marks the MZI RF switching curve given by the MZI transfer function plotted in Figure 2.3.

2.3 Capacitively loaded traveling-wave electrodes (TWE)

A thorough design of the RF electrodes is essential for high-speed operation of Mach-Zehnder modulators. A 50 Ω impedance is required to match commercial driver electronics and test equipment. Otherwise power loss due to reflections and standing wave effects on the electrical transmission line (TL) would occur resulting in a reduction of the signal modulation quality. State of the art modulators make use of the traveling-wave electrode concept where the electrical and the optical wave travel at the same speed allowing the phase modulation of the optical carrier signal to accumulate along the path through the active sections of the optical waveguide. This approach leads to an increased bandwidth compared to conventional lumped electrode designs. A velocity mismatch between the optical and electrical wave causees a phase walkoff that, in the worst case, results in a cancelation of the initial modulation. The achievable 3-dB frequency (f_{3dB}) in the presence of velocity mismatch is given by [7]

$$f_{3dB} = \frac{1.4c}{L\pi(n_\mu - n_{opt})} \tag{2.2}$$

if ohmic and impedance mismatch losses are neglected (c: speed of light, L: length of the transmission line, n_μ and n_{opt} are the electrical microwave and optical refractive index, respectively).

For semiconductor (e.g. InP or GaAs) based modulators, the optical refractive index is always larger than the microwave index ($n_{opt} > n_\mu$). The optical index can only be modified by a few percent by using electro-optic effects (cf. Section 2.6). The only way to achieve velocity matching is to increase the microwave refractive index, i.e. to slow down the traveling electrical

wave. This is achieved by introducing capacitive loads along the transmission line. A schematic layout of a corresponding modulator electrode geometry is shown in Figure 2.5a. The left hand side shows the unloaded transmission line while the right hand side depicts the complete structure with capacitors connected to the large electrical transmission line (e.g. by small air bridges). Figure 2.5b is a schematic 3D drawing of a single period of the modulator. Under the assumption that the p-i-n waveguide structure is a parallel-plate capacitor, the loading sheet capacitance C_L (capacitance per unit length) is a) determined by the intrinsic region thickness (IRT) of the p-i-n junction which represents the thickness of the parallel-plate capacitor, and b) by the waveguide width which determines the area of the parallel-plate capacitor with a constant length L. In order to get the required amount of capacitive load per unit length, two approaches are commonly used: a continuous or a segmented traveling-wave electrode. The disadvantages of the continuous loading are a generally lower f_{3dB} frequency [8] and a reduced degree of freedom for the design of the optical waveguide. The only option to modify the loading capacitance of a continuous TWE is to vary the width of the optical waveguide. The segmented traveling wave design is more flexible as the sheet capacitance for the load can be set by the so called filling or fill factor (FF) which is given by FF = L/P as shown in Figure 2.5. P is the period length and L is the active length within P. The quantities L and P are key parameters for the design of the modulator using loading segments distributed along the electrical transmission line.

The design task for the capacitively loaded electrode starts with an unloaded transmission line who's microwave index is defined by the effective dielectric constant of the materials involved. Assuming that identical fractions of the microwave travel in air and the substrate material (InP:
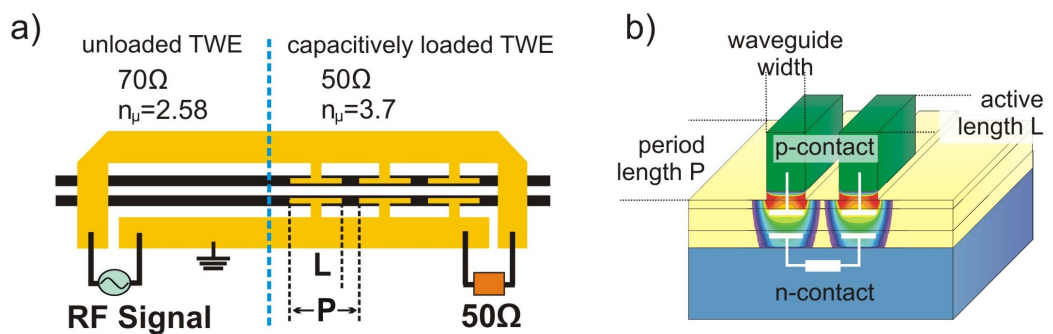
Fig. 2.5: Capacitive load principle of the traveling-wave electrode (TWE). a) unloaded TWE (impedance 70 Ω, microwave index n_μ=2.58) and the loaded TWE (impedance 50 Ω, microwave index n_μ=3.7). b) 3D schematic of the two waveguide capacitors of a single periodic section. The ratio L/P is the so called filling or fill factor (FF), which is an important quantity for RF design.

ϵ_r=12.5) the microwave refractive index is then given by [7]

$$n_\mu = \sqrt{(1 + \epsilon_r)/2} = 2.58 \tag{2.3}$$

The fundamental relations for the impedance and the microwave index [9] of a lossless transmission are given by

$$Z_\mu = \sqrt{\frac{L_\mu}{C_\mu}} \qquad\qquad n_\mu = c\sqrt{L_\mu C_\mu} \tag{2.4}$$

with L_μ and C_μ being the inductance and capacitance per unit length for the unloaded case. The inductance and capacitance per unit length in the case of capacitive loading are given by [8]

$$Z_0 = \sqrt{\frac{L_0}{C_\mu + C_L}} = 50\Omega \qquad\qquad n_\mu = c\sqrt{L_\mu(C_\mu + C_L)} = n_{opt} = 3.6. \tag{2.5}$$

From Equation (2.4) it is obvious that the unloaded inductance needs to be

$$L_\mu = \frac{n_{opt} Z_0}{c}. \tag{2.6}$$

Equation (2.4) also indicates that the load capacitance C_L of the transmission line should be

$$C_L = \frac{n_{opt}^2 - n_\mu^2}{c Z_0 n_{opt}}. \tag{2.7}$$

Simultaneous impedance matching and velocity matching can be achieved if the unloaded transmission line and the capacitive loading are designed to satisfy $n_\mu\, Z_\mu = n_{opt}\, Z_0$ and Equation (2.7). Using the microwave index from Equation (2.3), the unloaded sheet capacitance becomes $C_\mu \approx 121$ pF/m and the unloaded sheet inductance becomes $L_\mu \approx 600$ nH/m. The required load capacitance per unit length is $C_L \approx 119$ pF/m which is a fundamental value for a capacitively loaded transmission line having an unloaded microwave index of n_μ=2.58 and an optical waveguide group index of n_{opt}=3.7.

One design challenge is the so called Bragg frequency, which arises from the periodicity of the segmented capacitive loads. The Bragg frequency is the frequency at which the individual reflections from each of the periodically spaced air-bridges add up in phase to maximize the electrical reflection towards the input. The characteristic impedance of a transmission line goes to zero at the Bragg frequency, indicating no power transfer. This occurs at frequencies where the spacing between the small air bridges (= period length P in Figure 2.5) is 1/4 of the electrical wavelength on the transmission line. Due to the capacitive loading and the shunt inductance of the air-bridges, the Bragg frequency can be strongly reduced. It is given by [10]

$$f_{Bragg} = \frac{1}{\pi P\sqrt{L_\mu(C_\mu + C_L)}}. \tag{2.8}$$

with P being the period length. L_μ and C_μ are the transmission line inductance and capacitance, respectively, C_L is the capacitive load. As can be seen the from Equation (2.8) the Bragg frequency increases with shorter period lengths. An in-depth discussion of the traveling-wave electrode design will be given in Section 3.4.1.

2.4 The single drive series push-pull principle

In the Mach-Zehnder interferometric modulator, the active sections of both waveguide arms can be regarded as independent capacitors. Several possibilities exist to apply the required modulation voltage to both arms of the interferometer. A parallel cross-connection of the electrodes in the upper and the lower MZ arms is achieved by applying the voltages to both arms from two independent sources. If the two voltage sources are driven with 180° phase difference, push-pull operation is achieved but the capacitance is doubled at the same time. This operation mode is referred to as dual drive operation and requires an electrode layout comprising two signal lines, typically a twin GSG configuration (G=ground, S=signal). Mach-Zehnder modulators developed by NTT [3] make use of this electrode geometry. Single side drive operation is achieved if only one of the two individual interferometer arms is modulated.

A series connection of both p-i-n-diodes divides the modulating voltage between the two arms thus halving the external capacitance [11]. This is a big advantage because the filling factor of the segmented TWE can be twice the value as in the case of single side operation. Hence, the interaction length between the electrical and optical fields doubles which reduces the required driving voltage V_π. This single drive series push-pull drive is the most natural to be implemented in semiconductor modulators because of the built-in serial back-to-back connection of the two p-i-n diode capacitors via the n-contact (cf. Figure 2.5b). To achieve this series connection for the RF signal with simultaneous parallel connection for the DC bias, a monolithic RLC decoupling is implemented to permit a back-to-back connection of the p-i-n-diodes to float at RF while being held constant at DC level. Figure 2.6 gives a 3D sketch of the traveling wave electrode and the optical waveguides. While the RF signal floats through the n-contact between the two capacitors on a length of a few micrometers, the DC bias voltage is applied via the DC pad, which is typically several hundreds of micrometer away from the RF relevant capacitors. Another advantage of the push-pull operation is the ability to eliminate phase chirping of the output signal, which is due to the fact that the modulation voltage is always equally split between both MZI arms.
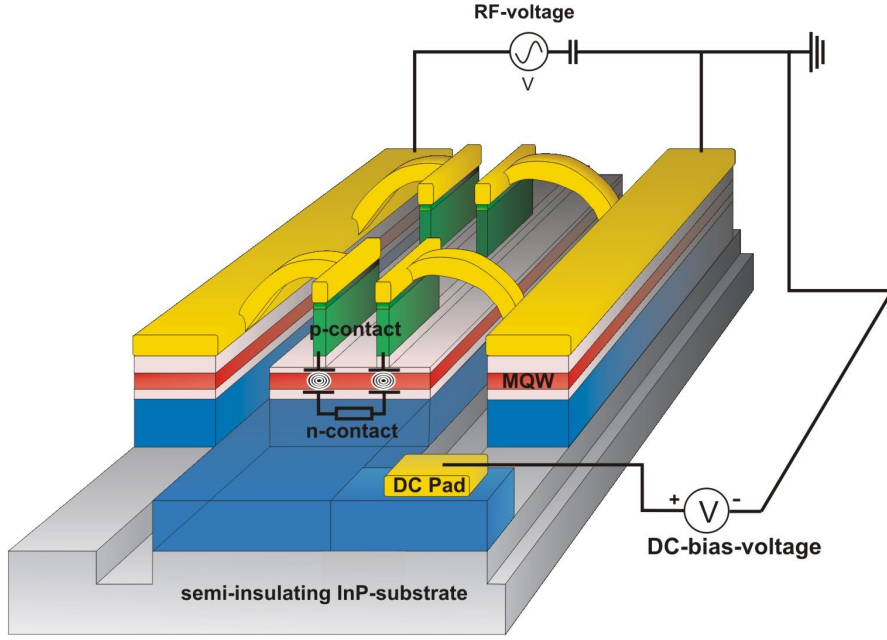
Fig. 2.6: 3D sketch of the traveling-wave electrode section with electric circuit for push-pull drive.

2.5 The interaction of light and matter

Absorption or gain and the refractive index of a material determine how light propagating through a medium is damped/amplified or changed in its frequency distribution. For the interferometric Mach-Zehnder modulator, a phase change induced by a variation of the refractive index is desired between both arms while no absorption of the optical power should occur. The interaction of an electrical field with a dielectric material is commonly described by its complex permittivity function [12]

$$\epsilon_{ij}(\omega) = \epsilon'_{ij}(\omega) + i \; \epsilon''_{ij}(\omega). \tag{2.9}$$

This permittivity depends on the angular frequency ω of the optical field having different values for high-frequency fields (ϵ_{opt}) and low frequency or static fields (ϵ_{st}). In case of homogenous and isotropic materials this tensor is reduced to a scalar function that can be written in terms of the complex refractive index

$$\bar{n}(\omega) = n_{opt}(\omega) + i \; \kappa(\omega) \tag{2.10}$$

which is often used instead of ϵ. n_{opt} denotes the real refractive index that reduces the free-space speed of light c_0 to $c = c_0/n_{opt}$. κ is the so called extinction coefficient which is related to the optical absorption coefficient by

$$\kappa(\omega) \;=\; \frac{1}{2}\frac{c}{\omega}\alpha(\omega) \;=\; \frac{1}{4}\frac{\lambda}{\pi}\alpha(\omega) \tag{2.11}$$

A set of only two material parameters fully describes the interaction between optical waves and matter: n_{opt} and $\kappa(\alpha)$, or ϵ' and ϵ''. The relation of the two sets is given by

$$\epsilon' = n_{opt}^2 - \kappa^2 \tag{2.12}$$

$$\epsilon'' = 2n_{opt}\kappa \tag{2.13}$$

$$n_{opt}^2 = \frac{1}{2}[\epsilon'(\omega) + \sqrt{\epsilon'^2(\omega) + \epsilon'^2(\omega)}] \tag{2.14}$$

$$\kappa^2 = \frac{1}{2}[-\epsilon'(\omega) + \sqrt{\epsilon'^2(\omega) + \epsilon''^2(\omega)}]. \tag{2.15}$$

In both cases the real and imaginary part satisfies the Kramers-Kronig relations [13]

$$\epsilon'(\omega_0) - 1 = \frac{2}{\pi\epsilon_0} \mathcal{P} \int_0^\infty \frac{\omega\epsilon''}{\omega^2 - \omega_0^2} d\omega \tag{2.16}$$

$$\epsilon''(\omega_0) = -\frac{2\omega_0}{\pi\epsilon_0} \mathcal{P} \int_0^\infty \frac{\epsilon'(\omega) - \epsilon_0}{\omega_0^2 - \omega^2} d\omega. \tag{2.17}$$

$\mathcal{P}$ indicates the Cauchy principle value that excludes the singular point $\omega_0 = \omega$. Kramers-Kronig relations allow the determination of either the real or the imaginary part of a physical response function provided that its complementary function is known over a sufficiently wide spectral range. For example, if the full absorption spectrum $\alpha_0(\omega)$ of a material is known the refractive index can be calculated at any frequency ω_0. It is quite common in theoretical material models to analyze the relevant absorption first and then derive the refractive index using Kramers–Kronig relations [14–18].

2.5.1 The dielectric function of harmonic oscillators

Electrons in the ground state of a semiconductor cannot move freely as they are bound to ions which keeps the 'ideal' semiconductor in an insulating state. However, in the excited states, electrons can move freely, similar to the conduction electrons of a metal. By absorbing a photon, an electron can be excited across the energy gap from the ground state to the lowest excited state. The classical oscillator model assumes that all electrons are bound to their positively charged ions by harmonic forces. If such a medium is excited by the periodic transverse electric field of a light beam, an electrical polarization is introduced due to a microscopic displacement of bound charges. This displacement of an electron from the equilibrium position can be described with the differential equation of motion of a classic harmonic oscillator. For a time harmonic

optical electromagnetic field $E(t) = E_0 e^{i(\omega t - kx)}$, the polarization density P_{den} due to N atoms per unit volume is given by [19]

$$P_{\text{den}} = Np = \frac{Nq^2 E(t)}{m_0(-\omega^2 - i\gamma\omega + \omega_0^2)} \tag{2.18}$$

where γ is the damping factor of the oscillator and $\omega_0 = \sqrt{k/m_0}$ is the resonance frequency with the spring constant k and the free electron mass m_0. The displacement vector D is then given by

$$D = \epsilon_0 E + P_b + P_{\text{den}} = \epsilon_0 \left[1 + \chi_b + \frac{Nq^2}{m_0\epsilon_0(-\omega^2 - i\gamma\omega + \omega_0^2)} \right] E \tag{2.19}$$

where the background polarization $P_b = \epsilon_0 \chi_b E$ has been included. The permittivity function (2.9) for the resonant dielectric medium is obtained as

$$\epsilon(\omega) = \epsilon_0 \left[1 + \chi_b + \chi(\omega) \right] \tag{2.20}$$

with

$$\chi(\omega) = \frac{\omega_p^2}{(-\omega^2 - i\gamma\omega + \omega_0^2)} \tag{2.21}$$

being the optical susceptibility where

$$\omega_p = \sqrt{\frac{Nq^2}{m_0\epsilon_0}} \tag{2.22}$$

is the plasma frequency at which the electron plasma density oscillates around the position of the positively charged nuclei. As the optical susceptibility is a complex function, it can be separated into a real and an imaginary part $\chi(\omega) = \chi'(\omega) + i\chi''(\omega)$. The permittivity or dielectric function is then given by

$$\epsilon'(\omega) = 1 + \chi_b + \chi'(\omega) \tag{2.23a}$$

$$\epsilon''(\omega) = \chi''(\omega) \tag{2.23b}$$

Absorption coefficient and refractive index

For the design of MQW electro-absorption or electro-refraction modulators the complex dielectric function needs to be known over a sufficiently wide spectral range. In addition, the chirp parameter, which is an important modulator parameter in an on-off keyed transmission system, can only be evaluated if both the real and imaginary parts are known. For a plane wave propagating through a dielectric medium the complex propagation constant can be written as [19]

$$k(\omega) = \omega\sqrt{\mu_0\epsilon} = k_0 n_b + k_0 \Delta n_{opt}(\omega) + i\frac{\alpha(\omega)}{2} \tag{2.24}$$

with the background refractive index $n_b = \sqrt{\epsilon_b/\epsilon_0}$.

The optical absorption coefficient α determines the decay of the power of a plane wave in a dielectric medium and is given as two times the imaginary part of the complex propagation constant (cf. Equation (2.24))

$$\alpha(\omega) = \frac{k_0}{n_b}\chi''(\omega). \tag{2.25}$$

The total refractive index is given by

$$n_{opt}(\omega) = n_b + \Delta n_{opt}(\omega) = n_b + \frac{1}{2n_b}\chi'(\omega). \tag{2.26}$$

So far the classical approach using the harmonic oscillator theory has been used to describe the interaction of a light beam with a dielectric medium. To study optical transitions in semiconductor heterostructures, especially in quantum wells with a dimensionality comparable to the *de Broglie* wavelength of the related carriers, quantum mechanics needs to be used in order to appropriately describe the interaction of electrons and holes with an electromagnetic field.

A common approach to determine the optical absorption spectrum of a semiconductor is the application of Fermi's golden rule to calculate the transition rate from one energy state to another due to a perturbation. In general the absorption coefficient α (1/cm) is the number of photons absorbed per unit volume divided by the number of photons injected per unit area. The absorption coefficient using the total transition rate R_α is then given by [19]

$$
\begin{aligned}
\alpha(\hbar\omega) &= \frac{\hbar\omega}{(n_{opt}c\epsilon_0\omega^2 A_0^2/2)}R_\alpha \\
&= C_0\frac{2}{V}\sum_k |\hat{\mathbf{e}}\cdot\mathbf{p}_{cv}|^2\,\delta(E_c - E_v - \hbar\omega)(f_v(k) - f_c(k))
\end{aligned} \tag{2.27}
$$

with

$$C_0 = \frac{\pi e^2}{n_{opt}c\epsilon_0\,m_0^2\,\omega} \tag{2.28}$$

and $f_v(k)$ and $f_c(k)$ being the Fermi-Dirac distributions of the electrons in the valence and conduction band, respectively. The Dirac-delta function δ in real QWs is commonly replaced by a Lorentzian function with a finite linewidth to account for scattering processes and material imperfections. The momentum matrix element $|\hat{\mathbf{e}}\cdot\mathbf{p}_{cv}|$ describes an electron transition probability from the valence to the conduction band by obeying the selection rules for allowed and forbidden transitions. The approach based on Fermi's golden rule requires the Kramers-Kronig relation (2.16) to calculate the refractive index in order to get the total complex dielectric function. As the integrals must be evaluated for each wavelength of interest, this approach is time-consuming and the result depends on the integration boundaries used.

An alternative to calculate the absorption coefficient of a semiconductor is to use the density matrix approach [20]. The semiconductor is described by quantum mechanical operator dynamics and the dielectric linear response of electron-hole pairs to an applied electric field is then described by wave equations. In contrast to Fermi's golden rule, no Kramers-Kronig calculations are required as the absorption and refractive index can be directly calculated from the real and imaginary part of the complex susceptibility. The application of the density matrix approach is superior to other approaches because it allows a flexible inclusion of physical effects (e.g. exciton and phonon interactions) as well as optical nonlinearities. An in depth discussion of this approach can be found in [21].

2.6 Electro-optic effects in semiconductors

This section introduces the main physical effects which can be used in electro-optic modulators to vary the dielectric function of the optical waveguide material. Electro-absorption modulators are based on a variation of the absorption coefficient while interferometric Mach-Zehnder type modulators make use of a refractive index change. In principle, all electro-optic effects can be separated into two classes: field effects (absorption and refractive index change are induced by an external electric field) and carrier effects (a variation of the free carrier concentration in a semiconductor varies the dielectric properties). The electric field related effects can again be divided into two subclasses. The Pockels effect and Kerr effect are present in every dielectric medium while the Franz-Keldysh effect (FKE) and the Quantum-Confined Stark effect (QCSE) are electro-optic effects that involve the band gap of semiconductors. Carrier induced electro optic effects, that are only present in semiconductors, do not play a role in high speed optical modulation today compared to a few decades ago [22–24] Today's modulation bandwidth requirements of ≈ 40 GHz can not be obtained by varying the free carrier density in a semiconductor. The contribution of carrier escape times from QWs is significant, as carrier tunneling through the barriers largely depends on the barrier height and width [25] as well as the applied reverse voltage [26]. The InP-based MZ modulator developed in this work rely on the QCSE which modulates the optical phase in the MQW core waveguide for high-speed modulation. Nevertheless, carrier injection to the phase electrodes (cf. Figure 2.2) can be used to set the correct working point of the MZM.

2.6.1 Field effects

Pockels and Kerr effect

The linear electro-optic effect (LEO), also known as Pockels effect, is related to the electric field induced biaxial birefringence which is caused by a redistribution of bound carriers leading to a variation of the materials polarization density [23]. The change of the inverse permittivity tensor ($\mathbf{S}= \epsilon^{-1}$) is, according to the name, linearly proportional to the applied electric field (first order Stark effect) and can be written as [19]

$$\epsilon_0 \Delta S_{ij} = \sum_k r_{ij,k} E_k ... \tag{2.29}$$

$r_{ij,k}$ are the so called Pockels coefficients and E_k is the applied electric field. The linear electro-optic effect only occurs in crystals which have no inversion symmetry as the index ellipsoid function has to be invariant against sign reversal of the electric field. For the case of cubic crystals which includes zinc-blende-type semiconductors like InP and GaAs, the matrix $r_{ij,k}$ of Pockels coefficients possesses only three non-zero and equal tensor components $r_{41} = r_{52} = r_{63}$ [27]. For an external electric field in z-direction ($E_1 = E_2 = 0$, $E_3 = z$), the new index ellipsoid takes the form

$$\frac{x^2}{n_{opt}^2} + \frac{y^2}{n_{opt}^2} + 2r_{41}E_3 xy + \frac{z^2}{n_{opt}^2} = 1. \tag{2.30}$$

where n_0 is the material refractive index without applied electric field. With the assumption that $r_{41}E_3 \ll n_0^{-2}$, the refractive index in the x-y-plane with an applied electric field can be written as

$$n_{x'} = n_{opt} + \frac{1}{2} n_{opt}^3 r_{41} E_3 \tag{2.31a}$$

$$n_{y'} = n_{opt} - \frac{1}{2} n_{opt}^3 r_{41} E_3 \tag{2.31b}$$

As can be seen in Equation (2.31), the change of the index of refraction

$$\Delta n_{\text{LEO}} = \frac{1}{2} n_{opt}^3 \, r_{41} \cdot E. \tag{2.32}$$

has a positive and a negative component depending on the crystal orientation. If the z-direction of an electric field is oriented along the (001) crystal axis an optical wave traveling along the (110) direction experiences a negative index change while an optical wave traveling along the ($\bar{1}$10) direction experiences a positive change of the index of refraction. One important aspect of Equation (2.31) is that the refractive index change only occurs in the x-y-plane. TM polarized light with an electric field vector in z-direction does not experience an index change at all. Only

TE polarized optical waves are influenced by the Pockels Effect. Table 2.1 lists Pockels coefficients for photon wavelengths within the C-band (1528 nm -1567 nm) derived from Adachi's model in [28]. The wavelength dependence for InP is negligible while an increasing photoluminescence wavelength of InGaAsP increases the wavelength dependence and the linear effect itself.

10^{-12} [m/V]	1528 nm	1540 nm	1550 nm	1560 nm	1567 nm
InP	-1.341	-1.341	-1.340	-1.340	-1.339
InGaAsP Q1.06	-1.437	-1.436	-1.435	-1.434	-1.433
InGaAsP Q1.15	-1.501	-1.499	-1.497	-1.495	-1.493
InGaAsP Q1.45	-1.916	-1.884	-1.857	-1.833	-1.813

Tab. 2.1: Pockels coefficients $r_{41}(10^{-12} m/V)$ of InP and related quaternaries derived from Adachi's model [28] for specific photon wavelengths within the C-band.

The extension of Equation (2.29) to include a second order distortion of the polarization density leads to the quadratic electro-optic effect (QEO), also known as Kerr effect. The change of the inverse dielectric constant is then expressed as

$$\epsilon_0 \Delta S_{ij} = \sum_k r_{ij,k} E_k + \sum_k \sum_l K_{ijkl} E_k E_l + ... \tag{2.33}$$

Higher than second order terms are generally neglected. The refractive index change in InP-based materials induced by the Kerr effect is much smaller compared to the Pockels effect for electrical field strengths (up to 100 kV/cm) that are commonly used in Mach-Zehnder modulators. Nevertheless in crystals having an inversion symmetry the quadratic electro-optic effect dominates because of the absence of the Pockels Effect. In zinc-blende-type crystals the only non-vanishing tensor components are K_{11}, K_{12} and K_{44}. In isotropic media the relation $K_{44} = \frac{1}{2}(K_{11} - K_{12})$ is valid. Therefore, Kerr coefficients are often expressed as $(K_{11} - K_{12})$ in the literature [29]. In analogy to the Pockels effect the change of the index of refraction due to the Kerr Effect is written as

$$\Delta n_{QEO} = \frac{1}{2} n_{opt}^3 (K_{11} - K_{12}) \cdot E^2. \tag{2.34}$$

The QEO is polarization independent as it is an isotropic effect. A detailed discussion of the Kerr effect in InP and InGaAsP was published by Adachi et al. [29].

Franz-Keldysh effect

In addition to the electro-optic effects introduced above, which are present in any crystalline material, the band gap of semiconductors introduces a new mechanism to change absorption and the refractive index with an applied electric field. The Franz-Keldysh effect, independently discovered by W. Franz [30] and V. Keldysh [31], is related to optical interband absorption near the semiconductor band gap in the presence of an electric field. It is a photon assisted tunneling effect. The energy band profile is tilted along the direction of the applied electric field allowing the wave functions of electrons and holes to penetrate into the band gap. A photon with an energy slightly below the gap energy can now be absorbed due to the non zero overlap between the electron and hole wave functions (cf. Fig. 2.7). Therefore, transitions from the valence to the conduction band are enhanced leading to an exponential tail in the absorption spectrum below the band gap (cf. Fig. 2.8). The work of Franz and Keldysh has been extended by Callaway [32] and Tharmalingam [33] for energies above the band gap. In this energy region the absorption spectrum shows a typical oscillatory behavior (cf. Figure 2.8) due to the nature of the wave functions of electrons and holes with an applied electric field. In order to calculate the absorption coefficient Tharmalingam [33] considers a free electron-hole pair in an electric field in z-direction where the Schrödinger equation is given by

$$\left(\frac{-\hbar^2}{2m_r} \frac{d^2}{dz^2} + qEz \right) \phi(z) = E_z \phi(z). \tag{2.35}$$
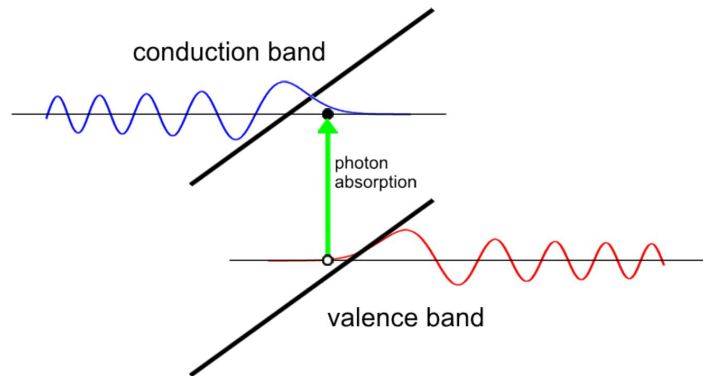
Fig. 2.7: Franz-Keldysh effect or photon-assisted absorption in a bulk semiconductor in the presence of an electric field. The wavefunctions of electrons and holes tunnel into the band gap region allowing absorption for photon energies below E_g.

21
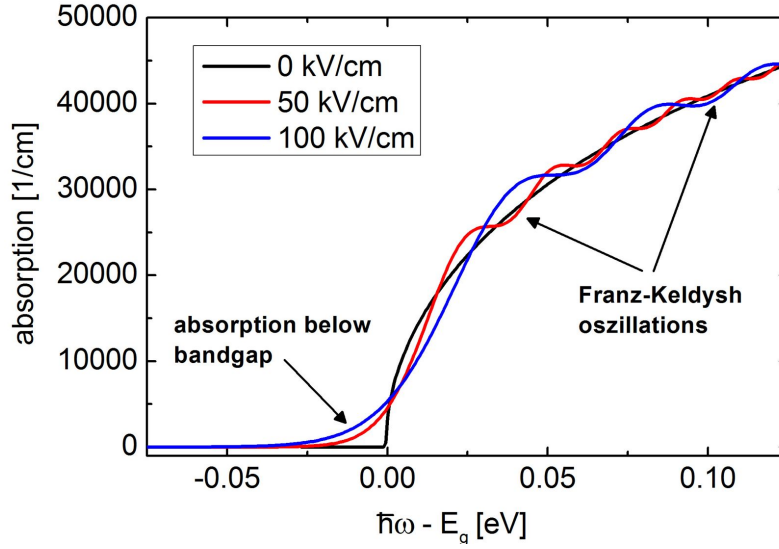
Fig. 2.8: Calculated absorption spectra of bulk InGaAsP (λ_g = 1420 nm) for applied electric fields of 0kV/cm, 50kV/cm and 100kV/cm using Equation (2.36). Typical Franz-Keldysh oscillations above the band gap and absorption tails below the bandgap are present for electric fields of 50kV/cm and 100kV/cm.

The solutions of a differential equation of this kind leads to an absorption coefficient that takes the form

$$\alpha(\hbar\omega) = \frac{A_0}{2\pi} \left(\frac{2m_r}{\hbar^2} \right)^{3/2} \sqrt{\hbar\theta_F} \left[-\eta Ai^2(\eta) + Ai'^2(\eta) \right]. \tag{2.36}$$

where the solution for a vanishing electric field $E \rightarrow 0$ leads to the well know absorption formula for intrinsic semiconductors

$$\alpha(\hbar\omega) \xrightarrow[E\to 0]{} \alpha_0(\hbar\omega) = A_0 \frac{1}{2\pi^2} \left(\frac{2m_r}{\hbar^2} \right)^{3/2} \sqrt{\hbar\omega - E_g}. \tag{2.37}$$

The factor $A_0 = C_0 \cdot |\hat{\mathbf{e}} \cdot \mathbf{p}_{lv}|^2$ is the momentum matrix element of a bulk semiconductor with C_0 given by Equation (2.28). Coulomb interaction between the electron and the hole involved in the absorption process are neglected for simplicity reasons. A detailed derivation of Equation (2.36) can be found in [19]. The Franz-Keldysh effect is polarization insensitive as the momentum matrix elements for incident optical waves with polarization vectors parallel and perpendicular to the electric field vector are similar in the case of allowed transitions. The refractive index change due to the Franz-Keldysh effect can by calculated using the Kramers-Kronig relation (2.16) of the obtained absorption spectrum.

$$\Delta n(\omega, E) = \frac{c}{\pi} \int_0^\infty \frac{\Delta\alpha(\omega', E)}{(\omega')^2 - \omega^2} d\omega' \tag{2.38}$$

Excitonic effects in semiconductors

The description of the Franz-Keldysh effect in the last section neglected the Coulomb interaction between electrons and holes generated during the absorption process. If the energy of an absorbed photon is larger than the band gap, a free electron is generated leaving an empty hole state in the valence band. Both the electron and the hole move to the lowest energy state within their respective band while the attractive potential between the negatively charged electron and the positively charged hole form an electron-hole pair known as 'exciton'. Photons with energies just below the band gap can be absorbed due to the reduced total energy of the exciton in a direct resonant exciton process. In general, the binding energy of excitons in bulk semiconductors is low and thus their influence on the absorption at room temperature is negligible. To include excitonic effects for bulk semiconductors [34] the Coulomb interaction

$$V(r) = \frac{-e^2}{4\pi\epsilon_s r} \tag{2.39}$$

has to be taken into account for the solution of the Schrödinger equation

$$\left(\frac{-\hbar^2}{2m_r} \frac{d^2}{dz^2} + V(r) \right) \phi(r) = E\phi(r). \tag{2.40}$$

As the hole mass is generally much greater than the electron mass, the electron-hole pair resembles a hydrogen atom. The binding energy and the orbital radius can thus be represented by Bohr's theory with the correction of replacing the electron mass with the reduced mass μ of the two-body system. The 3D exciton binding energy becomes [35]

$$E_{X3D} = -\frac{R_y}{s^2} \qquad R_y = \frac{m_r \, e^4}{2\hbar^2 (4\pi \, \epsilon_r \epsilon_0)^2} \tag{2.41}$$

where s is the number of the sth eigenvalue of Equation (2.40). R_y is the so called exciton Rydberg energy. The exciton binding energy of bulk InP using m_e=0.077 m_0 and m_{hh}=0.60 m_0 is $E_X \simeq 7$ meV. Compared to the thermal energy of a particle at room temperature which is $k_B T$ $\simeq 25$ meV it is obvious that 3D excitons in bulk InP dissociate in a very short time (typically a few hundred fs).

This dissociation time increases when the mobility of the electron-hole pair is restricted to a 2D plane in semiconductor heterostructures where the total energy of the exciton has additional components due to the electron and hole confinement energies [36]. In the case of a 2D exciton the binding energy can be written as

$$E_{X2D} = -\frac{R_y}{\left(s - \frac{1}{2}\right)^2} \tag{2.42}$$
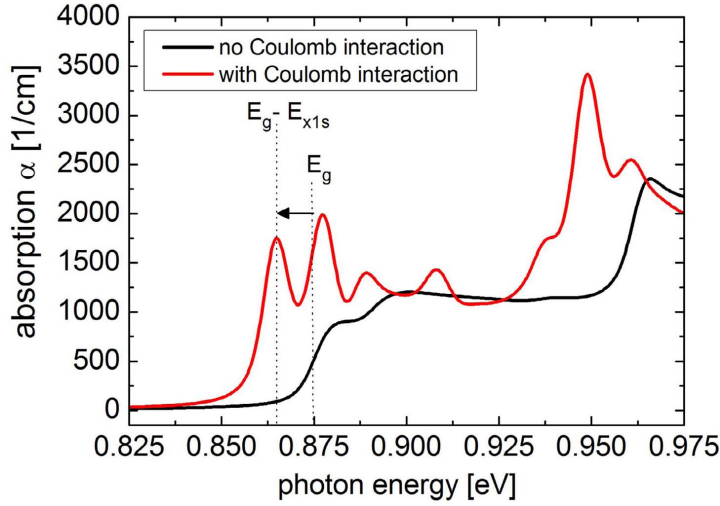
Fig. 2.9: Calculated room temperature absorption spectra of a single 12 nm wide InGaAsP/InP quantum well with (red) and without (black) excitonic effects due to Coulomb interaction.

giving a fourfold increase of the binding energy of the lowest energy state (s=1). For quantum well (QW) heterostructures with a finite thickness the true exciton binding energy lies somewhere between the 3D and 2D values. A detailed calculation of exciton binding energies can be found in reference [35]. The strength of the exciton binding energy is relevant for the absorption coefficient at photon energies close to the band gap. Figure 2.9 shows simulated absorption spectra for a single 12 nm wide quantum well at room temperature with and without excitonic effects due to Coulomb coupling of electrons and holes. The spectra have been calculated using *SimuLase* [37].

Quantum-Confined Stark effect

The impact of an electric field on the absorption and refractive index has only been discussed for bulk semiconductors so far. New phenomena arise if semiconductors are fabricated as heterostructures in such low dimensions that quantum effects dominate. The possibility to grow semiconductors in layers of only a few nm thickness enabled various combinations of thin semiconductor heterostructures such as coupled quantum wells (CQW) [14], asymmetric coupled quantum wells (ACQW) [38, 39], coupled three-quantum-well structures [18] and even more sophisticated structures like five-step asymmetric coupled quantum wells [40]. Considering a single quantum well placed in an electric field perpendicular to the quantum well layer, the so called Quantum-Confined Stark effect (QCSE) forces a shift of the band gap towards lower energies and a decrease of the absorption coefficient for energies above the band gap. An illustration of the Quantum-Confined Stark effect is shown in Figure 2.10. The explanation for
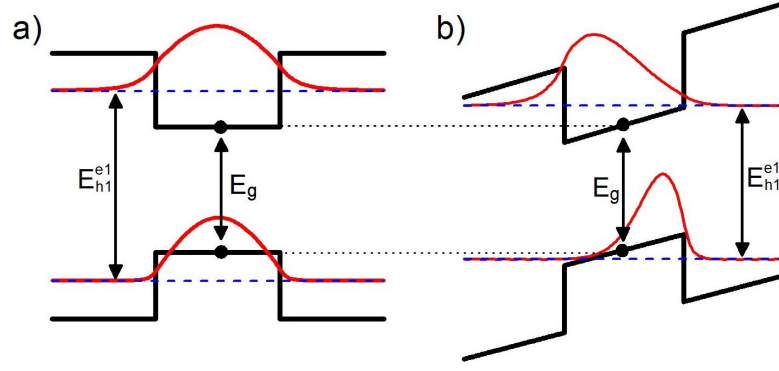
Fig. 2.10: Illustration of the Quantum-Confined Stark effect. The band edge and wavefunctions are plotted without (a) and with (b) applied electric field.

the QW band edge absorption has been given by Miller et al. [41] in 1984. The electric field pulls the electrons and holes towards opposite sides of the layer resulting in an overall net reduction to the energy of the electron-hole pair and a corresponding shift of the exciton absorption. Bastard et al. [42] found the following electric field dependence for the lowest transition energy

$$\Delta E_g = const. \cdot E^2 W_{\text{QW}}^4 \tag{2.43}$$

in a quantum well with infinite barrier height. The exciton energy shift is proportional to the square of the applied electric field E and the fourth power of quantum well width W_{QW}. The field-dependent binding energy of the exciton has been investigated by Brum et al. [43]. It was found that the binding energy is less affected by an electric field in thin quantum wells (<7 nm) but has an increasing field dependence for increasing well width. The result for a quantum well with finite well depth is that the exciton shift does not follow a simple squared relation as in Equation (2.43). A term linear in field has to be added to account for the described effects. In general to increase the energy shift and also the confinement of the optical field in the quantum well, thicker wells are desirable. However, as the well widens the absorption decreases as the overlap of electron and hole wavefunctions decreases, thus reducing the oscillator strength of the electron-hole pair. Unlike the Franz-Keldysh effect, the QCSE is highly polarization dependent. The momentum matrix elements $|\hat{\mathbf{e}} \cdot \mathbf{p}_{cv}|^2$ in Equation (2.27) differs for transverse electric (TE) and transverse magnetic (TM) polarized light. For TE polarized light, the matrix elements are [44]

$$|\hat{\mathbf{e}} \cdot \mathbf{p}_{lv}|^2 = M_b^2 \begin{cases} 3/2 & \text{for heavy holes} \\ 1/2 & \text{for light holes} \end{cases}. \tag{2.44}$$
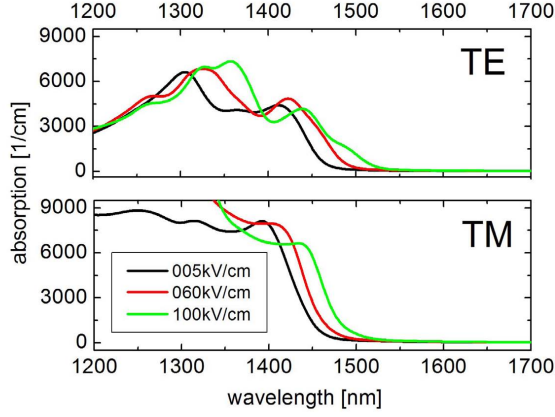
Fig. 2.11: Absorption spectra of a 12 nm InGaAsP QW at 5 kV/cm, 60 kV/cm and 100 kV/cm applied electric field for TE and TM polarization simulated with SimuLase [37].
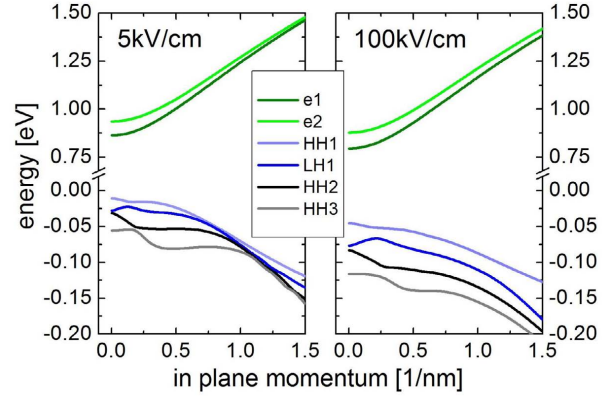
Fig. 2.12: Calculated subbands of the two lowest energy electrons and 4 lowest energy holes of a 12 nm InGaAsP QW for 5 kV/cm and 100 kV/cm electric field.

and for TM polarized light

$$|\hat{\mathbf{e}} \cdot \mathbf{p}_{lv}|^2 = M_b^2 \begin{cases} 0 & \text{for heavy holes} \\ 2 & \text{for light holes} \end{cases}. \tag{2.45}$$

where M_b^2 is the momentum matrix element of a bulk semiconductor. The fact that heavy and light hole subbands are degenerated in QWs (cf. Figure 2.12) and the finding that only light holes take part in the absorption process for TM polarized light prove the strong polarization dependence of the absorption in quantum wells. Furthermore, the degeneration of heavy and light hole levels in QWs is accompanied by a strong interaction causing a substantial deformation of the valence subbands. The non-parabolic shape of the subbands resulting from this interaction is shown in Figure 2.12 (calculated with *SimuLase* [37] using two electron and four hole subbands, 12 nm InGaAsP/InP QW, electric fields of 5 kV/cm and 100 kV/cm). To accurately model the electric field dependent absorption and refractive index change in MQWs the effective mass model for parabolic bands can no longer be applied. But reliable modeling of the electro-refraction in the MQW core waveguide of the MZ modulator developed in this work is essential. More sophisticated models like the multiband envelope function (k·p) method need to be used to accurately model the coupling between the subbands. Figure 2.11 shows simulated absorption spectra of a 12 nm InGaAsP/InP quantum well with applied electric fields of 5 kV/cm, 60 kV/cm and 100 kV/cm for TE and TM polarization. For TE polarization the exciton and the band absorption increases with increasing field from 5 kV/cm to 60 kV/cm which is contradictory to the general understanding of a reduced absorption due to a reduced oscillator strength. This effect is due to strong band mixing. At zero field the lowest band has heavy hole

(HH) character for very small in-plane momentum but then quickly turns to light hole (LH) character for higher in-plane momentums which can be seen for the HH1-band in Figure 2.12. In TM polarization, which only involves light holes, this leads to vanishing band absorption as with increasing field the character at higher momentum gets a larger admixture of heavy-hole character.

Wannier-Stark effect

The Wannier-Stark effect (WSE) is another electro-optic effect present in quantum well materials. Other than for the QCSE, two or more quantum wells separated by very thin barriers are required to get the so called Wannier-Stark localization resulting from a resonant tunneling effect. The effect can be observed by so called Stark ladders in absorption spectra of semiconductor superlattices [45]. If the barrier width is chosen small enough to allow electron and/or hole wavefunctions to tunnel through the barrier into adjacent wells, delocalized mini bands are formed in each quantum well if no electric field is applied. To some extent this structure exhibits a three dimensional behavior. The application of a low electric field to such a structure breaks the resonance when the energy levels of two neighboring quantum wells are misaligned by eFd (e: electron charge, F: applied field, d: the periodic length of the multi quantum wells). Under these conditions, electrons and holes localize and a pure two dimensional behavior is obtained. The Wannier-Stark effect has been used in optical modulators several times [18, 46, 47] and a better modulation efficiency in terms of drive voltage was reported many times [14, 48, 49]. But the barrier width of only several mono layers has to be controlled precisely, and as a consequence this approach is not suitable for high yield manufacturing of electro-optical devices using high volume MOCVD growth reactors.

2.6.2 Carrier effects

The carrier induced refractive index change has been used in semiconductor modulators a few decades ago but today's modulation bandwidth requirements of > 40 GHz does not allow their application anymore. But carrier related effects are still used to control the optimum working point of high-speed semiconductor Mach-Zehnder modulators by injecting current to the phase electrodes (cf. Figure 2.2). Another important area where carrier effects have to be taken into account is absorption and refractive index change in doped semiconductors. The refractive index change due to n-type doping has a strong impact on the calculation of optical waveguide modes which is demonstrated in Section 3.2.1. P- and n-type doping lead to an increase of

the optical absorption which negatively influences the total insertion loss of a modulator [50, 51]. This is of great importance when the waveguide doping profile of the MZ modulator is optimized for low insertion loss in Section 3.2.2. The three known electro-optic carrier effects will be introduced in the following sections.

Plasma effect

When free carriers are present in either the conduction or valence band of a semiconductor, photon absorption can occur which implies a transition to a higher-energy state in the same band. This absorption process is called Plasma effect. It requires the interaction with lattice vibrations via phonos or scattering with ionized impurities to satisfy the requirement of momentum conservation. Because transitions inside the same band involve small energy changes, the plasma effect especially contributes to the absorption at longer wavelengths. The change of the refractive index has been derived by Henry et al. [52]. Inserting the values of the fundamental constants gives [22]

$$\Delta n_{opt}(\omega) = \frac{-6.9 \cdot 10^{-22}}{n_{opt}(\hbar\omega)^2} \left(\frac{N}{m_e} + P_{\text{holes}} \left(\frac{m_{hh}^{1/2} + m_{lh}^{1/2}}{m_{hh}^{3/2} + m_{lh}^{3/2}} \right) \right) \tag{2.46}$$

where the electron concentration N and the hole concentration P_{holes} are expressed in $1/cm^3$. $\hbar\omega$ is the photon energy in eV and the effective masses are given in units of m_0. n_{opt} is the intrinsic refractive index of the material. If we choose for example InGaAsP with a band gap wavelength λ_g=1420 nm, the carrier effective masses are given as $m_e = 0.05m_0$, $m_{hh} = 0.46m_0$ and $m_{lh} = 0.062m_0$ [27]. The influence of the electron concentration on the free carrier refractive index change is seven times larger than that of holes and is $\Delta n = -6.7 \cdot 10^{-5}$ at λ=1550 nm for an electron and hole concentration N=P_{holes}=$1 \cdot 10^{16}$ cm^{-3}. The refractive index change induced by the Plasma effect is always negative for energies below the band gap and increases when the photon energy is decreased.

Bandfilling effect

Another carrier related electro-optic effect is the so called the Burstein-Moss effect [53, 54] or bandfilling effect. A decrease of the absorption coefficient for photon energies slightly above the band gap in doped semiconductors is observed and is most pronounced in semiconductors having small effective masses. In the case of n-doped semiconductors, the density of states in the conduction band is very low and a relatively small number of electrons fills the conduction band to a noticeable depth. With the lowest energy states in the conduction band occupied,

optically excited electrons from the valence band require larger energies than the nominal band gap. Thus, the 'observed' band gap is increased. For holes in p-doped semiconductors, the situation is similar, but their larger effective mass goes along with a higher density of states and hence a smaller bandfilling effect for a given carrier concentration [22].

$$\Delta\alpha(N, P_{\text{holes}}, \hbar\omega) = \frac{C_{hh}}{\hbar\omega}\sqrt{\hbar\omega - E_g}\left[f_v(E_h) - f_c(E_h) - 1\right]$$
$$+ \frac{C_{lh}}{\hbar\omega}\sqrt{\hbar\omega - E_g}\left[f_v(E_l) - f_c(E_l) - 1\right] \tag{2.47}$$

with $f_v(E_h)$, $f_c(E_h)$, $f_v(E_l)$ and $f_c(E_l)$ being the Fermi-Dirac distributions for the valence (v) and conduction (c) bands that determine the probabilities for a band state being occupied by a respective carrier. The subscripts h and l refer to heavy and light holes, respectively while C_{hh} and C_{lh} are fitting parameters for heavy and light holes that need to be derived from experimental absorption data. The refractive index change induced by band filling once again can be calculated via Kramers-Kronig transformation of the absorption spectrum.

$$\Delta n_{opt}(N, P_{\text{holes}}, \hbar\omega) = \frac{2c}{he^2}\mathcal{P}\int_0^\infty \frac{\Delta\alpha(N, P_{\text{holes}}, \hbar\omega')}{(\omega'^2 - \omega^2)}d\omega' \tag{2.48}$$

After Bennett et al. [22], the refractive index change is linear for carrier concentration in the range from $10^{16} - 10^{18}/cm^3$ for photon energies below the band gap in InP and can be expressed as

$$\Delta n_{opt}(\text{InP}) \cong -5.6 \cdot 10^{-21} \cdot K \quad (\lambda = 1550nm) \tag{2.49}$$

where K is the carrier concentration of either electrons (N) or holes (P_{holes}). Taking $C_{hh} = 2.1 \cdot 10^{12}cm^{-1} \cdot s^{-1/2}$ and $C_{lh} = 1.1 \cdot 10^{12}cm^{-1} \cdot s^{-1/2}$ from reference [22] into Equation (2.47) allows the calculation of the refractive index change for the quaternary alloy $In_{1-x}Ga_xAs_yP_{1-y}$ where x and y are the material composition parameters with x=0.47y in the case of lattice matching to InP. Using $E_g = 1.35 - 0.72y + 0.12y^2$ (after [55]) for the compositional variation of the band gap we get

$$\Delta n_{opt} \approx -3 \cdot 10^{-20} \cdot K \quad (\lambda = 1550nm) \tag{2.50}$$

for a material composition y=0.76 which is typically used for the modulators presented in this thesis. It can be seen that the bandfilling effect is larger in quaternary InGaAsP than in pure InP and is again negative for photon energies below the band gap thus adding to the index change induced by free carrier absorption.

Band gap shrinkage effect

The third carrier induced electro-optic effect leading to a variation of the dielectric function of semiconductors is the band gap shrinkage effect. The basic mechanism behind this effect is the occupation of bottom states in the conduction band by injected electrons. If the concentration of electrons is large enough their wavefunctions will start to overlap causing a repelling force due to Coulomb interaction. The net result is a screening of electrons and a decrease in their energy which lowers the energy of the conduction band. A similar effect for holes increases the energy of the valence band giving a total reduction of the band gap energy. A formula that expresses the bandgap shrinkage was originally derived by Wolff [56] and reads as follows:

$$\Delta E_g = -\left(\frac{q}{2\pi\epsilon_0\epsilon_s}\right)\left(\frac{3}{\pi}\right)^{1/3} \cdot K^{1/3} \tag{2.51}$$

ϵ_s is the static dielectric constant of the semiconductor and K denotes the concentration of electrons or holes. According to Bennett et al. [22] the bandgap shrinkage only occurs above a certain critical carrier density

$$K_{crit} = 1.6 \cdot 10^{24}\left(\frac{m_e}{1.4\,\epsilon_s\,m_0}\right)^3 \qquad [cm^{-3}] \tag{2.52}$$

The change of the total absorption spectrum is given by

$$\Delta\alpha(K,\hbar\omega) = \frac{C}{\hbar\omega}\sqrt{\hbar\omega - E_g - \Delta E_g(K)} - \frac{C}{\hbar\omega}\sqrt{\hbar\omega - E_g}. \tag{2.53}$$

Once more the refractive index change is calculated using Kramers-Kronig relation. In contrast to the plasma and bandfilling effect the change of the index of refraction induced by band gap shrinkage effects is positive. Using Equation (2.52) to calculate the critical carrier concentration for InGaAsP, a value of $K_{crit} = 3 \cdot 10^{16} cm^{-3}$ is obtained which is lower than the typical background doping concentration of $3 \cdot 10^{15} cm^{-3}$ to $7 \cdot 10^{15} cm^{-3}$ in nominally undoped optical waveguide layers. The band gap shrinkage effect becomes important when carriers are injected to the phase electrodes of the Mach-Zehnder modulator in a forward bias regime. For increasing carrier densities, the band gap shrinkage effect counterbalance the refractive index change induced by the Plasma and the band filling effect.

Chapter 3

Modulator performance optimization

3.1 Introduction

When comparing the performance of different modulator types only three parameters are commonly reviewed in the first place. These are the DC switching voltage V_π, the electro-optic 3-dB bandwidth f_{3dB} and the optical insertion loss (IL). Other parameters are closely related or can be derived from these three values. When designing and optimizing an InP-based Mach-Zehnder modulator, many of the available design variables influence only one of the three parameters but certain variables affect the modulator's performance in two or all three areas. The aim of this chapter is to analyze the influences of those design variables that have the largest impact on three aforementioned performance parameters V_π, f_{3dB} and IL and to analyze their interdependencies to allow an optimization of the Mach-Zehnder modulator. Appendix A gives an overview on the variables which are involved in the Mach-Zehnder modulator (MZM) design and explicitly lists the variables that are included (Table A.2) and excluded (Table A.1) in the MZM performance analysis in this chapter.

3.1.1 Investigated waveguide geometries

In general, the optical waveguide geometry of the modulator can be chosen from three different types which are shown in Figure 3.1. They are referred to as 'shallow etch' (SE), 'median etch' (ME) and 'deep etch' (DE). Figure 3.1a and 3.1d show the shallow ridge geometry where the waveguide rib is only etched to a height such that the waveguide core layer (MQW) is still covered with a certain amount of undoped material from the upper spacer layer (cap layer). To fabricate the so called 'median etch' structure of Figure 3.1b and 3.1e the waveguide rib etching is stopped on top of the waveguide core layer. The 'deep etch' waveguide geometry is structured by etching through the optical waveguide core layer, which leads to strong horizontal
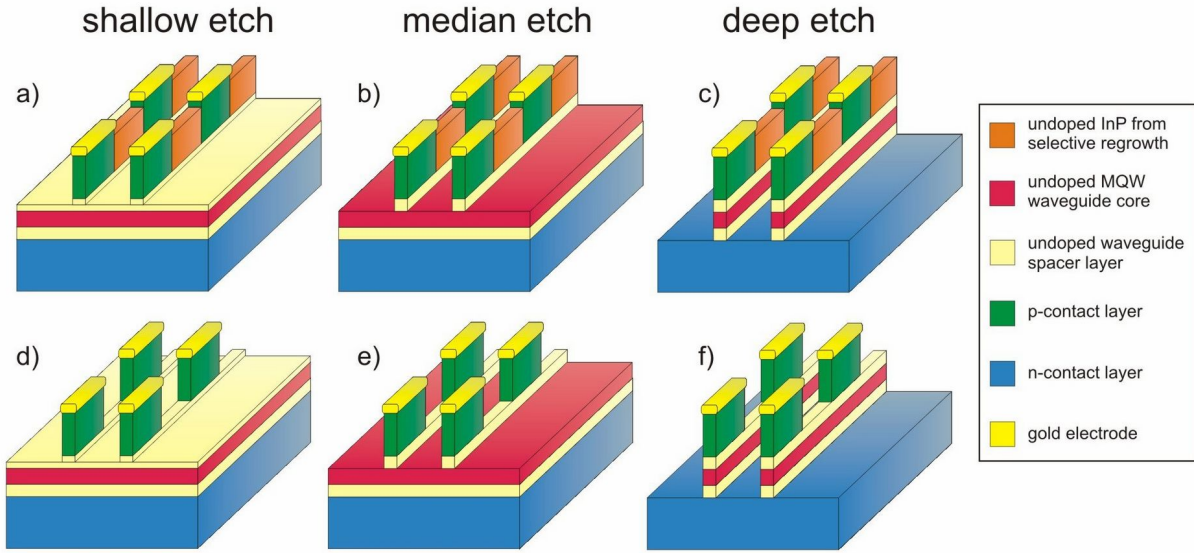
Fig. 3.1: Three investigated optical waveguide geometries 'deep etch'(DE), 'median etch' (ME) and 'shallow etch' (SE). Sketches a), b) and c) illustrate the three different waveguide types including undoped InP (orange) between the p-doped active waveguide sections which is incorporated by selective area regrowth.

mode confinement in the waveguide rib (cf. Figures 3.1c and 3.1f). The difference between the waveguide types shown in the upper and the lower half of Figure 3.1 is the presence of undoped InP in the passive waveguide sections. To incorporate this material a selective area regrowth step is required in the fabrication process which is correlated with an increase in fabrication time, cost and complexity. The three cases featuring no additional regrown material (d-e in Figure 3.1) need just a single epitaxial MOCVD step for growth of the entire epi-layer stack. The p-contact layers depicted by the green color in Figure 3.1 represent the active sections of the traveling-wave electrode shown in Figure 2.5. The advantage of using additional undoped material on top of the undoped spacer layer is a reduction of scattering losses at each transition from the active to the passive waveguide caused by a modal mismatch of both waveguides. Another benefit of using the regrowth step is the possibility to reduce the total intrinsic region thickness further than in the case without this additional material. This greatly improves the design freedom and will be analyzed in the following sections regarding optical losses (3.2.2) and the electric field distribution (3.3.2).

3.2 Strategies for the modulator optical insertion loss reduction

A fundamental necessity for a successful product for the telecommunication market is a modulator with sufficiently low insertion loss. The InP-based MZ modulator developed in this work has to compete with low-loss modulator architectures based on $LiNbO_3$ or polymers. Basically, three different loss mechanisms contribute to the total insertion loss of the MZ modulator: a) fiber-chip coupling losses, b) material absorption losses and c) scattering losses at the optical waveguide sidewalls. While the first two loss mechanisms can be minimized by design the last one is related to the fabrication process and the applied optical waveguide geometry. Multiple approaches to reduce the total insertion loss of the MZM are investigated in this section.

3.2.1 Integration of an optical spot size converter

The typical mode shape of the Mach-Zehnder modulator waveguide is elliptical and has a mode field diameter (MFD) which is lower than the minimum spot size of commercially available tapered fibers (~ 1.7 μm). Therefore, fiber-chip coupling losses due to mode mismatch sum up to ≈ 10 dB for input and output coupling from a cleaved single-mode fiber to a 2 μm wide waveguide. To minimize optical insertion losses from fiber-chip coupling the integration of an optical spot size converter (SSC) with the Mach-Zehnder modulator is essential. Various approaches for on-chip mode converter integration can be found in the literature [57–61]. One common way is to laterally taper the optical waveguide to increase the mode size for better overlap with tapered fibers. This approach includes epitaxial overgrowth ([57]) of cladding layers or even more advanced techniques like enhanced selective area growth (ESAG) steps ([58]) to vertically taper the thickness of the waveguide core and the related cladding layers. Another approach is to implement two individual, vertically separated, waveguides and a structural geometry to transfer the light from one waveguide to the other. The fiber-port waveguide mode is formed by a combination of diluted waveguides in the vertical direction. The horizontal mode confinement is achieved by etching sidewalls forming a wide slab waveguide. This guiding layer principle was developed by Weinert [62] and has been successfully demonstrated for example by Moerl at al. [59]. Koch et al. [60] presented a SSC based on adiabatic mode expansion including a single diluted guiding layer. All SSCs described here are based on the adiabatic mode expansion or compression principle. Spot size converters excluding overgrowth steps additionally use evanescent waveguide coupling as well as mode cutoff to transfer the light from the active device waveguide into the facet mode waveguide and vice versa.

The spot size converter analyzed and implemented in the MZ modulators presented in this

thesis is based on the guiding layer principle. The advantages of this approach are: a) all epitaxial layers are grown in a single step thus reducing fabrication costs. b) the possibility to easily design the SSC polarization independent. c) more design flexibility in comparison with ESAG-based designs.

In order to characterize the SSC functionality and to figure out the optimum design for the three different waveguide types introduced in Section 3.1.1, the following tasks have been addressed:

- fix design parameters (intended spot size, waveguide type (cf. Fig. 3.2), n-contact layers(y/n), wavelength range, TE/TM polarization)

- design and optimize the facet mode profile for optimum mode overlap with external coupling optics

- design the ramp profile for optimum adiabatic mode expansion

- find trade-offs between the facet mode shape and the ramp profile for optimum combined performance

- evaluate the impact of process and fabrication related tolerances on the SSC functionality and - if necessary - find acceptable trade-offs for relaxed tolerances and minimum total insertion loss for high yield

The general design path starts with fixing the desired modal spot size of the fiber-port waveguide depending on the type of optical fiber or micro lens to which the port waveguide has to be matched. Cleaved single mode fibers (SMF) with a core diameter of 8.6 μm form a Gaussian mode profile with a mode field diameter (MFD) of 10 μm and are commonly used to butt-join fibers and chips. Typical micro lenses built into opto-electronic module packages use a mode field diameter of 3.6 μm with a far field angle of ~20°. Tapered fibers are commercially available for any spot size between 1.8 μm and 9 μm. As the power transfer inside the SSC is based on adiabatic mode expansion, it is generally favorable to use small input facet mode size as the mode expansion factor is smaller. For example expanding the mode from 1 μm to 3.6 μm allows a much shorter SSC length than a mode expansion from 1 μm to 10 μm in case of a SMF-butt-joint.

The fiber port mode field diameter of the SSC developed in this work was chosen to be 3.6 μm. The epitaxial layer structure of the MZM waveguide must contain at least a 1 μm thick n-doped contact layer. The detailed design flow is describe for a type 1 transition ramp
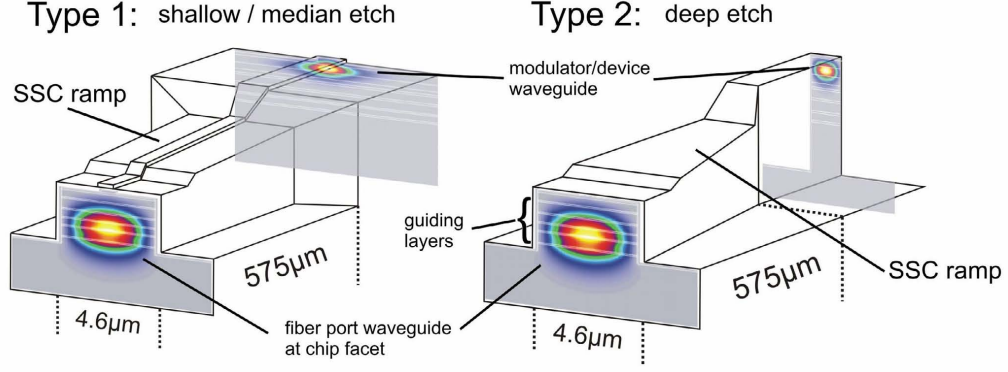
Fig. 3.2: Schematic of spot size converter (SSC) designs for three different waveguides. Type 1 is the design for transitions into a weakly confined 'shallow etch' ('median etch') waveguide. Type 2 is a SSC design for transferring light into a strongly coupled 'deep etch' waveguide.

into an active shallow etched waveguide. All simulations are performed using the commercial software package *FIMMWAVE* distributed by Photon Design Ltd. [63] which is based on a 2D waveguide solver using the film mode matching (FMM) method presented in [64]. The optical field propagation is modeled by using *FIMMPROP* that calculates the coupling efficiencies of the overall field distributions between two adjacent slices that are cut through the 3D geometry along the propagation direction *z*. All refractive indices used in the simulations are based on Adachi's model for InP and InGaAsP [65]. This model in discussed in detail in Appendix B. The change of the refractive index due to the incorporation of n-doped layers is taken into account based on the theory described in Section 2.6.2 (carrier effects). Specific values and parameters are listed in Appendix B.2 and - regarding absorption - in Appendix B.3. The mode mismatch between the optical fiber and the fiber port fundamental waveguide mode is calculated with the power overlap integral (POI) [66]

$$\gamma = \frac{\left| \int_0^\infty E_1(x,y) \cdot E_2(x,y) dx dy \right|^2}{\int_0^\infty \left| E_1(x,y) \right|^2 dx dy \cdot \int_0^\infty \left| E_2(x,y) \right|^2 dx dy}. \tag{3.1}$$

The spot size converter has to operate for TE polarization in the full C-band covering wavelengths from λ=1525 nm to λ=1565 nm with low insertion loss variation. After choosing the spot size for the fiber port mode (or facet mode) the type of the modulator waveguide needs to be fixed as this determines the geometrical shape of the SSC. In the following discussion two different types of SSC geometries are considered (Figure 3.2). Type 1 presents a spot size converter with an optical power transition to a weakly guide 'shallow etch' or 'median etch' waveguide while type 2 enables a transition into a strongly confined 'deep etch' waveguide.

The following in-depth discussion with detailed calculation diagnostics is based on the type 1 spot size converter.

A general design challenge for spot size converters in semiconductor based optoelectronic waveguide devices is - as mentioned before - the elliptical optical mode shape because a typical waveguide width is two to three times the height of the waveguide core thickness. Therefore, the required mode expansion or compression of the SSC in the vertical direction is around three times larger than in the horizontal direction if the fiber port mode is intended to have a circular shape. In the absence of doped epitaxial layers the design of the SSC is fairly easy. Commonly three guiding layers (cf. Figure 3.3) with a higher index material are used to form the facet mode in vertical direction. The important parameters are the relative position, the width of each individual guiding layer and the refractive index of each layer (=material composition). In this work quaternary InGaAsP with a band gap equivalent wavelength of 1.06 µm (Q1.06, n_{opt}=3.28) is used for the guiding layers while the surrounding material is InP (n_{opt}=3.18). A thicker guiding layer tends to decrease the exponential tails of the mode thus reducing the vertical diameter. It also attracts the facet mode center due to the presence of more high index material. A different material with a different refractive index allows a trade-off between the two effects described before. Maintaining the width but increasing the refractive index has a smaller impact on the mode diameter than on the centering of the large facet mode. The widths and the position of the three guiding layers needs to be chosen so that the vertical mode profile gives the best overlap to the desired coupling optics spot size (3.6 µm in this case). An easier way to design the mode overlap would be using more than three guiding layers but at the same time using more guiding layers favors the formation of a guided second mode inside the spot size converter which has to be avoided.

The lateral light confinement is achieved by etching sidewalls to form a large slab waveguide. The width of the slab is the only variable to adjust in order to optimize the overlap with the input beam spot. Figure 3.3a shows the fiber mode intensity profile with three guiding layers in the absence of n-doped material for a wavelength of 1550 nm and TE polarization. The overlap to a 3.6 µm MFD Gaussian beam was calculated to be 95.3%=0.2 dB loss. The lower part of Figure 3.3a depicts the average power along the propagation axis z. A smooth power transition from the left facet mode waveguide into the MQW core waveguide is achieved. The conversion efficiency is ~95%=0.23 dB loss. The total SSC coupling loss into the MQW device waveguide is only 0.43 dB (=0.2 dB mode overlap loss + 0.23 dB conversion loss).

The required incorporation of n-doped layers into the epitaxial layer structure to form the n-contact of the modulator has a strong impact on the performance of the spot size converter. Not
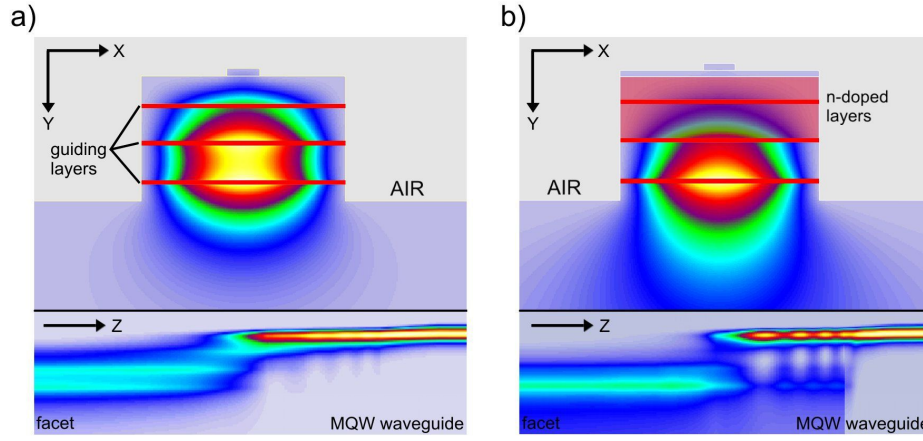
Fig. 3.3: Calculated intensity profiles of SSC facet modes at 1550 nm for TE polarization. The optical mode on the left (a) with undoped layers has a ~95% mode overlap with a 3.6 μm MFD Gaussian beam. The layer stack of the right mode (b) contains 1.5 μm n-doped material to form an n-contact. In this case, the mode center is shifted to the lowest guiding layer in comparison with (a).

only does the mode overlap with n-doped material adds absorption losses but also reduces the adiabatic power transfer from the facet mode waveguide into the upper MQW core waveguide and vice versa. Figure 3.3b shows the facet mode for identical layers as in Figure 3.3a but using 1.5 μm thick n-doped material. The refractive indices used for this calculation are reduced according to Table B.2 assuming an n-doping concentration of $1 \cdot 10^{18}$ cm $^{-3}$ for the top most 350 nm material and $2 \cdot 10^{18}$ cm $^{-3}$ for the layers below. The lower refractive index in the n-doped layers shifts the facet mode center towards the lowest guiding layer. While the mode overlap to a 3.6-μm MFD Gaussian beam is still over 90% the larger distance between the facet and MQW mode centers as well as the lower index material itself diminishes the power transition efficiency. The optical power transfer loss along the z-direction dramatically increases to almost 50% (2.9 dB) compared to 0.23 dB for the undoped case. The drawback of a decreased power transition efficiency is not only a much higher insertion loss of the MZ modulator. The fraction of the optical input power that is not transferred into the active modulator waveguide can be guided in the SSC's guiding layers towards the output and interfere with the modulated light in the output SSC. This results in so called 'bubbles' in the measured output intensity matrix which is exemplary shown in Figure 4.3a. The drawbacks that result from these 'bubbles' are a higher insertion loss and a degradation of the modulator's DC extinction ratio (on-off-ratio) (cf. Figure 4.3b).

The trick to overcome this issue is to place a fourth guiding layer into the epitaxial layer structure. Figure 3.4 shows the intensity facet mode profile at 1550 nm for TE polarization

Material	doping [cm^{-3}]	n_{opt}	thickness [nm]	definition
InP	$<1 \cdot 10^{15}$	3.181	200	spacer
MQW	$<1 \cdot 10^{15}$	3.348	408	WG core
InP	$<1 \cdot 10^{15}$	3.181	200	spacer
InP	$1 \cdot 10^{18}$	3.176	350	spacer
InGaAsP Q1.06	$2 \cdot 10^{18}$	3.257	85	GL 1
InP	$2 \cdot 10^{18}$	3.172	700	spacer
InGaAsP Q1.06	$2 \cdot 10^{18}$	3.257	128	GL 2
InP	$<1 \cdot 10^{15}$	3.181	550	spacer
InGaAsP Q1.06	$<1 \cdot 10^{15}$	3.268	120	GL 3
InP	$<1 \cdot 10^{15}$	3.181	600	spacer
InGaAsP Q1.06	$<1 \cdot 10^{15}$	3.268	90	GL 4
InP	$<1 \cdot 10^{15}$	3.181	500000	substrate

Tab. 3.1: Epitaxial layer structure used to build a spot size converter with four guiding layers. 1.2 μm n-doped layers are included for the n-contact of the modulator.
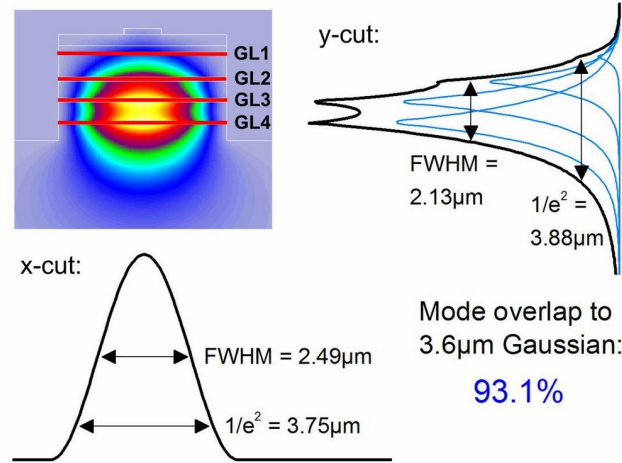
Fig. 3.4: Calculated intensity profiles of spot size converter (SSC) facet mode in *x*- and *y*-direction at 1550 nm for TE polarization. The modes of each single guiding layer (GL1 - GL4) are also plotted. The overlap integral gives 93.1% mode matching between the SSC facet mode and a 3.6-μm MFD Gaussian beam.

of the layer structure listed in Table 3.1. The layer stack has four guiding layers and 1.2 μm n-doped material for the n-contact of the modulator. Figure 3.4 also displays horizontal and vertical cuts through the center of the mode profile together with the full width at half maximum (FWHM) and 1/e^2 widths. The vertical cut also shows the contribution of each single guiding layer to the formation of the large mode. Computing the power overlap integral with a 3.6-μm MFD Gaussian beam using Equation (3.1) give a loss of only 0.3 dB (conversion efficiency of γ=93.2%).

Spot size converter ramp profile design

After finding a layer configuration with an excellent coupling efficiency to external coupling optics the SSC ramp profile is the next design task. The optical power transfer from the lower into the upper waveguide is achieved as follows. A shallow ramp etched into the semiconductor linearly increases the high refractive index material of the MQW waveguide core thus increasing the mode overlap with this material. Figure 3.5a shows a schematic side view of a ramp etched into the semiconductor. At a certain point there is enough MQW core material present to allow the existence of a guided mode in the upper waveguide. From this point on the light is transferred from the lower to the upper waveguide by evanescent coupling. This power transfer has to be adiabatic in order to prevent conversion losses. The only parameter which influences this adiabatic behavior is the increase of high index material per unit length along the z-axis of the spot size converter ramp. There are basically two geometrical design options to vary this parameter. The first obvious option is the slope of the ramp. A steeper ramp gives a larger increase of high index material per unit length. The ideal adiabatic behavior of the mode expansion is degraded and the power coupling efficiency between the two SSC waveguides is reduced. Because the height of the ramp is more or less fixed due to technological and processing reasons the simplest way two minimize the slope of the ramp is to make the ramp longer. On the other hand making the ramped section of the SSC longer increases the overall chip length which is not favorable. The way to overcome this length issue is to fabricate a SSC with three different ramp sections, e.g. a flat center section and two steep ramps in the outer sections. The advantage of the three-section SSC is to have a relatively flat ramp for the adiabatic mode expansion while maintaining a short total length of the SSC. This three ramp profile is shown in Figure 3.5a. The lengths of the two steeper ramps L_{steep} and $L1_{steep}$ are typically in the order of 75 μm while the flat ramp length L_{flat} varies depending on the trade-off between SSC performance and chip length. The second possibility two minimize the increase of high index material per unit length is given by the dimensions of the small rib on top of the 4.6 μm wide slab waveguide. A thinner rib means a slower increase of MQW core material thus supporting the adiabatic power transfer to the upper waveguide. On the other hand the thin rib has two be wide enough to allow the formation of a guided mode in the MQW waveguide. In the actual design the small rib in the ramped section has a width of 1 μm which is expanded to the 2 μm width of the regular waveguide in the third steeper ramp of the spot size converter (cf. Figure 3.5b). The center design of the vertical spot size converter ramp is pinned down by choosing a value for the flat ramp height H_{flat} such that processing tolerances do not drive the SSC out of the performance specifications
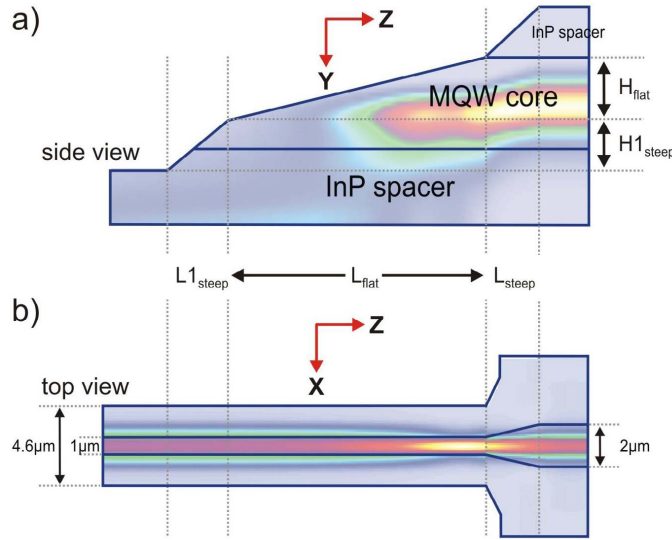
Fig. 3.5: Schematic of the spot size converter's (SSC) ramp section in etched semiconductor. a) side view in the y-z-plane of the three-step ramp design along the center line of b). b) top view of the SSC ramp profile in the x-z-plane.

limits. For the presented design the height H_{flat} is chosen to be 300 nm. The vertical position of the flat ramp is defined such that the power coupling from the lower to the upper waveguide occurs in the center of the flat ramp. The layer structure used for these calculations is listed in Table 3.1. It includes four guiding layers and 1.26 µm doped n-contact layers. The geometrical ramp dimensions are: $L_{steep} = L1_{steep} = 75$ µm, L_{flat}=700 µm, H_{flat}=300 nm.

Results of detailed calculations for an optimized spot size converter are shown in Figure 3.6. The top green curve in Figure 3.6 shows the mode filed diameter (MFD) of the first order mode. It can be seen that the mode expands along the z-direction as more and more MQW core material become present on top of the flat ramp. At a z-position of about 450 µm the mode diameter starts to shrink which is a consequence of increased mode coupling to the MQW waveguide core. This is the important parameter for the design of the spot size converter as the reduction of the mode diameter should be as slow as possible to avoid coupling of optical power to higher order modes. The decrease of the mode diameter per unit length gets even larger at a z-position of 550 µm. The blue curve in Figure 3.6 reveals that a guided second order TE_{01}-mode is appearing at a z-position of about 450 µm where the value for the side loss is 0 dB/cm. A side loss value different from zero means that the mode overlaps with the calculation boundaries which is a non physical solution. The black and red curve in the bottom inset in Figure 3.6 display the optical power of the first and second order mode in percent with respect to the input power at z=0 µm. The linear decrease of the optical power in the first mode is due to
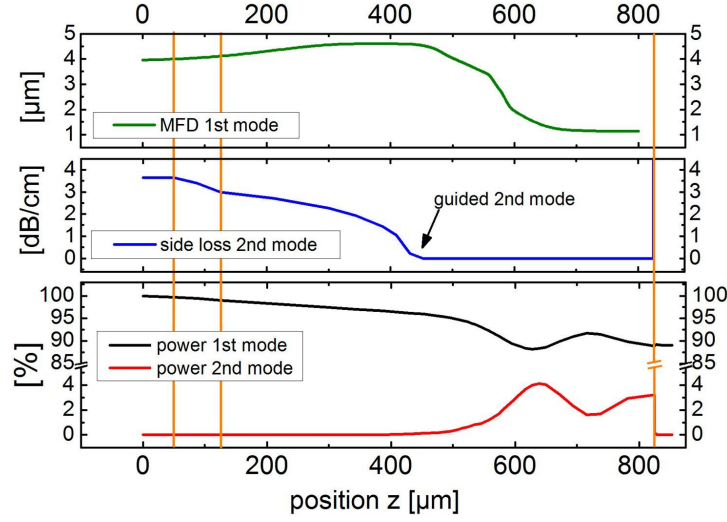
Fig. 3.6: Spot size converter ramped section calculation diagnostics along z-axis at 1550 nm. The green curve shows the mode field diameter of the 1st order mode. The blue curve represent the side loss of the 2nd order mode. A side loss of 0 dB/cm means a guided 2nd mode exists. The black and red curves show the mode power of the 1st and 2nd order mode respectively.

material absorption. At a z-position of 450 µm - where the guided second order mode appears - the optical power of the first mode starts to decrease non-linearly and the mode power of the second order mode starts to increase. At z=550 µm, where the MFD of the first mode starts to decrease faster, power coupling from the first to the second mode becomes even stronger. This is the main reason why the reduction of the first order mode field diameter should be as slow as possible. At a position z=630 µm the power in the second mode reaches a maximum. At higher z-positions the optical power is coupled back from the second mode into the first mode. Although this seems advantageous because more optical power is in the first mode again, this behavior varies when the vertical position of the ramp is slightly modified due to processing tolerances. The length of the flat ramp L_{flat} together with the height difference H_{flat} (cf. Figure 3.5) is crucial for the efficiency of the SSC. Figure 3.7 displays simulated conversion losses for the two SSC types shown in Figure 3.2. The steep ramps have the lengths L_{steep} = $L1_{steep}$ = 75 µm and the height H_{flat} of the flat ramp is kept constant at 300 nm. The black curves in Figure 3.7 are the pure conversion losses inside the SSC section without absorption losses due to overlap with n-doped material. As expected the losses decrease with increasing length of the flat section as the mode compression becomes more and more adiabatic. The red curves in 3.7 depict computed conversion losses together with absorption losses caused by mode overlap with n-doped material. The green curves show the difference between black and red curves to highlight the influence of the n-contact layers. The longer the optical interaction
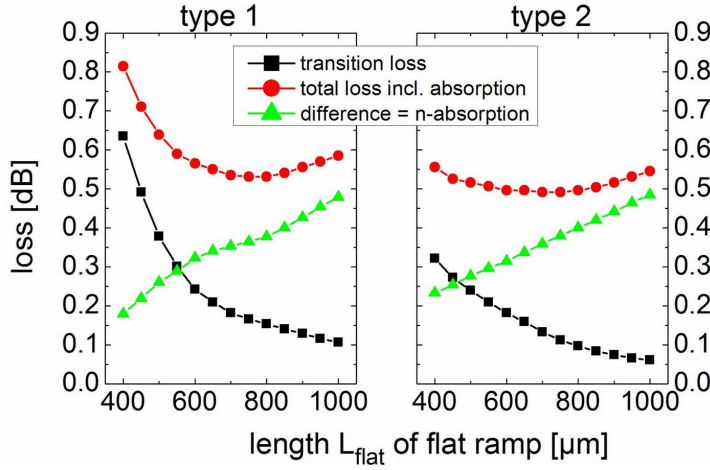
Fig. 3.7: Simulated loss curves plotted against flat ramp length for two different SSC types (cf. Figure 3.2) at 1550 nm. Black curves are pure power transfer losses. The red curves represent the total SSC loss comprising transfer and absorption losses in n-doped material. The green curves show the difference between the black and red curves showing the incremental loss due to overlap with n-doped material.

length with n-doped material the more absorption losses are generated inside the SSC. This effect causes the total loss of the spot size converter to increase again after passing the optimum length of the flat section which can be seen in the red curves for type 1 and type 2 SSC. Both SSC types have an optimum flat ramp length of L_{flat} = 750 μm with a total insertion loss of 0.5 dB and 0.55 dB, respectively. In general, the total loss of both SSC types is constant within ±0.1 dB for L_{flat} varying from 500 μm to 1000 μm indicating that a better conversion efficiency is counterbalanced by higher absorption losses or vice versa. At the optimum flat ramp length of L_{flat} = 750 μm two-thirds of the total loss are due to absorption. A possible solution for further SSC performance improvement is to avoid absorption losses in the n-contact layers. This could be achieved by using selective area growth (SAG) techniques in the areas with SSCs on the wafer. But the advantage of using undoped layers in the SSC region and thus reducing the overall insertion loss would be countervailed by the implementation of two epitaxially grown butt joint interfaces which usually have a coupling loss in the order of ∼0.5 dB. Thus the total power loss of the SSC as well as the fabrication complexity and time would increase leaving no benefit for this approach. Figure 3.8 shows the simulated wavelength dependence of the power conversion loss (black curve) in the spot size converter section excluding absorption losses from n-doped material. The red curve depicts the power coupling loss computed for a Gaussian beam with a mode field diameter of 3.6 μm. The blue curve in Figure 3.8 shows the total loss. It can be seen that the total loss slightly decreases with increasing wavelength. This feature is designed by purpose to give an almost flat wavelength response in the C-band from 1525 nm to
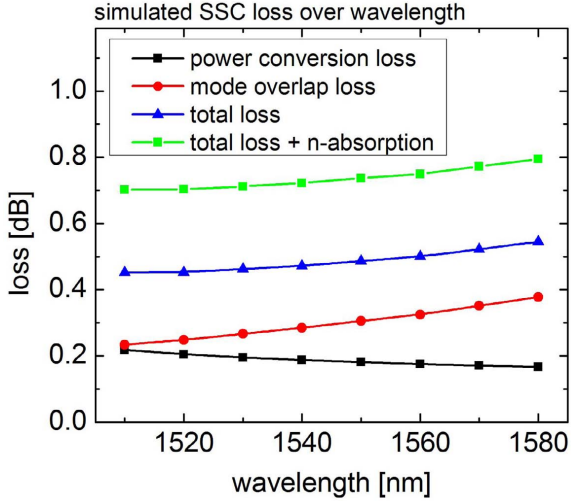
Fig. 3.8: Calculated wavelength dependence of transfer loss (black) and mode overlap loss (red). The blue curve represents the combined SSC loss (black+red). The green curve represents the SSC loss (blue) plus n-doping absorption losses.
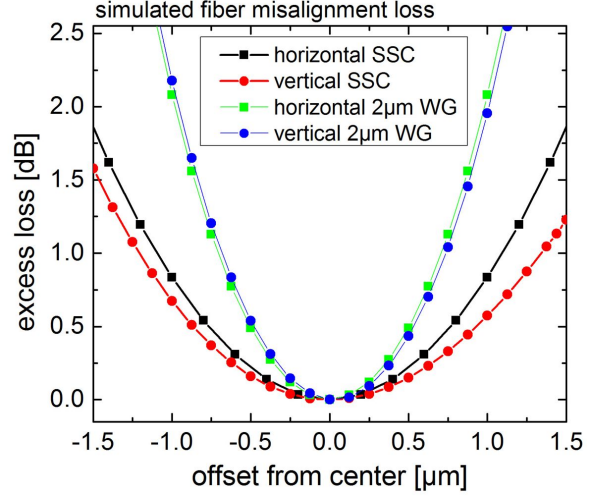
Fig. 3.9: Calculated excess loss tolerances for vertical (red) and horizontal (black) fiber misalignment. The tolerance for 1 dB additional insertion loss is > ±1 μm. Blue and green traces present alignment tolerance for a standard 2 μm wide 'deep etch' waveguide.

1570 nm when absorption from the MQW (cf. Section 3.3.1) is taken into account. The green curve in Figure 3.8 displays the sum of all three contributing loss mechanisms. It can be seen that the combined total loss is well below 0.8 dB in the complete C-band which is a remarkable value considering the fact that n-doping absorption losses contribute 0.25 dB to this value. Another important advantage of the spot size converter is presented in Figure 3.9. The black and red traces show simulated alignment tolerances for a horizontal and vertical offset between a tapered fiber and the facet mode waveguide with 3.6-μm MFD. The 1-dB excess loss tolerance is > 1 μm in either horizontal or vertical direction with the vertical offset having a slightly larger tolerance. The blue and green traces show similar power overlap calculation results for a standard 2 μm wide 'deep etch' waveguide. The tolerance window for 1 dB additional insertion loss is over 30% narrower than that of the SSC. Hence, the spot size converter not only reduces the fiber-chip coupling losses but also relaxes the accuracy requirements for fiber alignment during packaging of the MZM into a module.

Fabrication and process tolerances

The fabrication of the ramp profile requires a lithography exposure system that allows mask movement during exposure or the utilization of a greyscale mask. The utilization of a greyscale mask has been thoroughly evaluated but the reproducibility and quality of the fabricated spot
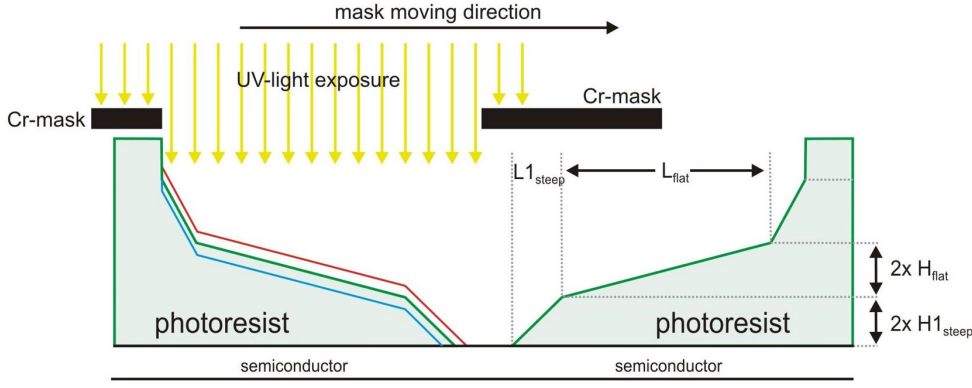
Fig. 3.10: Schematic of the spot size converter ramp in photoresist. The structure is realized by moving a slot mask over the photoresist during exposure. Different slopes are achieved by varying the speed of the mask. Steeper ramps are formed when the mask is moved slower. Different depths (red, green and blue lines) are realized by varying the exposure time before and after the mask movement.

size converter ramps did not match with those of the moving-mask process. Different slopes in the ramp profile are realized by moving a rectangular slot in the mask with different speeds over the photo resist. A slowly moving mask creates a steeper ramp compared to a section where the mask has been moved with a higher speed. Figure 3.10 shows a schematic of the photoresist profile after exposure. Because the etching rate ratio between the photoresist and InP-based semiconductors is almost 2:1 the height values H_{flat} and $H1_{steep}$ of SSC ramp profile in the photoresist must be two times the desired values of the final semiconductor ramp profile which is highly advantageous regarding process tolerances which are discussed later. As can be seen from Figure 3.10 the moving-mask technology always produces two SSC ramps at the same time with inverted profile. This is due to the fact that the left edge of the mask slot creates the left ramped profile while the right hand edge of the slot creates the right hand side profile. A height variation of the SSC profile is realized by changing the exposure time before and after the mask is moved over the photoresist.

To achieve good performance with a high yield throughout the whole wafer area, the impact of fabrication related tolerances needs to be taken into account during the design of the SSC. The first crucial point for the functionality of the spot size converters are epitaxial layer thickness fluctuations. They are generally in the order of $\pm 5\%$ over a two inch wafer having thinner layers close to the wafer edge. The SSC transition loss as well as the modal power overlap to external coupling optics need to be insensitive to the thickness variations. Figure 3.11 shows computed loss curves for the power transition (black), the modal power overlap (red) as well as the combined total loss (blue) of the spot size converter as a function of a layer thickness

variation of all layers involved (cf. Table 3.1) excluding the MQW. The calculation results are given for 1550 nm wavelength covering a layer thickness variation of ±10% excluding n-doping absorption losses. An interesting fact is that for thinner layers the power transition loss is smaller compared to the center design or thicker layers which can be explained by means of the facet mode diameter. When the initial mode diameter is smaller compared to the standard design (cf. Table 3.1) the mode compression or expansion to the size of the active waveguide mode is more efficient because the mode size change per unit length is smaller which was pointed out before as a crucial parameter for the SSC conversion efficiency (cf. Figure 3.6). But as the mode diameter decreases with thinner layers the mode power overlap to a 3.6 μm MFD Gaussian beam decreases at the same time which can be seen in the red curve of Figure 3.11. So there is a trade-off between a more efficient power transition in the SSC section or a better optical power overlap to external coupling optics. From the blue curve in Figure 3.11 it can be seen that for a variation of -5% to +10% there is almost no change in the total loss of the SSC as both effects described before counterbalance each other. For layers thinner than -5% compared to the center design the additional loss resulting from mode overlap mismatch becomes significant. At -10% thickness reduction, the additional loss is 0.18 dB compared to the center design.

An important process variable is the vertical position of the flat SSC ramp. Four major factors lead to a variation of the vertical ramp position during the fabrication process:

- A thickness variation of the photoresist over the entire wafer surface when the photoresist is spilled over the wafer.

- A non uniform distribution of the UV-light intensity during exposure.

- A non uniform development of the photoresist after exposure.

- An ion beam etching (IBE) etch rate variation.

The first three effects are related to the photoresist process where the typical standard deviation from the center design for the vertical position of the SSC ramp is ±70 nm. Due to the typical etch rate difference of 2:1 between photoresist and semiconductor material this 70 nm position distribution translates to a position variability in the semiconductor of ±35 nm. The ion beam etching (IBE) process lead to another ±25 nm height variability over the entire wafer. The total required tolerance window for a 68% (one σ) yield is therefore ±60 nm over the entire surface of a wafer. Figure 3.12 shows the simulated excess losses for a vertical position variation of the flat ramp at 1550 nm wavelength for the standard ramp profile design ($L_{steep} = L1_{steep} = 75$ μm,
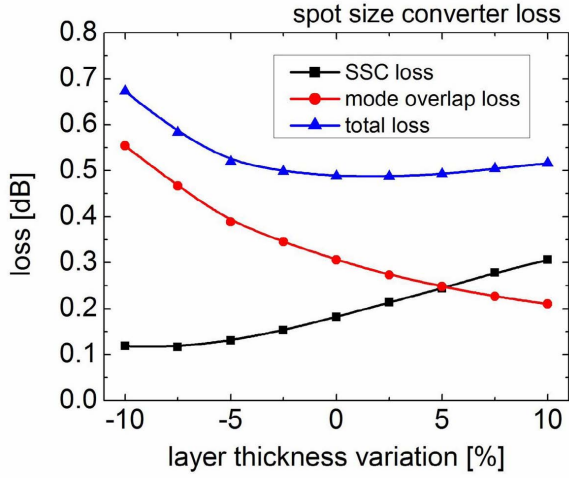
Fig. 3.11: Simulated total spot size converter loss (blue) for epitaxial layer thickness variations. The black curve depicts the SSC power transition loss. The red curve depicts the facet power overlap loss.
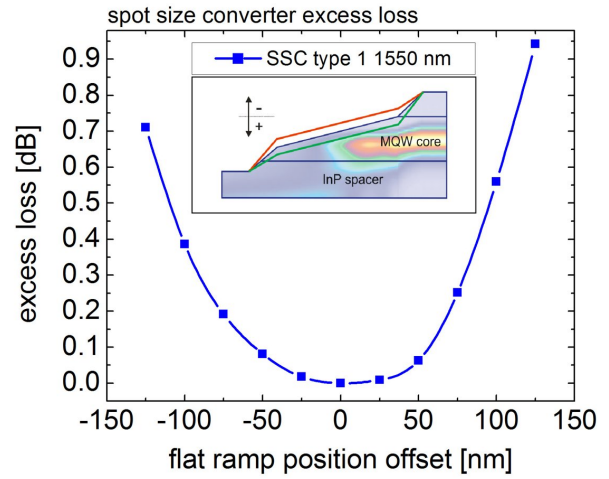
Fig. 3.12: Simulated spot size converter (type 1) excess loss at 1550 nm for a vertical position variation of the flat ramp. A positive value means a deeper etch (cf. inset).

L_{flat}=700 µm, H_{flat}=300 nm) of a type 1 spot size converter. For a height variation of ±50 nm in the semiconductor the additional loss is well below 0.1 dB while the 0.25 dB excess loss limit is ±75 nm. The standard deviation for the fabrication process of the SSC was calculated to be ±60 nm. Therefore ≈ 70% of all fabricated SSCs on a wafer should have an excess loss below 0.15 dB.

Experimental investigation of SSC-integrated waveguide structures

To evaluate the conceptual design of both spot size converter types, a test mask with different structural variations has been developed. The variation include two flat ramp lengths of 500 µm and 550 µm and three facet ridge waveguide widths of 4.4 µm, 4.6 µm and 4.8 µm. Furthermore, three different waveguide width of 1.8 µm, 2.0 µm and 2.2 µm are available on the mask set. The test devices have spot size converters on both facets for input and output coupling to tapered fibers. The input and output SSC are connected by a 4.7 mm long waveguide fabricated in the intended waveguide geometry ('shallow etch' or 'deep etch'). In the center of each connecting waveguide an S-bend is included to produce an offset between the input and the output SSC. A wafer having the epitaxial layer structure listed in Table 3.1 has been processed with multiple bars having test devices both spot size converter types. Figure 3.13 shows a typical profile etched into the semiconductor and measured with a surface profiler. The median height values of the eight significant corner points in the structure measured on 20 different spots across the
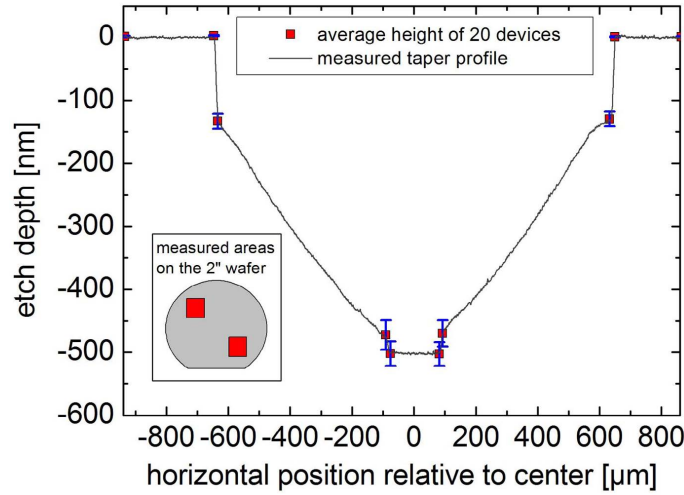
Fig. 3.13: SSC etch profile with average height tolerances of 20 fabricated SSC test devices measured in two different areas on a 2" wafer. The average deviation for the deepest points in the vicinity of the center of the structure is ±17 nm.

2" wafer are also shown. The standard deviation for the four points with the largest etch depth of about 500 nm, which are close to the center of the structure, is ±22 nm. The etch depth deviation for the upper points of the flat ramp is only ±10 nm due to lower etch depth and etch time. Both values of the etch variability show an excellent technological reproducibility and are within the allowed margin of ±50 nm, which has been calculated in the previous section.

Insertion losses of anti-reflection coated samples measured at 1550 nm are presented in Figure 3.14 for the type 1 SSC and in Figure 3.15 for the type 2 SSC. Only the best measured value is shown for each combination of facet ridge width and waveguide width. The results for the 500 μm long flat ramp design of type 1 in Figure 3.14 show a slight variation for the three investigated waveguide widths with the widest waveguide having the lowest loss. The explanation for this is sidewall roughness of the connecting waveguide. This will be discussed in detail for the type 2 SSC below. Interestingly all 500 μm flat-ramp devices with 4.6 μm facet ridge width have a higher loss than the smaller and wider types. For the type 1 SSC with the 550 μm long flat ramp a facet ridge width of 4.8 μm shows the highest insertion loss. All 550 μm samples with 4.4 μm and 4.6 μm facet ridge width have an insertion loss below 3 dB. The lowest loss value obtained for a type 1 SSC test device is 2.45 dB. Assuming an average waveguide loss per mm in the 'shallow etch' waveguide of 0.2 dB/mm, the connecting waveguide between both spot size converters of the measured sample adds 0.9 dB to the total loss. If the S-bend is taken into account with an additional loss of 0.1 dB, the pure loss of the two SSCs of the sample is 1.5 dB giving an insertion loss for each single SSC of 0.7 dB which is
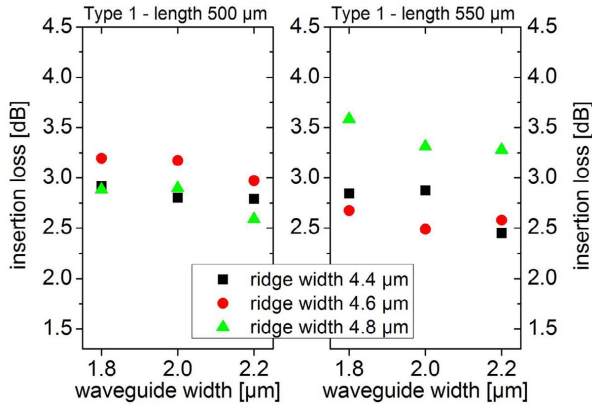
Fig. 3.14: Insertion losses measured at 1550 nm for type 1 SSCs with different geometrical waveguide dimensions.
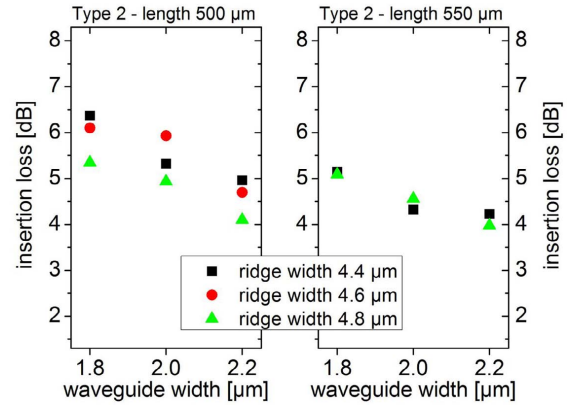
Fig. 3.15: Insertion losses measured at 1550 nm for type 2 SSCs with various geometrical variations.

only slightly higher than the value for the simulated conversion loss of 0.6 dB for a type 1 SSC shown in Figure 3.7. The possible reasons for this 0.1 dB higher insertion loss are numerous. A non-ideal mode match of the input and/or output fiber to the fiber port waveguide is the most likely cause. Higher waveguide losses or processing imperfections might also play a role.

Measurement results for the type 2 spot size converter show similar values for the SSC loss (cf. Figure 3.15) for test devices with the same geometrical variations as for the type 1 SSC before. The samples with a flat ramp length of 550 μm and a facet ridge width of 4.6 μm were damaged and could not be measured. Again as for the type 1 SSC, the average loss of samples featuring the longer flat ramp is lower which agrees with the simulations. A clear correspondence of wider WG width with lower insertion loss can be seen. This observation can be explained in terms of scattering losses due to sidewall roughness which is largely dependent on the waveguide width. This is explained at the end of the following section. Measurements of intrinsic waveguide losses of a 'deep etch' waveguide with varying width presented in Figure 3.22 reveal a loss of 0.7 dB/mm for a 1.8 μm wide waveguide. The scattering losses for the 2.0 μm and 2.2 μm wide WG are 0.6 dB/mm and 0.45 dB/mm, respectively. For the 4.7 mm long connecting waveguide and the S-bend in the test devices, 3.4 dB (1.8 μm), 2.9 dB (2.0μm) and 2.2 dB (2.2 μm) has to be subtracted from the measured insertion loss values to get the pure loss of the input and output SSC. The resulting loss value is divided by two to get the loss of only one SSC. The lowest loss for the 1.8 μm waveguide SSC is then 0.85 dB, for the SSC with 2.0 μm WG width it is 0.7 dB and for the 2.2 μm waveguide SSC it is 0.9 dB. The simulated loss of the type 2 SSC is 0.5 dB at 550 μm length according to Figure 3.7. Again, technological variations have a large impact on theses values. If the DE waveguides are only 0.1 μm thinner than their nominal width, the scattering losses in the straight waveguide would be 0.15 dB to
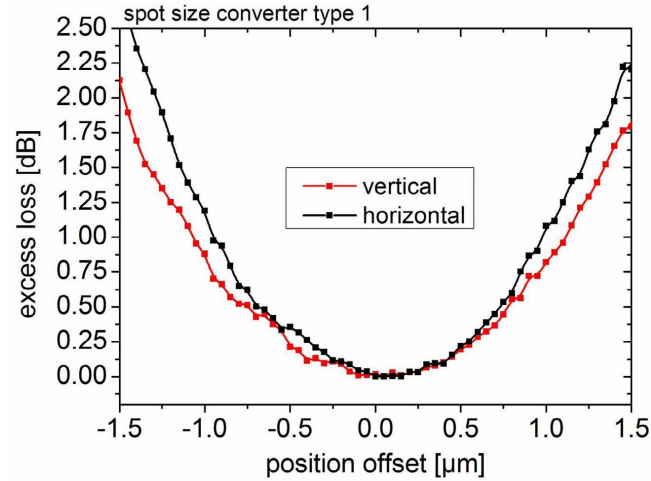
Fig. 3.16: Experimentally determined vertical and horizontal excess loss of a type 1 SSC as a function of misalignment. The results are in good agreement with the simulated values shown in Figure 3.9.

0.2 dB larger resulting in a lower loss of each SSC by half of that value.

Results of a fiber alignment tolerance measurement in horizontal and vertical direction for a type 1 SSC test device (cf. Figure 3.16) are in excellent agreement with the excess loss values obtained from power-overlap calculations presented in Figure 3.9. For the horizontal offset measurement, an additional 1-dB insertion loss is obtained for a fiber displacement of 0.95 μm in either positive or negative direction. The vertical direction gives slightly larger tolerances with ±1.1 μm offset for 1 dB excess loss. This relaxed tolerance for the fiber alignment is required for reliable low loss packaging of the Mach-Zehnder modulator into a module.

To conclude, two highly efficient spot size converter types including n-doped contact layers have been designed and evaluated theoretically. Both SSC geometries are suitable for low loss fiber-chip coupling to 'median etch' and 'shallow etch' (type 1) and 'deep etch' (type 2) modulator waveguides and have large fabrication tolerances for high-yield production. Experiments with fabricated SSC-integrated test devices show excellent performance. The lowest measured loss for a 'shallow etch' waveguide type 1 SSC is 0.75 dB and for the type 2 SSC is 0.7 dB. The fiber misalignment tolerance of the developed spot size converters is sufficient for reliable low loss module packaging.

3.2.2 Intrinsic optical waveguide loss reduction

The second possibility to reduce the overall insertion loss of a modulator is to reduce the loss of the waveguide itself, which originates from absorption and scattering losses. In contrast to the on-chip optical spot size converter, whose optimization has no influence on the MZ modulator's drive voltage and modulation bandwidth, the waveguide type has a strong influence on these parameters.

Doping profile variation for mode loss reduction

The switching behavior of the Mach-Zehnder modulator is related to an optical phase change which is induced by an electric field in the p-i-n-diode of the active modulator waveguide (cf. Section 2.2). A small intrinsic region thickness (IRT) in this p-i-n-configuration is beneficial to get a higher electric field per applied voltage which implies a lower switching voltage V_π. On the other hand, for a narrower intrinsic region the required n- and p-doped layers have to be placed closer to the multi quantum well waveguide core layer which increases the mode overlap with doped material and therefore increase optical absorption losses. It has been shown in the previous section that absorption losses due to mode overlap with doped material are a major contribution to the overall insertion loss of the modulator. While absorption losses in n-doped semiconductor material have acceptable values, the incorporation of p-doped material in the active waveguide sections of the modulators traveling-wave electrode have a major impact. The absorption for an identical doping concentration is ten times larger for p-type doping than it is for n-type doping (see Table B.3 in Appendix B.3). This fact requires a small mode overlap with p-doped material and the p-doping concentration to be as low as possible.

The following calculations are performed using the complex FMM mode solver of the FIMM-WAVE software package [63]. This solver directly computes the mode loss from the imaginary part of the propagation constant (2.10) of each complex mode. The values of the refractive indices and absorption losses used in the computations are derived in Appendix B and listed in Table B.1 and Table B.3, respectively. The wavelength dependence of absorption losses is neglected because the variability within the C-band is rather small (cf. Section 2.6.2). The following calculations for modal absorption losses are performed at 1550 nm wavelength for TE polarization. The effect of a reduced doping concentration on the electric field distribution and the RF frequency behavior is evaluated in Section 3.3.2.

Due to the fact that the optical mode overlap with n- and p-doped semiconductor material does not only depend on the vertical layer dimensions but also on the chosen lateral waveguide
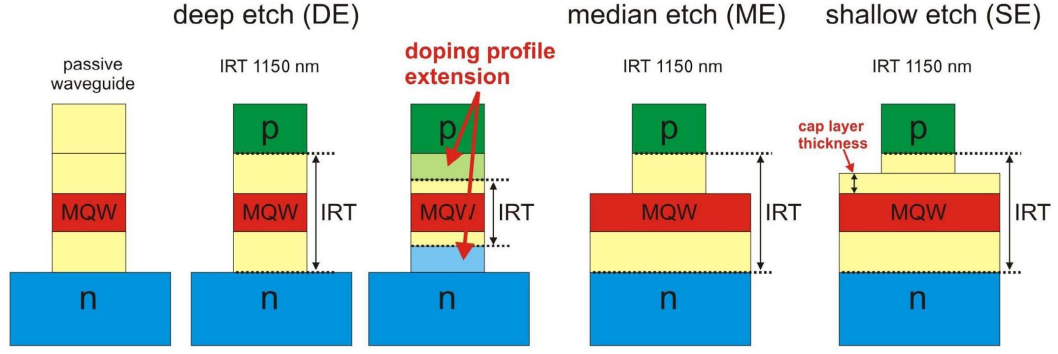
Fig. 3.17: Schematic of the three investigated waveguide geometries 'deep etch' (DE), 'median etch' (ME) and 'shallow etch' (SE). The DE case with two variations of the intrinsic region thickness is plotted. Left figure: DE passive waveguide. Cap layer thickness for the SE case is indicated.

geometry, the mode loss calculations need to be performed for the three waveguide designs 'shallow etch' (SE), 'median etch' (ME) and 'deep etch' (DE) introduced in Section 3.1.1. All three waveguide variants will be analyzed with respect to the modal absorption loss and the also important overlap of the electric field with the optical mode. For the DE waveguide, Figure 3.17 schematically explains the variation of the intrinsic region thickness for two different cases. An intrinsic region thinner than 1150 nm is achieved by bringing the doping profile closer to the wave guiding MQW layer so that the thickness of the undoped spacer layers above and below the MQW (cf. Fig 3.17 DE case) are reduced. Table 3.2 lists the regular doping profile and the so called 'light doping' profile with reduced doping concentrations in the extension layers. The

Layer name	regular doping profile	light doping profile
p standard	$5 \cdot 10^{17}$ [$1/cm^3$]	$5 \cdot 10^{17}$ [$1/cm^3$]
p extension	$5 \cdot 10^{17}$ [$1/cm^3$]	$2.5 \cdot 10^{17}$ [$1/cm^3$]
spacer	undoped	undoped
MQW	undoped	undoped
spacer	undoped	undoped
n extension	$1 \cdot 10^{18}$ [$1/cm^3$]	$5 \cdot 10^{17}$ [$1/cm^3$]
n standard	$1 \cdot 10^{18}$ [$1/cm^3$]	$1 \cdot 10^{18}$ [$1/cm^3$]

Tab. 3.2: Doping concentrations of regular and light doping profile of the active MZM waveguide.

overall thickness of all layers is kept constant. Figure 3.18a shows the calculated modal absorption loss for different intrinsic region thicknesses of a DE waveguide structure. The MQW waveguide core thickness used a as reference is 400 nm (Due to NDA restrictions the number of quantum wells used for the MZ modulator is not given). The passive waveguide structure is simulated including undoped regrown InP on top of the waveguide which was explained in
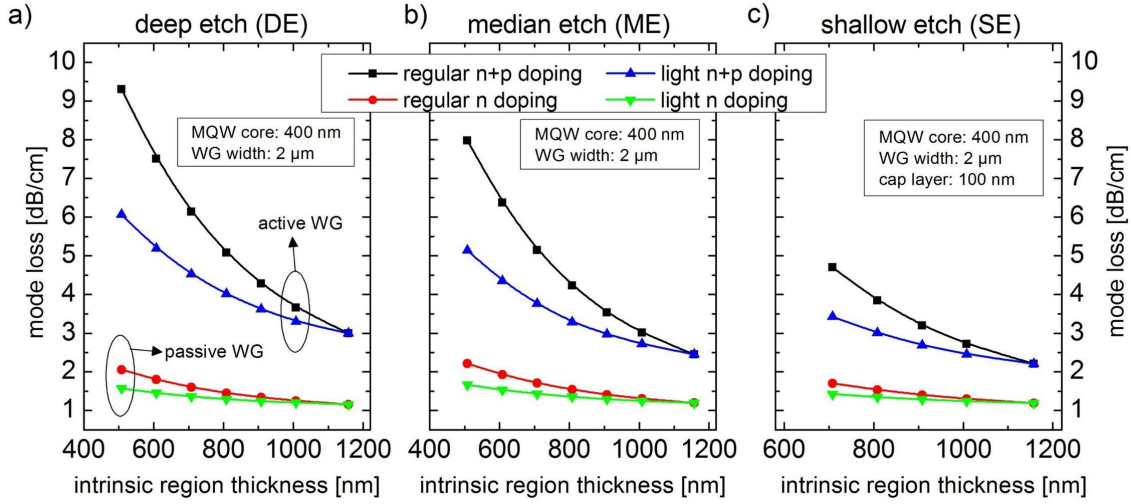
Fig. 3.18: Calculated mode loss in dB/cm for 'deep etch'(a), 'median etch' (b) and 'shallow etch' (c) waveguides as a function of the intrinsic region thickness for different doping profiles. The red and green curves show the mode loss for the passive waveguide with only n-doped layers underneath the WG core layer. The blue and black curves represent active waveguide losses with p- and n-type doped layers.

Section 3.1.1. The reduction of the intrinsic region thickness is done in such a way that the undoped spacer layers above and below the MQW always have equal thickness. The red and green curves in Figure 3.18a show the mode loss variation for passive waveguide material where only n-doped material is present below the waveguide core. The red curve shows results for the standard doping profile with an n-doping concentration of $1 \cdot 10^{18}$ $[1/cm^3]$ in all n-contact layers while the green curve with lower mode loss values shows the effect of the 'light doping' profile with a reduced donor concentration of $5 \cdot 10^{17}$ $[1/cm^3]$ in the n-extension layer. These changes of the doping concentration have a minor impact on the total mode loss. A noticeable effect occurs for intrinsic region thicknesses below 800 nm. The blue and black curves in Figure 3.18a highlight the mode loss of the active waveguide containing n- and p-doped material. The black curve represents the mode loss using the standard doping profile while the blue curve shows the calculation result for 'light doping' with reduced donor and acceptor concentrations of $5 \cdot 10^{17}$ $[1/cm^3]$ and $2.5 \cdot 10^{17}$ $[1/cm^3]$, respectively (cf. Table 3.2). Due to the high absorption losses in p-doped material, the reduction of the acceptor concentration in the 'light doping' version significantly reduces the total mode loss. For an intrinsic region thickness of 800 nm the mode loss per cm is reduced by 1 dB while it is lower by 2.3 dB for an IRT of 600 nm. For example, with an average total active material length of 2.5 mm in a standard modulator the total insertion can be reduced by 0.6 dB (IRT=600 nm). Figure 3.18b shows the results of similar calculations for the ME waveguide structure. The mode loss is generally lower

compared with the DE geometry due to a higher vertical confinement of the mode inside the intrinsic region. The fact that the intrinsic spacer layers above and below the MQW core are of equal thickness and the requirement of having at least 200 nm undoped material on top of the MQW to form the rib of the passive waveguide, intrinsic region thicknesses below 800 nm are only possible by using undoped epitaxial regrown material between the active waveguide sections (cf. Figures 3.1a, 3.1b, 3.1c). The calculated mode loss for a SE waveguide of 2 μm width is presented in Figure 3.18c. A cap layer thickness of 100 nm has been used to allow thin intrinsic regions. The overall absorption losses per centimeter are again lower compared to the ME structure because the mode confinement in the nominally undoped material is the largest in the SE waveguide. The lowest possible IRT is 700 nm for a MQW core thickness of 400 nm and a cap layer thickness of 100 nm (cf. Figure 3.18).

Influence of the waveguide width

The width of the optical waveguide plays a fundamental role in the optimization of the electrical modulator characteristics (cf. Section 2.3). Therefore, the analysis of waveguide absorption losses as a function of the waveguide width for the three waveguide architectures DE, ME and SE is important. Figure 3.19 highlights the simulated modal absorption losses for waveguide widths from 1.7 μm to 2.7 μm at 1550 nm wavelength for TE polarization. Again, the design with a MQW core of 400 nm thickness, IRT=1150 nm and the regular doping profile of the active waveguide has been used. The mode loss for a 'deep etch' (DE) waveguide slightly decreases (< 1%) with increasing width (see Figure 3.19a). In contrast to the DE geometry, the absorption loss in the other waveguide types ('median etch' ME and 'shallow etch' SE) increase when the waveguide is widened. This effect is caused by an increasing horizontal and vertical mode diameter which results in a larger overlap with p- and n-doped material and therefore increases the optical absorption loss. The calculation results for the ME waveguide (cf. Figure 3.19b) reveal an absorption increase of 15% between 1.7 μm and 2.7 μm width. The SE waveguide geometry has a 25% increase of the mode loss (Figure 3.19c). As a conclusion, ME and SE waveguide geometries favor the use of thin waveguides with respect to modal absorption losses while the influence of the waveguide width in a DE waveguide is negligible.

Influence of the MQW waveguide core position

So far, all mode loss calculations assumed the multi quantum well waveguide core in the center of the intrinsic region. Shifting the MQW core upwards to the p-contact or downwards to the n-
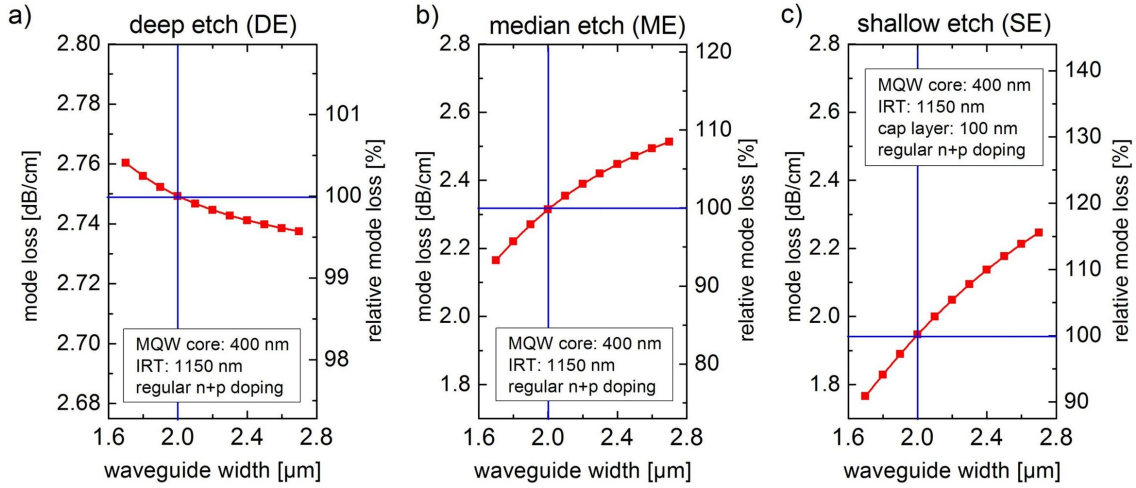
Fig. 3.19: Calculated modal absorption loss in dB/cm for DE (a), ME (b) and SE (c) waveguide geometries as a function of the waveguide width for the regular doping profile with n- and p-doping (MQW core thickness: 400 nm). The width of 2 μm is marked as reference width.

contact inside the nominally undoped space charge region will influence the optical absorption losses and the drive voltage V_π of the modulator (cf. Section 3.3.2). The active waveguide of the MZ modulator is formed by a p-i-n-diode with p-doping above and n-doping below the intrinsic region. With the knowledge that p-doping absorption losses are ten times larger than those of n-doping at the same doping concentration (cf. Appendix B.3) the overall mode loss can be reduced by placing the mode center further away from p-doped material. If the total width of the nominally undoped layers is kept unchanged this measure leads to an increased overlap with n-type material, which on the other hand increases the modal absorption losses in the passive waveguide (only n-doped layers are present). Figure 3.20 presents simulated mode losses for all three waveguide geometries. The calculations were done at 1550 nm wavelength for TE polarization using the standard multi quantum well width of 400 nm, a waveguide width of 2 μm and an intrinsic region thickness of 800 nm to visualize the difference between the 'standard doping' profile and the 'light doping' extension. The vertical position offset from the intrinsic region center is varied from +200 nm to -200 nm for the DE and ME type waveguide. A positive offset value equals a shift towards the lower n-contact and a negative offset equals a MQW position shift towards the p-contact. The limits of +200 nm and -200 nm are those cases where no more undoped material is present between the MQW and the respective contact layers. The maximum shift of the MQW towards the p-contact in the SE case is -100 nm as the covering cap layer of 100 nm thickness has to be present all the time and the p-doping must not extend into the cap layer.
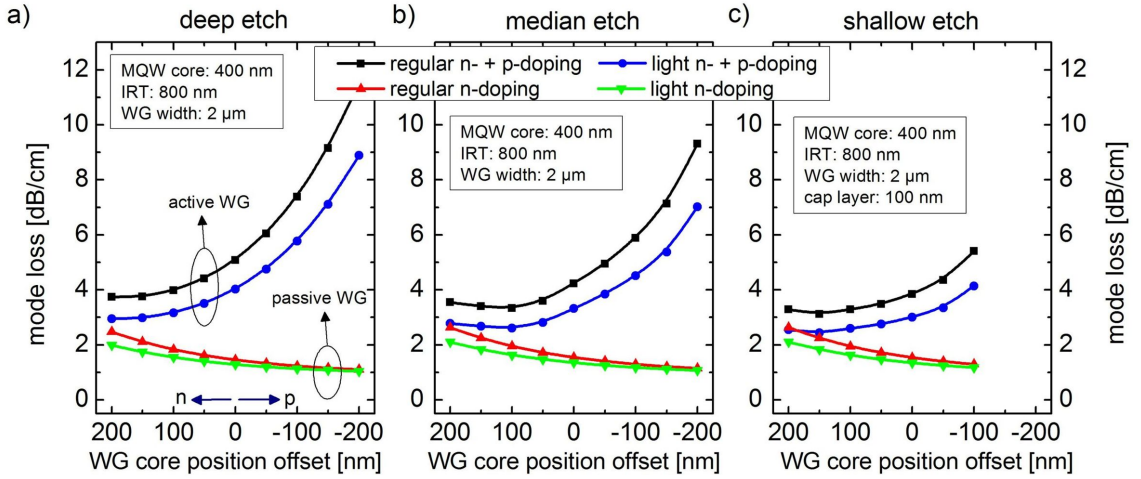
Fig. 3.20: Calculated modal absorption loss for DE (a), ME (b) and SE (c) waveguide geometries as a function of vertical waveguide core position offset for active and passive waveguide types using the regular and light doping profile (MQW core thickness: 400 nm, WG width: 2 μm, IRT: 800 nm, cap layer thickness of the SE waveguide: 100 nm).

The active waveguide losses for the DE waveguide geometry which are calculated for the regular doping and the light doping extension (cf. Table 3.2) show a strong position dependence (cf. Figure 3.20a). This position dependence is less pronounced for the light doping profile. Bringing the MQW closer to the n-contact by 200 nm from the center in the regular doping case reduces the mode loss from 5 dB/cm to 3.7 dB/cm while the same offset towards the p-contact increases the mode loss from 5 dB/cm to 11.5 dB/cm. As can be seen the total mode loss is identical for an offset of +150 nm and +200 nm. This saturation effect is due to the fact, that in this region the losses which result from mode overlap with p- and n-doped semiconductor material are identical. The reduction from reduced overlap with p-type material is counterbalanced by increased losses due to larger overlap with n-type material. For the 'light doping' profile a similar behavior is observed but with a reduced mode loss range from 3 dB/cm at +200 nm offset to 8.9 dB/cm at -200 nm offset. In the case of the passive waveguide structure, the modal absorption losses increase as expected, when to MQW is brought closer to the n-contact. The overall loss in the passive waveguide is of course smaller than in the active waveguide. The absorption characteristics of the ME waveguide shown in Figure 3.20b follows the trend from the DE case. Waveguide losses in the passive structure are nearly identical as those of the DE geometry, while the total modal absorption in the active ME waveguide with regular doping ranges only from 3.5 dB/cm to 9.3 dB/cm. For the reduced 'light doping' the values range from 2.8 dB/cm to 8 dB/cm. Interestingly, the lowest mode loss in the active ME waveguide occurs for a shift of +100 nm from the center of the intrinsic region. For larger shifts, the growing

overlap with n-doped material raises the overall absorption. Figure 3.20c shows the case of the SE waveguide with again almost identical values for the passive waveguide containing only n-doped layers. The active waveguide losses are slightly smaller than their ME counterparts and show a similar trend as the DE and ME geometries before. The lowest mode loss is obtained for a MQW shift of +150 nm.

Based upon these observations, one could be tempted to optimize the modulator waveguide loss by considering the active waveguide losses only as their mode loss values are much larger. However, the complete modulator device integrates only 2-4 mm active waveguide material depending on the specified drive voltage and modulation bandwidth. With common waveguide length of 8 mm to 9 mm - spot size converter not included - the large length of passive waveguide also adds loss to the total device absorption losses. In order to quantify the total waveguide absorption losses of a standard modulator device, the contributions of active and passive waveguide types have to be taken into account. Figure 3.21 shows calculated waveguide absorption losses for a complete modulator using the reference values for MQW thickness (400 nm) and waveguide width (2 μm). An intrinsic region thickness of 800 nm has been used for the calculations to demonstrate the differences between the standard and the reduced 'light doping' profile. The active waveguide length is fixed at 2.5 mm consisting of a 2 mm section in the MZ interferometer and another 0.5 mm long phase electrode, which allows to set the correct operation point. The passive waveguide length within the modulator is determined by the MMI couplers and S-bend length required for the different waveguide structures (see Figure 2.2). For the DE calculations a passive waveguide length of 5.5 mm was used and for ME and SE devices 6.0 mm and 6.5 mm, respectively. Due to the necessity of different passive waveguide lengths in DE, ME and SE devices, the advantage of lower modal absorption per centimeter in ME and SE waveguides vanishes. The plots in Figure 3.21 for DE, ME and SE geometries show identical loss data for both the regular and light doping examples. Just the offset for minimum overall device loss changes from +100 nm (DE) over +50 nm (ME) to 0 nm for the SE type. The loss curves of all three waveguide geometries show a similar lower device loss for the light doping profile compared to the regular doping levels. The total absorption loss of a MZ modulator with 800 nm IRT can be reduced by 0.4 dB to 0.5 dB if 'light doping' is used instead of 'standard doping'.

Impact of sidewall roughness on waveguide loss

Another source contributing to the total insertion loss of the modulator is roughness of the etched sidewalls of a waveguide. Rough sidewalls lead to scattering losses which are gener-
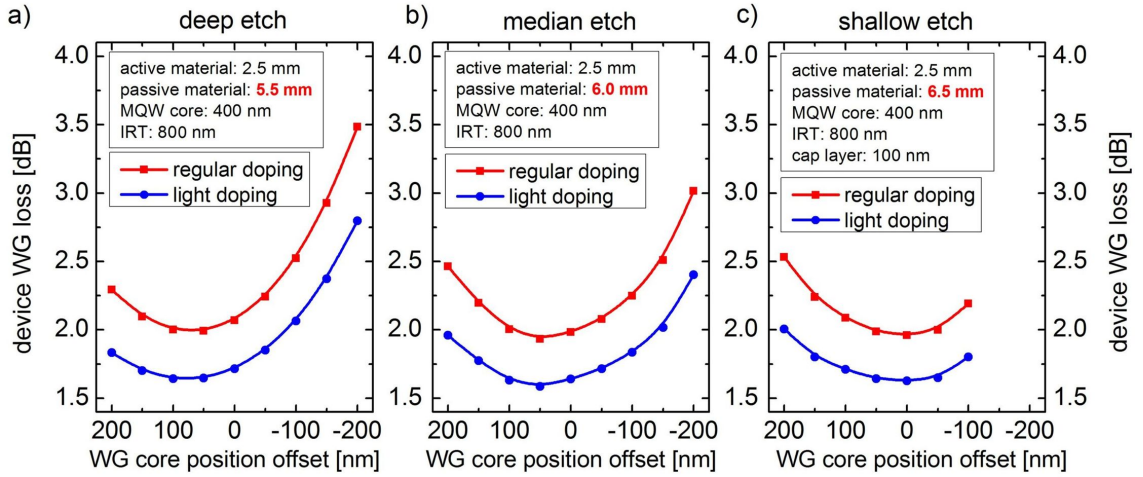
Fig. 3.21: Calculated device absorption losses for DE (a), ME (b) and SE (c) waveguide geometries as a function of vertical waveguide core position offset for active and passive waveguide types using the regular and light doping profile. The MQW core thickness is 400 nm, the WG width is 2 μm and IRT is 800 nm. The cap layer thickness of the SE waveguide is 100 nm. The active material length is 2.5 mm for all simulations and the passive length is 5.5 mm for DE, 6.0 mm for ME and 6.5 mm for the SE waveguide, which is due to different required MMI lengths.

ally larger for TE than for TM modes and depend reciprocally on the waveguide width [67]. The sidewall roughness itself depends on the etch depth [68], the applied etching process and the lithographic masking technique [69]. A common reason to use SE or ME waveguides in electro-optic devices is their potentially lower scattering loss due to a reduced overlap of the propagating optical mode with the scraggly semiconductor surface. Figure 3.22 presents measured DE waveguide losses for different waveguide ridge widths together with their respective simulated absorption losses. The simulated intrinsic mode loss can be regarded as constant for all waveguide widths, but the experimentally determined losses follow an exponential decrease with increasing waveguide width (see also Dupont et al. [67]). For 2 μm wide DE waveguides, the measured loss is 0.6 dB/mm while the mode loss derived from simulations is only 0.12 dB/mm (IRT=1150 nm), i.e. four times higher due to the contribution of scattering losses. Measured data taken from 2 μm wide SE waveguides exhibited an average intrinsic losses of 0.25 dB/mm. No measurement data is available for the ME waveguide type.
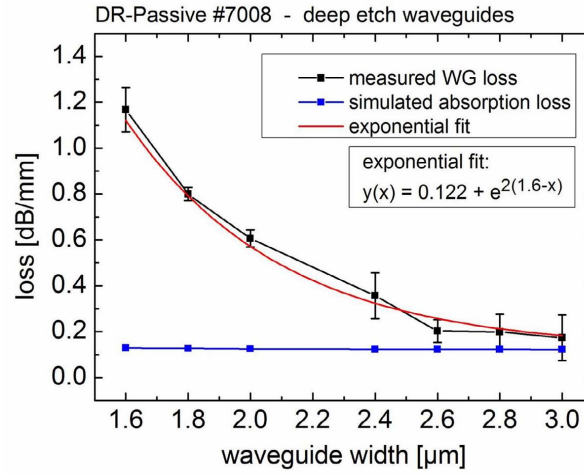
Fig. 3.22: Measured and calculated waveguide losses for DE waveguides with variable width and 1150 nm IRT. Each measured data point shows the average of three devices.

3.3 Optimization of the modulator switching voltage

The simplest reason to diminish the modulator's drive voltage V_π results from the wish to reduce the overall cost of the transmission system. A lower drive voltage does not only avoids the need for an expensive high power and high bandwidth driver amplifier, it also reduces the total power consumption of the packaged device and thus reduces the costs during operation. As discussed in chapter 2 the switching voltage of the modulator depends on three factors, namely the electro-optic efficiency of the selected quantum wells, the strength of the electric field generated in the p-i-n-diode structure by the applied voltage and the overlap of the optical mode with this electric field. These three factors including their interdependence will be discussed in the following sections.

3.3.1 Optimization of the MQW material

In InP-based modulators using a multi quantum well waveguide the so called Quantum-Confined Stark effect (QCSE) is the dominant electro-optic effect inducing an absorption and refractive index change. Eighty percent of the refractive index change which is used to modulate the optical phase in the Mach-Zehnder interferometer are related to the QCSE. A smaller fraction of approximately 15% is caused by the linear electro-optic effect (LEO) while the rest is related to the Franz-Keldysh effect in the undoped spacer layers above and below the MQW core [70]. If the semiconductor material system is chosen to be $In_{1-x}Ga_xAs_yP_{1-y}$ grown lattice matched on InP, then the only variables available for an optimization are the quantum well width and the material composition parameters x and y ($x = \frac{0.4541}{1-0.029\,y}$ for lattice matching to InP). In case of

a multi quantum well structure, the barrier width is the third degree of freedom for a material optimization using the Wannier-Stark effect (cf. Section 2.6.1).

In general, the epitaxial growth of quantum well structures is not limited to the lattice matched case. The binary compounds InP, InAs, GaAs and GaP included in $In_{1-x}Ga_xAs_yP_{1-y}$ for the four possible permutations of x and y being zero or one have different lattice constants. Therefore, the lattice constant of InGaAsP depends on the values of x and y. When two materials with different lattice constants are epitaxially grown on top of each other a force acts on the crystal lattice within the growth plane to equal out the different lattice constants. This so called strain can either be compressive or tensile and perturbs the electronic structure of the crystal. In particular, a modification of the energy levels of the valence and conduction band are observed which lead to a variation of the absorption and the refractive index for TE and TM polarized light. For example, strained MQWs allow polarization independent electro-optic field effects [71] in optical waveguides. In this thesis the theoretical evaluation of the InGaAsP MQW used as the waveguide core in the Mach-Zehnder modulators will be limited to the case of lattice matching to InP. A further analysis of the possibilities of strain-induced enhancement of the electro-optic modulation efficiency of the InGaAsP MQW is out of the scope of this thesis. An introduction to strain effects in semiconductor heterostructures can be found in the books of Harrison [35] or Chuang [19].

The techniques to calculate absorption and refractive index changes in quantum wells for electro-optic modulators have evolved over the past few decades. Simple effective mass based calculations using just one electron and one hole parabolic subband were used by Nojima et al. [15, 72] to evaluate quantum well structures of InP-based quaternary material systems in the 1.5 μm wavelength region. Exciton enhancement has been included in terms of an energy level shift but other carrier interaction effects were completely neglected resulting in an optimization curves of pure theoretical relevance. Susa [48] has calculated the refractive index enhancement in GaAs-based three-step coupled quantum wells by applying this technique and including the first heavy hole and the first light hole band. Common semiconductors with a diamond or zinc blende type crystal structure feature a more complicated valence band structure resulting from sp3 hybridization. The introduction of the multiband envelope function method, also known as k·p method, offered the possibility to perform detailed microscopic calculations of the band structure. For pure bulk material the single band approximation with definite energy eigenstates is still valid, but this is no longer true for position dependent potentials like quantum wells. In a quantum well type structure subbands are formed due to band coupling effects. Quantized energy states in a QW near the valence band edge comprise two or three of the respective bulk

valence bands with comparable contributions.

As a consequence the calculations in this work made for optimizing the InP-based quantum wells are performed using the commercial simulation tool *SimuLase* (NLCST Inc. [37]) which is based on an 8-band k·p model to solve the Schrödinger-Poisson equation in order to calculate single particle wavefunctions and energy subbands of a multi quantum well structure. This fully microscopic model allows to quantitatively predict the fundamental characteristics like absorption- gain- and PL-spectra and the carrier losses due to radiative processes. The optical properties are calculated using the polarization density matrix approach [20] described in Section 2.5.1 including a wide range of many-body interactions like electron-electron and electron-phonon scattering.

The starting point for the calculations with *SimuLase* in this work was to simulate photoluminescence spectra of a known quantum well structure in order to get a suitable value for the broadening factor required in *SimuLase* to account for crystal growth inhomogeneities. For excellent growth, the Gaussian broadening can be as small as about 8 meV while for typical growth it is about 12 meV -15 meV and for poor growth it may even be 25 meV. Figure 3.23 shows a measured photoluminescence (PL) curve (blue circles) of a MQW layer stack comprising the standard number quantum wells (the explicit number of quantum wells and the standard width of wells and barriers is not given due to NDA restrictions). The simulated PL spectrum (red line in Figure 3.23) is for a single 12 nm wide quantum well for TE polarization using two electron subbands and four hole subbands in the calculations. The Gaussian broadening parameter was automatically fitted to 17 meV by the *SimuLase* 'PL analyzer'. The dashed orange line indicates the wavelength of the lowest e1hh1 transition. The peak wavelength (green vertical line) in the PL spectrum is shifted to longer wavelengths due to excitonic effects. The fact that the PL intensity of the measured spectrum is larger than the simulated one below 1360 nm is due to the limited number of electron and hole subbands used in the calculation. The broadening factor of 17 meV is kept constant for all following simulations and a fixed sheet carrier density of $0.2 \cdot 10^{12} cm^{-2}$ is used. A variation of the sheet carrier density is important only when carrier effects (cf. Section 2.6.2) are taken into account. For high-speed modulation of the Mach-Zehnder modulator only electric field related effects are relevant. Figure 3.24 shows calculated PL peak wavelength contours of $In_{1-x}Ga_xAs_yP_{1-y}$ quantum wells lattice matched to InP for a variation of the quantum well width (8 nm to 15 nm) versus the material composition parameter y (0.7 to 0.9). These results are crucial for the following discussion. The PL spectra were calculated with no applied electric field and the previously determined broadening factor of 17 meV. The optimum working condition of the multi quantum well waveguide for the
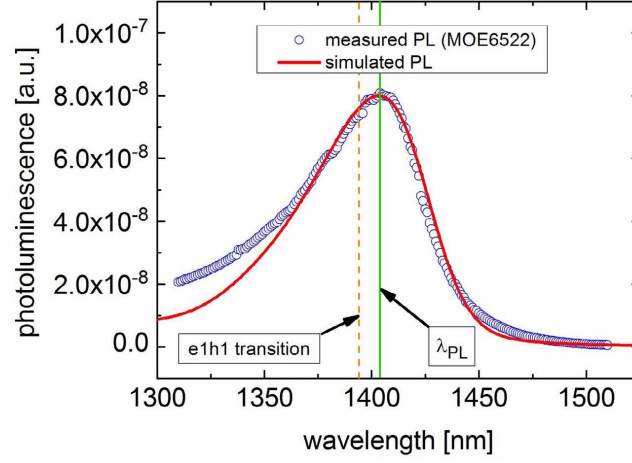
Fig. 3.23: Experimental photoluminescence spectrum for a standard MQW configuration (blue circles) and simulated PL spectrum for a single InGaAsP QW in TE polarization. The dashed orange line indicates the e1h1 transition wavelength.
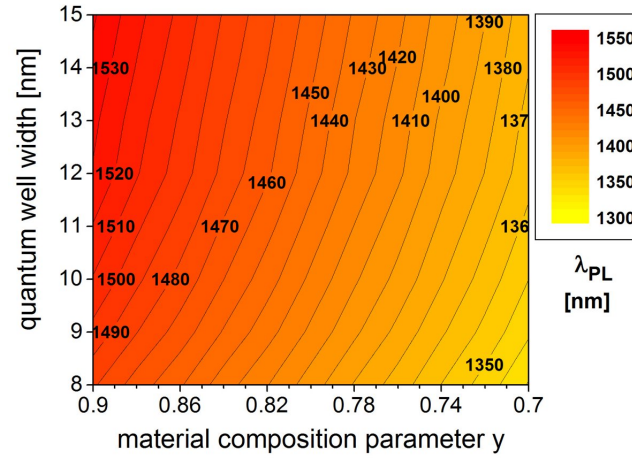
Fig. 3.24: Photoluminescence peak wavelength for InGaAsP/InP quantum wells using material compositions parameters y ranging from 0.7 to 0.9 and QW widths from 8 nm to 15 nm.

Mach-Zehnder interferometer modulator is given when the differential refractive index change is as large as possible while the differential absorption change or the absorption at zero applied electric field is as low as possible. The two approaches are used as a figure of merit (FOM) describing the performance of a certain quantum well. Nojima [15] and Susa [48] defined their Figure of merit as

$$\xi_1 = \frac{|\Delta n(\hbar\omega, E)|}{\alpha(\hbar\omega, 0)} \tag{3.2}$$

using only the specific absorption at zero electrical field as denominator, where n is the refractive index and α denotes the absorption. Alping and Coldren [16] used the differential

61
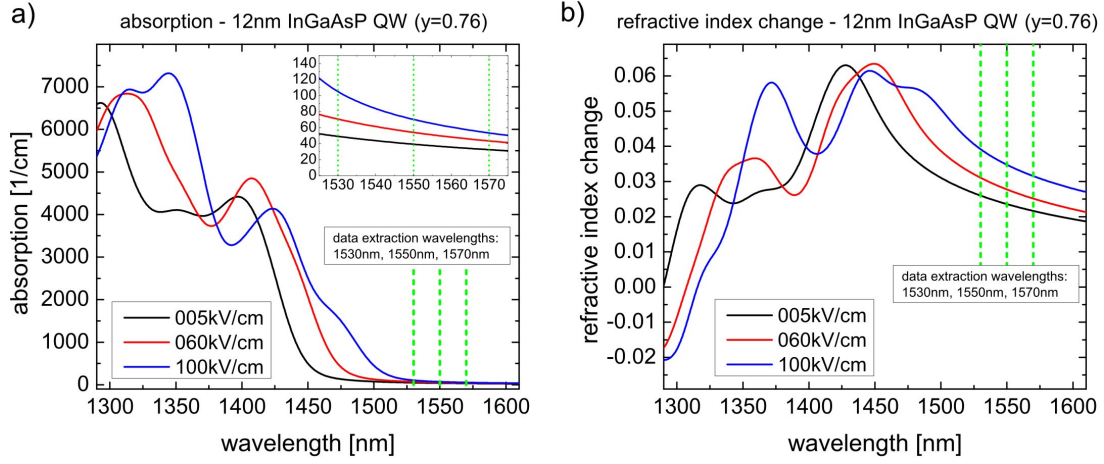
Fig. 3.25: Absorption (a) and refractive index change (b) spectra of a single 12 nm InGaAsP QW (5 kV/cm, 60 kV/cm and 100 kV/cm electric field, TE polarization). Inset in a) Absorption spectra from 1525 nm to 1575 nm in the C-band. The dashed green vertical lines indicate 1530 nm, 1550 nm and 1570 nm, where data is extracted for further evaluation.

absorption as denominator giving a figure of merit defined by

$$\xi_2 = \frac{|\Delta n(\hbar\omega, E)|}{\Delta\alpha(\hbar\omega, E)} \tag{3.3}$$

The two definitions correspond to different optimization targets. While ξ_1 corresponds to a minimization of the total device insertion losses by simply finding the quantum well with the lowest overall absorption, the optimization of ξ_2 has the objective to find a good overall system performance of the modulator by finding a design with low chirp. In order to find an optimum quantum well design, all combinations of QW widths and material composition parameters (MCP) y need to be analyzed by simulating their respective absorption and refractive index spectra. Figure 3.25a shows the resulting absorption spectra and Figure 3.25b the corresponding refractive index change spectra for 5 kV/cm, 60 kV/cm and 100 kV/cm applied electric field for TE polarization. The inset in Figure 3.25a illustrates the absorption spectra for the C-band in the range from 1525 nm to 1575 nm. The dashed green vertical lines indicate the three operating wavelengths 1530 nm, 1550 nm and 1570 nm, for which data will be extracted for further evaluation. An interesting result found in Figure 3.25a is the absorption peak at 1410 nm wavelength in the red trace for 60 kV/cm electric field. Usually one would expect the absorption peak to become weaker with increasing field strength as the exciton resonance becomes smaller due to a reduced wavefunction overlap. In the present case, the hole subband involved in the absorption process tends to switch from a light hole to a heavy hole character with increasing electric field. This leads to an increase in the oscillator strength (cf. Equation (2.44)) and hence to an increase of the absorption for TE polarized light.
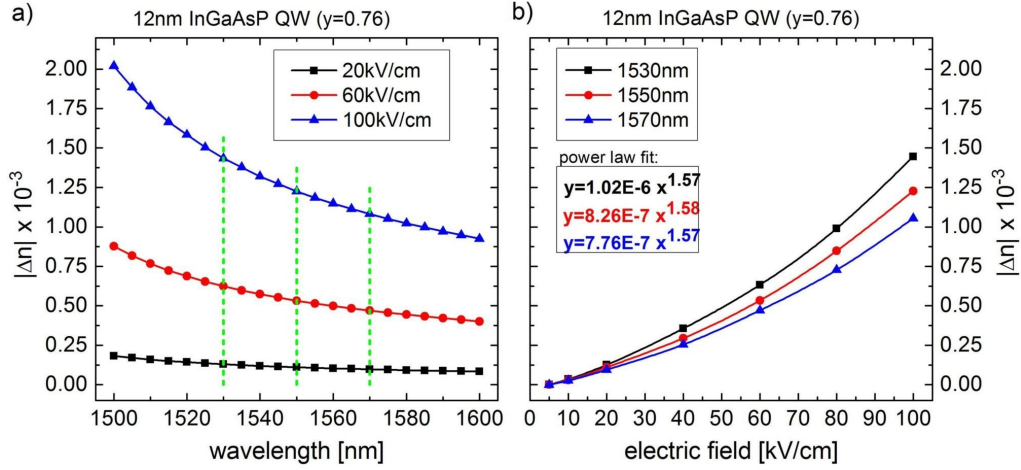
Fig. 3.26: Calculated refractive index change of a single 12 nm InGaAsP QW. a) refractive index change over wavelength for three different electric fields. For wavelengths closer to the band gap of the material, the refractive index change is larger. b) refractive index change over the electric field. Refractive index change data is fitted to a power law function given by the colored formulas.

The value of 5 kV/cm is chosen for zero applied bias voltage, which results from the built-in electric field in the p-i-n diode of the active modulator waveguide. The exact value varies for different background doping concentrations, intrinsic region thicknesses and waveguide geometries. This will be discussed in the following Section 3.3.2. *SimuLase* directly calculates the refractive index from the real part of the complex susceptibility. Exemplary details of the refractive index simulation results for a 12 nm QW (y=0.76) are shown in Figure 3.26. Figure 3.26a highlights the wavelength dependence of the differential refractive index for three electric fields (20 kV/cm, 60 kV/cm and 100 kV/cm). The plots are obtained by subtracting the refractive index spectrum at 5 kV/cm electric field from the spectrum at the respective E-field. In general, the index change Δn below the band gap is negative but the absolute value is taken in the figures for better understanding. The well known behavior of larger index changes for wavelengths, which are closer to the band edge of the material, can be observed. The vertical green dashed lines indicate again the specific wavelengths 1530 nm, 1550 nm and 1570 nm. Figure 3.26b depicts the electric field dependence of the differential refractive index for the three test wavelengths 1530 nm, 1550 nm and 1570 nm. Usually, the E-field dependence is a monotonic 2nd order polynomial function. For easier evaluation, it is assumed to follow a simpler power law given by

$$y = a \cdot x^b. \tag{3.4}$$

The fit formulas for the three wavelength's are given in Figure 3.26b and have an average scaling exponent of b=1.57±0.02. This scaling exponent is important for the electric field dependence
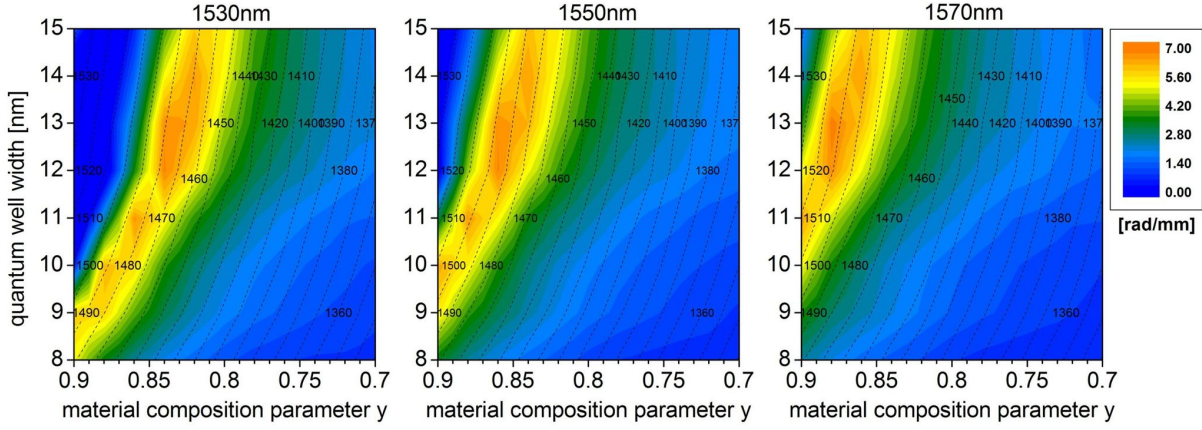
Fig. 3.27: Simulated phase changes (cf. Equation (3.5)) for 60 kV/cm E-field for $In_{1-x}Ga_xAs_yP_{1-y}$/InP quantum wells with different QW widths and material composition parameters y (As concentration). The dashed black contours show the associated photoluminescence wavelength from Figure 3.24.

evaluation in the following Section 3.3.2 as well as the derivation of unavoidable trade-offs in terms of optimum device performance discussed in Section 3.5. To find the best combination of width and material composition of a single $In_{1-x}Ga_xAs_yP_{1-y}$ quantum well for best electro refraction using TE polarized light the simulated absorption and refractive index data is taken for three selected wavelengths 1530 nm, 1550 nm and 1570 nm within the C-band. The resulting data for differential absorption $\Delta\alpha(\lambda, E)$ and differential index change $\Delta n(\lambda, E)$ is obtained by subtracting the value at 5 kV/cm from the respective value at 60 kV/cm. Figure 3.27 contains three plots showing phase changes $\Delta\Phi$ in units of [rad/mm] calculated from the refractive index change by

$$\Delta\Phi(\lambda, E) = \frac{2\pi}{\lambda}\Delta n(\lambda, E) \tag{3.5}$$

as a function of quantum well width and material composition y. The PL peak wavelengths from Figure 3.24 are given as black contours in each plot for better comparison. Keeping a fixed QW width and varying the material composition, the refractive index change is increasing if the QW's PL peak wavelength increased, which is a feature for all three wavelengths of interest. Interesting to point out is that the highest refractive index change is obtained for a QW with a PL chosen 60 nm below the test wavelength. For QWs with a PL wavelength closer than 60 nm to the respective test wavelength, the refractive index change strongly decreases which is undesirable for an efficient Mach-Zehnder modulator.

If the material composition parameter y is kept constant and the quantum well width is varied instead, larger QW thicknesses are clearly favorable due to their larger index change. When looking at QWs having the same PL peak wavelength, wider QWs have an advantage up to
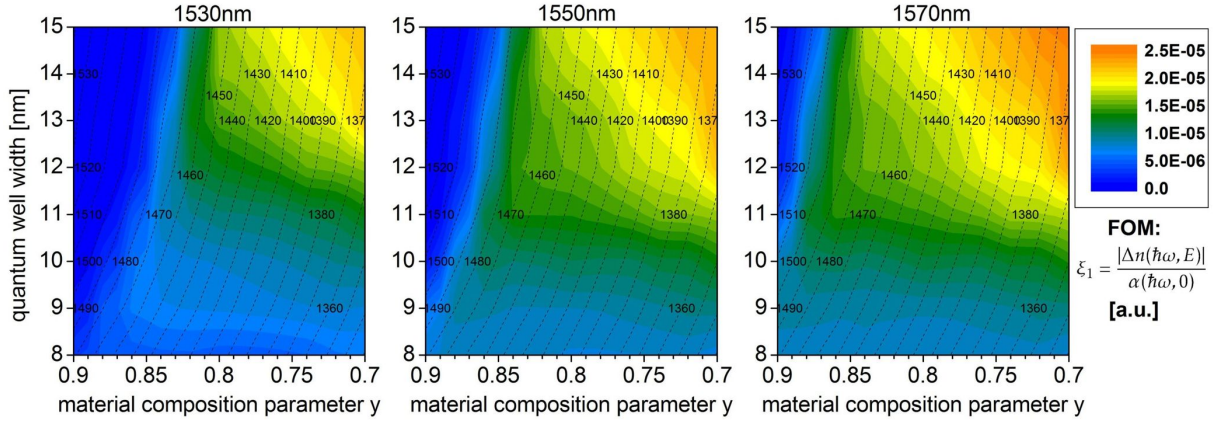
Fig. 3.28: Calculated contours of the figure of merit ξ_1 for 60 kV/cm for $In_{1-x}Ga_xAs_yP_{1-y}$/InP quantum wells with different QW widths and material composition parameters y (cf. Equation (3.2)). The dashed black contours show the associated photoluminescence wavelength from Figure 3.24.

13 nm. For larger QWs up to 15 nm the index change and PL contours run parallel giving no benefit for the one or the other.

Figure 3.28 shows contour plots of the figure of merit (FOM) ξ_1 defined in Equation (3.2) as a function of material composition y and QW width. Similar to Figure 3.27, the data is given for an electric field change from 5 kV/cm to 60 kV/cm for TE polarization and the three respective wavelength's in the C-band. The absorption α as denominator in (3.2) is fixed for an E-field of 5kV/cm. The dashed black lines indicate again the PL peak wavelengths. The first observation is that for PL wavelengths 50 nm or closer to the test wavelength the figure of merit ξ_1 is almost zero and independent of the QW width. Another interesting observation is that for PL wavelengths ≥ 80 nm from the test wavelength and QW widths below 12 nm, the ξ_1-contours run perpendicular to the PL contours. In this case higher ξ_1 values are obtained for larger quantum wells. For quantum wells thicker than 12 nm, the FOM contours start to tilt giving a gradient towards wider QWs with lower material composition y. In conclusion, the figure of merit ξ_1 is optimized by choosing a wide QW with a low As-content (material composition parameter y).

In Figure 3.29, contours showing the FOM ξ_2 after Equation (3.3) are given for 1530 nm, 1550 nm and 1570 nm wavelength. The calculated data is obtained similarly to Figures 3.27 and 3.28. An interesting finding is that for all three wavelengths the PL contours run almost parallel to the FOM contours favoring lower PL wavelengths.

In order to choose the optimum QW for electro refractive operation in a low loss Mach-Zehnder modulator, one should carefully define the desired operation conditions. It is obvious from both FOMs, that QWs thicker than 11 nm with shorter PL-wavelength have a better perfor-
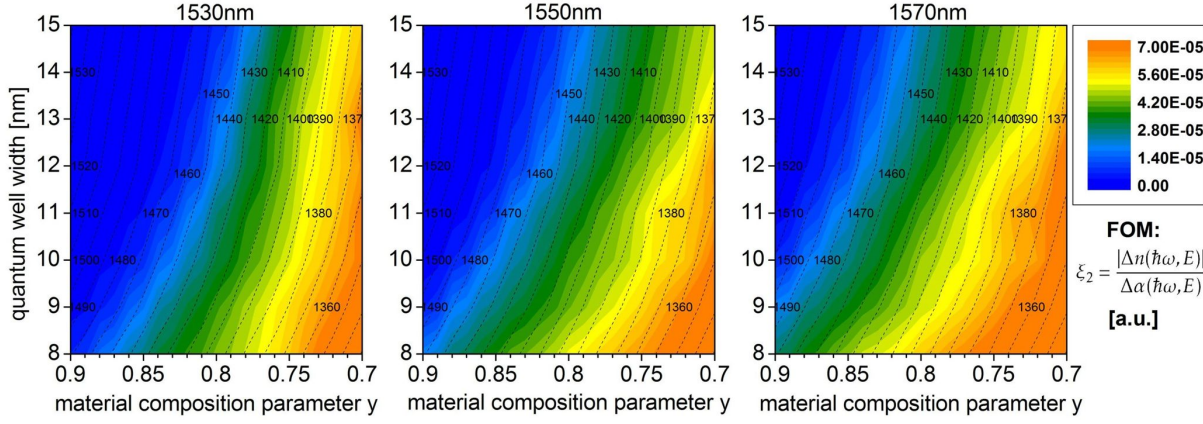
Fig. 3.29: Calculated contours of the figure of merit ξ_2 of $In_{1-x}Ga_xAs_yP_{1-y}$/InP quantum wells for different QW widths and material composition parameters y using Equation (3.3). The E-field is changed from 5 kV/cm to 60 kV/cm. The dashed black contours show the associated photoluminescence wavelength from Figure 3.24.

mance trade-off regarding high electro-refraction with low absorption. But on the other hand, choosing a low PL-wavelength QW implies a lower total refractive index change per mm material length, which finally requires a longer device.

3.3.2 Electric field dependence on waveguide geometry and material doping

In this section the geometrical dimensions of the modulator's waveguide cross-section will be investigated to optimize the electric field strength per applied voltage. This is the area with the largest optimization potential. The switching voltage V_π of the modulator depends on the electric field strength which is generated by a certain applied voltage. As demonstrated in the previous section, the refractive index change induced by the QCSE scales approximately with the power of 1.57 with the electric field (cf. Figure 3.26). Thus doubling the electric field per applied bias voltage reduces the required modulator switching voltage by a factor of $2^{1.57} \approx 3$. The spacial distribution of the electric field within the cross-section of the waveguide depends on the geometry of the optical waveguide and the background doping concentration (BDC) in the nominally undoped region of the p-i-n-diode.

In order to evaluate the electric field distribution for all three waveguide variations introduced in Section 3.1.1, various calculations have been done using the advanced materials general purpose 2D device simulator *ATLAS Blaze* from Silvaco Data Systems Inc. [73]. The program calculates the electric field distribution of a 2D or 3D structure by solving Poisson's equation, which relates the electrostatic potential to the space charge densities obtained from carrier continuity equations. The input parameters required are the semiconductor layer structure, wave-
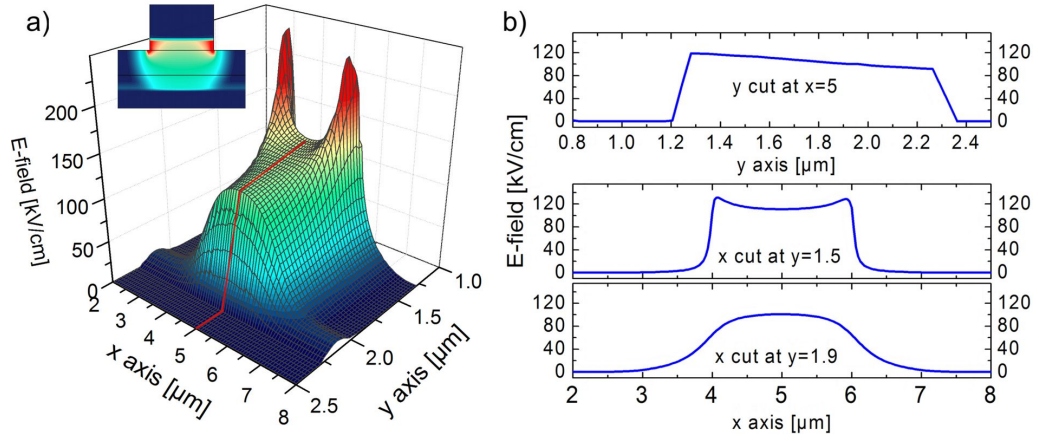
Fig. 3.30: Simulated electric field distribution of a 'median etch' (ME) waveguide (IRT=1000 nm, 10 V, background doping concentration: $1 \cdot 10^{15} cm^{-3}$). a) 3D representation of the field distribution (inset 2D). b) Y-cut through the 3D structure at x=5 μm, x-cuts at y=1.5 μm and y=1.95 μm.

guide material type and donor or acceptor concentrations. As an example, Figure 3.30a shows the electric field simulation results of a 'median etch' waveguide with 1000 nm intrinsic layer thickness in 2D and 3D representation. The applied reverse voltage is 10 V and the background n-doping concentration was set to $1 \cdot 10^{15} cm^{-3}$. Figure 3.30b shows three cuts through the field distribution plotted in a). The upper trace shows a cut along the y-axis at x=5 μm. The drop of the E-field from the left (p-doped) to the right (n-doped) is typical for a p-i-n-junction structure under the assumption that the background doping in the intrinsic region is of n-type. The lower plots in Figure 3.30b are x-cuts at y=1.5 μm and y=1.9 μm. A nonuniform field distribution is clearly observed, which results from the sharp edge between the waveguide rib and the waveguide core layer situated in the intrinsic region. At this edge the electric field spreads into the vertical direction. This leads to the formation of so called 'rabbit ears' at the two corner points in the case of a 'median etch' (ME) or 'shallow etch' (SE) waveguide geometry. The background doping concentration (BDC) is of great importance for the distribution of the electric field. Due to the intentionally grown p- and n-material to form the respective contacts, a built-in field exists with no applied voltage. The n-type nature of the background doping leads to the formation of the built-in field at the 'p-type-to-intrinsic' junction.

Depending on the background doping concentration, the built-in field reaches further towards the n-contact. For low background n-doping or very narrow intrinsic regions, the built-in field covers the entire intrinsic region with no applied voltage. If a bias voltage is applied, the E-field increases linearly all over the intrinsic region. For larger intrinsic regions with high background doping, the built-in in field covers only a small fraction of the intrinsic region close to the p-
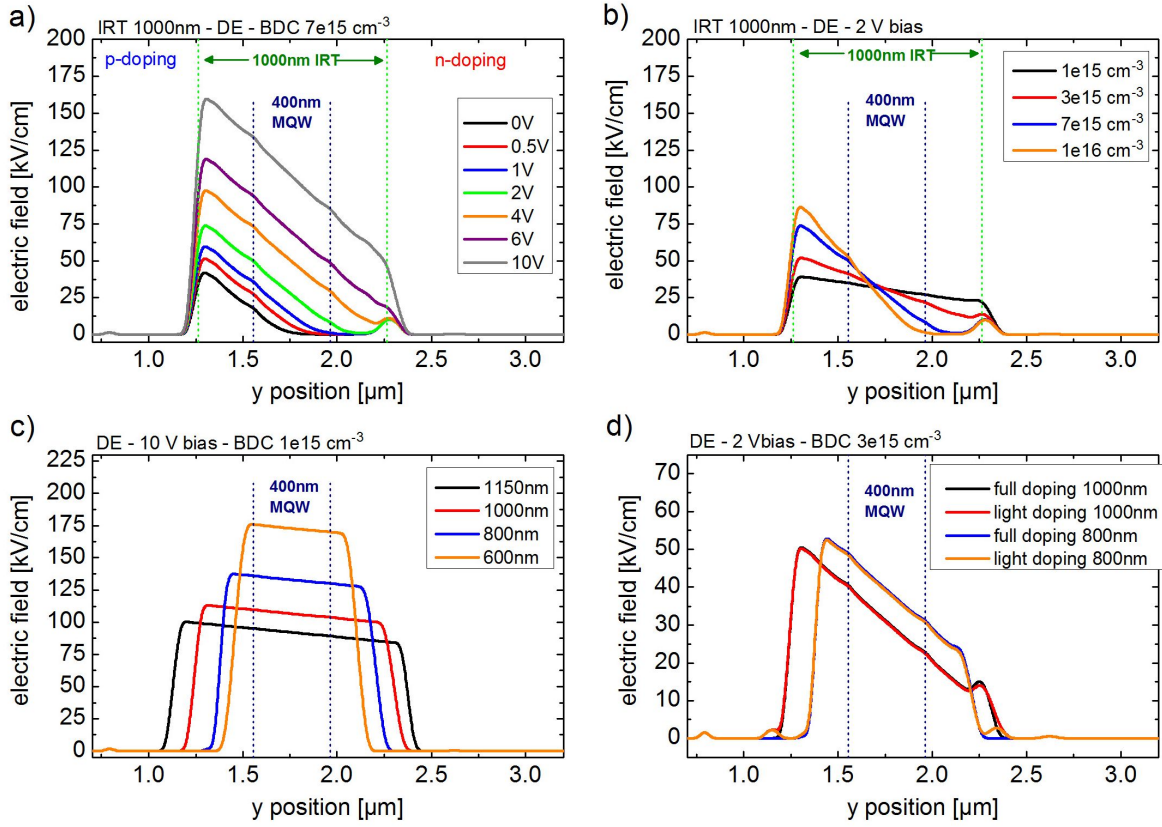
Fig. 3.31: Simulated 2D electric field plots in y-direction at x=1.5 μm (cf. Figure 3.30).

a) E-field distribution with increasing bias voltage (DE, BDC=$7 \cdot 10^{15} cm^{-3}$). b) E-field distribution at different BDC (2 V). c) E-field for nominally grown intrinsic region thickness variations (10 V, BDC=$1 \cdot 10^{15} cm^{-3}$). d) Traces at 1 V and 2 V bias voltage for a DE geometry(IRT=1000 nm, BDC=$3 \cdot 10^{15} cm^{-3}$) for full and light doping profiles (cf. Section 3.2.2).

doping. When a bias voltage is applied, the E-field widens until full carrier depletion is reached. Up to this punch-through voltage the electric field increases non-uniformly. Figure 3.31a shows electric field plots cut along the y-axis for a ME waveguide (IRT=1000 nm, BCD=$3 \cdot 10^{15} cm^{-3}$) for applied voltages from 0 V to 10 V. The large background doping was chosen to highlight the effect described before. At 0 V, the built-in field penetrates only half of the nominally intrinsic region. With increasing voltage the field widens and equals the thickness of the intrinsic region at a punch-through voltage of 4 V. The multi quantum well waveguide core, wich is the important region for the electro-optic function, is fully depleted for an applied voltage of ≈ 1.5 V.

Figure 3.31b shows the electric field strength at 2 V reverse voltage for varying BDCs of $1 \cdot 10^{15} cm^{-3}$, $3 \cdot 10^{15} cm^{-3}$, $7 \cdot 10^{15} cm^{-3}$ and $1 \cdot 10^{16} cm^{-3}$ and an intrinsic thickness of 1000 nm. The electric field width equals the complete intrinsic thickness for $1 \cdot 10^{15} cm^{-3}$ and $3 \cdot 10^{15} cm^{-3}$,

but the applied 2 Volts have not fully depleted the nominally intrinsic space charge region for BDCs of $7 \cdot 10^{15} cm^{-3}$ and $1 \cdot 10^{16} cm^{-3}$. A high background doping under low bias conditions prevents high frequency operation of the MZ modulator. The applied voltage in the Mach-Zehnder arms drops below the punch through voltage of the p-i-n-diode during modulation and results in a change of the balanced capacitive load which compromise the push-pull operation of the MZM (cf. Section 2.4).

Figure 3.31c presents calculated electric field plots for intrinsic region thicknesses variations (1150 nm, 1000 nm, 800 nm and 600 nm) at 10 V applied bias for a BDC of $1 \cdot 10^{15} cm^{-3}$. The electric field is 92 kV/cm in the center of the multiple quantum well for 1150 nm IRT, 107 kV/cm for 1000 nm, 133 kV/cm for 800 nm and 173 kV/cm for 600 nm intrinsic thickness. The field strength obviously almost doubles when the size of the depletion region is almost halved from 1150 nm to 600 nm. The drive voltage V_π of the modulator is expected to be reduced by a factor $(92/173)^{1.57} = 2.7$ due to the power law dependence of the QCSE (cf. Section 3.3.1). The electric field distributions for the DE waveguide type in Figure 3.31d reveal that the change of the doping profile from 'standard doping' to 'light doping' (cf. Table 3.2) does not change the electric field distribution. The plots show the electric field for IRTs of 800 nm and 1000 nm with a BDC of $3 \cdot 10^{15} cm^{-3}$ and an applied voltage of 2 V. The 'light doping' profile has been introduced in Section 3.2.2 to reduce absorption losses. The results of the 'light doping' profile using a p-type doping concentration of $2.5 \cdot 10^{17} cm^{-3}$ and an n-type doping concentration of $5 \cdot 10^{17} cm^{-3}$ do not show a difference to the 'standard doping' profile, therefore the 'light doping' profile can be used for the p-i-n-diode of the modulator's optical waveguide.

In the following discussion, all simulation data will be taken from simulations using the 'standard doping' profile and the results will be considered to be identical for the 'light doping' profile. To investigate the modulation efficiency Γ_{EO} of a certain waveguide geometry or doping profile, the overlap integral of the electric field and the optical intensity (squared optical field strength) profile is calculated by using a slightly modified version of the formula given by Alferness [74]:

$$\Gamma_{EO} = \frac{\iint_{EO\,core} \left(E_{ele}(x,y)\right)^{EOE} \cdot \left|E_{opt}(x,y)\right|^2 dxdy}{\iint_{-\infty}^{+\infty} \left|E_{opt}(x,y)\right|^2 dxdy}. \tag{3.6}$$

The overlap integral is calculated only in the active MQW waveguide core layer denoted by '*EO core*' in the integral for the y direction. The overlap integral is normalized by the total power confined in the optical mode. To account for the nonlinear phase change due to the Quantum-
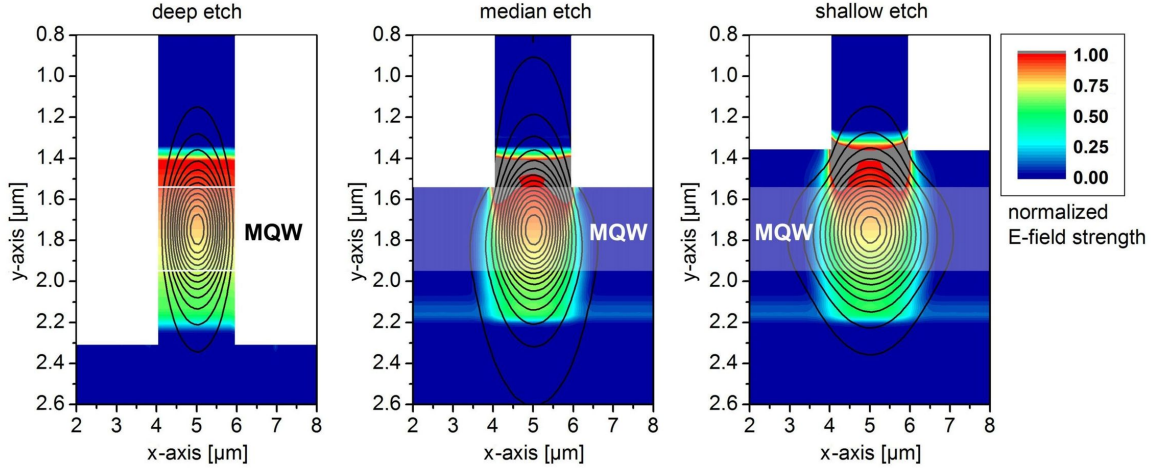
Fig. 3.32: Electric field (colored) and optical field (black lines) distributions for 'deep etch', 'median etch' and 'shallow etch' waveguide geometries. The electric field strength is normalized to the maximum value in the 'deep etch' case. The grey shaded areas in the median and shallow etch E-fields indicate a higher electric field (BDC=$7 \cdot 10^{15} cm^{-3}$).

Confined Stark effect, the electro-optic efficiency (EOE) factor is introduced which is applied to the electric field as an exponential factor in Equation (3.6). The origin of the exponential factor is the power law fit given in Equation (3.4). Figure 3.32 shows electro-optic field overlaps for the three waveguide geometries investigated ('deep etch' (DE), 'median etch' (ME) and 'shallow etch' (SE)). The width of the intrinsic region is 800 nm and the background doping was chosen to be $7 \cdot 10^{17} cm^{-3}$ for better visualization of the electric field drop from the top to the bottom. The electric fields in all three plots of Figure 3.32 are normalized such that the maximum E-field value in the DE strcture equals 1. The active waveguide core is highlighted by the bright stripe between y=1.55 and y=1.96 and the label 'MQW' in each plot. The electric field plots of the ME and SE geometry contain areas where the field is stronger (grey) than the maximum electric field strength in DE case (red=1). These areas indicate the so called 'rabbit ears' shown in Figure 3.30 which originate from the waveguide rib corners existing in the intrinsic region.

For a quantitative analysis of the modulation efficiency of the three waveguide geometries, an evaluation software has been programmed that uses the electric field data simulated with *ATLAS Blaze* and the optical mode profiles obtained from simulations using *FIMMWAVE*. The software first normalizes the optical mode profile and then linearly interpolates the mode data onto the same 321x16 (10μm on x-axis and 0.4μm on y-axis) point grid used for the numerical calculation of the electric field. The 400 nm electro optic core thickness is used as a reference thickness (standard multi quantum well number). For the DE waveguide, a grid size of 65x16 (2 μm on x-axis and 0.4 μm on y-axis) is used because only the actual waveguide width of 2 μm
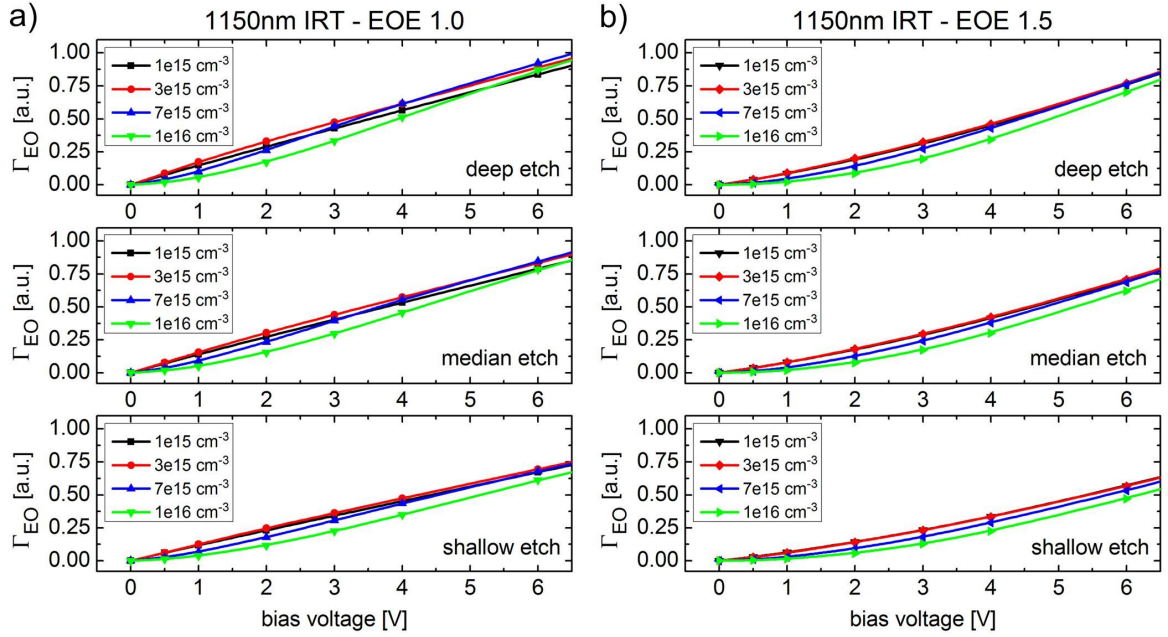
Fig. 3.33: Modulation efficiency Γ_{EO} over bias voltage for 'deep etch' (DE), 'median etch' (ME) and 'shallow etch' (SE) waveguide geometries and different background doping concentrations calculated with Equation (3.6). a) EOE-factor=1.0 b) EOE-factor=1.5.

is accounted in the overlap integral. The last step is to calculate the electro-optic modulation efficiency Γ_{EO} given by Equation (3.6) for an EOE-factor which can be chosen between 1 and 2. For example, the fitted theoretical data for the QCSE shown in Figure 3.26 revealed EOE=1.57. Details on the evaluation tool and its functionality can be found in Appendix C.1.

For a general evaluation of the electric field overlap with the optical mode in DE, ME and SE waveguides, an 'electro optic efficiency' factor EOE = 1 is used. Figure 3.33a shows the calculation results of Γ_{EO} for the DE (upper plot), the ME (middle plot) and the SE (lower plot) waveguide structure for different applied bias voltages and an intrinsic region thickness (IRT) of 1150 nm. Γ_{EO} of each waveguide configuration is given for BDCs of $1 \cdot 10^{15} cm^{-3}$, $3 \cdot 10^{15} cm^{-3}$, $7 \cdot 10^{15} cm^{-3}$ and $1 \cdot 10^{16} cm^{-3}$. An interesting observation is, that for the two lower BDCs, the increase of Γ_{EO} is sub linear and that this effect is most pronounced for the DE waveguide type. This effect is associated to a fully depleted space charge region at 0V that widens with increasing applied voltage reducing the overall field increase in the electro optic core. For BDCs of $7 \cdot 10^{15} cm^{-3}$ and $1 \cdot 10^{16} cm^{-3}$, the nominally intrinsic region is not fully depleted at 0 Volts. With increasing applied bias voltage, the width of the depleted area rapidly increases while the electric field strength in the waveguide core is only slowly increasing. For a background doping of $7 \cdot 10^{15} cm^{-3}$ this effect vanishes at about 4 V bias while for a higher BDC of $1 \cdot 10^{16} cm^{-3}$, Γ_{EO} shows a higher than linear increase up to a bias voltage of 6 Volts.

Figure 3.33b shows Γ_{EO} calculated similarly with EOE=1.5. Each of the curves for the individual BDCs can be fitted with the previously used power law function y(x)=a·x^b. Calculating Γ_{EO} with EOE=1.5 and applying a power law fit for the DE waveguide with BDC=$1 \cdot 10^{15} cm^{-3}$ gives a scaling exponent b=1.31±0.015 and for the largest BDC of $1 \cdot 10^{16} cm^{-3}$ the fitted exponential factor becomes b=1.6±0.05. This is a significant difference which can be used to determine the background doping of a wafer using simple DC-Matrix measurements. The evaluation of the modulation efficiencies of different wafers shown in Figure 5.5 of Chapter 5 is done using this technique.

The most interesting question when comparing the three different waveguide geometries is which one is the best waveguide type for a low drive voltage MZ modulator. Figure 3.32 suggests that the 'deep etch' (DE) waveguide has the best Γ_{EO}. In the following discussion, where the different waveguide geometries are compared under different conditions, the DE case is referenced as 100% . Figure 3.34a shows the relative modulation efficiency $\Delta\Gamma_{EO}$ versus the applied bias voltage for EOE-factors of 1.0, 1.3 and 1.6 using an intrinsic region with IRT=1150 nm and a BDC of $1 \cdot 10^{15} cm^{-3}$. For EOE=1.0, the 'median etch' (ME) waveguide has a modulation efficiency of 94% compared to the DE type while the 'shallow etch' (SE) waveguide has a maximum of 80% modulation efficiency. For increasing EOE factors, which more likely reflects real devices, the relative modulation efficiencies $\Delta\Gamma_{EO}$ of the ME and SE waveguide become even smaller compared to the DE type. Using EOE=1.6, the largest $\Delta\Gamma_{EO}$ is 92% for the ME waveguide and only 74% for the SE type waveguide. In the bias region from 0 V to 4 V the relative modulation efficiencies of the ME and the SE type geometry slightly increase with increasing bias voltage.

In Figure 3.34b relative modulation efficiencies are plotted over the applied bias voltage for all four investigated background doping concentrations (BDC) (IRT=1150 nm,EOE-factor=1.3). With increasing BDC, the relative efficiency of the ME and SE type waveguides get worse when compared to the DE type. The second interesting observation is the dependence on the applied bias voltage which becomes stronger with increasing BDC. The lowest $\Delta\Gamma_{EO}$ of only 66% originates from a SE waveguide ($BDC = 1 \cdot 10^{15} cm^{-3}$, 3 V bias).

Figure 3.34c depicts the relative modulation efficiency $\Delta\Gamma_{EO}$ for intrinsic region thicknesses (IRT) of 1150 nm, 1000 nm and 800 nm (EOE=1.3, BDC=$3 \cdot 10^{15} cm^{-3}$). An interesting point to figure out is that for smaller nominal IRTs the advantage of the DE waveguide geometry is smaller. For IRT=800 nm, the ME and DE type waveguide have identical modulation efficiencies above 4 V applied bias. The voltage dependence of the relative efficiency $\Delta\Gamma_{EO}$ is due to the fact, that BDC=$3 \cdot 10^{15} cm^{-3}$ was chosen for plotting.
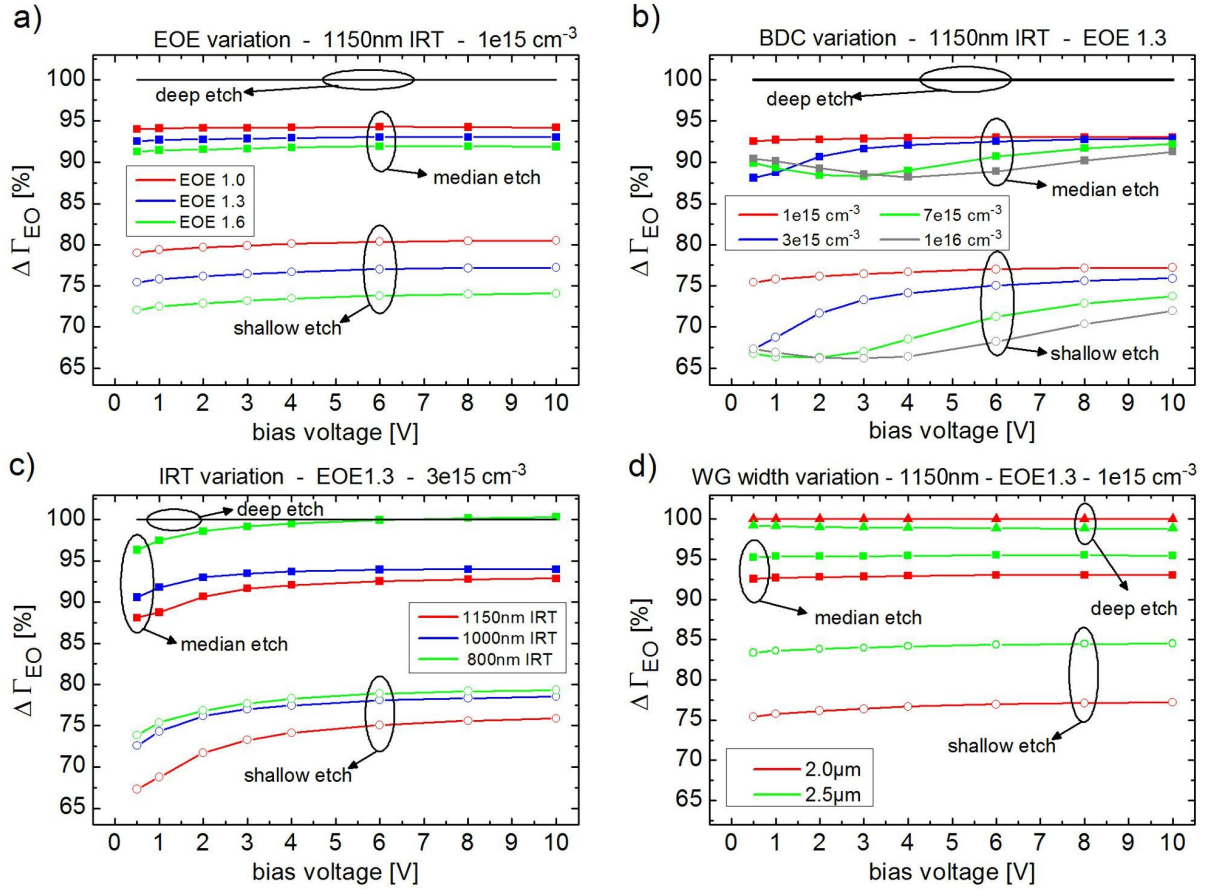
Fig. 3.34: Relative modulation efficiencies $\Delta\Gamma_{EO}$ of the three waveguide geometries as a function of the applied bias voltage. a) $\Delta\Gamma_{EO}$ for EOE-factors of 1.0, 1.3 and 1.6. a) Effect of different background doping concentrations. c) $\Delta\Gamma_{EO}$ for IRTs 1150 nm, 1000 nm and 800 nm. d) $\Delta\Gamma_{EO}$ for waveguide widths of 2.0 µm and 2.5 µm (IRT=1150 nm, EOE=1.3, BDC=$1\cdot 10^{15}cm^{-3}$).

Another possibility to influence the electro optic overlap is to change the width of the active waveguide. Figure 3.34d highlights the differences of the relative modulation efficiency between the standard 2.0 µm wide waveguide and an identical configuration using 2.5 µm width. The data is normalized such that the 2.0 µm wide DE waveguide is the 100% baseline (IRT=1150 nm, BDC=$1\cdot 10^{15}cm^{-3}$, EOE-factor=1.3). Interestingly, the DE waveguide of 2.5 µm width features a slightly lower Γ_{EO} compared to the 2.0 µm wide waveguide while in the ME and SE case, the wider 2.5 µm waveguide has a better modulation efficiency than the 2.0 µm one. For the 2.5 µm wide ME waveguide the improvement is relatively small with 2.6% but for the SE waveguide the required driving voltage V_π can be reduced by 9% when the waveguide width is increased from 2.0 µm to 2.5 µm.

To this point, only a relative evaluation regarding the intrinsic thickness of all three waveguide types has been done. To understand the benefit of reducing the nominal thickness of the
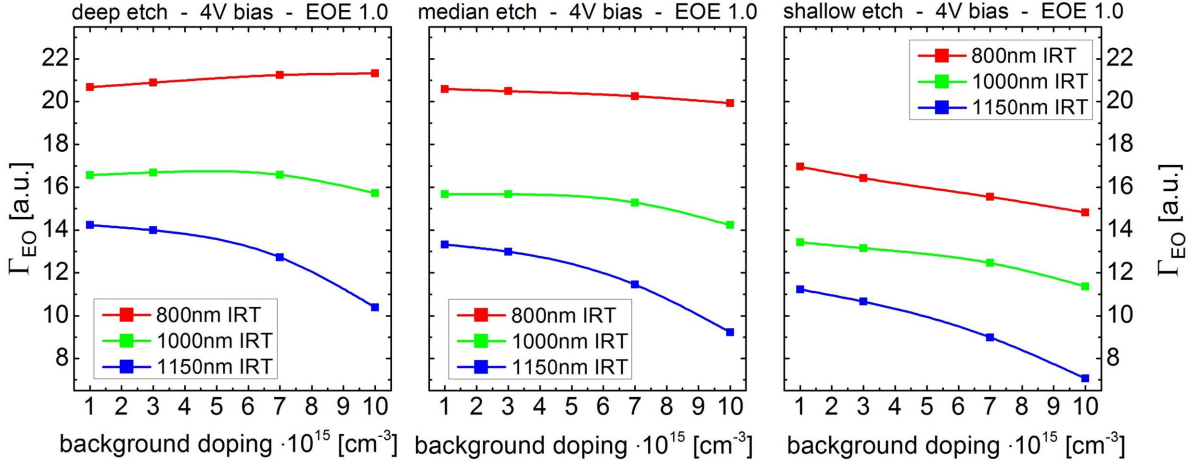
Fig. 3.35: Modulation efficiencies Γ_{EO} of 'deep etch', 'median etch' and 'shallow etch' waveguides as a function of background doping (EOE-factor=1.0, 4 V bias).

undoped space charge region the absolute modulation efficiency of each waveguide type has to be analyzed separately. Figure 3.35 shows modulation efficiencies Γ_{EO} of DE, ME and SE type waveguides as a function of background doping (4 V bias, EOE-factor=1.0). For DE type waveguides, the result is very interesting because a thin intrinsic region of 800 nm, the modulation efficiency increases with increasing BDC. But this should not be understood as a reason to favor high background doping concentrations in the modulator because the effect is only in the order of 3%. The negative influence of doping to optical losses and the modulation bandwidth counterbalances this 3% benefit. For ME and SE type waveguides, a higher background doping always reduces the modulation efficiency Γ_{EO}. For the reference intrinsic thickness of 1150 nm, the loss in modulation efficiency with increasing BDC from $1 \cdot 10^{15} cm^{-3}$ to $1 \cdot 10^{16} cm^{-3}$ is severe and sums up to 25% for the DE waveguide, 30% for the ME type and 37% for the SE geometry. For all three waveguide types, the negative effect of background doping becomes less prominent for thinner intrinsic regions. In general, the DE waveguide type is found to be the most efficient geometry for the modulator waveguide from an electro-optic overlap point of view.

The next major question is how much the required modulation voltage can be reduced by shrinking the intrinsic region, which implies a larger electric field with the same applied bias. Figure 3.36 shows calculation results of the relative drive voltage V_π as a function of the intrinsic region thickness (IRT) for all four background doping concentrations using the DE waveguide geometry. The plots are normalized such that the relative drive voltage is 100% for the reference IRT=1150 nm. The relative drive voltages are calculated for EOE factors of 1.0,
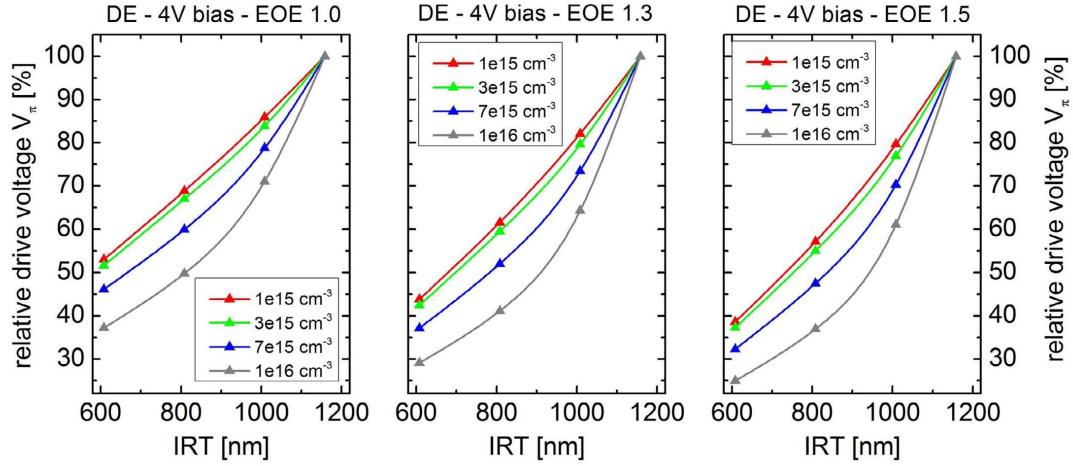
Fig. 3.36: Relative drive voltage V_π as function of the intrinsic region thickness for different background doping concentrations (DE waveguide). EOE-factors of 1.0, 1.3 and 1.5 are used in the left, middle and right plot, respectively.

1.3 and 1.5. The required modulation voltage V_π of the modulator can be significantly reduced by shrinking the intrinsic region. Assuming an EOE-factor of 1.3 (BDC=$1 \cdot 10^{15} cm^{-3}$, IRT=800 nm) for the modulator, the modulation voltage can be reduced to only 61% of that of a modulator with reference IRT=1150 nm. Similar drive voltage reductions are obtained for the ME and SE type waveguides. The curves of Figure 3.36 again imply, that a higher background doping is favorable when using smaller IRTs because the drive voltage reduction is larger. But as shown before, the absolute modulation efficiency is larger for lower BDCs.

The modulation efficiency has been quantified for a waveguide core layer situated in the center of the intrinsic region. Because of the non homogenous distribution of the electric field along the vertical axis caused by background doping, a change of the position of the MQW layers within the non-intentionally doped space charge region can lead to an increase or a reduction of the required drive voltage of the MZ modulator. Due to the n-type nature of background doping, the electric field is stronger in the vicinity of the p-contact (cf. Figure 3.31) and decreases towards the n-contact. Thus, placing the multi quantum well closer to the p-contact increases the modulation efficiency. At the same time, this implies a larger overlap with p-doped material which increases optical absorption losses. Trade-off calculations for an optimal modulator design will be presented in Section 3.5.

The evaluation tool presented in Appendix C.1 allows to shift the optical mode profile relative to the electric field in the y direction to simulate a vertical position offset of the MQW waveguide core inside the intrinsic region. Figure 3.37a shows calculated modulation efficiencies Γ_{EO} for a DE waveguide (BDC=$1 \cdot 10^{16} cm^{-3}$, IRT=1150 nm, EOE=1.3). The large value

75
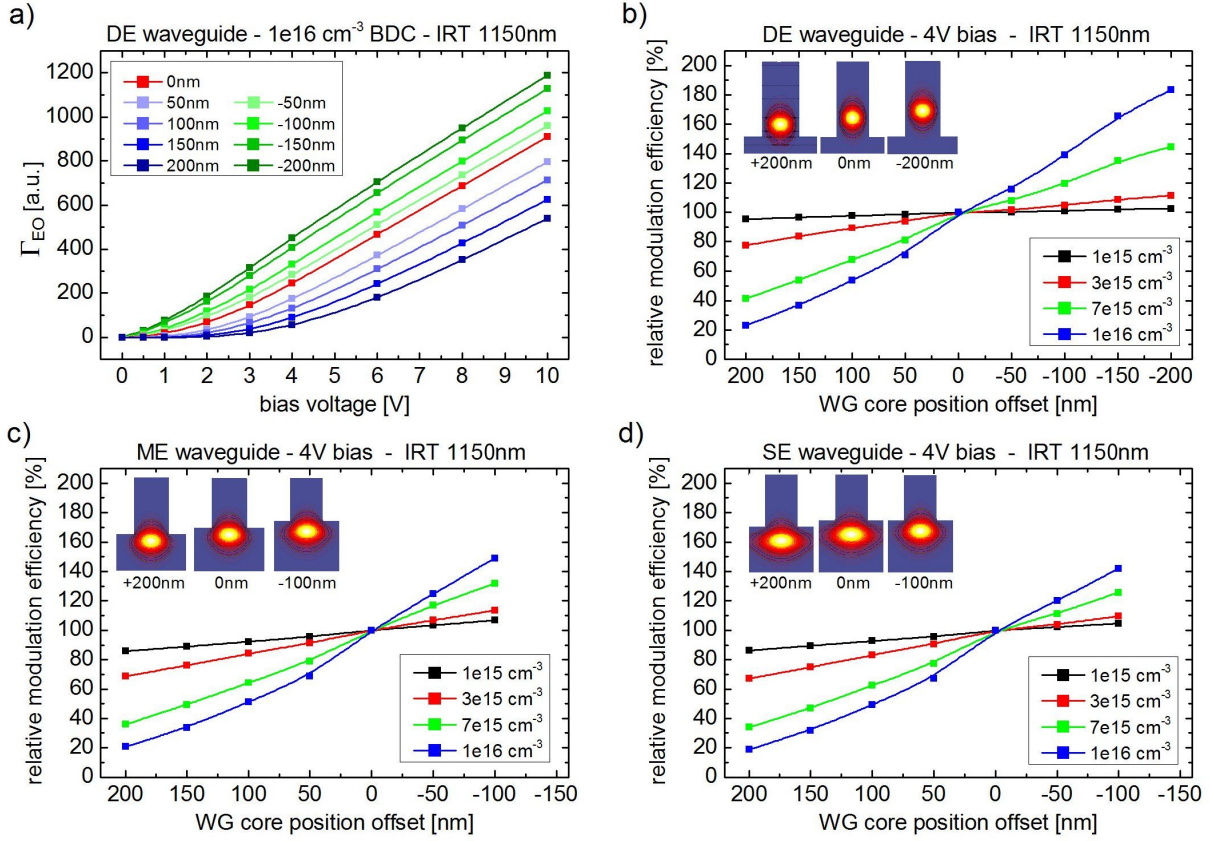
Fig. 3.37: Simulated modulation efficiencies for varying waveguide core positions inside the intrinsic region. a) shows Γ_{EO} as a function of the applied bias voltage for a DE waveguide with $1 \cdot 10^{16} cm^{-3}$ BDC, IRT=1150 nm and EOE=1.3. b) shows the modulation efficiency for the DE waveguide geometry for different offsets relative to the center position. c) and d) show identical plots as b) for the ME and SE waveguide geometry, respectively. A positive offset denotes a position closer to the n-contact.

for the background doping concentration has been chosen as the position dependence of Γ_{EO} is most pronounced for high values of the BDC. As can be seen in Figure 3.37a the slope of the voltage dependent Γ_{EO} and hence the scaling exponent of the power law fit is heavily influenced by the position of the waveguide core. While a negative offset up to -200 nm gives an almost linear voltage dependence (EOE=1.0) of Γ_{EO} after a distinct bias voltage, a positive offset of the MQW core results in an increasing EOE-factor. When gathering the EOE-factor of real devices by evaluating DC intensity matrix measurements, this has to be kept in mind. Figure 3.37b shows relative modulation efficiencies of the DE waveguide structure as a function of the MQW core position offset for the four known values of the BDC. (IRT=1150 nm, EOE-factor=1.3). A positive offset denotes a waveguide core layer shift closer to the n-contact. While a low BDC of $1 \cdot 10^{15} cm^{-3}$ has little influence on the position dependence of Γ_{EO} with only -4.6% for a 200 nm shift towards the n-contact and +2.8% for a 200 nm shift towards the p-contact,

the positional variability of Γ_{EO} increases with increasing BDC. For a BDC of $1 \cdot 10^{16} cm^{-3}$, +200 nm offset leads to a 77% reduction of Γ_{EO} and -200 nm offset towards the p-doped layers increases Γ_{EO} by 83%. The two waveguide geometries (ME and SE) with a nonuniform electric field distribution suffer from an even larger variability of Γ_{EO}. This is highlighted in Figure 3.37c and Figure 3.37d for the ME and SE waveguide type, respectively. Even for a low BDC of $1 \cdot 10^{15} cm^{-3}$, a +200 nm offset of the WG core in a ME structure reduces the modulation efficiency by 13.1%. Interestingly, the Γ_{EO} variability of the ME geometry is similar to that of the SE geometry within a 1% margin.

In summary the simulations have shown that the DE waveguide geometry has the best modulation efficiency. When the Mach-Zehnder modulator is intended to operate in a low bias region from 2 V to 4 V, than the DE waveguide has an even bigger advantage over the ME and SE waveguide geometries. As a rule of thumb, it can be noted that the ME waveguide has 92% and the SE waveguide 75% relative modulation efficiency compared to the DE geometry. A high background doping concentration of $1 \cdot 10^{16} cm^{-3}$ has been found to significantly reduce the absolute modulation efficiency by 25% for the DE waveguide compared to a low BDC of $1 \cdot 10^{15} cm^{-3}$. The influence of a high BDC on the ME and SE waveguide types is even worse. Using a thinner intrinsic region lowers the required modulation voltage and reduces the negative impact of high background doping.

3.3.3 The electro optic core confinement factor

After having analyzed the MQW material system with respect to the Quantum-Confined Stark effect in Section 3.3.1 and having optimized the waveguide geometry of the modulator for optimum electro-optic overlap in Section 3.3.2, the last step in the drive voltage optimization process is to quantify the overlap of the optical mode profile with the electro optic active material. Thicker quantum wells and thinner barriers and a larger number of quantum wells are desirable. The width of the quantum wells should be chosen according to the figure of merits derived in Section 3.3.1. Furthermore, the barrier widths should not be too small such that the coupling between adjacent wells occurs (cf. Section 2.6.1). A varying number of quantum wells strongly effects the optical waveguide core which changes the shape of the optical mode. The quantity that describes the power overlap of the optical mode profile with a certain area of the
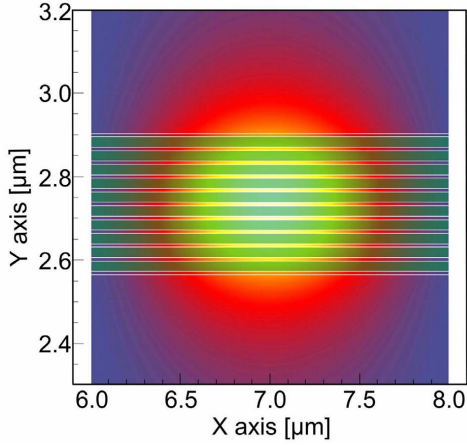
Fig. 3.38: Optical mode intensity profile in a MQW deep etch waveguide. The green shaded areas indicate 10 quantum wells where the optical confinement factor is calculated using Equation (3.7).
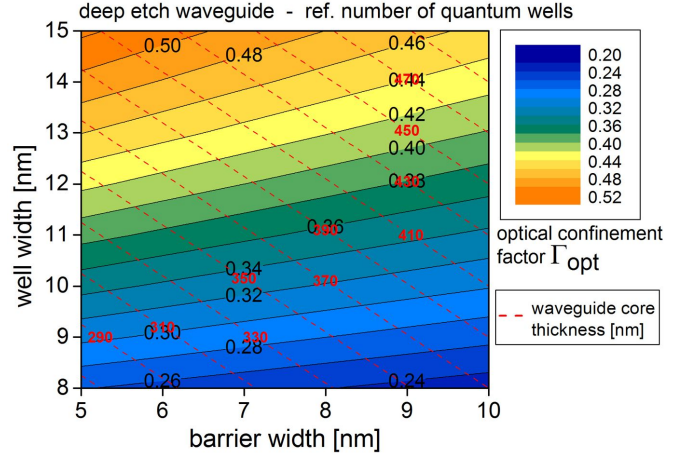
Fig. 3.39: Optical confinement factors for QW widths from 8 nm to 15 nm and barrier widths from 5 nm to 10 nm using the standard number of wells. The dashed red lines show the respective waveguide core thickness.

waveguide material is the optical confinement factor which is calculated by [19]

$$\Gamma_{opt} = \frac{\iint_{layer} |E_{opt}(x,y)|^2 \, dx \, dy}{\iint_{-\infty}^{+\infty} |E_{opt}(x,y)|^2 \, dx \, dy}. \tag{3.7}$$

Figure 3.38 exemplary shows the optical mode profile of a waveguide with ten QWs (green stripes). The optical confinement factor is calculated only for the area of the wells which contribute to the electro-refraction in the optical waveguide of the MZ modulator. A larger number of QWs increases the confinement factor of all quantum wells which is beneficial for a low drive voltage. On the other hand increasing the number of QWs increases the thickness of the intrinsic region which lowers the applied electric field per voltage if the thickness of the undoped spacer layers is kept constant. A general constraint limiting the possible number of quantum wells is ability of the epitaxial growth to deliver high quality multi quantum wells. An increasing number of quantum wells leads to an aggregation of defects in the crystal structure due to strain effects at the hetero structure interfaces. The MOCVD growth of a layer stack comprising the standard number of unstrained quantum wells is feasible with an acceptable number of defects but growing quantum wells in the order of 25 or more QWs becomes challenging depending on the material of wells and barriers. Figure 3.39 presents optical confinement factors for the standard number of QWs for varying well and barrier width calculated using Equation (3.7). Obviously, wider QWs have a larger Γ_{opt}. This is of special importance because the positive

effect of wider wells on the drive voltage has to be included in the evaluation of the modulation efficiency of the QWs presented in Section 3.3.1. All these aspects are included in the trade-off calculations that will be presented in Section 3.5.1.

3.4 Design optimization for optimum electro-optic bandwidth

The electro-optic modulation bandwidth of the Mach-Zehnder modulator (MZM) is the most critical among all other characteristic device parameters. A fundamental lower bandwidth limit to achieve a certain channel data capacity is given by the Shannon theorem [75] which is well-known from information theory. In optical fiber communication the modulation bandwidth requirement depends on the applied modulation format and can be derived from its spectral efficiency given in units of bit/s/Hz. Technical measures to increase the electro-optic bandwidth of the modulator to obtain error-free operation at a specific data rate are much more complicate compared to overcome a high optical insertion loss or a high drive voltage of the MZM. Optical filtering [76] and electronic signal processing on the transmitter and receiver side [77] which could be introduced to compensate for a too low modulation bandwidth are expensive options likely to be avoided by telecommunication companies.

The fundamental design requirements for the capacitively loaded traveling-wave electrode (TWE) of the Mach-Zehnder modulator has been derived in Section 2.3. A 50-Ω impedance is required from the electronics side to match commercial test and measurement equipment while a distinct microwave index equal to the optical group index is essential to achieve velocity-matching. In this section, geometrical design rules for the traveling-wave electrode will be derived that can be used in conjunction with design aspects developed in the previous sections to find the optimum Mach-Zehnder modulator.

3.4.1 Traveling-wave electrode design

The essence of accurately predicting the electro-optic 3-dB bandwidth of the Mach-Zehnder modulator is to have a simulation tool flexible enough to model geometrical device changes as well as a wide variety of material parameters. For the following simulations, *HFSS* from Ansoft LLC Corporation [78] (3D full-wave electromagnetic field simulation) is used to model electrical S-parameters of a modulator structure. To speed up the simulations, it is a common approach [79] to only simulate a single period of the modulator and then to concatenate the resulting S-parameter files in an electrical circuit simulation tool like *NEXXIM* from Ansoft LLC Corporation [78]. The advantage of using a circuit simulation program is that it allows

to include mathematical formulas to calculate the velocity mismatch effect after each period in the modulator structure. The modulation response of the MZ modulator depends on the voltage that is applied to each single electrode during operation. The circuit simulator allows to calculate the voltage response over frequency for a sinusoidal excitation at each desired point within the circuit design. Figure 3.40 shows the circuit design of a modulator having eight sections. The probes in the circuit are used to monitor the voltage response after each section. The 3D drawings in Figure 3.40 represent the HFSS models for the bended input section, the center section and the bended output section which are used to calculate the S-parameters. The schematic on the top right side shows important structural notations for TWE width W_{TWE}, gap width G_{TWE}, period length L_{period} and active length L_{active}. To calculate the electro-optic modulation response M(f) by using the voltage data obtained from the circuit simulator, a modified version of the formula given by Li et al. [8] is used

$$M(f) = 20 \cdot log\left[\frac{1}{N \cdot 1V} \sum_{i=1}^{N} V_i(f) \cdot cos\left(\frac{2\pi f(i-1)L_{period} \cdot (n_\mu - n_{opt})}{c}\right)\right] \qquad (3.8)$$

with c being the speed of light and n_μ and n_{opt} are the microwave and optical index of refraction, respectively. L_{period} denotes the length of a single period and N is the number of periods used for the complete traveling-wave electrode. The basic idea behind the formula is to sum up the frequency dependent voltages of each single modulator section. The cosine term represent the velocity mismatch effect introduced by different group velocities of the electrical and the optical wave. The term (i-1) accounts for the fact, that there is no velocity mismatch in the first modulator period. Figure 3.41a shows calculated electro-optic response curves of three different modulator structures with 40 Ω, 50 Ω and 60 Ω impedance at 1 GHz modulation frequency. The device structure features 16 periodic sections with 250 μm length, an intrinsic thickness of 800 nm, and the optical waveguide is designed in the 'deep etch' (DE) version. The p-contact sheet resistance (PSR), which is of special importance for high frequency operation, was set to $1 \cdot 10^{-5}\Omega/cm^2$ and the filling factor (FF=L_{active}/L_{period}) is 0.6. A variation of the TWE impedance is achieved by varying W_{TWE} and G_{TWE} such that the microwave index n_μ is kept constant at a frequency of 30 GHz. It can be seen that a TWE impedance different from the ideal 50 Ω causes a strange behavior of the electro-optic modulation response in the low frequency region by introducing ripples. This effect can be explained by standing waves which are caused by reflections at the input and the output of the modulator's TWE. When the transmission line of the modulator is impednace mismatched a fraction of the available power from the electrical driver is reflected back. In this case not all drive voltage is available for modulation. An introduction to the properties of terminated transmission lines can be found in
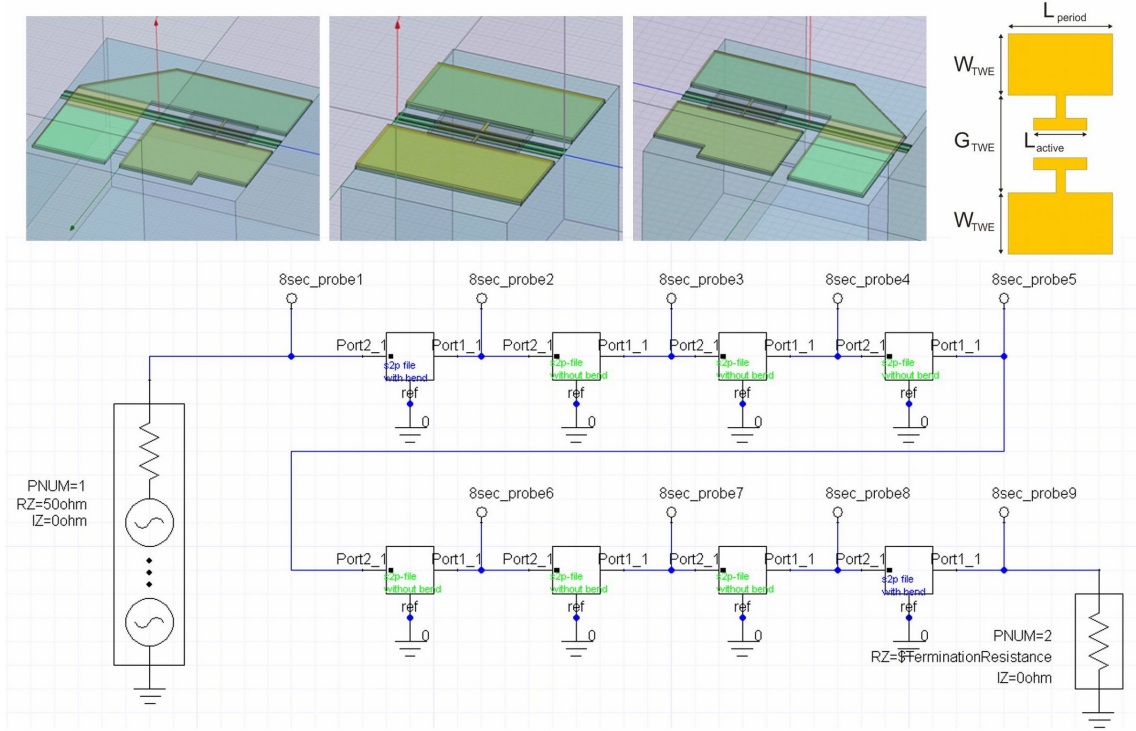
Fig. 3.40: Circuit simulator model for an eight section modulator. Each cell in the circuit design holds S-parameter data simulated with *HFSS*. Probes after each section allow voltage data extraction to calculate the electro-optic response using Equation (3.8). The 3D drawings show - from left to right - the input bend section, one center section and the output bend section. The schematic on the top right shows structure notations for TWE width W_{TWE}, gap width G_{TWE}, period length L_{period} and active length L_{active}.

Chapter 2.4 in the book of Pozar [9].

The electrical S11 parameter is the reflection coefficient that describes the amplitude and phase which is reflected back from the device. Figure 3.41b depicts the S11 parameter for the three modulator structures with 40 Ω, 50 Ω and 60 Ω impedance. For an ideal modulator having 50 Ω impedance, S11 is below -25 dB up to a frequency of 60 GHz. The oscillatory behavior of the S11 is related to the period length L_{period} of the capacitive loads of the TWE. Modulators with an impedance 10 Ω above or below the ideal 50 Ω have an S11 value above -15 dB at a frequency of 5 GHz. Customer specifications for 40-Gbit/s MZ modulators require a reflection coefficient S11 below -15 dB for frequencies up to 40 GHz. The maximum electrical S11 in the frequency range from 0.1 GHz to 40 GHz as a function of the TWE impedance is presented in Figure 3.41c. The -15 dB limit is indicated by the orange line. This limits the allowed impedance mismatch for the modulator chip to ±6 Ω which includes a margin of 3 dB for module packaging. Figure 3.41d presents the effect of velocity mismatch between the electrical and the optical wave. The electro-optic 3-dB bandwidths values are given as a
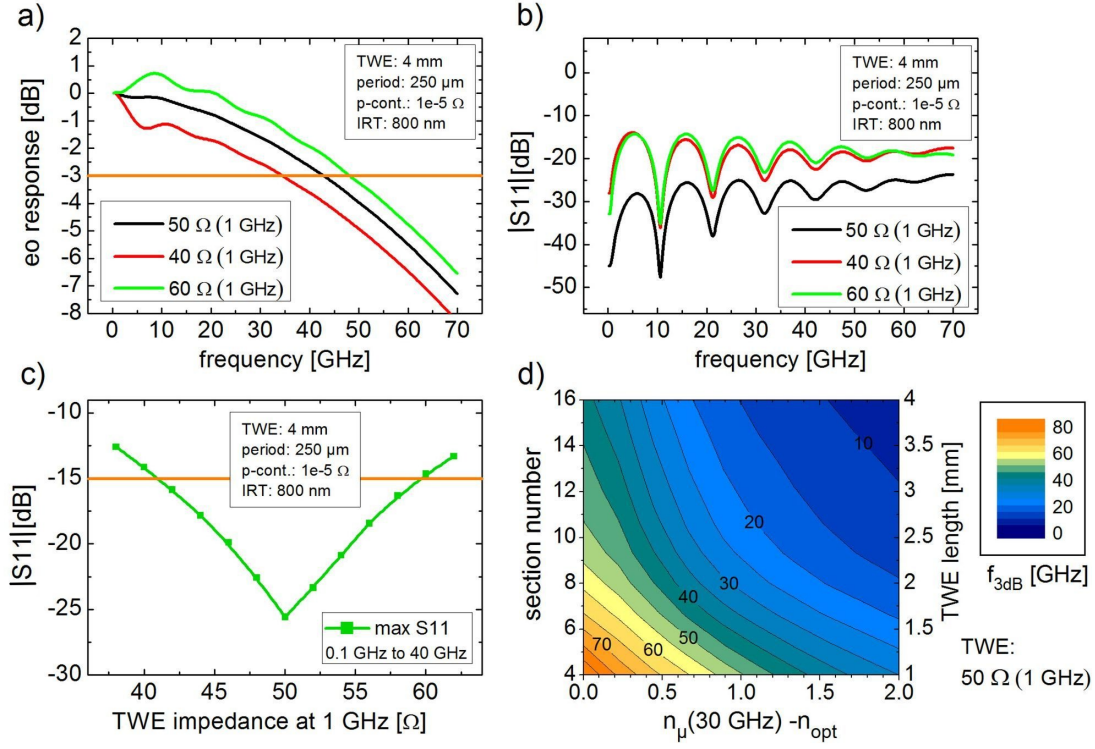
Fig. 3.41: Effect of impedance and velocity mismatch on the modulator's electrical and electro-optical parameters (16 sections, L_{period}=250 μm, IRT=800 nm, FF=0.6 and 40 Ω, 50 Ω and 60 Ω impedance). a) Electro-optic response calculated with Equation (3.8). b) Electrical S11 parameter as a function of frequency. c) Maximum S11 (0.1 GHz to 40 GHz) as a function of TWE impedance. d) 3-dB frequency as a function of refractive index difference vs. number of sections for a fixed impedance of 50 Ω (at 1 GHz).

function of the number of sections in the TWE and the refractive index difference between the optical and electrical wave (n_μ-$n_{optical}$). The scale on the right denotes the total TWE length. The impedance is matched to 50 Ω at 1 GHz. The degradation of the 3-dB bandwidth for an increasing section number in the case of perfect velocity match (Δn=0) originates from ohmic microwave losses which are higher for longer TWEs. While a 3-dB bandwidth of 30 GHz can still be realized for a 1 mm long TWE with Δn=2.0 the velocity mismatch influence is stronger for longer TWEs. A modulator with a 4 mm long traveling-wave electrode and Δn=2.0 has a bandwidth below 10 GHz.

A general design rule for the TWE is that the impedance should be matched to 50 Ω at a low frequency (e.g. 1 GHz) to avoid ripple in the electro-optic response function and electrical reflections resulting in high electrical S11 values. Contrary to the impedance, the microwave index should be matched to the optical group index at a high frequency (30 GHz) because the velocity mismatch is worse for higher frequencies due to the shorter wavelength of the electrical drive signal.

The design requirements for simultaneous impedance and velocity matching have been introduced in Section 2.3. From Equations (2.5) and (2.6)

$$Z_\mu = \frac{n_\mu}{c\left(C_\mu + C_L\right)} \tag{3.9}$$

is obtained. It is obvious that only one specific capacitive load can guarantee impedance and velocity matching at the same time.

As shown before in Sections 3.2.2 and 3.3.2, the intrinsic region thickness (IRT) is a significant parameter for the switching voltage V_π and the optical losses in the waveguide. A change of IRT has a strong impact on the high frequency behavior of the modulator as well because it changes the load capacitance of the TWE. In general, the capacitance of a parallel plate capacitor can be changed by either varying the area of or the distance between the plates if the dielectric medium is not changed. The following considerations assume a constant waveguide width of 2 μm (DE type) which leaves the fill factor (FF) as the only variable that can change the load capacitance of the TWE. The IRT of the modulator waveguide is the second design parameter for the sheet capacitance of the traveling-wave electrode as it defines the distance between the plates. As C_L needs to remain constant, the ratio of FF and IRT needs to be constant:

$$C_L = const. \cdot \frac{FF}{IRT}. \tag{3.10}$$

Figure 3.42 shows the impedance and the microwave index as a function of IRT and FF calculated by using Equations (3.9) and (3.10). The required load capacitance C_L is obtained from an optimized design which is verified for IRT=800 nm and FF=0.5 (indicated by the blues spots), a period length of 250 μm and a p-contact sheet resistance of $1 \cdot 10^{-5} \Omega/cm^2$ using the *HFSS* software package. Figure 3.42a depicts the TWE impedance for a fixed microwave index of n_μ=3.6. The green area indicates the ideal design space for a target impedance between 47 Ω and 53 Ω required to avoid ripple in the electro-optic response function and a large value of S11. The microwave index variation when the TWE impedance in Equation (3.9) is fixed at 50 Ω is shown in Figure 3.42b. The green shaded area indicates the design space for a microwave index of $n_\mu = 3.6\pm0.1$ which is crucial to obtain a 3-dB bandwidth > 40 GHz for a 4 mm long TWE (cf. Figure 3.41d). It is noteworthy, that each pair of IRT and FF in the green areas of Figures 3.42a and 3.42b require a redesign of the TWE width (W_{TWE}) and the gap between them (G_{TWE}). In order to obtain a low drive voltage modulator, it is evident to use a large fill factor which guarantees a long interaction length. Therefore, only IRT-FF pairs with the highest FF inside the green areas should be considered for the TWE design. Because the calculated IRT-FF design space (green area) of the microwave index is much narrower than that for the
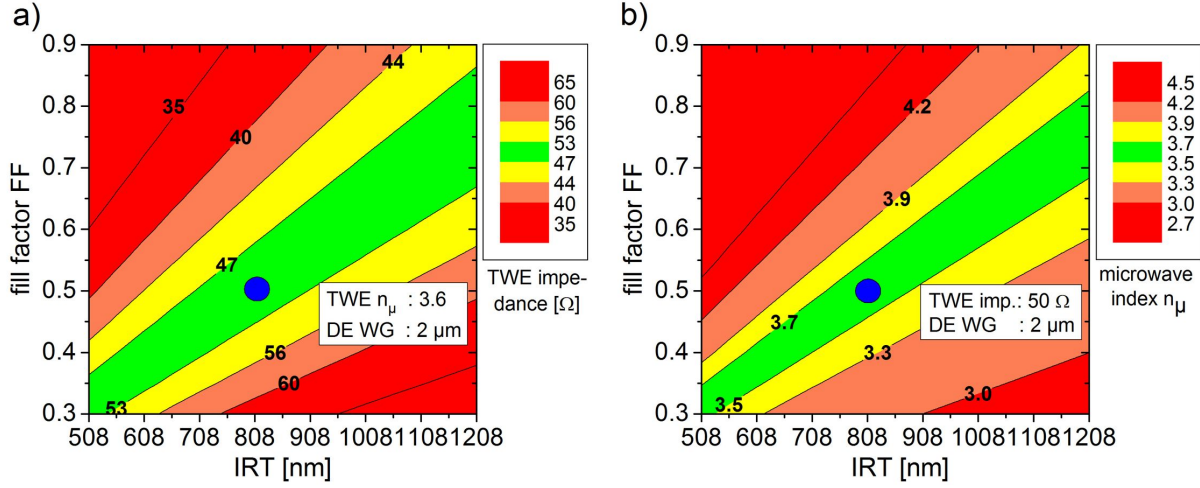
Fig. 3.42: Traveling-wave electrode (TWE) impedance and microwave index for various intrinsic region thicknesses (IRT) and fill factors (FF) after Equations (3.9) and (3.10). The TWE design is verified for IRT=800 nm and FF=0.5 (blue spots) with a period length of 250 µm using *HFSS*.

a) TWE impedance as a function of IRT and FF for a constant microwave index of n_μ=3.6. b) Microwave index as a function of IRT and FF for a constant impedance of 50 Ω. Green area indicates the design space for n_μ = 3.6±0.1 to obtain $f_{3dB} > 40$ GHz for 4 mm TWE length (cf. Fig. 3.41d).

impedance with a p-contact sheet resistance (PSR) of $1 \cdot 10^{-5} \Omega/cm^2$, a microwave index of n_μ = n_{optical} + 0.1 = 3.7 is the target for the design of the TWE. This rule can of course change, if the allowed Δn becomes larger due to relaxed velocity matching constraints. This happens, if the TWE length is designed shorter because the drive voltage specifications of the modulator allow larger values.

The initial impedance and velocity matched electro-optic bandwidth of the designed modulator is much larger than 40 GHz due to a very good p-contact sheet resistance. In this case, where the design space of the microwave index (Δn=n_μ-$n_{optical}$) is larger than that of the impedance. The lower boundary impedance of 47 Ω is the limitation for the electrode design which is given by the fact that it delivers the required capacitive load with the lowest drive voltage at the same time. This value is a hard limit to the traveling-wave electrode design because the impedance needs to remain close to 50 Ω for the reasons mentioned above (ripple, high S11).

As discussed before, changing the IRT and the FF in order to remain inside the allowed design window requires to change the dimensions of the TWE. Figure 3.43 shows the traveling-wave electrode impedance Z_μ and the microwave index n_μ for a 250 µm long modulator period with IRT=800 nm and a p-contact of $1 \cdot 10^{-5} \Omega/cm^2$ calculated using *HFSS*. The variation of Z_μ and n_μ for TWE width from 90 µm to 150 µm and TWE gap widths from 40 µm to 70 µm keeping a constant fill factor FF=0.5 is presented in Figure 3.43a. It can be seen that the microwave index
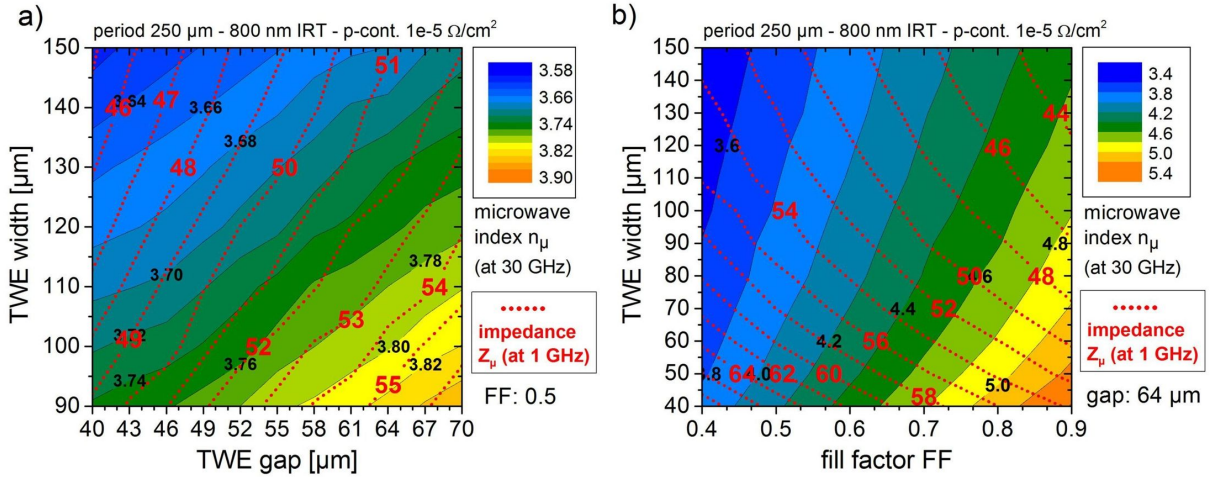
Fig. 3.43: Traveling-wave electrode impedance and microwave index for a single modulator period with 250 μm length, 800 nm IRT and p-contact $1 \cdot 10^{-5} \Omega/cm^2$. a) shows Z_μ and n_μ as a function of the TWE width and the TWE gap using a constant fill factor FF=0.5. b) shows Z_μ and n_μ as a function of TWE width vs. FF using a TWE gap width of 64 μm.

can only be varied from 3.62 to 3.85 throughout the entire parameter space which means that the velocity of the electrical wave can moderately be influenced by changing just the width and the gap size of the traveling-wave electrode. The electrode impedance can fairly be set in the range from 45 Ω to 56 Ω in the range of the evaluated TWE widths and gaps. One interesting finding is that the contours of the impedance and the microwave index run under a very small angle to each other, which means that both parameters cannot be changed independently from each other.

A much larger variation of Z_μ and n_μ is observed, when the capacitive load of the electrode is changed. Figure 3.43b reveals the TWE's impedance and microwave index for a variation of the TWE width versus fill factors from 0.4 to 0.9 for a constant gap width of 64 μm. Changing the capacitive load by varying the fill factor has a much larger impact on Z_μ and n_μ than just changing the geometrical dimensions of the TWE. For a thin electrode (40 μm width) the impedance can be varied from 54 Ω to 69 Ω if the fill factor is reduced from 0.9 to 0.4. For wider TWEs, this effect is less pronounced but still high with over 10 Ω variation for a TWE width of 150 μm. The influence of the fill factor on the microwave index is tremendous. For a 40 μm wide TWE n_μ changes from 3.9 to 5.3 for an increasing fill factor (0.4 to 0.9) At 150 μm width the variation of n_μ from 3.5 to 4.6 is still large. Interestingly, the contours of Z_μ and n_μ run almost perpendicular (cf. Figure 3.43b) allowing to set the impedance and the microwave index independent from each other. IRT and period length are variables which are defined by the designer during the design process while the p-contact sheet resistance is a fabrication process related parame-
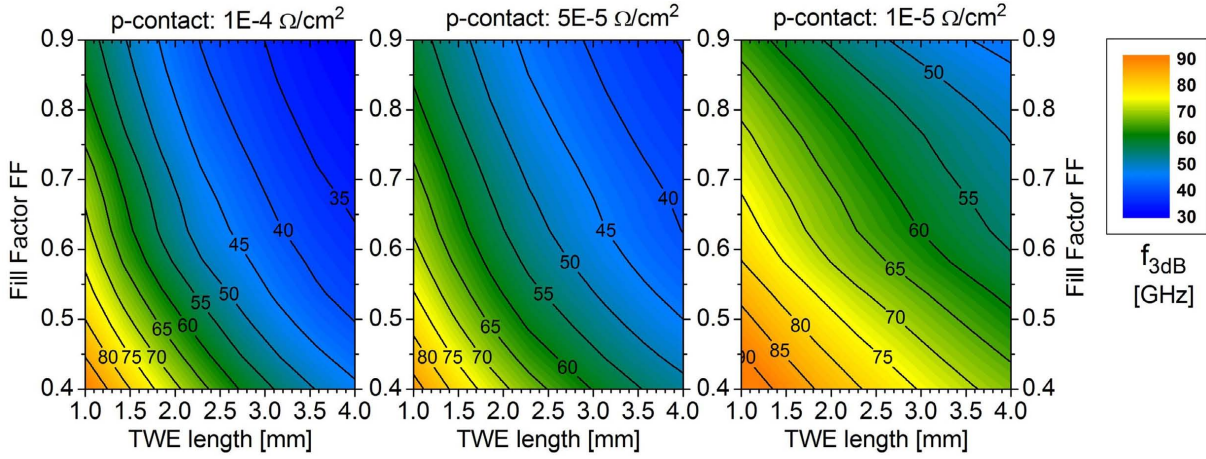
Fig. 3.44: Electro-optic 3-dB bandwidth as function of TWE length and fill factor for p-contact sheet resistances of $1 \cdot 10^{-4}\Omega/cm^2$, $5 \cdot 10^{-5}\Omega/cm^2$ and $1 \cdot 10^{-5}\Omega/cm^2$ (DE waveguide, IRT=1150 nm). Perfect velocity and impedance matching is assumed.

ter (e.g. $< 1 \cdot 10^{-5}\Omega/cm^2$). The impact of the p-contact resistance on the electro-optic 3-dB bandwidth is depicted in Figure 3.44 for a 250 μm period modulator with an intrinsic region thickness (IRT) of 1150 nm. The three plots show the 3-dB bandwidth dependence as a function of fill factor and TWE length for PSRs of $1 \cdot 10^{-4}\Omega/cm^2$, $5 \cdot 10^{-5}\Omega/cm^2$ and $1 \cdot 10^{-4}\Omega/cm^2$. Perfect velocity and impedance matching is assumed for every point. For a real modulator this would require a modification of the TWE geometry. In case of the bad PSR ($1 \cdot 10^{-4}\Omega/cm^2$) the fill factor must be lower than 0.5 for a 4 mm long TWE in order to obtain 40 GHz bandwidth. The maximum allowed FF increases by over 20% for $5 \cdot 10^{-5}\Omega/cm^2$ and can be freely chosen for $1 \cdot 10^{-5}\Omega/cm^2$ because the bandwidth is always larger than 40 GHz in the latter case. The decrease in bandwidth for an increasing TWE length is related to ohmic losses of the electrical wave which travels along the transmission line. The decrease in bandwidth with a growing fill factor has two root causes. The first obvious reason is the increasing capacitance that needs to be charged which is equivalent to the decreasing cut-off frequency of an RC circuit. The second cause for a smaller bandwidth with growing FF is the Bragg frequency of the periodic electrode structure which scales with the inverse square root of the capacitive load (cf. Equation (2.8)).

An interesting aspect of the electro-optic response of the Mach-Zehnder modulator is the interplay between the bandwidth limitations due to the RC circuit and the velocity mismatch effect. The RC circuit is limited by the p-contact sheet resistance (PSR) and the sheet capacitance of the reverse biased p-i-n diodes. The latter is controlled by the intrinsic region thickness and the fill factor (FF). Figures 3.45a and 3.45b show calculated 3-dB frequencies for fill factors of 0.6 and 0.9 as a function of the PSR and the velocity mismatch (expressed as difference
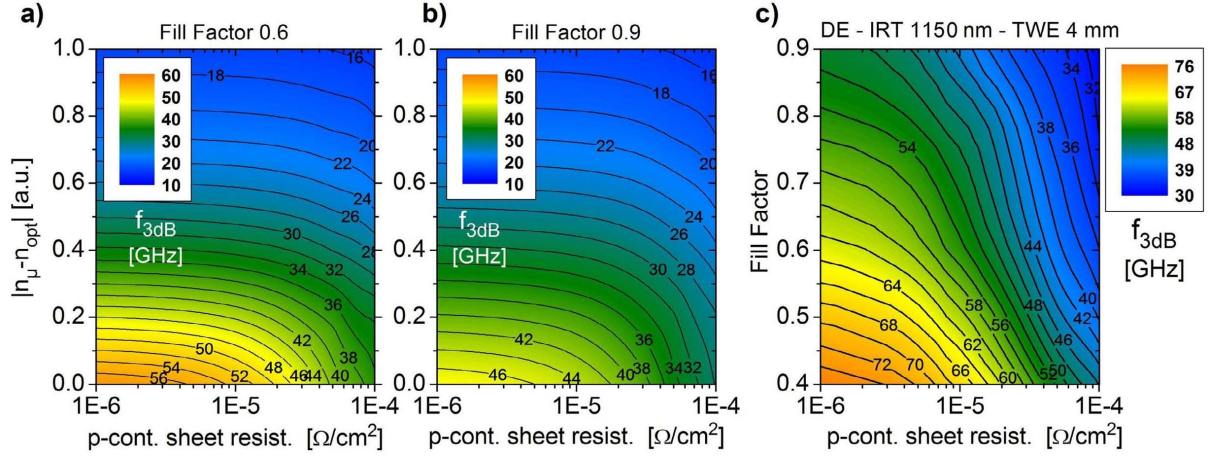
Fig. 3.45: Electro-optic 3-dB bandwidth as function of p-contact sheet resistance and velocity mismatch (TWE length:4 mm, IRT=1150 nm).

a) FF=0.6. b) FF=0.9. c) MZM 3-dB bandwidth as function of p-contact sheet resistance and fill factor for perfect velocity matching.

between the optical and microwave group index, TWE length=4 mm, IRT=1150 nm). A remarkable observation is the fact that with increasing velocity mismatch the resistance of the p-contact becomes less important to the bandwidth. While f_{3dB} is still increasing for $\Delta n=0$ when the p-contact is improved from $1 \cdot 10^{-5}\Omega/cm^2$ to $1 \cdot 10^{-6}\Omega/cm^2$ this is no longer the case for n_μ-n_{opt}> 0.3. The gain in bandwidth for this condition is negligible. Furthermore, at $\Delta n \geq 0.5$, the bandwidth becomes independent of FF and is completely dominated by the mismatch of the optical and electrical wave velocities. This behavior is identical for all IRTs from 1150 nm to 600 nm. An identical observation is made, when the intrinsic thickness is reduced from the standard 1150 nm down to 600 nm (not shown in the graph). The desired MZ modulator 3-dB bandwidth of 40 GHz for 50 Gbit/s operation is achieved by fixing a velocity mismatch margin $\Delta n=0.15$ for FF=0.9 or $\Delta n=0.3$ for FF=0.6.

Figure 3.45c depicts the 3-dB bandwidth for a variation of FF versus PSR for a 4 mm long TWE (IRT=1150 nm). A perfect velocity and impedance matching is assumed and thus the plot represents the pure cut-off frequencies of the RC circuit. While the resistance is the dominant contributor to f_{3dB} for a bad p-contact (PSR=$1 \cdot 10^{-4}\Omega/cm^2$), this behavior inverts with improving p-contact. For a good PSR of $1 \cdot 10^{-6}\Omega/cm^2$ the MZM bandwidth is primarily dependent on the capacitance. As the fill factor is desired to be as large as possible to reduce the switching voltage V_π, the PSR must be kept as small as possible during wafer processing so that only the capacitance of the RC circuit, controlled by the fill factor, limits the bandwidth.

For a 4 mm long TWE with IRT=1150 nm, the maximum allowed PSR to achieve 40-GHz
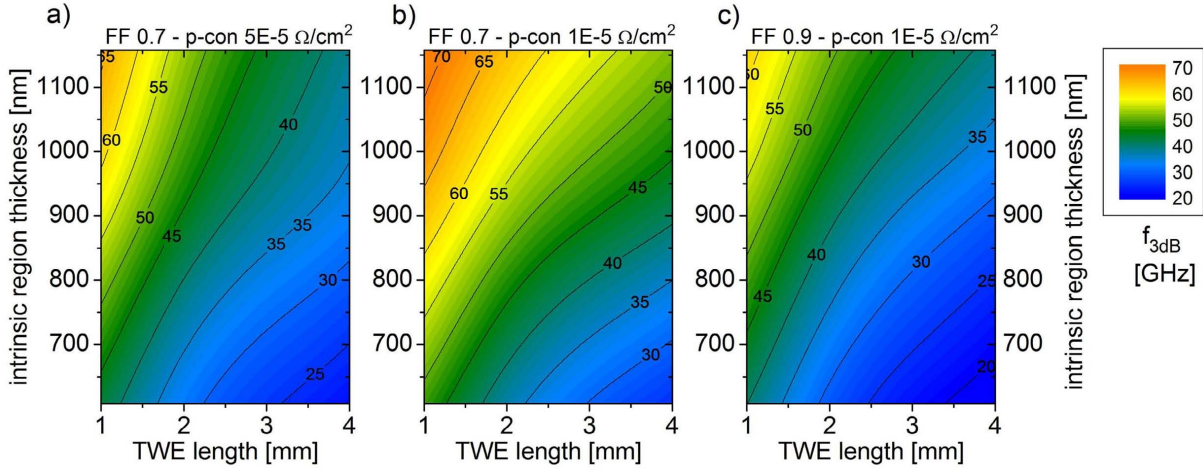
Fig. 3.46: Electro-optic 3-dB bandwidth as function of intrinsic region thickness and traveling-wave electrode length. a) FF=0.7 and p-contact $5 \cdot 10^{-5} \Omega/cm^2$. b) FF=0.7 and p-contact $1 \cdot 10^{-5} \Omega/cm^2$. c) FF=0.9 and p-contact $1 \cdot 10^{-5} \Omega/cm^2$. Impedance matching is assumed. Velocity mismatch is calculated for an optical group index of 3.7.

MZM bandwidth with an refractive index margin of Δn=0.15 is $1 \cdot 10^{-5} \Omega/cm^2$. If IRT is reduced, not only the capacitance but also the resistance of the RC circuit is increased due to thicker p- and n-doped material. Therefore, the maximum 3-dB bandwidth of the MZ modulator is reduced, when the thickness of the nominally undoped semiconductor layers is decreased.

The impact of varying IRT and the TWE length is depicted in Figure 3.46. Impedance mismatch has been neglected because the impedance of the traveling-wave electrode can be matched by changing the electrode and gap width according to Figure 3.43a. The effect of velocity mismatch on the other hand is included in the calculations for an optical group index of 3.7. Increasing the load capacitance by choosing a smaller IRT or a larger FF leads to an increase of the microwave index which reduces the electro-optic bandwidth of the modulator. The calculation results shown in Figure 3.46a are obtained for FF=0.7 and PSR=$5 \cdot 10^{-5} \Omega/cm^2$. The bandwidth reduction due to a thinner intrinsic region is severe. To obtain 40 GHz modulator bandwidth the maximum TWE length is 3.7 mm for IRT=1150 nm, 2 mm for IRT=800 nm and only 1.25 mm for IRT=600 nm. Figure 3.46b shows similar calculation results for a good p-contact (PSR=$1 \cdot 10^{-5} \Omega/cm^2$). All IRTs down to 880 nm allow 40 GHz operation for a 4 mm long TWE. The maximum TWE length for IRT=600 nm is 1.75 mm. As seen before, an increasing fill factor reduces the electro-optic bandwidth. Figure 3.46c present calculation results similar to those in Figure 3.46b but with FF=0.9. Operation at 40 GHz is achieved for TWE lengths ≤3.7 mm at IRT=1150 nm. For 800 nm IRT the maximum electrode length is 1.7 mm and for 600 nm IRT it is only 1 mm.
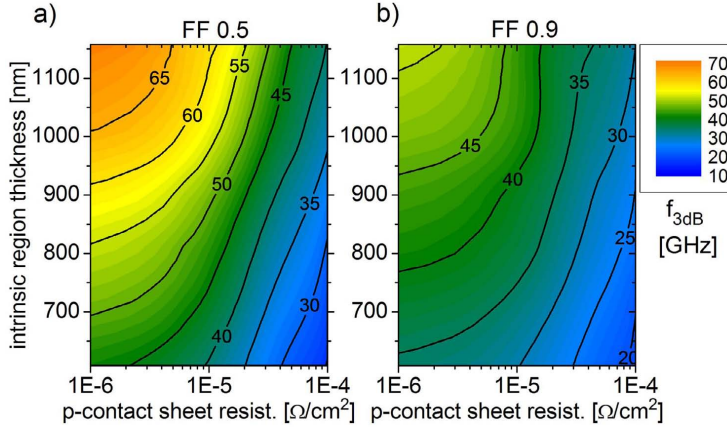
Fig. 3.47: Electro-optic 3-dB bandwidth as function of p-contact sheet resistance and intrinsic thickness for 4 mm TWE length. a) FF=0.5. b) FF=0.9. Perfect velocity and impedance matching is assumed.
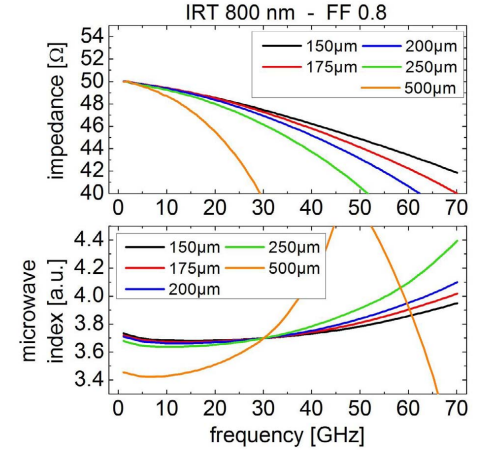
Fig. 3.48: Dispersion of impedance and microwave index over frequency for different period lengths using IRT=800 nm.

The variation of the electro-optic 3-dB bandwidth due to a change of IRT (1150 nm to 600 nm) and PSR ($1 \cdot 10^{-4} \Omega/cm^2$ to $1 \cdot 10^{-6} \Omega/cm^2$) is presented in Figures 3.47a and 3.47b for fill factors of 0.5 and 0.9, respectively. Perfect impedance and velocity matching is assumed. For FF=0.5, a 40 GHz modulation bandwidth is achieved for all evaluated IRTs down to 600 nm, if the PSR is better than $1 \cdot 10^{-5} \Omega/cm^2$. For FF=0.9 and PSR=$1 \cdot 10^{-5} \Omega/cm^2$ the minimum intrinsic thickness is 950 nm. Similarly to Figure 3.45c a bad p-contact is the main contribution to the bandwidth variation while for a good p-contact ($1 \cdot 10^{-6} \Omega/cm^2$) the major contribution to the f_{3dB} variability comes from the changing sheet capacitance of the TWE.

As mentioned before the period length of the traveling-wave electrode L_{period} (cf. Figure 3.40) has been fixed at 250 μm for all calculations. As introduced in Section 2.3 the bandwidth of the transmission line is limited by the periodicity of the capacitive loads which is expressed by the Bragg frequency (cf. Equation (2.8)). As the characteristic impedance Z_0 of the transmission line is zero at the Bragg frequency and 50 Ω at 1 GHz by design there has to be a dispersion of Z_0 with frequency. The same idea applies to the microwave index of the electrical wave which should be designed to match the optical group index at the desired frequency. At the Bragg frequency, no power is transmitted over the TWE which, in other words, mean that the microwave index n_μ becomes infinite. The dispersion over frequency of Z_0 and n_μ for IRT=800 nm and a FF=0.8 are plotted in Figure 3.48 for period lengths L_{period} from 150 μm to 500 μm. The impedance is matched to 50 Ω at 1 GHz and the microwave index is matched to the optical group index 3.7 at 30 GHz. The impact of the different period lengths on the dispersion is clearly visible. The high capacitive load (IRT=800 nm, FF=0.8) reduces the Bragg

frequency to about 50 GHz for L_{period}=500 µm. The impedance falls through the ± 5 Ω limit (cf. Figure 3.41c) slightly above 20 GHz and the microwave index n_μ varies between 3.42 and 4.1 in the range from 1 GHz to 40 GHz inhibiting a desired modulation bandwidth of 40 GHz. The microwave index n_μ does not reach infinity (lower graph of Figure 3.48 for L_{period}=500 µm) because only four concatenated periods have been simulated. In case of a real modulator with more than four periods, the dispersion of the microwave index is even bigger than in the shown case because more periods shift the value of n_μ towards infinity. In case of a lower capacitive load - meaning a smaller FF or a larger IRT - the dispersion of Z_0 and n_μ is less pronounced. In order to avoid a bandwidth reduction due to the Bragg frequency, the period length for the 40-GHz MZ modulator should be 200 µm or less.

The presented results of the high frequency simulations were calculated by using the 'standard doping' profile (cf. Section 3.2.2). The 'light doping' profile was introduced to reduce absorption losses in the optical waveguide. To evaluate the impact of the 'light doping' profile on the 3-dB bandwidth of the MZ modulator electrical simulations similar to those shown in Figure 3.45b has been conducted (IRT=800 nm and IRT=600 nm) to evaluate the impact of the reduced doping concentration on f_{3dB}. The largest bandwidth reduction observed was 1.5 GHz for high a fill factor (FF=0.9) and high p-contact resistance (PSR=$1 \cdot 10^{-4} \Omega/cm^2$). Smaller FF and a lower PSR lead to less bandwidth reduction. Therefore, all RF simulation results obtained for the 'standard doping' profile are regarded as identical for the case of using the 'light doping' profile.

3.5 Trade-offs for optimum device performance

The performance of an InP-based Mach-Zehnder modulator has been optimized by considering the crucial parameters optical insertion loss (IL), modulation voltage (V_π) and electro-optical bandwidth (f_{3dB}) independent from each other. This section aims on finding design trade-offs to optimize at least two or even all three parameters simultaneously. It will be shown that no ideal modulator design exists that gives best performance for all three parameters at the same time. However, reasonable trade-offs will be presented that allow the fabrication of high performance Mach-Zehnder modulators for commercial applications.

Due to restrictions from a non disclosure agreement (NDA) some design variables in this section are not given with specific numbers. Instead, relative values are given in the text and the plots.

3.5.1 Modulation efficiency versus optical insertion loss

The first optimization is performed by looking at the optical absorption losses and modulation efficiencies for various background doping concentrations (BDC) as a function of the vertical MQW core position in the intrinsic region. To quantify the ratio of modulator absorption losses and the modulation efficiency a new figure of merit (FOM) is introduced:

$$\Lambda_1 = \frac{\Gamma_{EO}}{\Phi_{MZM}} \tag{3.11}$$

with Γ_{EO} being the modulation efficiency given by Equation (3.6) and Φ_{MZM} being the device absorption loss shown exemplary in Figure 3.21. As introduced in Section 3.2.2 the optical modulator loss originates from a combination of passive and active waveguide absorption. A MZ modulator usually has active waveguide sections between 2.5 mm and 3.5 mm length in each interferometer arm where 0.5 mm are used for the phase electrodes. The passive waveguide length depends on the waveguide geometry. The 'deep etch' (DE) geometry for example enables the shortest device length because the required S-bends and MMI couplers (cf. Figure 2.2) can be fabricated very short due to the strong light confinement. The required length for S-bends and MMIs increases for 'median etch' (ME) and 'shallow etch' (SE) waveguides by approximately 0.5 mm and 1 mm, respectively. Figure 3.49 shows the figure of merit Λ_1 as a function of the waveguide core position offset at 4 Volts applied bias for four background doping concentrations (BDC) ($1 \cdot 10^{15} cm^{-3}$, $3 \cdot 10^{15} cm^{-3}$, $7 \cdot 10^{15} cm^{-3}$ and $1 \cdot 10^{16} cm^{-3}$). The intrinsic region thickness (IRT) is 1150 nm and the 'standard doping' profile (cf. Section 3.2.2) has been used. The upper plots a), b) and c) in Figure 3.49 presents Λ_1 for an active waveguide length of 2.5 mm while the lower plots d), e) and f) are for 3.5 mm long active waveguides. Obviously, the highest Λ_1 correspond to the lowest BDC ($1 \cdot 10^{15} cm^{-3}$). Higher BDCs lead to a decrease of Λ_1 which is mainly caused by a reduction of the modulation efficiency. Another result is that the maximum achievable Λ_1 depends on the BDC. The optimum MQW position within the intrinsic region shifts from positive to negative offsets with increasing background doping.

For example, the maximum moves from +100 nm for $1 \cdot 10^{15} cm^{-3}$ BDC to -150 nm for $1 \cdot 10^{16} cm^{-3}$ BDC in the DE waveguide structure (cf. Figures 3.49a and 3.49d). The maximum FOM is obtained in the ME waveguide geometry although the MZM length is assumed to be 0.5 mm longer compared to the DE geometry. The SE type waveguide has the lowest values of Λ_1 due to a low modulation efficiency.

Calculation results are not shown for the 'light doping' profile because the characteristics of the Λ_1 curves are identical to those calculated for the 'standard doping' profile (cf. Figure 3.49).
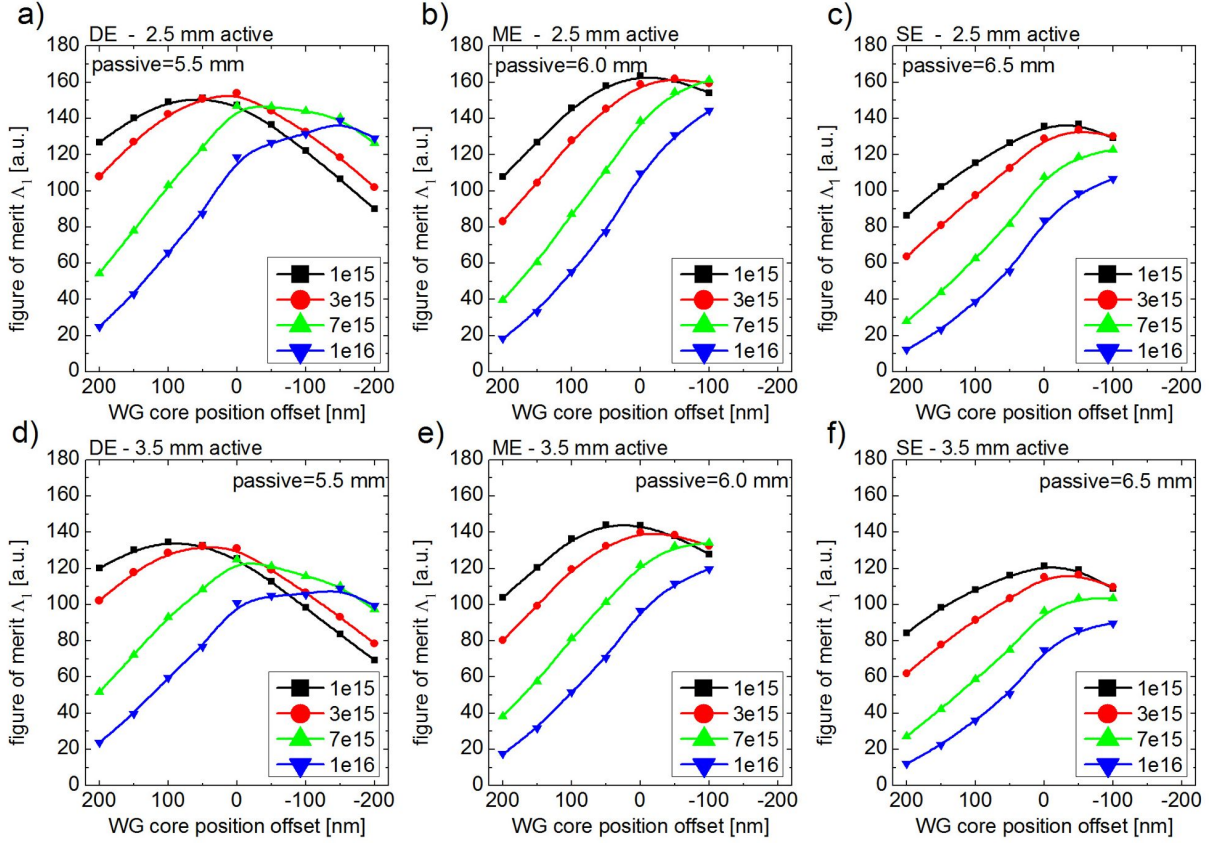
Fig. 3.49: Figure of merit Λ_1: modulation efficiency to device loss trade-off different BDCs as a function of WG core position offset (4 Volts bias, IRT=1150 nm). a) DE waveguide with 2.5 mm active length. b) ME waveguide with 2.5 mm active length. c) SE waveguide with 2.5 mm active length. d) DE waveguide with 3.5 mm active length. e) ME waveguide with 3.5 mm active length. f) SE waveguide with 3.5 mm active length. Positive offset values denote a shift closer to the n-contact.

The only difference is that due to the lower absorption losses in the 'light doping' waveguide a $\sim 23\%$ larger Λ_1 is found.

A point to keep in mind is that these observations do not include additive device insertion losses caused by light scattering at rough waveguide sidewalls. In the DE waveguide, scattering losses are typically much higher than absorption losses (cf. Figure 3.22). Insertion loss measurements performed on passive SE reference waveguides (2 µm width) have shown an average loss of 2.3 dB/cm, i.e. there is an almost equal contribution of absorption and scattering losses taking the calculated modal absorption loss of 1.2 dB/cm (cf. Figure 3.18c). The trade-offs presented in Figure 3.49 were calculated for the reference IRT of 1150 nm and the standard number of quantum wells.

In the next evaluation step optical losses and the modulation efficiencies for a variation of the intrinsic region thickness and varying quantum well numbers (standard QW number ±5) are
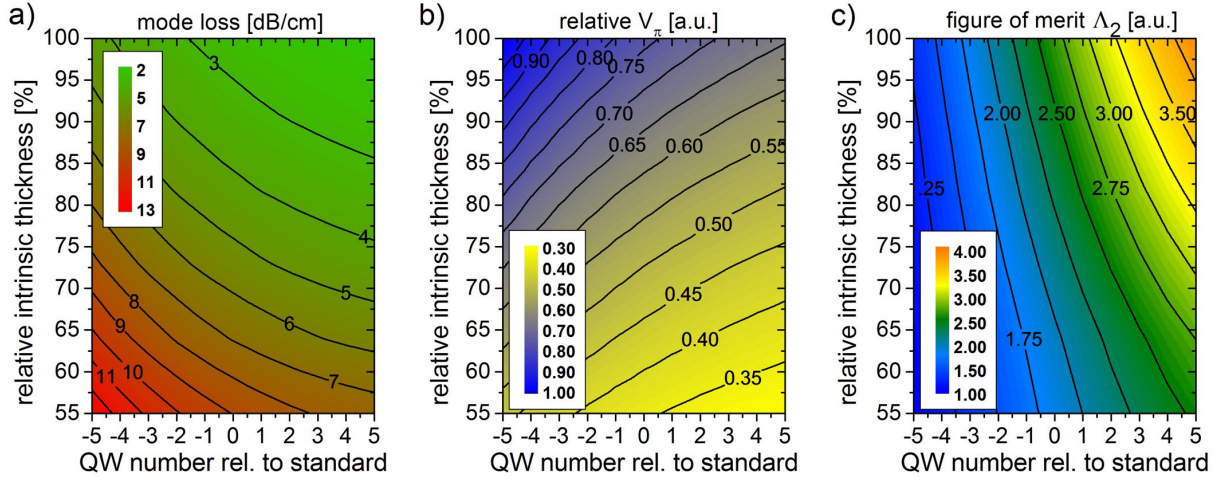
Fig. 3.50: Mode loss a), relative V_π b) and figure of merit Λ_2 c) as function of the relative intrinsic region thickness (IRT) and the relative quantum well number (EOE=1.3, 4V bias, BDC=$1 \cdot 10^{15} cm^{-3}$).

taken into account. In order to include the influence of a varying quantum well number a new figure of merit Λ_2 has been defined that includes the optical confinement factor (cf. Section 3.3.3). This figure of merit is given by

$$\Lambda_2 = \frac{\Gamma_{EO} \cdot \Gamma_{opt}}{\Phi_{MZM}} \tag{3.12}$$

where Γ_{EO} is the modulation efficiency, Γ_{opt} is the optical confinement factor (cf. Equation (3.7)) in the quantum wells and Φ_{MZM} is the mode loss of the respective waveguide. The modal absorption losses due to a change of IRT and the quantum well number are shown in Figure 3.50a. The 'standard doping' profile and the reference thicknesses of quantum wells and barriers have been used. As expected, the mode loss increases with smaller IRT due to larger modal overlap with doped material. The interesting point is that the mode loss decreases with increasing quantum well number. The reason for this is that the waveguide core thickness becomes larger but the mode diameter and hence the overlap with the doped material becomes smaller. For example, the mode loss for a waveguide with the reference intrinsic thickness (rel. IRT=100%) is reduced from 3 dB/cm to 2.4 dB/cm if the standard number of QWs is increased by 5 QWs. The absolute absorption reduction due to a larger number of QWs is even higher when IRT is reduced. For example, the shrinkage of IRT to 70% of the reference thickness (no given due to NDA restrictions) reduces the modal loss from 6 dB/cm for the standard number of QWs to less than 5 dB/cm with 5 QWs more in the WG core.

In parallel with increasing QW number the optical confinement in the QWs increases which leads to a lower drive voltage V_π. Figure 3.50b shows the relative drive voltage as a function of relative IRT and relative QW number. The modulation efficiency Γ_{EO} was calculated by using

an electro-optic-efficiency factor (EOE) of 1.3 at 4 V bias voltage and a BDC=$1 \cdot 10^{15} cm^{-3}$. Next, Γ_{EO} was multiplied with the optical confinement factor Γ_{opt} that primarily varies with the QW number. The marginal variance of Γ_{opt} with IRT results from a variation of the waveguide refractive index profile due to doping. As expected, the highest drive voltage is given for the reference intrinsic region thickness (rel. IRT=100%) and the lowest number of QWs. For this case the drive voltage is normalized to one (cf. Figure 3.50b). The drive voltage is reduced by 34% (0.76 to 0.50 rel. V_π) when IRT is reduced by 30% (assuming the standard number of QWs). When the well number is increased by adding 5 QWs to the standard value (at rel. IRT=70%), the drive voltage is reduced by another 14% from 0.50 to 0.43 rel. V_π. Mode losses are reduced with a larger number of quantum wells and at the same time the drive voltage is reduced. This is presented in Figure 3.50c where the figure of merit Λ_2 is plotted for the same simulation conditions used in Figures 3.50a and 3.50b. The lowest Λ_2 is normalized to one. If the QW number is kept constant and IRT is reduced, then Λ_2 is reduced too. The best option to significantly increase Λ_2 is to use a larger number of QWs in the core of the waveguide. The isolines in Figure 3.50c represent identical conditions for device loss and switching voltage. For example, using the standard IRT with the standard number of QWs gives the same Λ_2 as for a relative IRT of 60% with 4 QWs added. For the latter condition, the loss is increased by 60% while the relative V_π is reduced by 60%. Hence, a Mach-Zehnder modulator with a relative IRT of 60% of the standard value and additional 5 QWs can have a 60% shorter traveling-wave electrode (TWE) in order to have identical absorption loss and V_π. The shorter TWE is also beneficial for the electro-optic bandwidth and the total modulator length.

The shapes of the contours shown in Figure 3.50c are similar when calculated for the 'median etch' (ME) or 'shallow etch' (SE) waveguide types. If only the relative drive voltage or the modal absorption losses are considered, a difference between all three waveguide geometries exists, as has been shown in Figure 3.35 and Figure 3.18 for the modulation efficiencies Γ_{EO} and for the mode loss, respectively. But the relative differences of both parameters for the three geometries are identical. Their figure of merits Λ_2 are identical within 5%. The difference between the three waveguide types is the active material or active waveguide length which has not been included in the trade-off evaluation so far. The DE waveguide allows a 5% shorter electrode length compared to the ME type and a 19% shorter electrode than the SE type to get identical drive voltage and absorption loss.

3.5.2 Drive voltage and device loss vs. electro-optic bandwidth

In order to include the electro-optical response in the trade-off calculations the TWE length, the active waveguide length excluding the phase electrodes and the fill factor (FF) are evaluated. The specified electro-optic 3-dB bandwidth of the investigated Mach-Zehnder modulator is 40 GHz, i.e. the first goal is to find all possible combinations of TWE-length, fill factor and intrinsic region thickness that meet this bandwidth requirement. The following evaluation is performed for a 2 μm wide DE waveguide using absorption and drive voltage data calculated for the standard number of QWs, BDC=$1 \cdot 10^{15} cm^{-3}$, PSR=$1 \cdot 10^{-5} \Omega/cm^2$ and EOE=1.3. The velocity mismatch effect, if applied, was included in the 3-dB bandwidth calculations assuming an optical group index of 3.7 and the impedance of the transmission line was matched to 50 Ω at 1 GHz. Figure 3.51a shows the 40 GHz-contours for different relative IRTs (standard IRT=100%) as a function of FF and TWE length. The arrows indicate towards higher frequencies. As the modulator is intended to have the lowest possible drive voltage at 40 GHz the only relevant traces in Figure 3.51a are those crossing the top border at FF=0.9. The bandwidth limitation for these points originate from the RC time constant and the velocity mismatch effect. The additional pink, bright blue and dark blue contours in the bottom right corner of Figure 3.51a result from velocity mismatch due to a microwave index well below 3.7.

The next step is to extract the maximum allowed TWE length for 40 GHz operation for each allowed combination of FF and IRT from Figure 3.51a. The resulting contours are shown in Figure 3.51b where TWE-lengths values of 4.5 mm are extrapolated from Figure 3.51a. Larger TWE lengths are not examined (grey shaded area). After knowing the maximum allowed electrode length and the corresponding FF, the length of the electro-optic active waveguide can be calculated for each value of IRT (cf. Figure 3.51c). The maximum allowed fill factor is plotted as function of the active length versus the relative intrinsic thickness, where the active length is the product of TWE length and FF. It should be clear that every data point in Figure 3.51c represents an electro-optic bandwidth of 40 GHz. All possible combinations of TWE lengths (1 mm and 4.5 mm) and fill factors (0.4 and 0.9) are included.

Knowing all possible TWE designs that allow to obtain 40 GHz bandwidth, the relative drive voltage and absorption loss for each data point can be calculated. The relative drive voltage is given by the modulation efficiency of each IRT multiplied with the active material length. The calculation results are shown in Figure 3.52a (the largest value is normalized to one). The lowest drive voltages are achieved for large active waveguide lengths with no favorable intrinsic thickness in the region between 55% and 80% of the standard IRT. The optical loss is evaluated for
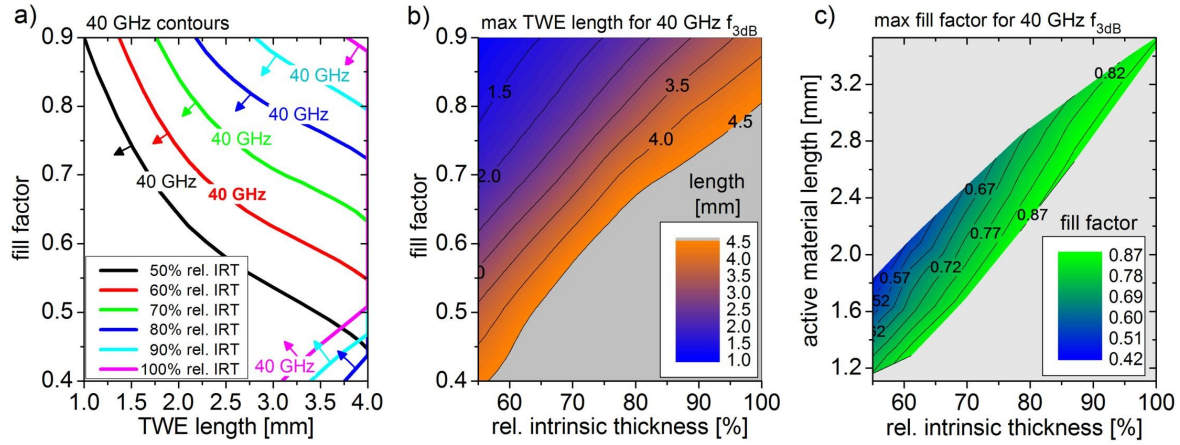
Fig. 3.51: a) 40 GHz contours of FF vs. TWE length for different relative IRTs. b) max. TWE length for 40 GHz MZM bandwidth as a function of FF and relative IRT. c) FF as a function of active length vs. relative IRT for 40 GHz MZM bandwidth.

the TWE as a combination of active and passive material losses according to Figure 3.18. The calculations have been done for the 'standard doping' and the 'light doping' profile. The active material length is multiplied with the intrinsic modal loss for the active waveguide and added to the loss of the passive waveguide section given by its length multiplied with the respective loss value. The numerical results are presented in Figure 3.52b for the 'standard doping' profile and in Figure 3.52c for the 'light doping' profile. The highest loss is seen for long active waveguides with thin IRTs. The loss contours of the 'standard doping' profile slightly favor low intrinsic region thicknesses. The lowest waveguide loss for varies only from 0.9 dB (rel. IRT=60%) to 1.1 dB (rel. IRT=100%). A larger difference is observed for the 'light doping' profile shown in Figure 3.52c where the lowest loss of 0.65 dB is given for 55% to 65% relative IRT. For thicker intrinsic regions, the loss increases up to 1.1 dB for the standard intrinsic region thickness. In the case of 'light doping' thin intrinsic regions are clearly favored.

As a low drive voltage design generally involve high absorption losses the best 40-GHz-bandwidth design emerges from an evaluation of a slightly modified figure of merit Λ_1 given by Equation (3.11). Instead of the pure modulation efficiency, the relative drive voltage including the active material length (cf. Figure 3.52a) is used to calculate Λ_1. Figure 3.53a shows the results for the 'standard doping' profile (the lowest Λ_1 is normalized to one). Obviously, a 35% larger figure of merit for is observed for the standard IRT compared to the case with 55% relative IRT. A completely different result is obtained for the 'light doping' profile (cf. Figure 3.53b). The largest Λ_1 are found for small intrinsic thicknesses (55% to 60% of the standard IRT). In this case, the lower absorption losses due to the reduced doping levels favor the use of
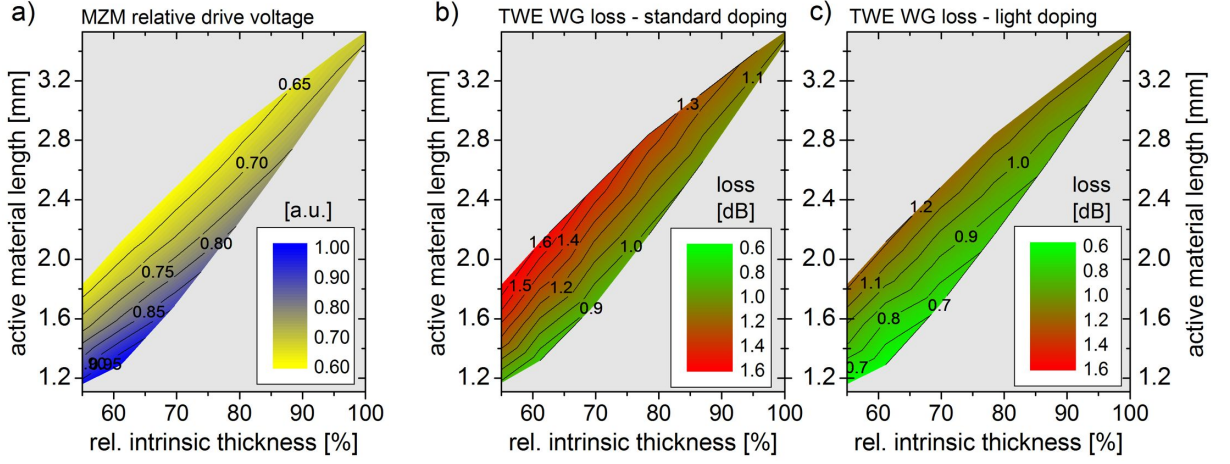
Fig. 3.52: a) relative drive voltage for all 40 GHz designs from Figure 3.51c. b) Traveling-wave electrode section waveguide absorption losses for all 40 GHz designs from Figure 3.51c using the 'standard doping' profile. c) Same data as b) but using the 'light doping' profile.

a thin intrinsic region with a short TWE and a high FF.

In general, the presented FOM modeling results for the 'standard doping' and 'light doping' profiles show an advantage of using a shorter active waveguide length in a 40-GHz MZ modulator. This implies the use of a shorter TWE length with a higher FF. But it should be clear that the considered FOM only gives the best trade-off between drive voltage and optical insertion loss. As mentioned, there is no optimum device configuration which optimizes these two relevant device parameters at the same time. The scope of the intended modulator design must be clear. A 40-GHz MZ modulator can either have a low drive voltage or is intended for low insertion loss. In the first case the design has to be chosen from Figure 3.52a. In the latter case the electrode configuration has to be designed based on Figure 3.52c.
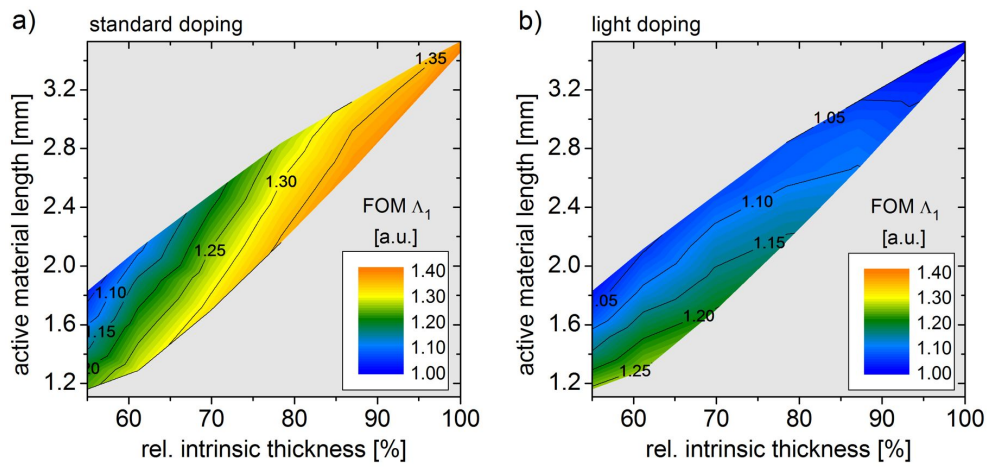
Fig. 3.53: a) figure of merit Λ_1 for 40 GHz designs from Figure 3.51c with 'standard doping' profile. b) Same data as a) but using 'light doping' profile.

Chapter 4

The dual-parallel IQ modulator

4.1 Introduction

The development of the next generation 100-Gbit/s Ethernet standard for long-haul transmission links is driven by the demand for cost effective upgrades of currently deployed WDM networks. This growing demand for high data rates in optical transport networks has led to the investigation of advanced modulation formats [1]. Phase shift keying (PSK), which is well known from digital radio communication, attracted a growing interest for optical fiber communication since 2000 [80]. In 2002, Griffin et al. [81] suggested the utilization of quadrature phase shift keying (QPSK) for optical fiber networks. QPSK is a phase modulation format where each symbol is coded with one out of four possible phase states [82, 83]. Two bits are transmitted for each symbol, and the symbol rate is therefore half the bit rate. QPSK is the only advanced modulation format that received noticeable attention as a possible candidate for the 100-Gbit/s Ethernet standard in the past few years. Instead of detecting the absolute phase as with phase shift keying (PSK), the phase change between two consecutive bits can also be detected. Modulation formats relying on this phase change coding are referred to as 'differential' modulation formats (e.g. DPSK and DQPSK). QPSK offers a higher spectral efficiency compared to standard on-off keying (OOK) or binary-phase-shift-keyed (BPSK) formats by transmitting two bits per symbol. This is a tremendous advantage from the driver electronics point of view, as the system components need to deliver a 50 Gbaud/s symbol rate only to achieve 100 Gbit/s data transmission. In contrast to 100 Gbaud/s symbol rate, broadband amplifiers, bit pattern generators and related test equipment is commercially available for 50 Gbaud/s already today. To generate optical QPSK signals a so called IQ modulator (IQM) is required that allows to address each of the four constellation points of the complex IQ-plane (cf. Figure 4.1a), where I and Q stand for 'in-phase' and 'quadrature', respectively. Depending on the desired modulation format,
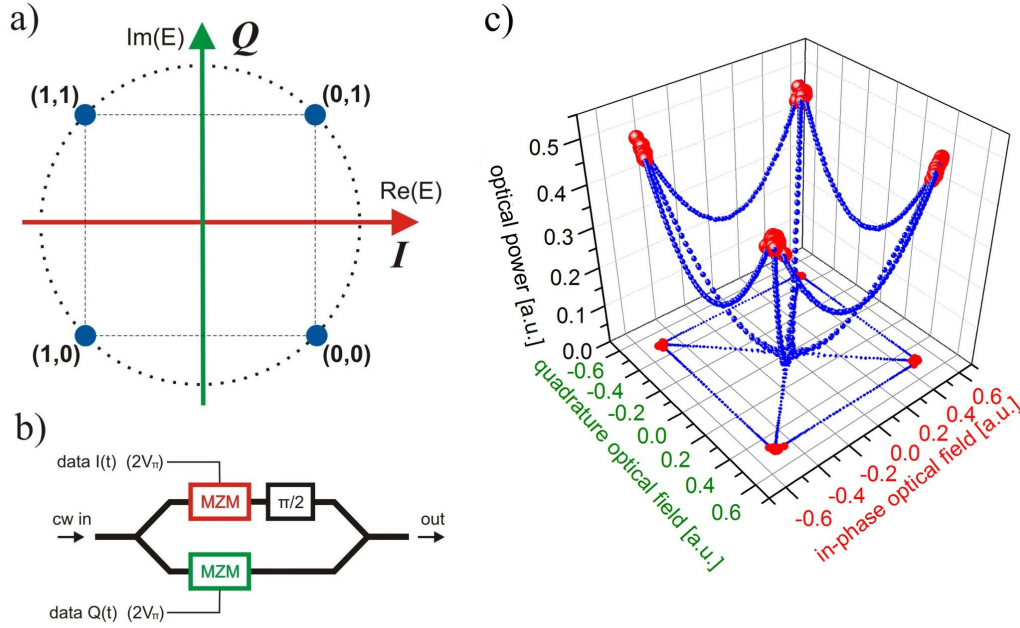
Fig. 4.1: QPSK modulation principle. a) Complex plane constellation diagram of the four level QPSK modulation scheme. Transmitted bit pairs are noted for each phase state. The angle denotes the phase and the distance from the origin denotes the amplitude of the optical signal. b) IQ modulator schematic with two parallel Mach-Zehnder modulators. The colors indicate the respective modulation axis in a). c) QPSK constellation diagram with optical power as third dimension to facilitate the comprehension of plot a).

several possibilities exist to realize an IQ modulator (IQM). All phase-shift-keyed transmission formats can be generated by a simple phase modulator, while quadrature-amplitude-modulated (QAM) signals require at least one amplitude modulator. Gnauck and Winzer [84] compared the transmitter performance of simple in-line phase modulators and Mach-Zehnder modulators (MZM) for DPSK modulation and found that the Mach-Zehnder modulator is advantageous. The inherent zero-chirp modulation resulting from push-pull operation and the amelioration of drive waveform imperfections due to the cosine transfer function (cf. Figure 2.3) are the two strongest arguments in favor of a Mach-Zehnder type modulator.

In principle, a single MZ modulator (dual-drive) is capable of addressing the full complex plane which is necessary to generate QPSK signals. But this requires a drive voltage swing of $2\,V_\pi$ for each MZ interferometer arm [85], and the drive signal generation of the two quadrature tributaries (I-data and Q-data) can not be accomplished independently of each other. A possibility to overcome these limitations is to provide a true quadrature modulator, that consists of two parallel Mach-Zehnder modulators. This configuration is shown schematically in Figure 4.1b where the upper MZM modulates the I-data on the real axis in Figure 4.1a and the lower MZM modulates the Q-data on the imaginary axis. The $\pi/2$ phase difference between the I-

an Q-data signals assures the orthogonal modulation of the I and Q tributaries. Griffin et al. presented successful operation of such a dual-parallel IQ modulator (IQM) at 2×5 Gbit/s in 2003 [86] and at 2×10 Gbit/s in 2005 [87] using GaAs-based modulators.

The IQ modulator developed in this thesis takes advantage of the potential of the InP material system for high bandwidth and low drive voltage that has been demonstrated several times in the past for single MZ modulators [2, 3, 79, 88]. Non-return-to-zero (NRZ) on-off-keyed operation at 80 Gbit/s of a single MZ modulator will be demonstrated in Section 5.4.1 which is sufficient for 2×53.5 Gbit/s = 107 Gbit/s DQPSK data transmission. This data rate is commonly used in transmission experiments for the 100-Gbit/s Ethernet standard and includes 7% overhead for forward error correction (FEC) coding.

This chapter will first give an introduction to the basic layout of the dual-parallel IQ modulator and the required adaptions made to the optical waveguides and the traveling-wave electrode. Afterwards, a mathematical model for the single MZM and the dual-parallel IQM is being developed that allows to predict the large signal modulation performance depending on possible impairments in the IQM. An analysis of the so called error vector magnitude (EVM) will reveal narrow limits for variations of the optical phase and power inside the IQM waveguide structure to obtain error-free QPSK transmission. The last section covers IQM chip packaging and layout requirements for the module.

4.2 IQ modulator layout

A schematic layout of the IQ modulator developed in this thesis is presented in Figure 4.2. The optical input waveguide is split into two waveguides using a Y-branch splitter. S-bends provide a vertical separation of the waveguides to access the upper and the lower single MZM. Alternatively, a 1x2 multi-mode-interference (MMI) coupler can be used instead of the Y-branch splitter. In contrast to the standard MZM design investigated before, the waveguide splitting in the upper and lower MZ modulators is achieved by using 2x2 MMI splitters. This is crucial for an inherent 90° phase difference between the MZI arms which is the required operation state for binary-phase-shift-keyed modulation (normally off-state at zero optical power in Figure 4.1c). The output waveguides of the upper and the lower MZ modulator are recombined using feeding S-bends and a 2x2 output MMI. This 2x2 output MMI has two advantages compared to a simple Y-branch or 1x2 MMI combiner: 1) The required 90° phase difference between the I and Q coded optical signals is inherently achieved without the need of an additional phase shifter. 2) All residual light generated during operation is guided out of the chip via the dump
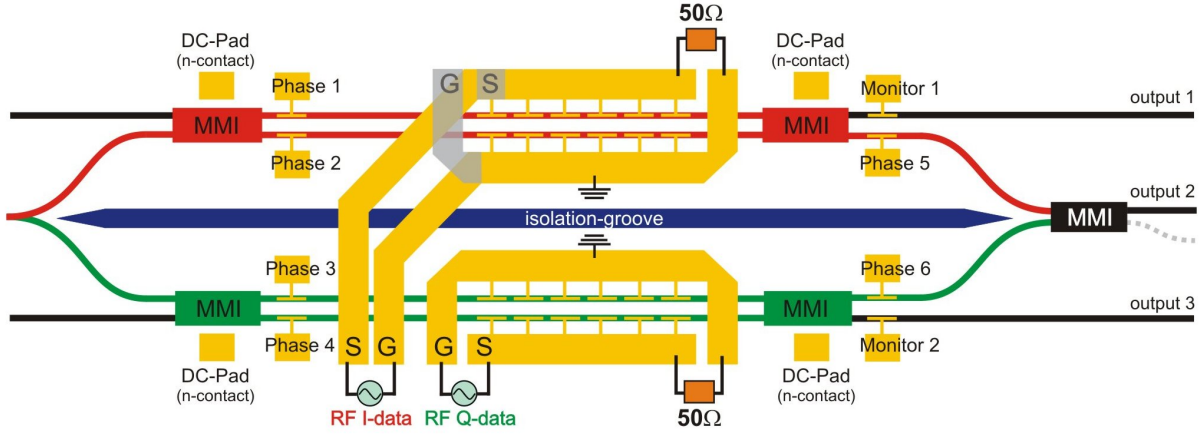
Fig. 4.2: Schematic layout of the IQ modulator consisting of two parallel Mach-Zehnder modulators.

waveguide port. Self heating of the modulator and parasitic back reflections are therefore largely suppressed in this configuration.

Due to waveguide width variations resulting from fabrication related tolerances, a stable phase difference of 90° in each single MZM and between both MZMs cannot be achieved for every device on a fabricated wafer. Therefore, phase electrodes are placed in each interferometer arm (cf. 'Phase 1' to 'Phase 6' in Figure 4.2). These phase electrodes can also be operated as variable optical attenuators (VOA) to give equal optical intensities in each Mach-Zehnder arm, which is necessary for a high extinction ratio (on-off ratio). In this case, the induced phase shift has to be counterbalanced by the phase electrodes in the second interferometer arm. The electrodes denoted 'monitor' in Figure 4.2 on the dump output ports are used to detect photocurrents which are used to set the correct phase states. This procedure will be explained in detail in Section 5.2.1. The layout of the traveling-wave electrodes in Figure 4.2 illustrates an improved version. In the first design revision of the dual-parallel IQM the upper MZM was just a mirrored copy of the lower MZM (grey TWE sections in the upper MZM in Figure 4.2), while the improved design features RF contact pads on just one chip side. This is a design requirement for successful low microwave loss module packaging because the RF bonding wires have to be kept as short as possible, and this is only possible for wire bonding from one chip side. The inner RF electrode of each MZM is the electrical ground (G) electrode while the outer electrode is the signal electrode (S). This design reduces electrical crosstalk, which is a potential source of impairments of the modulated optical signal during large signal operation of the IQ modulator. [89].

4.3 The mathematical Mach-Zehnder interferometer model

The theoretical understanding of the large signal modulation performance of the IQ modulator developed in this work is essential for reducing test time on real devices. Therefore, an accurate model of the electro-optic modulation properties of the IQ modulator is required. The mathematical MZM model presented hereafter is an improved version of that given by Lagali et al. [90]. It is based on the transfer-matrix method and includes a mathematical description of each individual sub-component of the Mach-Zehnder modulator. The improvements added to the model introduced in this work include the introduction of a modulation voltage dependent phase and amplitude of the optical field and a term for an unmodulated fraction of light that interferes with the modulated light. Table 4.1 lists all individual components and their mathematical expression. The Y-branch splitter is characterized by the field split ratio s, that accounts for unequal light intensities in the upper and lower MZI-arms. The 2x2 MMI expression includes a phase offset δ. The upper and lower MZI arm expression contain the voltage dependent absorption $\Delta\kappa(V)$ and refractive index change $\Delta n(V)$, the length L of the active waveguide section, the wavelength λ, and a variable phase difference ϕ between both MZ-arms. The term $\Delta\kappa(V)$ for the absorption change originates from the power law fit for the QCSE (cf. Section 3.3.1). $\Delta n(V)$ has a linear coefficient representing the linear fractions of all electro-optic effects. The quadratic coefficient reflects the quadratic fractions of the QCSE and the square-root coefficient accounts for possible carrier effects due to a high background doping in the intrinsic layers. A special case, where a fraction of the modulator's optical input field is not modulated in the interferometer waveguide but is guided in the guiding layers of the optical spot size converter (cf. Figure 3.3b), is accounted for by the expression $u \cdot exp(i\,\theta)$. u denotes the fraction of the optical field amplitude and θ is the respective phase.

The transfer matrix expression of a single Mach-Zehnder modulator with two output ports is given by

$$\begin{pmatrix} out1 \\ out2 \end{pmatrix} = MMI(\delta) \cdot \begin{pmatrix} \text{upMZIarm}((1+\eta) \cdot V_{up}) & 0 \\ 0 & \text{lowMZIarm}((1-\eta) \cdot V_{low}) \end{pmatrix} \cdot Y(s) \quad (4.1)$$

where η characterizes a possible electrode efficiency imbalance between the upper and the lower arm of the MZ interferometer (η: -1 to +1, a positive value denotes a higher efficiency of the upper electrode). The output power and phase of the upper output port are calculated by using

$$MZM_{intensity} = \sqrt{real(out1)^2 + imag(out1)^2} \quad (4.2)$$

component	mathematical description
Y-branch	$Y(s) = \begin{pmatrix} \sqrt{s} \\ \sqrt{1-s} \end{pmatrix}$
2x2 MMI	$MMI(\delta) = \begin{pmatrix} \cos\left[\frac{\pi}{4}+\delta\right] & -i\,\sin\left[\frac{\pi}{4}+\delta\right] \\ -i\,\sin\left[\frac{\pi}{4}+\delta\right] & \cos\left[\frac{\pi}{4}+\delta\right] \end{pmatrix}$
refr. index change	$\Delta n(V) = a \cdot V + b \cdot V^2 + c \cdot \sqrt{V}$
absorption change	$\Delta\kappa(V) = (d \cdot V)^e$
upper MZI arm	$upMZIarm(V_{up}) = (1-u) \cdot exp\left(-\frac{2\pi i}{\lambda}\left[\Delta n(V_{up}) - i\,\Delta\kappa(V_{up})\right]L - i\,\phi\right) + u \cdot exp(i\,\theta)$
lower MZI arm	$lowMZIarm(V_{low}) = (1-u) \cdot exp\left(-\frac{2\pi i}{\lambda}\left[\Delta n(V_{low}) - i\,\Delta\kappa(V_{low})\right]L\right) + u \cdot exp(i\,\theta)$
	s: field split ratio $\qquad\qquad$ δ: MMI phase offset a: linear eo coefficient $\qquad\quad$ b: quadratic eo coefficient c: square root eo coefficient d: absorption multiplier $\qquad\quad$ e: absorption scaling exponent λ: wavelength $\qquad\qquad\qquad$ L: active material length ϕ: MZI arm phase difference u: fraction of unmodulated light $\quad$ θ: unmodulated light phase

Tab. 4.1: Mathematical descriptions of MZM subcomponents for the transfer matrix model.

and

$$MZM_{phase} = arctan\left(\frac{imag(out1)}{real(out1)}\right) \qquad (4.3)$$

where $real(out1)$ and $imag(out1)$ denote the real and imaginary part, respectively. The model has been implemented by using the high-level programming language *MATLAB* from The Math-Works Inc. [91] for fast and easy data visualization. The presence of an unmodulated fraction u of the optical field leads to so called 'bubbles' in the DC intensity matrix which originate from constructive and destructive interference between the modulated and unmodulated optical fields. The origin of the unmodulated optical field is a non-ideal operation of the spot size converter (cf. Section 3.2.1) which does not transfer all light into the MZ waveguide. A corresponding intensity matrix is presented in Figure 4.3a for u=30%. The problem that arises from such a 'bubble' matrix is a degradation of the MZ extinction ratio and an increase in insertion loss for different bias voltages. The Mach-Zehnder transfer functions at 3 V and 5 V bias voltage are shown in Figure 4.3b. For 3 V bias the DC extinction ratio (ER) of the MZM is excellent with 24.5 dB while at 5 V bias the ER is degraded by 10 dB to 14.5 dB and the insertion loss is increased by 2.8 dB. Another issue is a variation of the correct 3-dB working point which has to be compensated by changing the phase electrode settings.
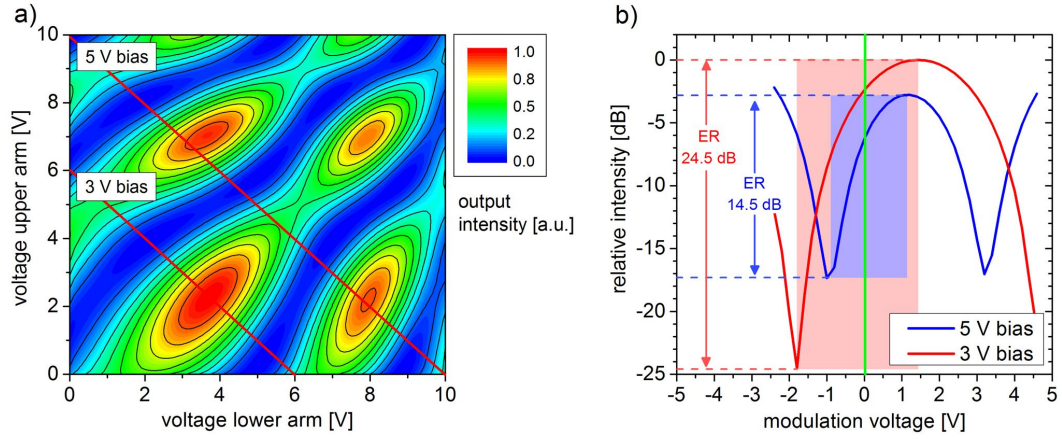
Fig. 4.3: Calculated output intensity matrices. a) 'Bubble' matrix. 30% of the optical field are unmodulated and interfere with the modulated signal. b) MZ transfer functions for 3 V and 5 V bias.
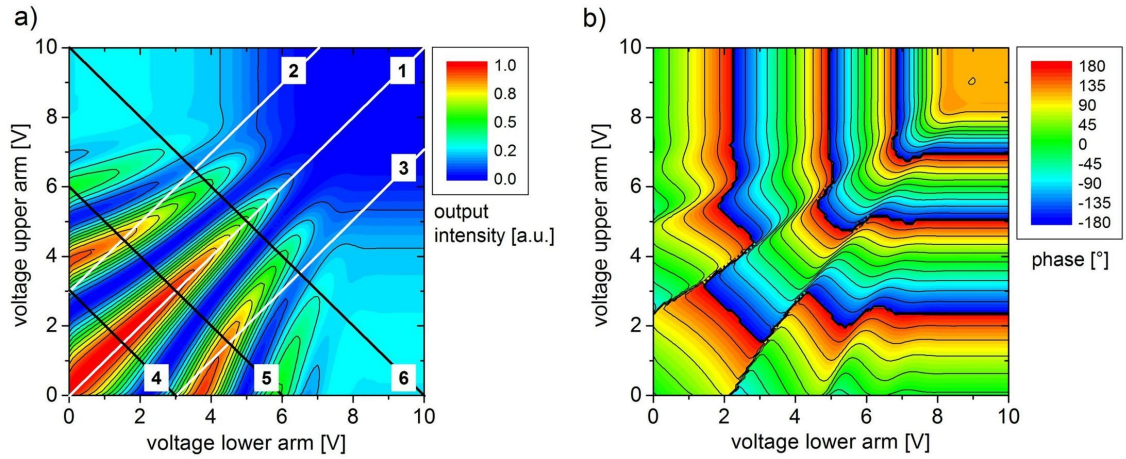
Fig. 4.4: a) Calculated output intensity matrix using Equation (4.2) for applied voltages from 0 V to 10 V on both MZ-arms. The numbered lines indicated cutting lines for data fitting shown in Figure 4.5. b) Calculated output phase matrix using Equation (4.3) and voltages from 0 V to 10 V on the MZ-arms.

Figure 4.4a shows a calculated output intensity matrix at 1550 nm that was fitted to measured data (#7018-F6, 3.2 mm active waveguide length). The voltage dependent absorption $\kappa(V)$ is strong and turns the modulator off at 7 V bias applied to each MZI arm. The numbered white and black lines indicate cuts, along which data is extracted for fitting to experimental data. Figure 4.4b shows the corresponding output phase matrix calculated with Equation (4.3) where the phase is presented in a range from -180° to +180°. The excellent accuracy of this improved mathematical model is highlighted in Figure 4.5. The cuts from the measured intensity matrix were fitted almost perfectly to the matrix cuts from simulation by taking the input data shown on the right hand side of Figure 4.5. The fit error is evaluated by first calculating a 'difference matrix' between the measured and the simulated matrix and then dividing the integrated 'differ-
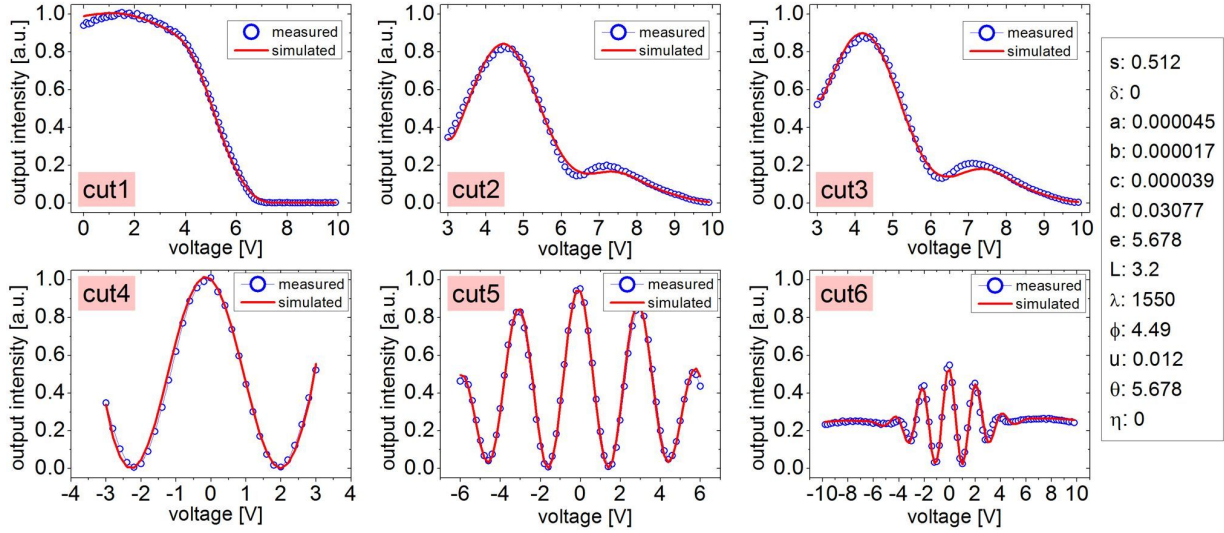
Fig. 4.5: Simulated and measured DC data along six cuts shown in Figure 4.4. The measured device is #7018-F6 (3.2 mm active waveguide length, wavelength=1550 nm). The fit error is less than 5%. Values used for the fit are shown in the table on the right.

ence matrix' by the integrated 'measured matrix'. The fit error for the example in Figure 4.5 is less than 5%.

Extending this model for the IQ modulator is straight forward. The dual-parallel arrangement of Figure 4.2 is a super-Mach-Zehnder interferometer, where the upper and the lower arm consist of one single Mach-Zehnder interferometer. Then, the mathematical expression of the complete IQ modulator is given by

$$
\begin{pmatrix} \text{IQ-out1} \\ \text{IQ-out2} \end{pmatrix} = \text{IQ-MMI}(\delta_{\text{IQ}}) \cdot \begin{pmatrix} out2(V_{I,up}, V_{I,low}) \cdot e^{i\phi} & 0 \\ 0 & out1(V_{Q,up}, V_{Q,low}) \end{pmatrix} \cdot
$$
$$
\text{IQ-Y}(s_{\text{IQ}}). \tag{4.4}
$$

IQ-MMI(δ_{IQ}) is the matrix for the output 2x2 MMI of the IQM and IQ-Y(s_{IQ}) is the input Y-splitter of the IQM. The phase difference ϕ between the upper and the lower MZI is controlled by the expression $e^{i\phi}$. This model allows to accurately model all parameters of the real dual-parallel IQ modulator including voltage dependent absorption and phase changes induced by the electro-optic effects as well as power and phase imbalances between all four MZI arms caused by fabrication related variations. The power and the phase of the modulated optical output signal are calculated by using Equations (4.2) and (4.3), respectively. Furthermore, this mathematical model allows to compute the output characteristics of a dual-parallel IQ modulator fabricated of any material with arbitrary voltage-dependent phase and absorption changes.

4.4 Modeling of large signal IQ modulator performance

A detailed understanding of the impact of fabrication-related variations of the optical waveguide and the traveling-wave electrode on the QPSK performance of the IQ modulator is important. Incorrect phase states and unequal optical intensities in the four Mach-Zehnder interferometer arms have to be corrected in order to obtain an ideal IQ modulator constellation diagram (cf. Figure 4.1a). This is of even higher importance for the QPSK modulation format than in standard NRZ-OOK modulation because multi level modulation formats require a high device complexity on the receiver side. For the detection of phase modulated signals, it is not possible to use standard photodiodes as they only detect the optical power nut not the phase. The phase information can be decoded by interfering the incoming signal with a local oscillator. This detection is known as coherent detection [92]. Phase modulated signals can also be detected by using so-called delay line interferometers, where the incoming signal is split into two branches and the signal in one of the branches is delayed by one symbol period. Thus, phase information of two consecutive symbols is transferred into an optical amplitude modulation and can be detected by using standard photodiodes. This receiver concept is known as direct detection. The utilization of balanced detectors improves the receiver sensitivity by 3 dB [93]. Both detection methods increase the number of required optical components, which adds non-idealities to the complete transmission system.

To evaluate the performance of the dual-parallel IQ modulator a large signal model of the push-pull operation was developed using *MATLAB* and combined with the mathematical IQ-modulator model described in Section 4.3. The model includes a generator for pseudo-random-bit-sequences (PRBS) that delivers bit sequences of 2^n-1 bits length. The model allows to set a user defined modulator bias voltage (V_{bias}) and a peak-to-peak RF drive voltage (V_{pp}), which - both together - give the voltage applied to the upper and lower arms of the two Mach-Zehnder interferometers according to

$$V_{up}(t) = V_{bias} + V_{pp} \cdot (PRBS\_sequence(t) - 0.5) \tag{4.5}$$

$$V_{low}(t) = V_{bias} - V_{pp} \cdot (PRBS\_sequence(t) - 0.5). \tag{4.6}$$

The top graph of Figure 4.6a shows an arbitrarily chosen fraction of a 40-Gbit/s PRBS 2^7-1 bit sequence and the bottom graph the corresponding drive voltage waveforms for V_{bias}=2 V and V_{pp}=1 V. The drive voltages can be calculated with a variable rise and fall time to simulate a limited electrical bandwidth of the driver and the modulator (10 ps and 15 ps in Figure 4.6a). For the voltage sequence calculated with 10 ps rise time a shift of two bits have been introduced
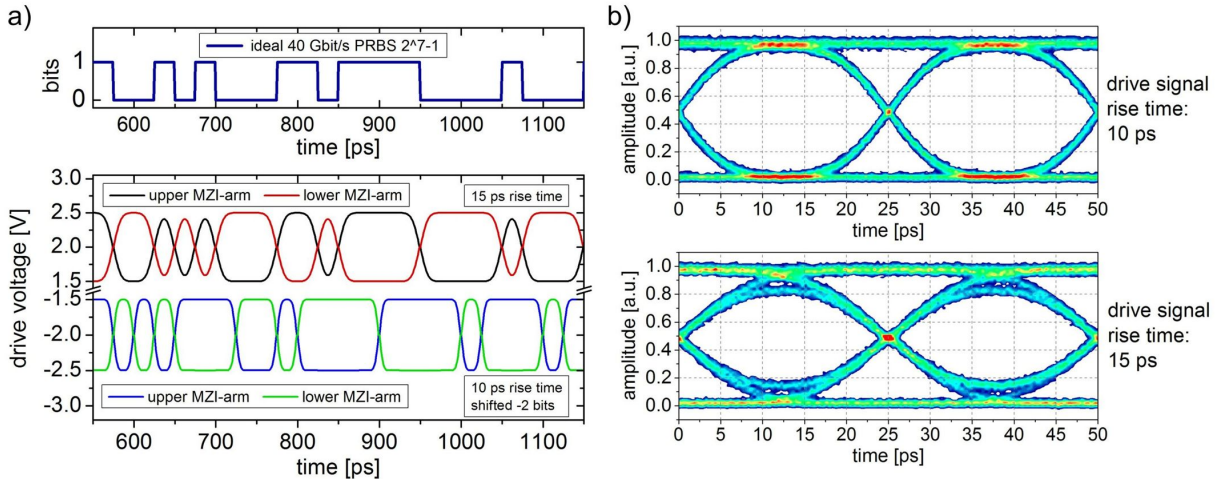
Fig. 4.6: a) Fraction of an 40 Gbit/s PRBS 2^7-1 bit sequence (top graph). Drive voltage sequences (1 V_{pp}) for upper and lower MZ-arm at 2 V bias with a signal rise time of 10 ps and 15 ps (bottom graph). The 15 ps voltage signal is shifted by -2 bits. b) Simulated single MZ modulator output power eye diagrams at 40 Gbit/s for drive signal rise times of 10 ps (top) and 15 ps (bottom). White Gaussian noise with σ=0.1 has been added for better visualization.

to visualize the effect of a shifted bit. The resulting calculated optical power eye diagrams for a single MZ modulator are shown in Figure 4.6b. The top graph is the power eye diagram for a signal rise time of 10 ps while the lower graph is for 15 ps rise and fall time. White Gaussian noise (standard deviation σ=0.1) has been added to the signal power. Because 15 ps is more than half of the bit length of 25 ps at 40 Gbit/s, the eye diagram in Figure 4.6b is not fully 'open' which means that consecutive bits in a 010- or 101-sequence do not reach the full-on or full-off state.

Similar to calculating the large signal information of a single Mach-Zehnder modulator, the drive-voltage model can be applied to the IQ modulator model (cf. Equation (4.4)). Setting the upper and lower Mach-Zehnder modulator to the normally-off state ($V_{pp} = 2\ V_{\pi}$) and setting the phase offset between both MZMs to the ideal 90°, QPSK modulated signals are obtained. Figure 4.7a shows the calculated output power eye diagram of the dual-parallel IQM for QPSK modulation (2^7-1 PRBS, signal rise time 10 ps). White Gaussian noise with σ=0.08 has been added and the point density is visualized by using a color grade. Due to the interference of the two binary-phase-shift-keyed signals under 90° angle, the IQ modulator inherently looses 3 dB optical power. Therefore, the maximum optical power in the QPSK eye diagram is 0.5. The origin of the IQM power eye diagram (Figure 4.7a) can be explained as follows. During switching between the four different phase states, the output power varies depending on the path through the complex constellation diagram. If only one of the two single MZMs changes
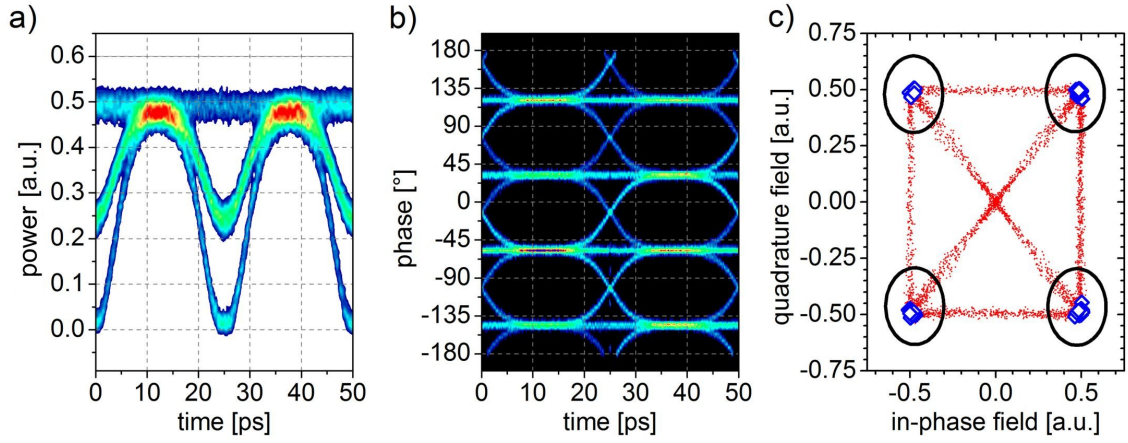
Fig. 4.7: a) Calculated QPSK power eye diagram for 40 Gbaud/s symbol rate (white Gaussian power noise with $2\sigma=0.08$ is added). b) Calculated QPSK phase eye diagram for 40 Gbaud/s symbol rate (white Gaussian phase noise using $2\sigma=15°$ is added). c) Calculated complex constellation diagram at 40 Gbaud/s symbol rate with amplitude and phase information. Red dots: data points of one 2^7-1 PRBS bit sequence. Blue squares: data symbol positions. Black circles: limit for 50% error vector magnitude (EVM) (cf. Equation (4.7)) for each constellation point.

its phase the output power drops to 25% of the input power (assuming no additional losses). When both MZMs are switched simultaneously, the path through the constellation diagram passes zero optical power. A 'so called' phase eye diagram indicating the phase states of the QPSK signals is plotted in Figure 4.7b (white Gaussian phase noise $\sigma=15°$ is added). This phase eye diagram presents the ideal case with exactly 90° phase difference between each of the four phase states. A complex plane constellation diagram of the same modulated optical signal is shown in Figure 4.7c that enables the direct reading of the amplitude and phase of the optical signal. The red dots mark all data points of one 2^7-1 PRBS bit sequence using 100 sample points per bit. The distortion-free signal is identified by the perfect symmetry of the traces between the four symbol points, which are highlighted by the blue squares. The black circles represent a reasonable boundary for the characterization of IQM non-idealities.

4.4.1 Modeling IQ modulator distortions

Phase and power imbalances induced by modulator fabrication imperfections and the non-linear voltage dependence of the phase- and absorption change in the QW-based optical waveguides have an impact on the constellation diagram quality of the IQ modulator. For optical on-off-keying modulators, the chirp or alpha parameter (α) is a measure of the contribution to the signal distortion, when the optical signal is propagating through a dispersive single mode fiber (SMF). The situation is different in PSK-related modulation formats. Here, the small signal

chirp parameter [94] has no real meaning as it is infinite for an ideal binary PSK modulator. For advanced multi level modulation formats like QPSK, it is more important to trace the signal path through the complex plane and describe deviations from the ideal power/phase path. Expressing these deviations in terms of a bit error ratio (BER) could be misleading because the BER is depending on the receiver quality and concept (coherent or direct detection) used in the transmission system [82]. Moreover, a constructed four-level bit sequence (typically two PRBS 2^n-1 sequences multiplexed with a cyclic shift for decorrelation) does not contain all possible subsequences of length n. Therefore, the BER is strongly pattern dependent [95]. Other than in digital radio communication, no standardized BER measurement procedure for optical quadrature amplitude modulation has been defined today. Instead of the BER, the more general 'error vector magnitude' (EVM) is used to quantify the transmitter or receiver performance. The EVM is a measure of the distances between all actually measured constellation points and their respective ideal location. Information about both amplitude and phase errors of the received signal can be obtained from the EVM so it gives a more complete picture of possible modulation distortions [96]. The EVM is defined as the ratio of the power of the error vector P_{error} to the root mean square power of the reference P_{ref} and is expressed in dB or %

$$EVM(dB) = 10 \cdot log_{10}\left(\frac{P_{error}}{P_{ref}}\right) \qquad EVM(\%) = \sqrt{\left(\frac{P_{error}}{P_{ref}}\right)} \cdot 100\% \qquad (4.7)$$

with the error and reference vector defined as

$$P_{error} = \frac{1}{N}\sum_{r=1}^{N}|\mathbf{S}_{ideal,r} - \mathbf{S}_{meas,r}|^2 \qquad (4.8)$$

and

$$P_{ref} = \frac{1}{N}\sum_{r=1}^{N}|\mathbf{S}_{ideal,r}|^2. \qquad (4.9)$$

N is the number of symbols, $S_{ideal,r}$ and $S_{meas,r}$ are the vectors of the ideal and measured symbols, respectively. Figure 4.8 gives a graphical representation of the error vector.

A simulated relation between the bit error rate (BER) and the error vector magnitude (EVM) for a 4-QAM wireless communication signal is shown in Figure 4.9 (Shafik et al. [97]). The simulation was performed under the assumption of an ideal receiver which adds no additional errors to the system. For this case it can be seen that the EVM must not exceed 17% in order to obtain a BER lower than 10^{-9}. To evaluate the impact of phase and power imbalances in the dual-parallel IQM on the EVM, Equation (4.7) is implemented into the IQ modulator *MATLAB* model. Figure 4.10 present calculated error vector magnitudes of the four individual
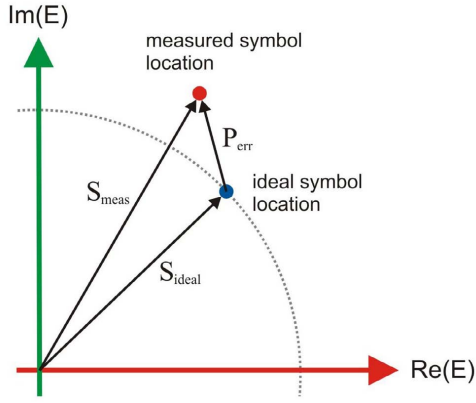
Fig. 4.8: Graphical representation of the error vector. The error vector magnitude is given by the root mean square of the length of the error vector divided by the length of the ideal symbol vector (in E-field representation).
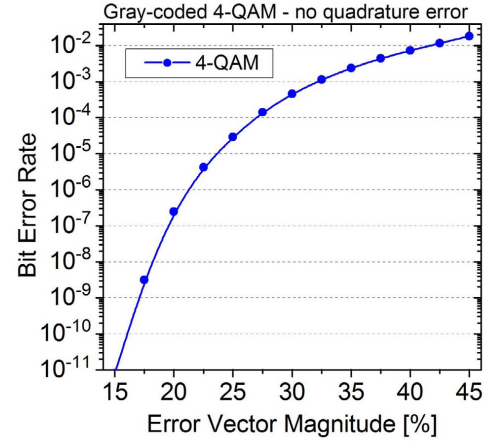
Fig. 4.9: Simulated relation between the bit error rate (BER) and the error vector magnitude (EVM) for ideal 4-QAM modulation in a wireless radio communication system [97].

QPSK symbols and the resulting constellation diagram for intentional optical phase and power variations in the IQ modulator. The input variables used for the IQM modeling are chosen to match the DC intensity matrix measurement of device #7018-F6 (3.2 mm active waveguide length, 1550 nm wavelength, see Figure 4.5). The colored triangles in Figures 4.10b, 4.10d, 4.10f and 4.10h show the constellation point walkoff from the ideal symbol location. The black solid circles in these figures represent the 50% EVM margin for each symbol location. Figures 4.10a and 4.10b illustrate the influence on the EVM of an increasing deviation from the ideal 90° phase difference between the upper I- and the lower Q-data MZM. The EVM hits the 50% margin for all four symbols at 75° phase difference. Figures 4.10c and 4.10d highlight the case of an optical power imbalance, when more optical power is coming from the I-data MZM. In this case the [1,1]-symbol and the [0,0]-symbol remain at their origin, while the other two symbols walk away from their initial location. The two changing symbols reach the 50% EVM margin for an optical power imbalance of 57%/43%. Figures 4.10e and 4.10f present the influence of a changing phase in the upper single MZM while the other keeps the ideal 90°. Interestingly, the impact on all four symbols is different. While the [1,0]-symbol reaches the margin at 75° phase difference, the [0,0]-symbol crosses the 50% EVM limit for MZI phase offset lower than 45°. Figures 4.10g and 4.10h feature the case of an optical power imbalance occurring in either the I-data or Q-data single MZM. An noteworthy observation is that even for an optical power imbalance of 75%/25% in one single MZM the EVM of all four symbols remain always below 50%.
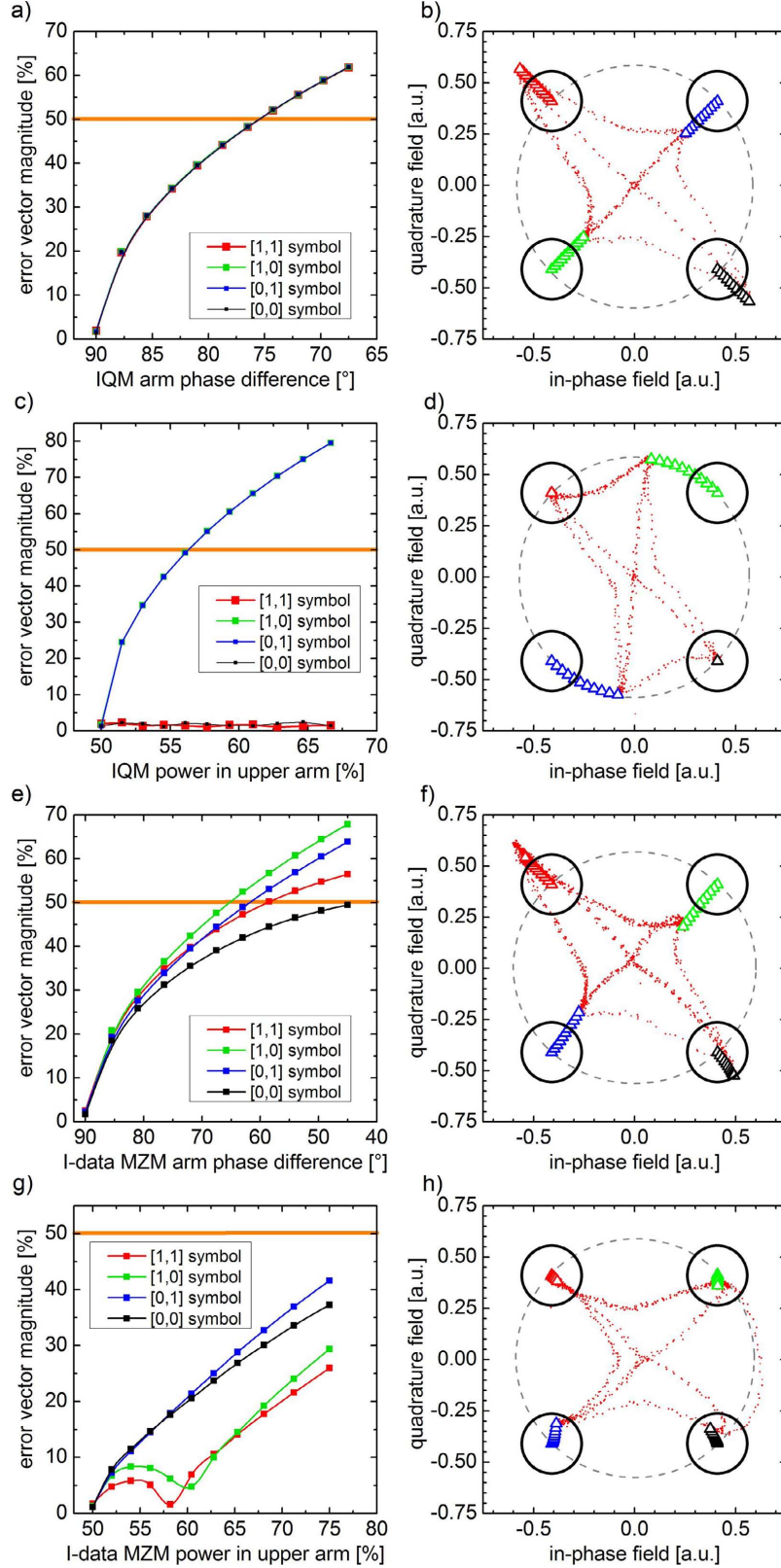
Fig. 4.10: Error vector magnitudes (EVM) of four QPSK symbols and the respective constellation diagram. Red dots in the constellation plots present the modulation traces for the last symbol quadruples of the left hand figure. Black solid circles in constellation plots depict 50% EVM margin. a+b) Decreasing phase difference between the I- and Q-data MZM. c+d) Increasing optical power going to I-data MZM. e+f) Decreasing phase difference between both arm of I-data MZM. g+h) Increasing power imbalance between I-data MZM arms.

After finding the EVM dependence of each QPSK constellation symbol for non-idealities occurring independently of each other, the next interesting question is, how the error vector magnitude varies, when two of the explored signal impairments appear at the same time. Depending on the EVM requirements for error-free operation of the IQM, the contour plots shown in Figure 4.11 allow to specify the allowed tolerances for IQM operation. The cumulative EVM (cf. Equation (4.9)) originating from all four symbols is visualized for a simultaneous variation of two IQM parameters. Figure 4.11a displays the EVM for a variation of the IQM phase difference versus a phase variation in just the upper I-data MZI arms. An interesting finding is, that an EVM increase due to a decreasing IQM phase difference can be counterbalanced by intentionally inducing the phase difference in one of the single MZMs. Note that this phase balancing must occur in the correct direction. Otherwise, the EVM would increase even further. Figure 4.11b presents the influence of unequal power split ratios in the IQ modulator arms versus that in one single MZM. An unequal power distribution between the upper and lower branch of the IQM has a much larger impact on the EVM than a power imbalance in just one of the single Mach-Zehnder modulators. Figures 4.11c and 4.11d show the EVM correlations to si-
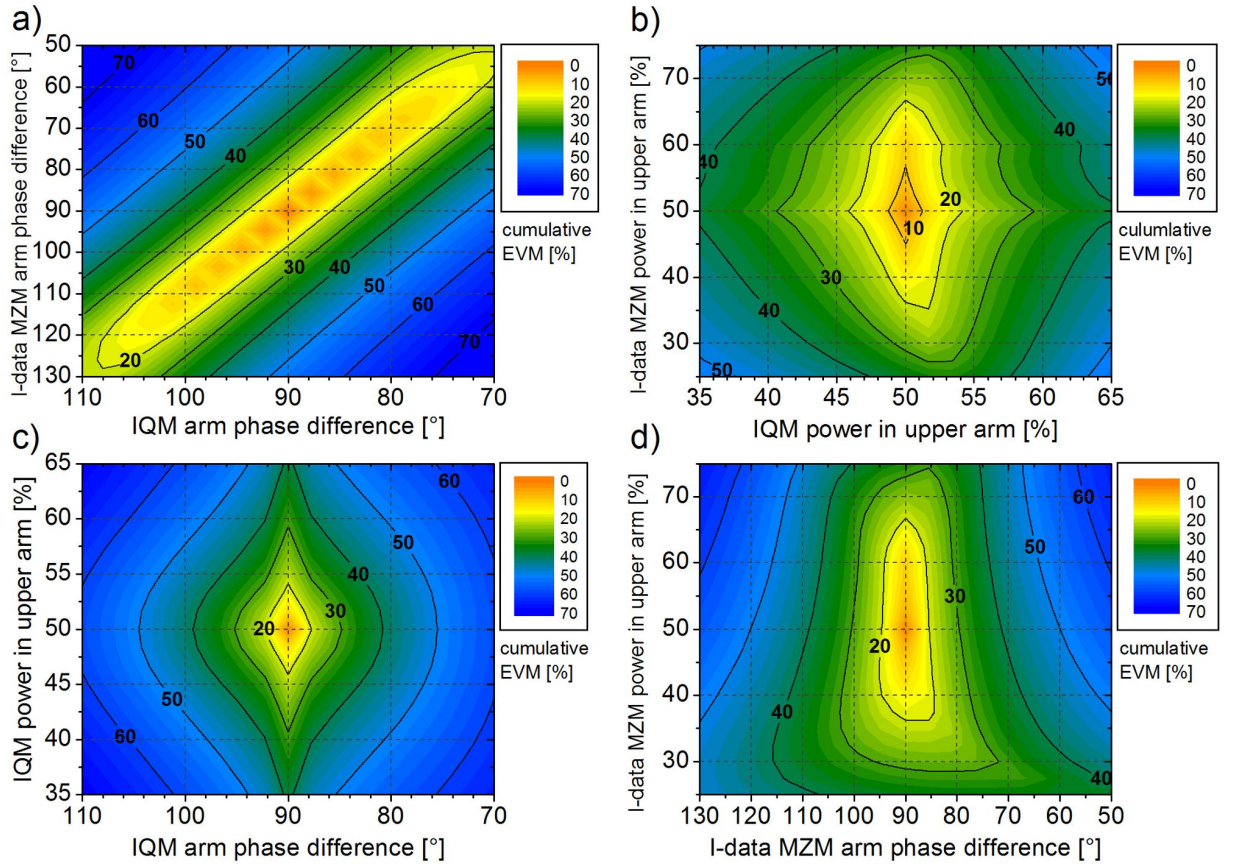
Fig. 4.11: Cumulative error vector magnitude for various IQM settings.

multaneous phase and power variations. The case for the IQM is demonstrated in Figure 4.11c. Obviously, simultaneous power and phase impairments have a huge impact on the cumulative EVM leaving narrow margins for the IQM operation. When these impairments occur in just one of the single MZMs the EVM margins for error-free operation (<17%) are more relaxed.

A general conclusion from this analysis is, that modulation signal impairments originating from optical power and phase imbalances in the IQ modulator have a larger impact on the EVM than phase and power imbalances in just one single Mach-Zehnder modulator. Thus, maintaining a minimal deviation from the ideal 50%/50% power split ratio and the 90° phase difference between the I-data MZ modulator and the Q-data MZ modulator is inevitable for the generation of error-free QPSK modulated data signals.

4.5 Module Packing

In order to evaluate the fabricated IQ modulator in a transmission system environment, the modulator chip needs to be packaged into a robust module. A high-frequency module featuring two GPPO® (trademark by Corning Gilbert) or SMPM coaxial connectors has been developed in cooperation with Kyocera. The GPPO® connector is a sub-miniature, push-on, microwave interconnect system operating from DC to 65 GHz. It is considerably smaller than a V-type connector, which is an advantage if two connectors are placed side-by-side. This is the case for the dual-parallel IQM developed in this work. The center-to-center pin distance of the two GPPO connectors is only 5.5 mm. Therefore, the transmission lines in the module, which route the RF drive signal from the connector to the chip, can be designed much smaller than in the case of V-connectors. Figure 4.12 shows a CAD-drawing of the Kyocera module equipped with IQM chip, optical fibers, DC connection board and diodes and capacitors for built-in electrostatic-discharge (ESD) protection. A design challenge for the dual-connector module is the necessity to counterbalance the ~800 μm additional length of the input transmission line of the upper I-data MZM on the IQ chip, which has been introduced to have both RF connections on one side of the IQM chip (cf. Figure 4.2). This 800 μm additional electrode length equals an electrical group delay of 7 ps. Hence, the RF line going from the right side GPPO® connector to the lower Q-data MZM on the IQM chip has to compensate these 7 ps and must therefore be designed longer than the transmission line of the left GPPO® connector. The Kyocera module for the IQ modulator has been specifically designed to fulfill this group delay requirement. On the opposite side of the RF connectors, the package provides 14 DC feedthroughs to allow connection to the thermoelectric cooler (TEC), the thermistor, the six phase electrodes, the two

monitor diodes and the n-contact. One pin is used to supply the DC bias voltage to the IQM. The electrical ground is externally connected to the module chassis. A photograph of a packaged IQ modulator module is shown in Figure 4.13. The different lengths of the RF lines connecting both GPPO connectors with the IQ chip can be clearly seen on the white ceramic substrate. The optical input (left side) and output fibers (right side) are fixed within a glass ferule in front of the input or output spot size converter which guarantees a stable and robust coupling with low insertion loss.
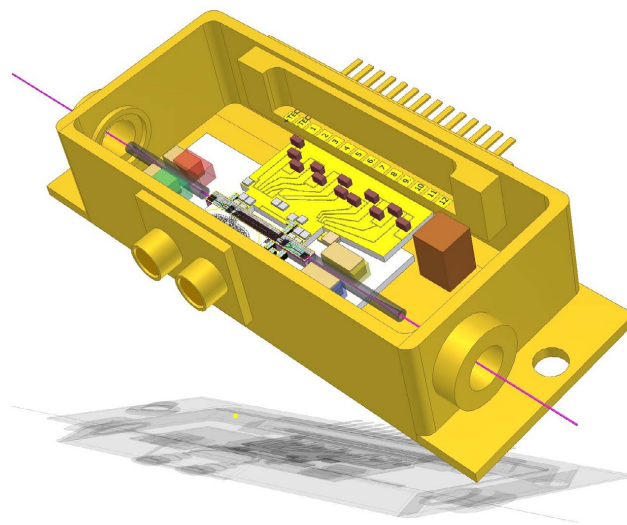
Fig. 4.12: CAD drawing of equipped IQM Kyocera module.
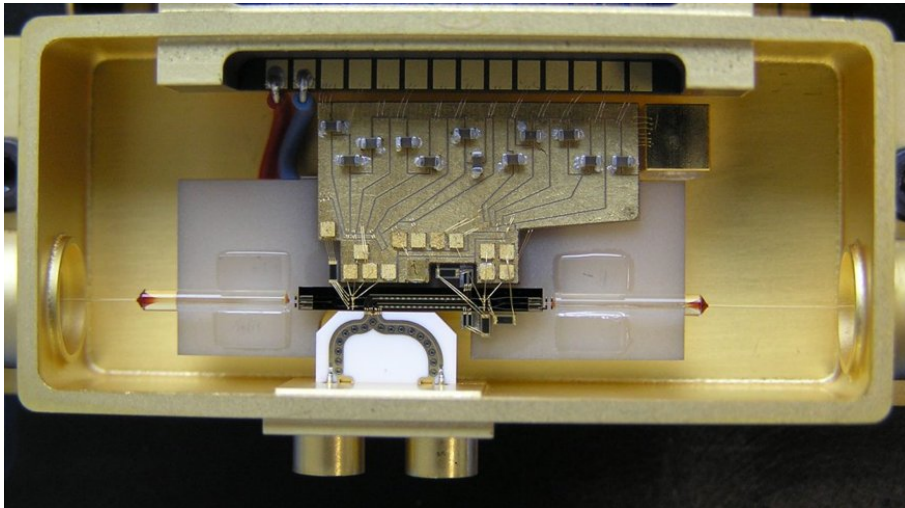
Fig. 4.13: Photograph of an IQ modulator chip build into a module manufactured by Kyocera Corporation. The external RF connection is realized by GPPO-connectors.

Chapter 5

Modulator characterization and experimental results

5.1 Introduction

This chapter gives an introduction to the experimental techniques used to characterize the standard single Mach-Zehnder modulator (MZM) and the newly developed dual-parallel IQ modulator. These experimental techniques include DC and RF characterization and their introduction is accompanied by measurement results from a variety of experiments. The general test of the single MZM is split into three parts. The procedure starts with a check of the basic functionality under DC conditions. Modulators that prove to work correctly are then measured on the RF small signal test station (bar level) to acquire their electro-optic small signal modulation bandwidth. Large signal RF testing of the modulators is generally performed on diced and packaged modulator chips. If necessary, large signal RF measurements can also be performed on bar level.

After the presentation and evaluation of single MZM DC measurement results that reveal good agreement with theory, a simple but yet effective IQ modulator characterization algorithm will be introduced. This test algorithm allows to derive phase electrode bias settings for IQM large signal operation from a DC test of all phase electrodes and monitor diodes. Experimental data of a fabricated IQM will be presented that validates the principles of this test algorithm. Hereafter, measurement results from small signal RF testing of selected single MZMs as well as an IQ modulator chip will be shown, that prove the large modulation bandwidth capability of the InP-based material system. Selected results from large signal RF testing of fabricated and module-packaged modulators will be presented afterwards. Beginning with measured data obtained from NRZ on-off-keying operation of a standard Mach-Zehnder modulator error-free operation at 40 Gbit/s and clear eye opening at 80 Gbit/s will be shown. In the following for the first time ever, successful operation of a packaged InP-based dual-parallel IQ modulator will be

highlighted for 2x20 Gbit/s and 2x40 Gbit/s operation using different measurement techniques.

5.2 DC characterization

The DC characterization of single MZ modulators is performed to measure the characteristic parameters drive voltage V_π, optical insertion loss and extinction ratio (ER). The ER is given by the optical power ratio between the on and the off state. All mentioned parameters are extracted from so called DC intensity matrices, that has been introduced before (cf. Figures 2.4 or 4.4a). DC intensity matrices are acquired by simultaneously voltage sweeping both MZ arms and are generally measured at four wavelength within the C-band (1528 nm to 1567 nm). Further requirements for the DC characterization of the dual-parallel IQ modulator will be discussed in the following section. A schematic layout of the DC test station used to characterize single MZ and IQ modulators on bar level is shown in Figure 5.1. An external-cavity laser (ECL) operating from 1460 nm to 1590 nm with up to 6 dBm output power is used as laser source. The TE light polarization state is software controlled and maintained by a polarization beam splitter. The optical power which is launched to the modulator chip is set by an optical attenuator prior. Cleaved or tapered fibers according to mode diameter of the on-chip spot size converter are used for fiber-chip coupling. The modulated signal from the output facet of the modulator is coupled into a fiber or is collimated using a microscope objective in a free-space optical assembly. The detection of the optical power is done by an InGaAs photodiode connected to a fast low-noise current amplifier with a flat frequency response up to 1 MHz. High speed data acquisition is done with a National Instruments DAQ 6259M board. The fiber or objective alignment is achieved using motorized stages for coarse positioning and a three-axis piezo-electric NanoCube for precise alignment with sub-micron resolution. Contacting the modulator is done by either using individual probe needles positioned by a micro-manipulator or by using a probe card with a preconfigured number of contacts in a fixed arrangement. The voltages or currents to sweep and control the phase electrodes are provided by Keithley sourcemeters (2400 or 26xx). The RF electrode sweep voltages to acquire the DC output intensity matrices are provided by the National Instruments DAQ 6259M board capable of sampling over two million times per second. A standard DC intensity matrix with 10.000 (0 V to 10 V with 0.1 V step size on both MZ arms) data points is measured in $\approx$ 40 seconds using an averaging of 200 samples per data point. A photograph of the DC test station can be seen in Figure 5.2a showing the motors and piezo-electric NanoCubes for input and output fiber alignment and the chip stage with probe card in the center. The inset shows a close-up of the chip stage. Figure 5.2b is a
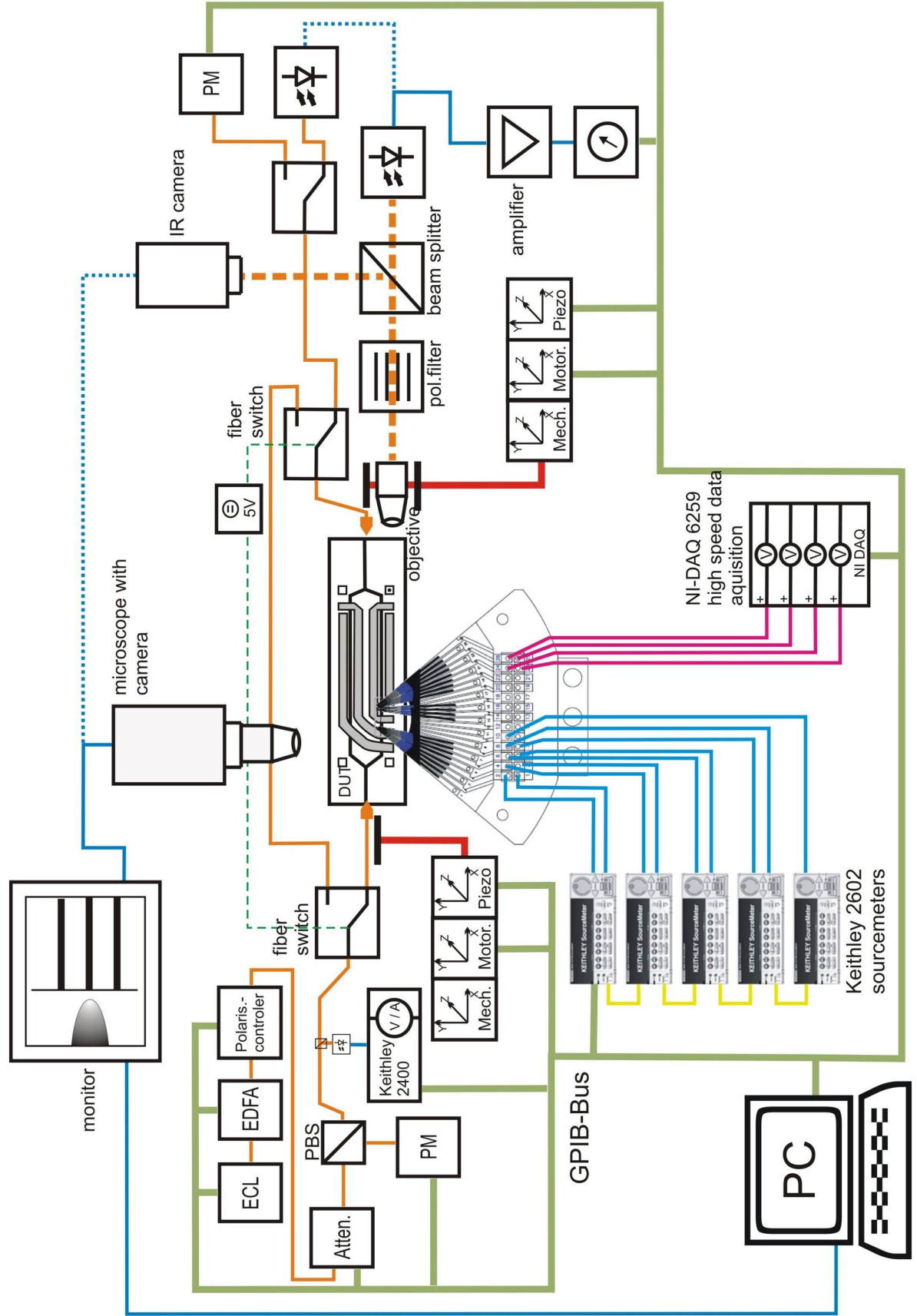
Fig. 5.1: Schematic of DC test station for evaluation of insertion loss, drive voltage V_π and extinction ratio on bar level.

a)

b)
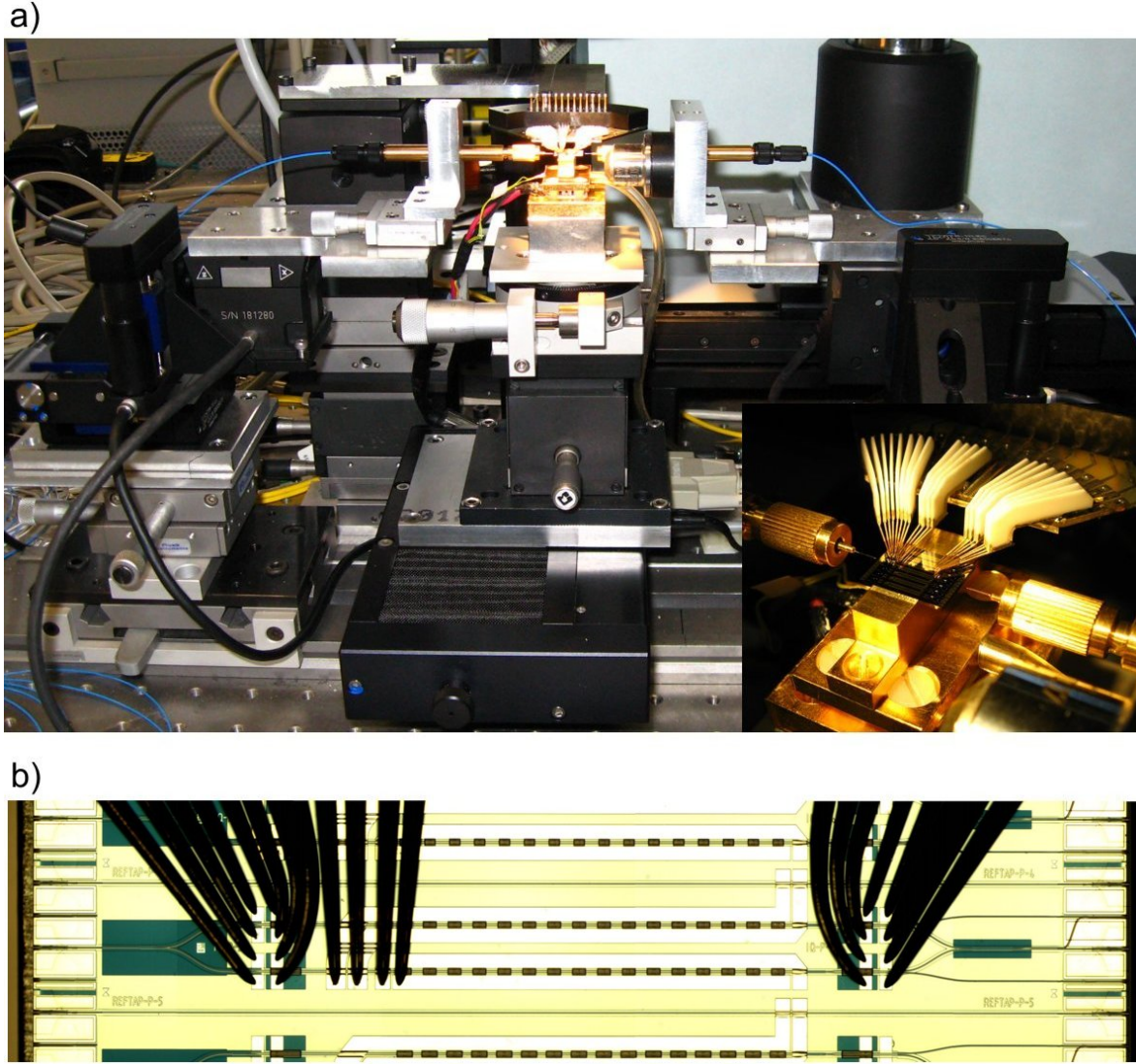
Fig. 5.2: a) Photograph of the DC test station. b) Microscope image of IQ modulator chip contacted with 20-pin DC probe card.

microscope image showing an IQ modulator chip contacted by a 20-pin DC probe card.

Additionally to the DC intensity matrix a wavelength scan to measure the device insertion loss from typically 1500 nm to 1580 nm is performed. This wavelength scan allows to determine the correct operation of the integrated spot size converters (SSCs) as well as the waveguide-integrated multi-mode interferometers (MMIs). Figure 5.3 shows DC intensity matrices of modulator device #7018-F6 (3.2 mm active material length, IRT=600 nm) measured at 1530 nm, 1540 nm, 1550 nm and 1560 nm. The wavelength dependence of the phase- and absorption change is clearly visible. Due to the large active material length and the thin intrinsic region, the switching voltage V_π at 5 V bias and 1550 nm is only 1.05 V. For the shorter wavelengths, V_π is even lower but at the same time, the absorption is larger. For a bias volt-

#7018-F6 3.2mm active material length
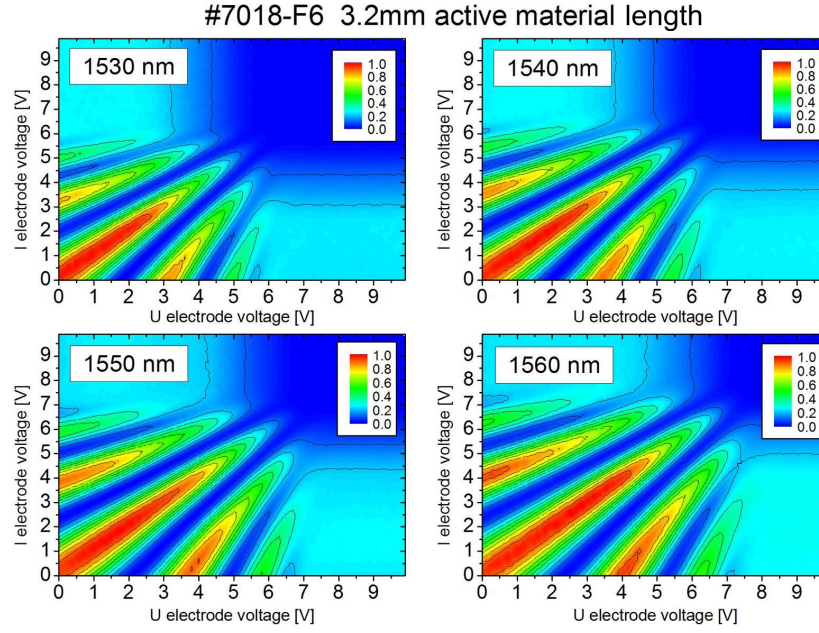
Fig. 5.3: DC intensity matrices of device #7018-F6 with 3.2 mm active material length and 600 nm IRT measured at 1530 nm, 1540 nm, 1550 nm and 1560 nm. The switching voltage and the bias dependent absorption are decreasing with increasing wavelength.

age of 5 V applied to both electrodes, the output power at 1530 nm is reduced to only 10% of the maximum power, meaning a 10 dB additional insertion loss of the device compared to the on-state. At 1540 nm and 5 V bias, the absorption induced excess loss is 5.2 dB. The excess loss at 1550 nm (5 V bias) is 2.6 dB and at 1560 nm wavelength only 1.5 dB (5 V bias). To express the modulation efficiency of a complete wafer having different modulator variations, the DC matrices are evaluated using the mathematical MZ model presented in Section 4.3. This allows the comparison with theoretical modulation efficiency data obtained in Chapter 3. The software tool presented in Appendix C.3 is used to perform the required fit and to extract the electric field induced refractive index change by using

$$\Delta n = \Delta \phi \frac{\lambda}{2\pi \cdot L_{act}} = \frac{\lambda}{2 \cdot L_{act}} \tag{5.1}$$

with λ being the wavelength, L_{act} the active material length and $\Delta \phi$ the desired phase change π. Figure 5.4 depicts the voltage dependent refractive index change obtained from fitting a 1550 nm DC matrix of device #7018-F6. The fit error for the entire matrix is less than 6% which is mainly resulting from a deviation of the absorption fit. The fit error of the refractive index change is in the order of 2% which is less than the accuracy of given by the measurement resolution of 0.1V. For an active material length of 3.2 mm (MZM #7018-F6), the required index change is Δn=2.422E-4 to induce a π phase shift between the two arms of the MZ inter-
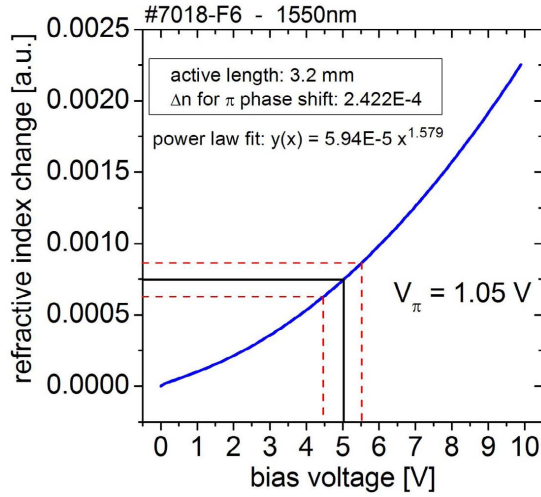
Fig. 5.4: Refractive index change over bias for MZM #7018-F6 (3.2 mm active material length). The required refractive index change for a π-phase shift after Equation (5.1) is $\Delta n = 2.422\text{E-}4$. The drive voltage V_π at 5 V bias is 1.05 V.
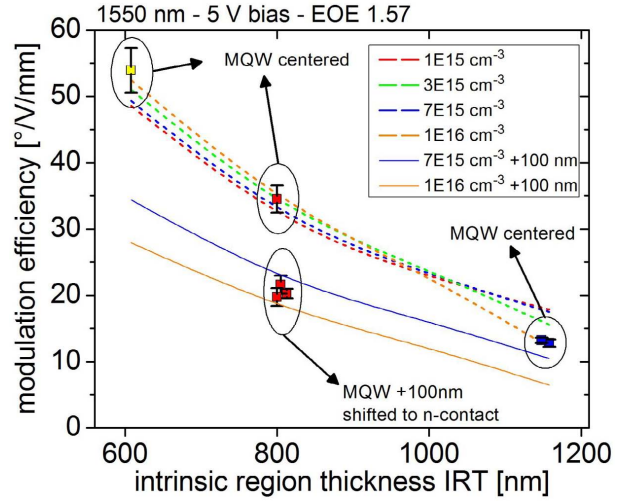
Fig. 5.5: Measured modulation efficiencies of wafers with different intrinsic region thicknesses and MQW offsets. Dashed lines: simulated modulation efficiencies for different background doping concentrations according to Figure 3.35 but with an EOE-factor of 1.57. Continuous lines: simulated modulation efficiencies for a MQW offset of +100 nm (cf. Fig. 3.37).

ferometer. From Figure 5.4, the resulting drive voltage can be determined for each bias voltage. At 5 V bias, the π-switching voltage is as low as 1.05 V.
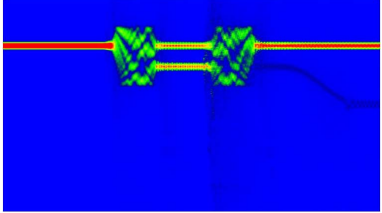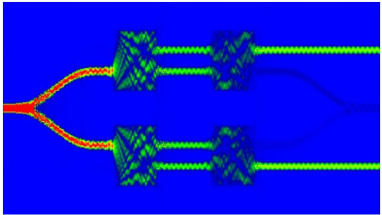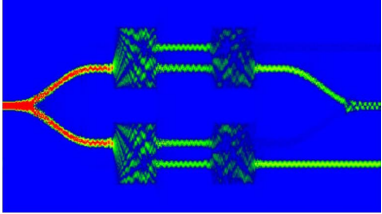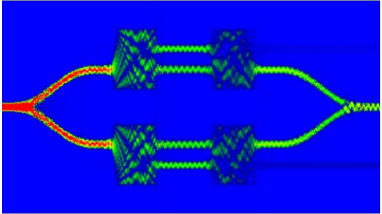
To quantify the modulation efficiency of a specific epitaxially grown multi quantum well and the respective waveguide geometry (DE, ME or SE), the common figure of merit ζ [°/V/mm] [98] for phase shifters is used. Generally, a processed wafer has a large variety of devices with different Mach-Zehnder parameters to evaluate their general performance influence. The figure of merit ζ expresses the induced phase change in degrees per applied voltage and per millimeter active material length and is therefore an efficiency measure which is independent of for example the traveling-wave electrode length or the fill factor. The value of ζ can be easily calculated from the matrix fit for each bias voltage. Figure 5.5 highlights the measured modulation efficiencies of several wafers with intrinsic region thicknesses of 1150 nm (blue squares), 800 nm (red squares) and 600 nm (yellow square) and compares them with calculated theoretical data derived in Section 3.3.2. All modulators are fabricated using the 'deep etch' waveguide geometry. The large error bar for the wafer with IRT=600 nm originates from the measurement resolution of 0.2 V, which is approximately 20% of the switching voltage V_π for these modulators. To compare the measured values of ζ with the theoretical data given in Figure 3.35, the calculated values have to be mapped to the experimental value of 12.2 °/V/mm for the

reference intrinsic region thickness (IRT) of 1150 nm. The modulation efficiency is varying with background doping concentration (BDC), thus only one value of BDC can be matched to the measured ζ=12.2 °/V/mm. The best fit of the computed data to the experimentally measured values is obtained if the largest evaluated background doping concentration $1 \cdot 10^{16} cm^{-3}$ is taken. It gives the largest slope for ζ versus IRT and fits best to the measured data. The dashed orange line for BDC=$1 \cdot 10^{16} cm^{-3}$ matches best to the measured data of all centered-MQW wafers. For the given calculations, an electro-optic efficiency (EOE) factor of 1.57 (the exponent in the power law fit of Figure 5.4) was used. Another interesting observation is made for the wafers with IRT=800 nm. While the efficiency for the wafer with the centered MQW is 34.7 °/V/mm, wafers with the same IRT but an MQW waveguide core shifted 100 nm towards the bottom n-contact have a much lower modulation efficiency of only 20.8 °/V/mm. This is another strong indication for a high background doping concentration. The calculations presented in Figure 3.37 have shown, that such a strong modulation efficiency variation is only observed for a high BDC. The thin continuous blue and orange line in Figure 5.5 present calculated modulation efficiencies (for BDCs of $7 \cdot 10^{15} cm^{-3}$ and $1 \cdot 10^{16} cm^{-3}$) for epitaxial waveguide structures whose MQW core is shifted 100 nm towards the bottom n-contact. The measured matches well to the calculated data.

5.2.1 The IQ modulator characterization algorithm

In contradiction to the standard Mach-Zehnder modulator with its two RF and two phase electrodes, the dual-parallel IQ modulator requires a more sophisticated characterization algorithm due to its six phase electrodes and four RF electrodes. The theoretical derivation of the required IQM performance in Section 4.4.1 showed that a precise control of the optical power and phase in each interferometer arm is essential for error-free operation. An IQM characterization algorithm has been developed that allows the derivation of necessary bias settings of all six phase electrodes which are used during large signal quadrature-phase-shift-keyed (QPSK) modulation. Table 5.1 lists this algorithm. In the right column, optical power plots from BPM (beam-propagation method) simulations of the IQM waveguide structure are shown to facilitate the comprehension of the intended phase state setting. The basic principle behind this algorithm is to first bias each single Mach-Zehnder modulator in the off state which is the correct working point for binary PSK.

For the upper single MZM, phase electrodes 1 and 2 (cf. Figure 4.2) are adjusted using either an applied reverse voltage or a forward current. As both single Mach-Zehnder modulators has to be operated in PSK mode, the correct working point is the off-state, where no light is guided

step #		image
1a	single MZ characterization: • use Input 1 and Output 1 to measure intensity matrix of upper single MZM • sweep phase electrodes P1 and P2 (voltage or current), acquire output power and photocurrent in P5 and M1 • use Input 3 and Output 3 to measure intensity matrix of lower single MZM • sweep phase electrodes P3 and P4 (voltage or current), acquire output power and photocurrent in P6 and M2 • P1-P2 setting giving maximum current in M1 is optimum for QPSK modulation • P3-P4 setting giving maximum current in M2 is optimum for QPSK modulation information obtained: voltage and current response of P1, P2, P3 and P4	
1b	single MZ characterization (if only Input 2 is available): • use Input 2 and Output 1 to measure intensity matrix of upper single MZM • sweep phase electrodes P1 and P2 (voltage or current), acquire output power and photocurrent in P5 and M1 • use Input 2 and Output 3 to measure intensity matrix of lower single MZM • sweep phase electrodes P3 and P4 (voltage or current), acquire output power and photocurrent in P6 and M2 • P1-P2 setting giving maximum current in M1 is optimum for QPSK modulation • P3-P4 setting giving maximum current in M2 is optimum for QPSK modulation information obtained: voltage and current response of P1, P2, P3 and P4	
2	IQM characterization (with Input 2): • set P1 and P2 such that photocurrent in P5 maximized, all light from upper MZM going to the center output (see image on the right) • set P3 and P4 such that photocurrent in P6 maximized, all light from lower MZM going to the center output • record minimum insertion loss of IQM information obtained: minimum insertion loss of IQM correct setting of P1, P2, P3 and P4 for step 3	
3	IQM characterization (with Input 2): • sweep phase electrodes P5 and P6 (voltage or current), acquire output power • find minimum and maximum output power in recorded data • the P5 and P6 setting giving 50% output power is the 90° point for QPSK modulation information obtained: voltage and current response of P5 and P5 correct 90° phase setting for QPSK modulation	

Tab. 5.1: IQ characterization algorithm to acquire bias settings for the six phase electrodes for optimum QPSK modulation. The images on the right show the respective optical intensities in the IQ modulator waveguides (obtained from BPM simulations).

to the center output of the IQM. The monitor diode 1 measures maximum photo current while phase electrode 5, operated as a detector, should not detect any photocurrent. The lower MZM is adjusted in the same way using phase electrodes 3 and 4 to set the phase and monitor diode 2 and phase electrode 6 as detector. The next step is to set both MZMs to the on state to determine the 90° phase difference by adjusting phase electrodes 5 and 6. Both phase electrodes need to be swept such that a minimum and a maximum can be observed in the output power curve. From theory, the correct 90° phase difference point should correspond with the 50% power setting. This is only correct if the light intensities coming from both single MZMs are identical. If that is not the case, the correct 90° phase setting can only be found during device testing under large signal modulation.

5.2.2 Phase electrode characterization

To facilitate the characterization of the phase electrodes, a software implementation of the algorithm described before has been added to the DC test stations measurement program. The graphical user interface is shown in Figure 5.6. It allows to automatically perform all required phase electrode sweeps with reverse bias voltage or forward current or to manually adjust all applied voltages or currents while detecting the output power of the IQM. A total of eight source measure units (SMU) is controlled for the six phase electrodes and two monitor diodes of the IQ modulator. The software allows to measure IV-curves of each electrodes p-i-n-junction with and without optical excitation to prove the correct functionality. A DC intensity matrix can be acquired for each phase setting by either sweeping the RF electrodes of the upper or the lower single MZM. The detected signal for the matrix sweep can be selected from either the fiber coupled output power or the photo current measured in the monitor diode of the swept MZM. Exemplary results of voltage sweeps performed on the phase electrode of IQ modulator chip #6009-P1 at 1550 m wavelength are presented in Figure 5.7. The photocurrents detected in monitor diode 1 (cf. Figure 4.2) and phase electrode 5 are shown in Figure 5.7a. A reverse bias voltage swept from 0 V to 16 V has been applied to phase electrodes 1 and 2. The typical behavior of a MZ modulator can be observed. The light is switched between both outputs depending on the phase difference between both MZ arms. The regular 3-dB operating point for on-off-keying modulation with equal optical power going to both outputs is set with a reverse bias of 7.5 V applied to phase electrode 1. The working point for phase-shift-keyed modulation is the off-state, where no light is guided to the center output passing phase electrode 5. This state is set with a reverse bias voltage of 17 V applied to phase electrode 1, which is non-ideal, because with such high bias voltages, the absorption in the electrode becomes a significant factor. Figure
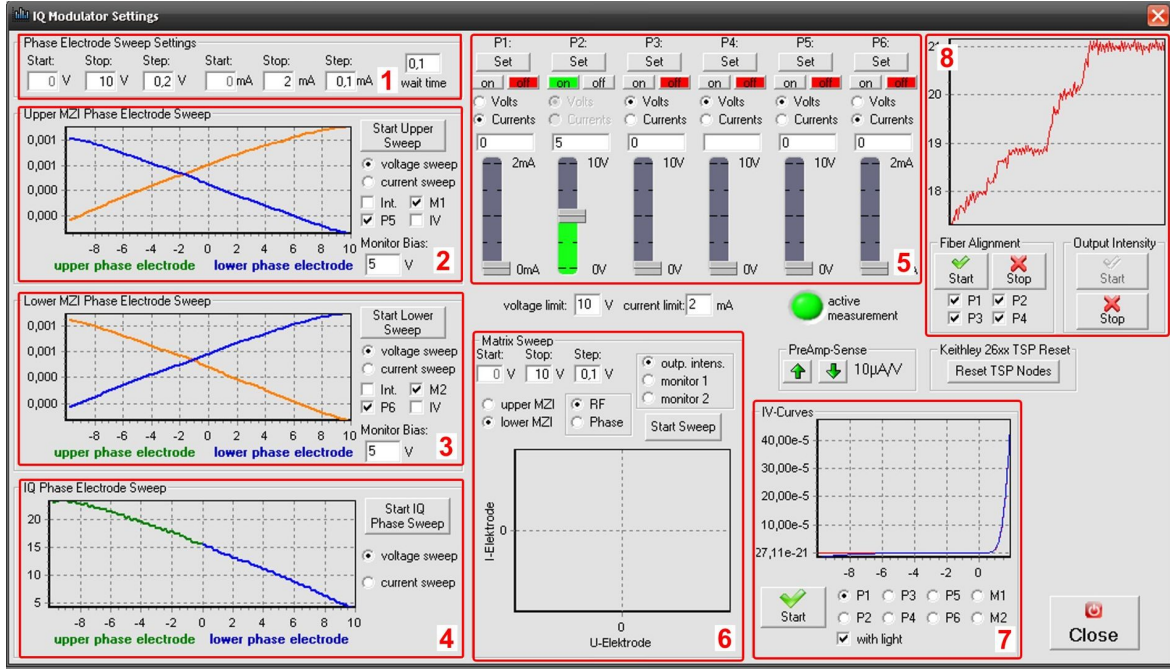
Fig. 5.6: Graphical user interface of the IQM phase electrode control software. 1) Settings for voltage and current sweeps. 2) Data acquisition sweep for phase electrodes P1 and P2. 3) Data acquisition sweep for phase electrodes P3 and P4. 4) Data acquisition sweep for phase electrodes P5 and P6. 5) Manual controls for all phase electrodes to set voltage or current. 6) Matrix acquisition for phase or RF electrodes. 7) IV-curve measurements of all phase and monitor diodes. 8) Monitor for diode photo currents or output power used for fiber alignment.

5.7b shows the measured output power at the center output of the IQM. The curvature of the data is almost identical to the photocurrent data of phase electrode 5 in Figure 5.7a. This is a strong evidence that there is no additional light coming from the lower single MZ modulator because this light would deviate the output curve due to interference effects. The finding that the lower MZ is in the off-state with no applied bias is confirmed by the voltage sweep results shown in Figure 5.7c. The photocurrent in phase electrode 6 has the lowest value with no bias applied to either phase electrode 3 or 4 while monitor diode 2 measures a high photo current. Figure 5.7d depicts the acquired IQM center output power, when sweeping phase electrodes 3 and 4. It can be seen that this curve does not follow the photocurrent data of phase electrode 6 (cf. Figure 5.7c). At zero bias voltage the output power is $\approx$ 17.5 μW, which is the same value as in Figure 5.7b for zero bias voltage. Thus, the measured power at 0 V bias shown in Figure 5.7d is coming from the upper MZM. It interferes with the light from the lower MZM which increases when phase electrodes 3 or 4 are swept. Therefore, only measuring the output power from the center output waveguide of the IQM is not sufficient to determine the correct phase states of the upper and the lower MZM for PSK operation. The correct settings for phase
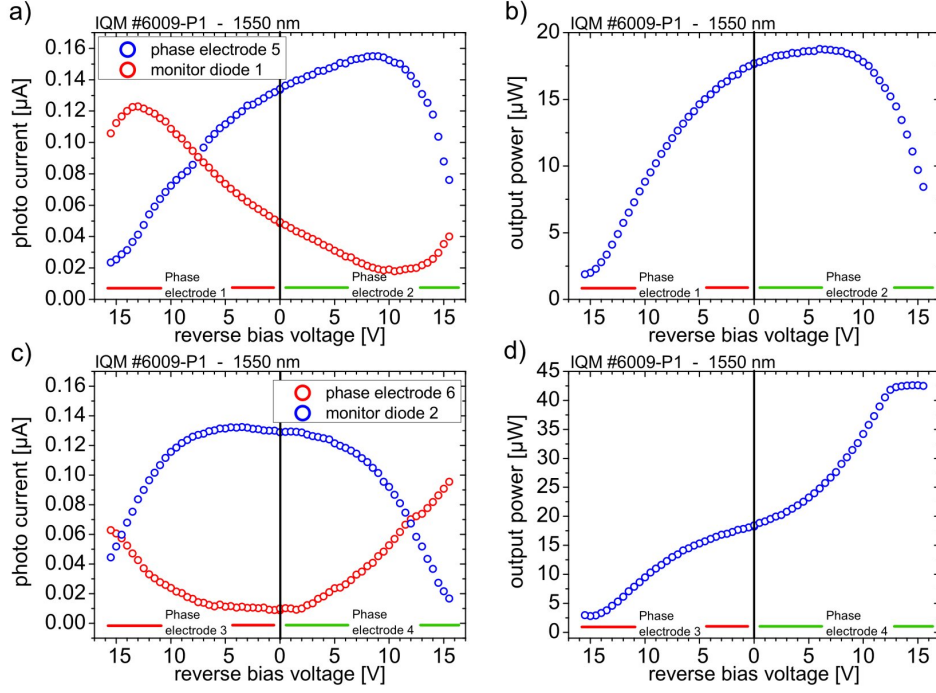
Fig. 5.7: IQ modulator phase electrode voltage sweep response measured at 1550 nm. a) Photocurrent in monitor diode 1 and phase electrode 5 for a voltage sweep of phase electrodes 1 and 2. b) Output power for a voltage sweep of phase electrodes 1 and 2. c) Photocurrent in monitor diode 2 and phase electrode 6 for a voltage sweep of phase electrodes 3 and 4. d) Output power for a voltage sweep of phase electrodes 3 and 4.

electrodes 1 to 4 can only be found by either recording the photocurrents in monitor diodes 1 and 2 and phase electrodes 5 and 6 or by measuring the output power from each single MZM at the respective dump output ports 1 and 3 (cf. Figure 4.2). The latter requires to reposition the optical fiber at the output which is only possible during measurements on bar level but not in packaged module.

5.3 RF small signal characterization

The small signal electro-optic response function of the single MZ modulator is measured from 100 MHz up to a frequency of 67 GHz using an Agilent Lightwave Component Analyzer (LCA) N4373B [99]. For bar-level RF measurements, a test station similar to the DC version described in Section 5.2 is used. Electrical signal feeding to the modulator device and termination with a 50 Ω resistor is done with two Cascade Microtech Infinity probes. All small-signal frequency response measurements were performed using an electrical signal power of -7 dBm and an optical input power of 0 dBm. To compensate the varying optical insertion loss of the modu-
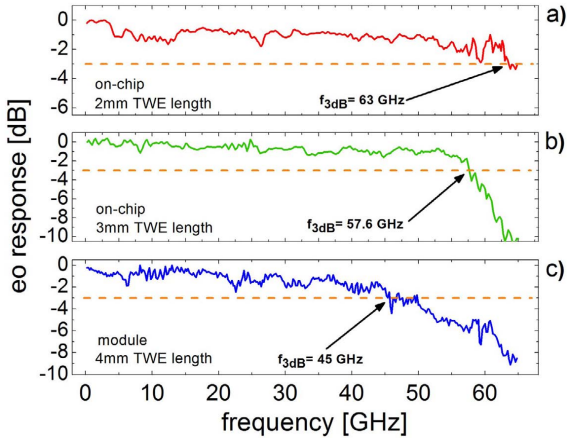
Fig. 5.8: On-chip electro-optic response of single MZ modulators with traveling-wave electrode length of 2 mm, 3 mm and 4 mm. The f_{3dB}-values are 63 GHz, 57 GHz and 45 GHz, respectively.
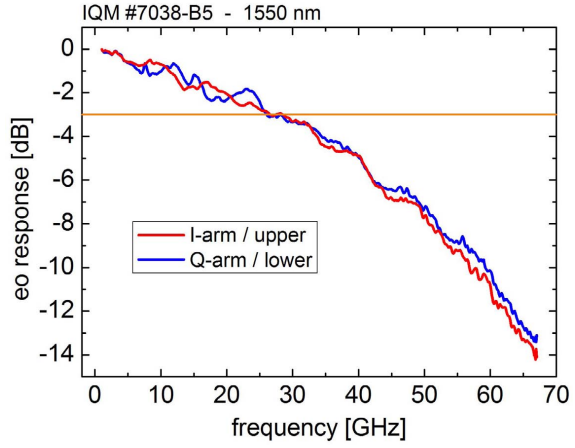
Fig. 5.9: I-arm and Q-arm on-chip small-signal RF response of IQM #7038-B5. The 3-dB frequencies are 26.4 GHz and 25.7 GHz for the I-data and Q-data MZM, respectively.

lator, the optical output signal is amplified to 0 dBm using an EDFA followed by a 2 nm wide optical filter to reduce amplified spontaneous emission (ASE). Prior to the acquisition of the modulation bandwidth response, the correct working point and TE polarization are set. The quadrature operating point in the MZ transfer function (cf. Figure 2.3) has the highest slope thus giving the highest response under small-signal modulation. Therefore, the phase electrodes and the polarization are set to give the maximum modulation response at 1 GHz. Figure 5.8 presents electro-optic modulation response measurements of single Mach-Zehnder modulators with three different traveling-wave electrode (TWE) lengths. The on-chip 3-dB bandwidth of the 2 mm TWE modulator presented in Figure 5.8a is 63 GHz, that of the 3 mm TWE MZM in Figure 5.8b is 57 GHz. Figure 5.8c shows the modulation response of a packaged single Mach-Zehnder modulator with 4 mm TWE length (f_{3dB}=45 GHz). The 2 mm TWE MZM has a fill factor of 0.4 while the other two have a fill factor of 0.5. All three types have a nominal intrinsic region thickness of 1150 nm. To compare these measurement results with theoretical data from Section 3.4.1, the calculated f_{3dB} values presented in Figures 3.46a and 3.46b are used assuming a p-contact sheet resistance of $5 \cdot 10^{-5} \Omega / cm^2$ and $1 \cdot 10^{-5} \Omega / cm^2$, respectively. Because these values were calculated for a fill factor of 0.7, corrections for a fill factor of 0.4 and 0.5 using the information from Figure 3.44 has to be added. The theoretical f_{3dB} values for a p-contact of $5 \cdot 10^{-5} \Omega / cm^2$ are 73 GHz, 52 GHz and 46 GHz for 2 mm, 3 mm and 4 mm, respectively. Those for $1 \cdot 10^{-5} \Omega / cm^2$ are 80 GHz, 65 GHz and 59 GHz for 2 mm, 3 mm and 4 mm, respectively. The expected theoretical 3-dB frequencies for the 2 mm TWE MZ modu-

lator are much higher, than the measured ones. This is due to the fact that the limits are beyond the measurement capabilities of the test station. All V-type RF connectors and the RF probe heads as well as the Lightwave Component Analyzer itself are specified up to a frequency of 67 GHz. The calculated f_{3dB} for the 3 mm and 4 mm MZMs with $5 \cdot 10^{-5} \Omega/cm^2$ p-contact are lower than the measured ones. For the 4 mm TWE-length MZ modulator, the on-chip bandwidth is of course larger than the measured bandwidth after module packaging. The module small signal response is worse due to frequency dependent microwave loss induced by wire bonding, RF connectors and the 50 Ω termination resistor. The theoretical 3-dB bandwidths for the better p-contact ($1 \cdot 10^{-5} \Omega/cm^2$) are much higher than then measured values indicating that the real p-contact sheet resistance of the fabricated modulators is somewhere between the examined theoretical p-contact values.

Figure 5.9 shows the measured on-chip electro-optic response functions of the I-data and Q-data MZM of IQ modulator #7038-B5. The 3-dB frequencies are 26.4 GHz and 25.7 GHz for the I-data and Q-data MZM, respectively. This IQM chip has been designed for low drive voltage using a high fill factor of 0.8 and an intrinsic thickness of only 736 nm. Hence, the chip has a too large capacitive load to obtain velocity matching. The drive voltage V_π was measured to be only 2 V for the I-data and Q-data MZM. Considering the theoretical data from Figures 3.46a and 3.46b assuming a p-contact slightly worse than $1 \cdot 10^{-5} \Omega/cm^2$, the theoretically expected 3-dB frequency is ≈ 30 GHz. Subtracting 3 GHz for the larger fill factor (cf. Figure 3.45c) of the fabricated IQM compared to the theoretical data, the expected f_{3dB} is ≈ 27 GHz, which gives an excellent match with the measured results.

5.4 Large signal characterization

The motivation for the development of the dual-parallel IQ modulator is to enable high data rate transmission at 100 Gbit/s by using a symbol rate of of only 50 Gbaud/s. To verify the functionality of the IQM under large signal drive conditions, error-free operation of the standard single Mach-Zehnder modulator has to be proven at first.

5.4.1 Back-To-Back Mach-Zehnder modulator characterization

Transmission performance testing of a packaged single MZM is done using the non-return-to-zero (NRZ) on-off-keyed modulation format. Optical power eye diagram measurements where performed using an Anritsu bit pattern generator MP1775A BPG and a MP1801A multiplexer at 43.3 Gbit/s. The electrical pulse patterns where amplified using an SHF 804EA broadband
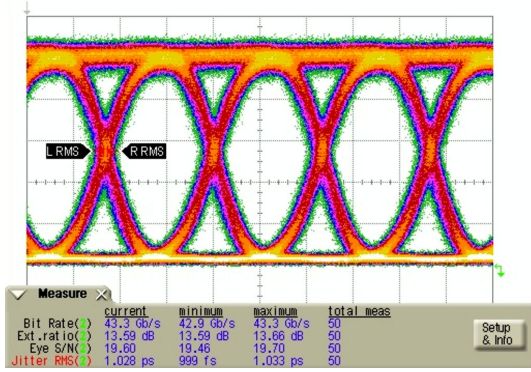
Fig. 5.10: 43.3 Gbit/s NRZ eye diagram of Mach-Zehnder modulator #50-A70 (4 mm TWE length, FF 0.4). Drive conditions: PRBS $2^{31} - 1$, V_{pp}=3.0 V, 1550 nm, 25°C.
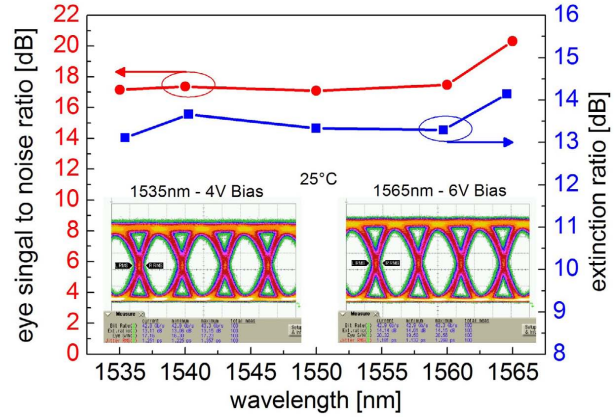
Fig. 5.11: MZM #50-A70 (4 mm TWE length, FF 0.4) eye signal-to-noise ratio and dynamic extinction ratio within the C-band at 43.3 Gbit/s. Drive conditions: PRBS $2^{31} - 1$, V_{pp}=3.0 V, 25°C.

amplifier having a maximum voltage swing of V_{pp}=3.5 V. The 80 Gbit/s bit pattern was generated by multiplexing two 40-Gbit/s data streams from the Anritsu bit pattern generator with an SHF 408 2x1 multiplexer. An erbium-doped fiber amplifier (EDFA) at the output of the modulator ensured a constant optical power level of 7 dBm at all wavelengths across the C-band, when the optical output power of the modulator varied due to different absorption at different wavelengths. An 2-nm optical filter was used to attenuate the amplified spontaneous emission (ASE) from the EDFA. The modulated optical signal was detected using a high-speed photodiode (u2t XPDV2020R).

The packaged single Mach-Zehnder modulator (#50-A70, 4 mm traveling-wave electrode length, fill factor 0.4) has DC switching voltage V_{π} of 2.5 V (5 V bias, 1550 nm wavelength), the DC extinction ratio is 24 dB and the small-signal 3-dB bandwidth is 26 GHz. Figure 5.10 shows the acquired 43.3 Gbit/s non-return-to-zero (NRZ) eye diagram at 1550 nm using a PRBS pattern length of 2^{31}-1. A peak-to-peak drive voltage of 3 V has been used. The dynamic extinction ratio (ER) is excellent with 13.6 dB and the eye signal-to-noise ratio (SNR) is 19.6 dB. Figure 5.11 shows measured ER and SNR for wavelengths of 1535 nm, 1540 nm, 1550 nm, 1560 nm and 1565 nm within the C-band. The dynamic extinction ratio is above 13 dB and the signal-to-noise ratio is above 17 dB for all wavelengths. The bias voltage was adjusted from 4 V at 1535 nm to 6 V at 1565 nm to compensate the wavelength-dependent variation of the modulators drive voltage. Error-free NRZ on-off-keyed modulation at 43.3 Gbit/s of the single MZ modulator is shown in Figure 5.12 at 1550 nm wavelength. The black trace displays the bit error rate (BER) versus the received optical power for back-to-back transmission. The red trace
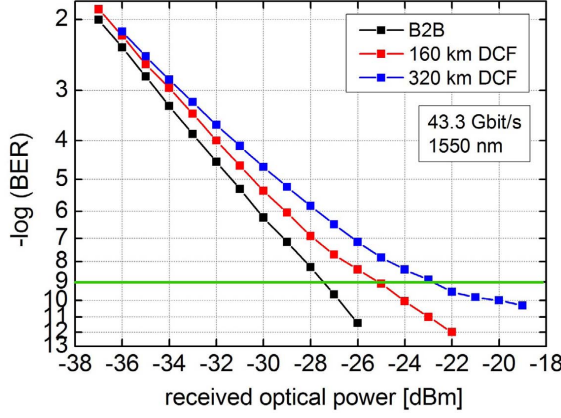
Fig. 5.12: 43.3 Gbit/s bit error rate for back-to-back and 160 km and 320 km transmission. PRBS $2^{31}-1$, V_{pp}=3.0 V, 25°C, 1550 nm.
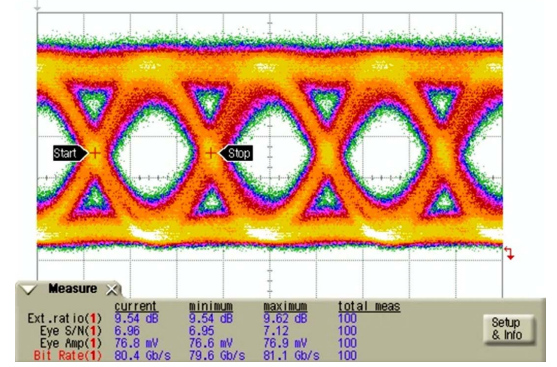
Fig. 5.13: 80 Gbit/s NRZ eye diagram. PRBS $2^{31}-1$, V_{pp}=3.5 V, 1550 nm, 25°C.

is the error rate for a transmission of 160 km dispersion-compensated fiber (DCF). The blue trace shows the corresponding error rate for a transmission over 320 km DCF. Both error rates from 160 km and 320 km experiments feature a small error floor (deviation from a straight line) giving evidence for a non-ideal dispersion compensation of the optical fiber or a small chirp of the Mach-Zehnder modulator. The error floor is more pronounced in the 320 km transmission but error free operation (BER<10^{-9}) is still achieved. A power penalty of 1.2 dB at BER=10^{-9} is added each time when 160 km DCF are linked into the transmission path.

A second packaged MZ modulator #45-A50 with V_{π}=2.8 V at 5 V bias and a small-signal 3-dB bandwidth of 45 GHz (cf. Figure 5.8) is tested at 80 Gbit/s using a higher peak-to-peak voltage of 3.5 V to slightly overdrive the modulator at low frequencies for better eye opening. The measured eye diagram is shown in Figure 5.13 and features a dynamic extinction ratio of 9.5 dB. This is sufficient for error-free data transmission at 80 Gbit/s. No bit error rate could be measured to prove error-free operation because no demultiplexer for such a high bit rate was available. But the measured 80 Gbit/s power eye diagram is promising for a successful generation 2x50 Gbit/s QPSK modulated optical signals with the dual-parallel IQ modulator.

5.4.2 Back-To-Back IQ modulator characterization with APEX OCSA

In order to perform a large signal characterization of the developed IQ modulator, the modulated optical signal needs to be analyzed in the time domain regarding its power and phase. Standard optical spectrum analyzers only measure the power and wavelengths of an optical signal. The APEX Technologies optical complex spectrum analyzer (OCSA) [100] is able to additionally measure the optical phase. The measurement principle is based on a frequency-domain spectral

analysis of the optical field, where the amplitude and the phase of each frequency component are analyzed with all components spaced by a fixed frequency provided by a local oscillator (f=2.5 GHz). Knowing the amplitude and the phase of each spectral component, the temporal variations of the amplitude and the phase are calculated by the Fourier transform, providing the optical field strength and phase as a function of time. Due to the measurement principle, the maximum number of bits that can be analyzed is the device bit rate divided by the local oscillator frequency (40 Gbit/s / 2.5 GHz = 16 bits). The advantage of this measurement approach is, that there is no limit for the measurement bit rate. Even bit rates of 80 Gbit/s, 160 Gbit/s or higher can be analyzed. A complex QPSK constellation diagram of the packaged IQ modulator #6009-P1 at 2x40 Gbit/s=80 Gbit/s is plotted in Figure 5.14. Two 16 bit sequences with a synchronized delay were fed to both RF inputs of the packaged IQM after amplification with SHF 804EA broadband amplifiers. The optical input power was set to 7 dBm. The phase electrodes were controlled by the software presented in Figure 5.6 and set to the values obtained from the DC characterization algorithm. Using the data from Figure 5.7a, the phase electrode 1 of the upper I-data MZM was set to 17 V reverse bias and no voltage was applied to phase electrode 2. Phase electrode 3 of the lower Q-data MZM was set to 3 V and no voltage was applied to phase electrode 4. To set the 90° phase difference between the I-data and Q-data MZM, a reverse voltage of 4 V was applied to phase electrode 5. With these phase electrode settings, a constellation diagram has been acquired (not shown) which was highly distorted due to the voltage-related absorption in phase electrodes 1 and 5. To compensate the optical power imbalance, the reverse voltage on phase electrode 1 was reduced to 11.8 V and the lower phase shift was counterbalanced by a forward current induced phase shift (using 1.3 mA) in phase electrode 2. Secondly, the optical power in the lower Q-data MZM was reduced by applying reverse voltages of 6.6 V and 7.8 V to phase electrodes 3 and 4, respectively. Due to the phase shift induced by this action, the reverse voltage in phase electrode 5 had to be increased to 9.5 V to attain the 90° phase difference between the upper I-data and the lower Q-data MZM. The measured 16 bits are highlighted by the red dots in the reconstructed power constellation diagram shown in Figure 5.14a. The blue dots mark the transition traces during switching of the IQM. Figure 5.14b depicts the measured 80 Gbit/s phase eye diagram, which corresponds to the theoretically predicted phase eye diagram in Figure 4.7b. The four phase states of the QPSK modulation can be clearly distinguished. Unfortunately, no error analysis can be performed using the spectral data acquired with APEX OCSA.
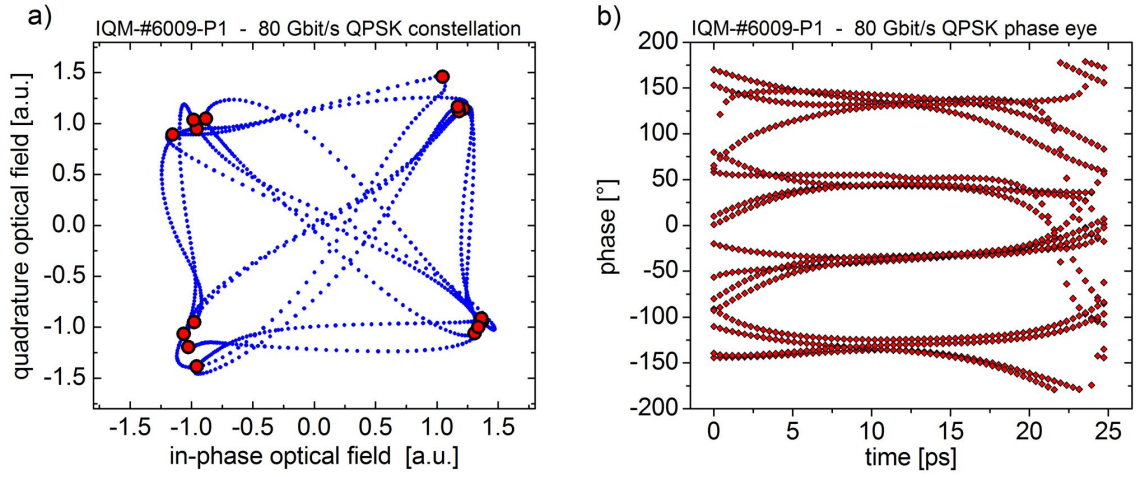
Fig. 5.14: QPSK modulation of IQ modulator at 2x40 Gbit/s=80 Gbit/s measured with APEX OCSA. a) optical complex constellation diagram with 16 phase points (red) and traces(blue) (cf. Figure 4.7c). b) Phase eye diagram composed with transient data of power and phase (cf. Figure 4.7b).

5.4.3 Back-To-Back IQ characterization with Agilent Optical Modulation Analyzer

The generation of QPSK modulated signals at 2x40 Gbit/s=80 Gbit/s has been successfully demonstrated but no evaluation of the signal quality could be performed with the analysis principle of the APEX OCSA. This possibility is given with the Agilent optical modulation analyzer (OMA) N4391A. The Agilent N4391A provides an in-depth analysis of optical transmission signals operating with advanced modulation formats. It consists of a 13 GHz real-time oscilloscope and an optical polarization-diverse coherent receiver allowing optical signal analysis up to 20 GHz in an optical wavelength range from 1528 nm to 1630 nm. Other than the APEX optical complex spectrum analyzer, the optical modulation analyzer is a time-domain measurement instrument, which is the main reason for the 20 GHz frequency limit. The advantage of the time-domain measurement principle is, that a true pseudo-random bit sequence (PRBS) representing real data traffic can be used to analyze to signal quality. A QPSK modulation analysis at 20 GHz (=40 Gbit/s) of the packaged IQ modulator #6009-P1 is presented in Figure 5.15. Two PRBS 2^{31}-1 bit sequences with a synchronized delay were fed to both RF inputs of the packaged IQM after amplification using SHF 804EA broadband amplifiers. The probe wavelength is 1550 nm. The two traces to the left show the received complex E-field constellation diagram (bottom with signal traces). In the top center, the optical spectrum of the received signal is shown. The table in the bottom center of Figure 5.15 displays evaluated data such as the error vector magnitude (EVM) , the quadrature phase error and the gain imbalance between the I-data and Q-data streams. The two traces to the right show the I-data and Q-data phase eye
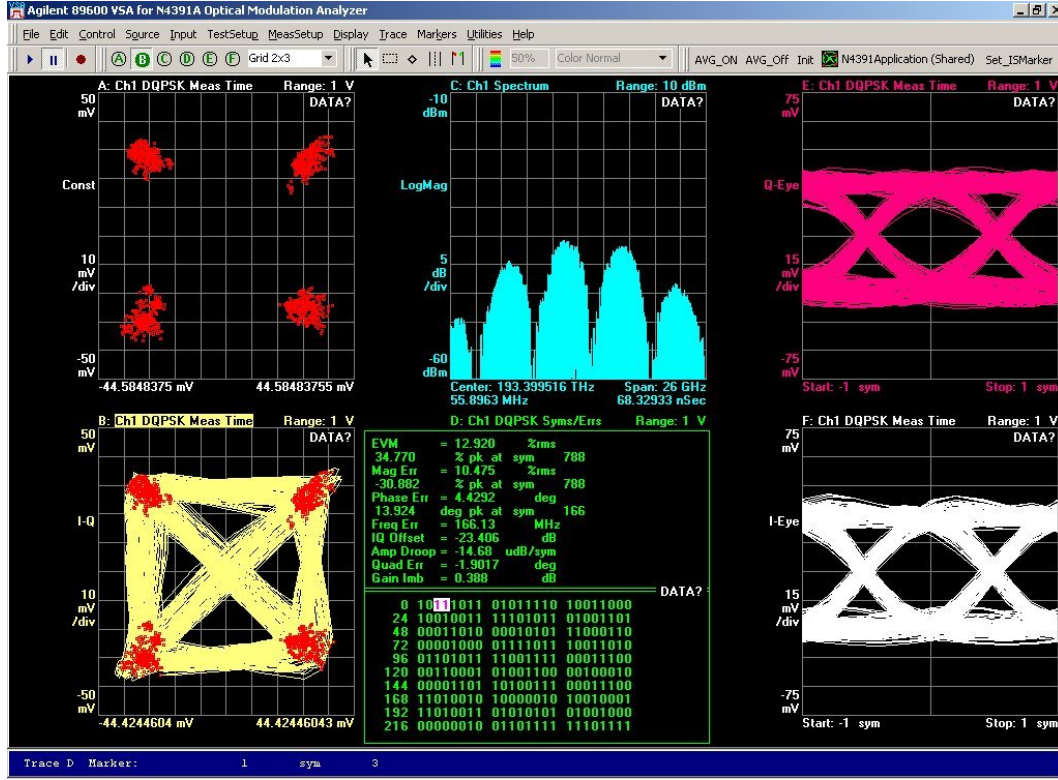
Fig. 5.15: QPSK modulation of the InP IQ modulator at 2x20 Gbit/s=40 Gbit/s using a PRBS 2^{31}-1 signal measured with an Agilent Optical Modulation Analyzer N4391A at 1550 nm. Left figures: E-field constellation diagram (bottom image with traces). Top center: optical spectrum. Bottom center: evaluated data. Right figures: I-data and Q-data phase eye diagrams. The cumulative error vector magnitude (EVM) is 12.9% RMS.

diagrams. The measured cumulative EVM is 12.9%, which is equivalent to an error-free data transmission at a data rate of 40 Gbit/s. The BER vs. EVM correlation has been given in Figure 4.9 and revealed a required EVM=17% for BER=10^{-9}.

In conclusion, QPSK modulated signal have been successfully generated with the dual-parallel IQ modulator invented in this work. The maximum tested bit rate was 80 Gbit/s and showed a clear open phase eye diagram for all phase states of the four QPSK symbols. Error-free quadrature-phase-shift-keyed modulation has been demonstrated at 40 Gbit/s and 1550 nm wavelength.

Chapter 6

Conclusion

In this thesis, a novel InP-based monolithically integrated IQ modulator (IQM) consisting of two parallel Mach-Zehnder modulators (MZM) has been developed and fabricated. This IQ modulator is intended for fiber-optic data transmission using the quadrature phase shift keying (QPSK) modulation format which transmits two bits per symbol (2x50 Gbit/s). QPSK offers a high spectral efficiency and is therefore a possible candidate for the next generation 100-Gbit/s Ethernet standard in WDM long haul transmission links. The functionality of the developed IQM has been successfully verified in a transmission experiment where, for the first time, 80 Gbit/s (2x40 Gbit/s) QPSK modulation of a packaged InP-based IQM was demonstrated. Several design optimizations including the reduction of the optical insertion loss (IL) and the drive voltage V_π of the standard single MZM were required to make this design a candidate for a successful low cost product for telecommunication companies. This goal has been achieved by addressing the following tasks.

An introduction to the structural properties of the Mach-Zehnder interferometer, which is the basis of the developed IQ modulator, has been given to gain a basic understanding of the operation principles of the MZM. The concept of the segmented capacitively loaded traveling-wave electrodes (TWE), that enable high-frequency operation, has been explained and the advantages of the single drive push-pull principle to operate the Mach-Zehnder modulator (MZM) has been pointed out. This was followed by an introduction to the physics of the fundamental electro-optic effects which enable the optical phase shift in the multi quantum well (MQW) core of the MZM's active optical waveguide.

After pointing out the fundamental operation principles of the MZM great emphasis was placed on developing optimization strategies for the three most important modulator parameters: optical insertion loss (IL), drive voltage (V_π) and modulation bandwidth (f_{3dB}). Three different waveguide geometries ('deep etch' DE, 'median etch' ME and 'shallow etch' SE) were

chosen and evaluated with respect to the aforementioned three characteristic MZM parameters. To minimize the optical insertion loss of the MZ modulator an on-chip optical spot size converter (SSC)has been successfully developed that includes n-doped contact layers. Highly efficient input and output coupling to tapered fibers have been experimentally demonstrated with a total coupling loss of only 0.7 dB (ME and SE waveguide) and 0.75 dB (DE waveguide) per SSC. As another possibility to reduce the optical insertion loss of the modulator variations of the p-i-n-junction's doping profile and vertical position changes of the MQW core inside the intrinsic region of the optical waveguide have been analyzed. The introduction of a so called 'light doping profile' with reduced p- and n-doping concentrations led to a reduction of the modulator's insertion loss by 5% to 10% (0.3 dB to 0.6 dB) depending on the intrinsic region thicknesses (IRT) (800 nm to 600 nm).

The necessity of a low drive voltage (V_π) originates from the fact that for QPSK modulation each single MZ modulator needs to be driven with 2 V_π and telecommunication companies intend not to use expensive high-power and high-bandwidth amplifiers. The reduction of V_π has been addressed by a modulation efficiency analysis of different designs of the multi quantum well (MQW) which is used as the electro-optic active core in the modulator waveguide. A high QW phase modulation efficiency with low absorption was found for wide quantum wells with low PL wavelength. As a further possibility to reduce the drive voltage of the MZM narrowing of the intrinsic region and a MQW core position shift inside the intrinsic region were analyzed for the three waveguide geometries DE, ME and SE. The DE waveguide geometry is the most efficient design. An analysis of the influence of different background doping concentrations (BDC) in the nominally undoped intrinsic region gave evidence that the absolute modulation efficiency decreases with increasing background doping and that his effect becomes less pronounced when the intrinsic region thickness (IRT) is decreased. In addition, it has been theoretically shown that the influence of the vertical MQW core position on the MZM's drive voltage is stronger for larger BDCs.

All design changes introduced to reduce the optical insertion loss and drive voltage of the MZ modulator also alter its high frequency response. Therefore, the influence of IRT, the fabrication process related p-contact sheet resistance and geometrical TWE variations on the high frequency modulation response of the MZM have been investigated. TWE design rules for impedance (50 Ω) and velocity matching that allow a 3-dB bandwidth of over 40 GHz are given.

Final conclusions drawn from the evaluation including trade-off calculations between optical insertion loss, drive voltage and 3-dB bandwidth revealed the following:

- The highest absolute modulation efficiency is obtained for waveguides with low background doping.

- The so called 'light doping profile' reduces the insertion loss of the modulator by up to 0.6 dB and has no negative impact on V_π and f_{3dB}.

- The amount of background doping in the intrinsic region of the optical waveguide largely influences the optimum position of the MQW. For low background doping ($1 \cdot 10^{15} cm^{-3}$) an MQW shifted 100 nm towards the bottom n-contact gives the best trade-off between absorption loss and drive voltage. For high background doping ($1 \cdot 10^{16} cm^{-3}$) a shift of 100 nm towards the top p-contact gives the best trade-off.

- The best trade-off between absorption loss and drive voltage for a variation of IRT and the number of QWs in the modulator's waveguide core is found for large IRTs and a high number of quantum wells.

- No configuration was found that optimizes optical insertion loss, drive voltage and 3-dB bandwidth of the MZ modulator at the same time. The best trade-off between optical loss and drive voltage for an electrical 40-GHz bandwidth modulator is obtained for TWE length=1.8 mm, IRT=700 nm and a FF=0.7 using the 'light doping profile'.

After the elaboration of promising MZM design changes that allow a reduction of IL and V_π while giving a 3-dB bandwidth >40 GHz the schematic of the dual-parallel IQ modulator has been introduced and the advantages of the applied QPSK modulation format have been discussed. A mathematical model of the single MZM and the dual-parallel IQM has been developed in order to evaluate the influence of optical phase and power imbalances between the MZ interferometer arms on the modulation performance. This model accounts for the linear and non-linear voltage dependence of the involved electro-optic effects. The excellent accuracy of this model has been verified by a fit to experimental data of a single MZ modulator. The mathematical model was extended with a flexible PRBS drive signal generator to model large signal modulation of the IQM. To reveal modulation impairments introduced by optical phase and power variations in the interferometers of the IQM the so called error vector magnitude (EVM) has been analyzed. It was shown theoretically that error-free operation of the IQM requires precise control of the optical phase and power in all four interferometer arms.

Finally, the relevant aspects of the modulator characterization metrology and the presentation of measurement results from various experiments has been given. The evaluation of experimentally derived DC modulation efficiencies of modulator wafers that were grown with three dif-

ferent nominal intrinsic region thicknesses (IRT) showed an excellent agreement to theoretical data derived in Chapter 3 and revealed the presence of a high background doping concentration of $1 \cdot 10^{16} cm^{-3}$ in the nominally undoped semiconductor layers. This result was supported by analysis results from wafers grown with identical IRT (800 nm) but with two different vertical position of the MQW core in the optical waveguide.

A simple but yet very effective characterization algorithm for the dual-parallel IQM's phase electrodes has been developed. It allows to easily derive the correct settings of the IQM's six phase electrodes for QPSK large signal operation from simple DC photocurrent measurements. A software implementation of the algorithm successfully prove the practicability of this algorithm in an experiment.

The excellent high bandwidth capabilities of the developed MZMs and IQMs, which is the prerequisite for the intended 2x50 Gbit/s=100 Gbit/s QPSK operation, was verified by small signal RF testing. The single MZMs characterization resulted in electro-optical 3-dB bandwidths of 63 GHz, 57 GHz and 45 GHz for three devices having a traveling-wave electrode (TWE) length of 2 mm, 3 mm and 4 mm, respectively. The on-chip RF measurements for an IQ modulator with 4 mm TWE length resulted in f_{3dB}=26.4 GHz for the I-data and f_{3dB}=25.7 GHz for the Q-data MZM. The relatively low 3-dB bandwidth originated from a design that was intended for a very low drive voltage V_π of 2 V at 5 V bias voltage.

Finally, large signal RF testing has been conducted on various packaged modulator devices to prove error-free operation in a transmission-system-like environment. NRZ-OOK testing at 40 Gbit/s of single MZ modulators showed excellent signal-to-noise (> 17 dB) and dynamic extinction (> 13 dB) ratios for wavelength from 1535 nm to 1565 nm. Transmission experiments at 40 Gbit/s over up to 320 km dispersion compensated fiber at 1550 nm showed error-free data transmission and back-to-back experiments at 80 Gbit/s NRZ-OOK and 1550 nm wavelength showed a clear eye opening which indicates error-free performance.

Unfortunately, no test equipment to generate a 2x50 Gbit/s=100 Gbit/s drive signals was available at the time of testing but QPSK modulation of a packaged dual-parallel IQ modulator has been successfully shown at 2x20 Gbit/s=40 Gbit/s and 2x40 Gbit/s=80 Gbit/s using two broadband amplifiers for the I-data and Q-data MZM with a drive voltage as low as V_{pp}=3.5 V. At 40 Gbit/s QPSK demodulation showed an excellent error vector magnitude below 13% which is considered to be error-free. Quadrature-phase-shift-keyed modulation at 80 Gbit/s has been successfully shown for the first time for a packaged InP-based IQ modulator by measuring the complex constellation diagram with four clear distinguishable symbol points in the complex plane.

6.1 Outlook

Several theoretical MZM design optimizations have been derived in this thesis that could be evaluated in future modulator devices.

The utilization of the 'light doping' profile (cf. Section 3.2.2) promise a 10% (0.6 dB for a single MZM device) reduction of the total insertion loss due to reduced absorption losses in the p- and n-doped layers. No impact on the switching voltage V_π is expected and the reduction of the 3-dB bandwidth is expected to be in the order of only 2 GHz.

A further reduction of the IQM's (10 mm chip length) optical insertion loss by $\approx$1 dB can be achieved by utilizing the 'median etch' waveguide geometry instead of the 'deep etch' type due to lower scattering losses at rough waveguide sidewalls. The impact on V_π is found to be negligible (<3%) for intrinsic region thicknesses below 900 nm and the slight variation of the capacitive load can be easily compensated by changing the dimensions of the traveling-wave electrode.

The experimentally verified reduction of the modulation efficiency of the MZM due to a down-shift of the MQW waveguide core within the intrinsic region was related to a high background doping concentration in the nominally undoped waveguide region. If a high background doping concentration is present, then shifting the MQW core towards the p-contact by only 50 nm promise a reduction of the required drive voltage by 15%. The increase of the total insertion loss is expected to be 0.2 dB for a standard MZM and negligible for the IQM due to the longer passive waveguide.

Current discussions on the next generation 100-Gbit/s Ethernet standard include the utilization of dual-polarization quadrature phase shift keying (DP-QPSK - 4x25 Gbit/s=100 Gbit/s) for DWDM networks due to it's reduced requirement for spectral width. The single drive push-pull drive concept of the IQM developed in this thesis facilitates the design of a monolithically integrated Dual-IQ modulator that is suitable for DP-QPSK modulation. A clear advantage from the RF testing and module packaging perspective is seen because only four RF inputs are required for such a dual-IQ modulator. One of the two monolithically integrated IQMs would modulate the standard TE polarization while the modulated light from the other IQM would be launched on the transmission fiber after polarization rotation to the orthogonal TM state. The InP/InGaAsP material system is clearly favorable for this high-level monolithic integration of several subcomponents in one chip as it keeps the footprint of the chip small compared to other material systems like lithium niobate or polymers.

Appendices

Appendix A

Mach-Zehnder modulator design variables

The functionality of the InP-based Mach-Zehnder modulator (MZM) described in this thesis depends on numerous design variables. The three characteristic MZM parameters drive voltage V_π, insertion loss (IL) and 3-dB bandwidth f_{3dB} have to meet certain values in order to deliver a successful product to the telecommunication market. The MZM design variables that allow a variation of V_π, IL and f_{3dB} are listed in the following tables. The first column gives the name of the variable, the second column lists the parameter of the MZ modulator that is influenced by changing the respective design variable. The third column gives the characteristic MZ parameter that is effected by the design variable.

The design variables can be separated into two groups. The first group comprises all geometrical design variables that alters the three dimensional layout of the MZ modulator (listed in blue color). The second group include variables that influence the physical properties of the semiconductor material or vary the two dimensional cross section of the optical waveguide

variable	influence on	global impact
TWE contact space	impedance	f_{3dB}
TWE support material	impedance, microwave index	f_{3dB}
TWE cover material	impedance, microwave index	f_{3dB}
TWE material thickness	ohmic loss	f_{3dB}
MZI waveguide separation	stray capacitance	f_{3dB}
active mesa width	stray capacitance	f_{3dB}
active WG electrode width	stray capacitance	f_{3dB}
number of air bridges	inductance, velocity matching, ohmic loss	f_{3dB}
width of air bridges	inductance, ohmic loss	f_{3dB}
air bridge position	velocity matching	f_{3dB}
confinement layer material	EO efficiency, absorption, n_{gr}	V_π, IL

Tab. A.1: Structural MZM design variables which are not analyzed in this thesis and for whom no explicit values are given due to non-disclosure agreement restrictions.

variable	influence on	global impact
TWE width	impedance, microwave index, ohmic loss	f_{3dB}
TWE gap	impedance, microwave index	f_{3dB}
TWE length	ohmic loss	f_{3dB}
period length	Bragg frequency	f_{3dB}
active length	fill factor, capacitive load	V_π, f_{3dB}
WG width	EO efficiency, scattering loss, capacitive load	V_π, f_{3dB}, IL
WG etch depth	EO efficiency, scattering loss, capacitive load	V_π, f_{3dB}, IL
MQW well thickness	EO efficiency, absorption, IRT, n_{gr}	V_π, IL
MQW well material	EO efficiency, absorption, n_{gr}	V_π, IL
MQW barrier thickness	EO efficiency, absorption, IRT, n_{gr}	V_π, IL
MQW barrier material	EO efficiency, absorption, n_{gr}	V_π, IL
MQW number	EO efficiency, absorption, IRT, n_{gr}	V_π, f_{3dB}, IL
p-contact sheet resistance	RC time constant	f_{3dB}
p-doping concentration	IRT, EO efficiency, absorption	V_π, f_{3dB}, IL
n-doping concentration	IRT, EO efficiency, absorption	V_π, f_{3dB}, IL
MQW vertical position	EO efficiency, absorption	V_π, IL
background doping	EO efficiency	V_π
sidewall roughness	scattering loss	IL

Tab. A.2: First row: structural MZM design variables which are analyzed in this thesis. Second row: MZM parameter influenced by the design variable. Third row: global characteristic MZM parameters (3-dB bandwidth f_{3dB}, switching voltage V_π, insertion loss IL) that are related to the design variable. Blue: geometrical/structural 3D design variables. Green: variables that influence the physical properties or the cross section of the optical waveguide

(listed in green color).

Table A.1 lists the design variables of both groups that are not analyzed in this thesis or whose explicit values are not given due to non disclosure agreement (NDA) restrictions. The variables which are not analyzed or given are primarily variables that has an impact on the high frequency modulation bandwidth performance of the MZ modulator. The MZM design variables that are analyzed in this thesis are listed in Table A.2. All variables listed in blue color belong to the first group that change the geometrical layout of the MZM. The variables listed in green color belong to the second group. In addition to these structural design variables several characteristic parameters exist that are derived from the design variables listed in Tables A.1 and A.2. These characteristic parameters are commonly used in the discussion of semiconductor-based Mach-Zehnder modulators featuring a capacitively loaded traveling-wave electrode (TWE). Table A.3 gives an overview of the MZM parameters that are discussed in this thesis.

parameter	influence on	global impact
ohmic loss	microwave attenuation	f_{3dB}
fill factor	capacitive load	V_π, f_{3dB}
Bragg frequency	RF response	f_{3dB}
microwave index	velocity matching	f_{3dB}
impedance	RF response	f_{3dB}
capacitive load	RC time constant	f_{3dB}
WG optical group index n_{gr}	velocity matching	f_{3dB}
MQW EO efficiency	EO efficiency	V_π, IL
mode overlap with n-material	absorption	IL
mode overlap with p-material	absorption	IL
intrinsic region thickness IRT	capacitive load, E-field	V_π, f_{3dB}, IL
optical confinement factor	EO efficiency	V_π
PL wavelength	EO efficiency, absorption	V_π, IL

Tab. A.3: Characteristic parameters that influence the Mach-Zehnder modulator performance derived from the structural MZM design variables listed in Table A.1 and Table A.2.

B | Appendix

Optical material parameters used in simulations

B.1 Adachi's refractive index model for InP and InGaAsP

To accurately model the InP-based modulator waveguide it is important to have reliable data of the refractive indices of the involved materials. The refractive indices of InP [101] and InGaAsP [102] are well known from experimental data. Adachi [103] has developed a theoretical model to calculate the refractive index of $In_{1-x}Ga_xAs_yP_{1-y}$ alloys with respect to the material composition parameters x and y. As a special case the model includes the refractive index of InP for $x = 0$ and $y = 0$. The following discussion is simplified for $In_{1-x}Ga_xAs_yP_{1-y}$ grown lattice matched to InP. In this case the material composition parameters x and y are related by:

$$x = \frac{0.4541}{1 - 0.029\,y} \tag{B.1}$$

which is commonly simplified to $x = 0.47y$. The refractive index model of Adachi requires the knowledge of the direct bandgap energy at the Γ-point which is given by [104]

$$E_g = 1.35 - 0.72\,y + 0.12\,y^2 \quad [eV]. \tag{B.2}$$

for T=300 K. The refractive index from Adachi's [103] model is then given by

$$n_r = \sqrt{A(y)\left[f(z) + \frac{1}{2}\left(\frac{E_g}{E_g + \Delta_0}\right)^{3/2} f(z_0)\right] + B(y)} \tag{B.3}$$

with

$$
\begin{aligned}
&f(z) = (2 - \sqrt{1+z} - \sqrt{1-z})/z^2 \\
&z = E/E_g \\
&z_0 = E/E_g + \Delta_0 \\
&A(y) = 8.616 - 3.886y \\
&B(y) = 6.621 + 3.461y \\
&\Delta_0 = 0.118 + 0.225y
\end{aligned} \tag{B.4}
$$
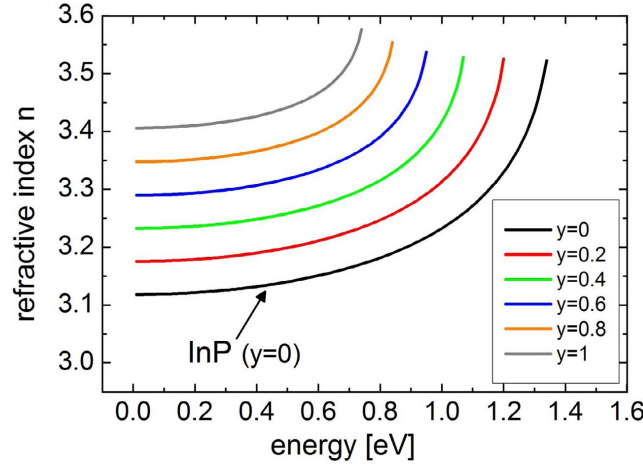
Fig. B.1: Composition dependent refractive index of InGaAsP over energy calculated with Equation (B.3). InP is depicted as special case with $y = 0$.

where A(y) and B(y) are fitting parameters used to match experimental data from [102]. Δ_0 is the split-off valence band gap at room temperature. Figure B.1 shows the refractive indices of $In_{1-x}Ga_xAs_yP_{1-y}$ lattice matched to InP for material composition parameters from $y = 0$ to $y = 1$. InP is shown as the special case with $y = 0$. The indices were calculated using Equation (B.3). Table B.1 lists refractive indices of InP and InGaAsP for five different wavelengths within the C-band for InP and for InGaAsP using four different material compositions parameters y.

	1530 nm	1540 nm	1550 nm	1560 nm	1570 nm
InP	3.1836	3.1826	3.1815	3.1806	3.1796
InGaAsP Q1.06 y=0.263	3.2706	3.2692	3.2679	3.2667	3.2654
InGaAsP Q1.10 y=0.331	3.2933	3.2919	3.2904	3.2891	3.2877
InGaAsP Q1.15 y=0.406	3.3206	3.3189	3.3174	3.3158	3.3143
InGaAsP Q1.42 y=0.76	3.4739	3.4694	3.4652	3.4613	3.4577

Tab. B.1: Refractive indices of InP and InGaAsP for 5 wavelengths (1530 nm to 1570 nm) used in optical simulations. The values were calculated using Equations (B.2) and (B.3).

B.2 Carrier induced refractive index change in n-doped InP and InGaAsP

The refractive index change induced by free carriers due to n-type or p-type doping has been introduced in Section 2.6.2. Table B.2 lists the index change calculated for the plasma effect (Equation (2.46)), the band filling effect (Kramers-Kronig transform (KKT) of Equation (2.47)) and the bandgap shrinkage effect (KKT of Equation (2.53)). The sum of all three effects for different n-doping levels at $\lambda = 1550$ nm is also given. The p-doping level is kept constant at

$1 \cdot 10^{16} cm^{-3}$. The referenced equations and their Kramers-Kronig transform were implemented with *Mathematica*. This data is of special importance for the simulations of the integrated optical spot size converter in Section 3.2.1. Without these corrective values the optimization of the spot size converter delivers wrong results which lowers the mode conversion efficiency.

B.3 Carrier induced absorption change in n- and p-doped InP and InGaAsP

The carrier induced absorption change due to n-type or p-type doping has been introduced in Section 2.6.2. The importance of the implementation of absorption variation due to n-type doping InP and InGaAsP is demonstrated in the simulations of the integrated optical spot size converter in Section 3.2.1. The additional absorption of a waveguide mode due to overlap with n- or p-doped material is evaluated in Section 3.2.2 where various doping profiles have been studied to minimize the overall insertion loss. Measurements of the optical absorption coefficient in p-type InP by Casey et al. [51] for various doping concentrations revealed a linear dependence between the absorption coefficient and the hole concentration at 1.5 μm wavelength. It is given by

$$\alpha = 20(P_{\text{holes}} \cdot 10^{-18}) \qquad [1/cm]. \tag{B.5}$$

where P_{holes} is the doping induced acceptor concentration in [1/cm^3]. Figure B.2a shows experimental data for p-type InP from Casey et al. [51] (blue circles) and Ballman et al. [105] (green square). The black linear fit matches excellently with Equation (B.5). Similar experiments for n-type InP have been performed by Ballman et al. [105] and Bugajski et al. [106]. Figure B.2b shows the experimental data taken from Ballman et al. [105] (red squares). The linear fit gives

$$\alpha = 20/10.58(N \cdot 10^{-18}) \qquad [1/cm]. \tag{B.6}$$

with N being the donor concentration in [1/cm^3]. It is noteworthy that p-doping causes an absorption increase which is approximately 10 times higher compared to n-doping. Table B.3 lists absorption coefficients of p- and n-type InP for different doping concentrations calculated with Equations (B.5) and (B.6). An relevant material in mode loss modeling is the ternary $In_{1-x}Ga_xAs$. It is the first semiconductor layer below the Ti-Pt-Au-metallization below the gold electrodes and allows high p-doping concentrations of $1 \cdot 10^{19} cm^{-3}$ to form a good ohmic contact. The importance of including the InGaAs layer into loss modeling comes from the fact that its band gap energy is below the operating wavelengths in the C-band so the absorption coefficient is very high. Although the optical mode confinement inside the InGaAs layer is
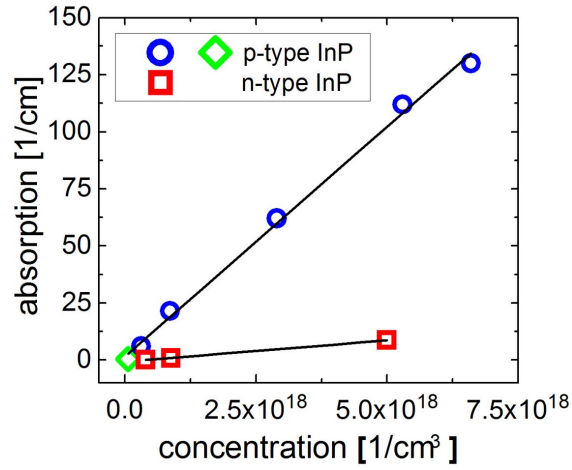
Fig. B.2: Experimental doping concentration dependent absorption of p- and n-type InP. The values printed as blue and green circles for p-doped InP are from references [51] and [105] respectively. Red squares represent data for n-doped InP from reference [105]

only a fraction of a percent depending on the distance to the waveguide core, the absorption of InGaAs is an important factor in the overall mode loss. The value for the optical absorption coefficient is taken from Backer et al. [107] and listed in Table B.3 for a band gap wavelength of 1.6 μm.

λ = 1550 nm	doping [cm^{-3}]	plasma	band filling	band gap shrink.	TOTAL
InGaAsP Q1.42 y=0.760	$3 \cdot 10^{18}$	-0.01900	-0.00469	0.00246	**-0.02123**
InGaAsP Q1.42 y=0.760	$2 \cdot 10^{18}$	-0.01300	-0.00353	0.00211	**-0.01442**
InGaAsP Q1.42 y=0.760	$1 \cdot 10^{18}$	-0.00634	-0.00203	0.00160	**-0.00677**
InGaAsP Q1.42 y=0.760	$5 \cdot 10^{17}$	-0.00317	-0.00110	0.00120	**-0.00307**
InGaAsP Q1.15 y=0.406	$3 \cdot 10^{18}$	-0.01500	-0.00368	0.00180	**-0.01688**
InGaAsP Q1.15 y=0.406	$2 \cdot 10^{18}$	-0.00990	-0.00270	0.00155	**-0.01105**
InGaAsP Q1.15 y=0.406	$1 \cdot 10^{18}$	-0.00495	-0.00150	0.00110	**-0.00535**
InGaAsP Q1.15 y=0.406	$5 \cdot 10^{17}$	-0.00247	-0.00080	0.00076	**-0.00251**
InGaAsP Q1.10 y=0.331	$3 \cdot 10^{18}$	-0.01400	-0.00350	0.00174	**-0.01576**
InGaAsP Q1.10 y=0.331	$2 \cdot 10^{18}$	-0.00946	-0.00256	0.00145	**-0.01057**
InGaAsP Q1.10 y=0.331	$1 \cdot 10^{18}$	-0.00473	-0.00142	0.00100	**-0.00515**
InGaAsP Q1.10 y=0.331	$5 \cdot 10^{17}$	-0.00237	-0.00075	0.00069	**-0.00243**
InGaAsP Q1.06 y=0.263	$3 \cdot 10^{18}$	-0.01400	-0.00337	0.00165	**-0.01572**
InGaAsP Q1.06 y=0.263	$2 \cdot 10^{18}$	-0.00910	-0.00245	0.00138	**-0.01017**
InGaAsP Q1.06 y=0.263	$1 \cdot 10^{18}$	-0.00455	-0.00135	0.00097	**-0.00493**
InGaAsP Q1.06 y=0.263	$5 \cdot 10^{17}$	-0.00227	-0.00071	0.00063	**-0.00235**
InP	$3 \cdot 10^{18}$	-0.01200	-0.00288	0.00135	**-0.01353**
InP	$2 \cdot 10^{18}$	-0.00793	-0.00207	0.00110	**-0.00890**
InP	$1 \cdot 10^{18}$	-0.00396	-0.00112	0.00074	**-0.00434**
InP	$5 \cdot 10^{17}$	-0.00198	-0.00059	0.00043	**-0.00214**

Tab. B.2: Carrier induced refractive index change in InP and InGaAsP for different N-doping levels. The P-doping level is kept constant at $1 \cdot 10^{16} cm^{-3}$. The index change was calculated with *Mathematica* using the formulas for the three carrier effects introduced in Section 2.6.2.

	doping [cm^{-3}]	alpha	dB/cm		doping [cm^{-3}]	alpha	dB/cm
p-InP	$5 \cdot 10^{17}$	10	-43.6	n-InP	$5 \cdot 10^{17}$	0.94	-4.1
p-InP	$1 \cdot 10^{18}$	20	-87.3	n-InP	$1 \cdot 10^{18}$	1.89	-8.2
p-InP	$1.5 \cdot 10^{18}$	30	-130.9	n-InP	$1.5 \cdot 10^{18}$	2.83	-12.3
p-InP	$2 \cdot 10^{18}$	40	-174.5	n-InP	$2 \cdot 10^{18}$	3.77	-16.4
p-InP	$5 \cdot 10^{18}$	100	-436.3	n-InP	$5 \cdot 10^{18}$	9.43	-41.0
InGaAs	T1.6 μm	7000	-30400				
i-InP	$< 5 \cdot 10^{15}$	0.14	-0.61				
i-InGaAsP	$< 5 \cdot 10^{15}$	0.2	-0.87				

Tab. B.3: Absorption coefficients and loss of n- and p-type InP for different doping concentrations [105, 106] and undoped InGaAs [107]. The same values are adopted for quaternary InGaAsP due to the lack of experimental data. The values for intrinsic i-InP and i-InGaAsP are from reference [27].

Appendix C

Evaluation software

C.1 Electro-optic overlap calculator

The electro-optic overlap calculator is used to determine the modulation efficiency of different waveguide geometries by calculating the overlap integral of the electric and the optical field in a waveguide. It is used to calculate the influence of background doping and the optical waveguide geometry on the modulation efficiency. The program was written in Visual Basic 6. The graphical user interface is shown in Figure C.1. The first step is to load the calculated
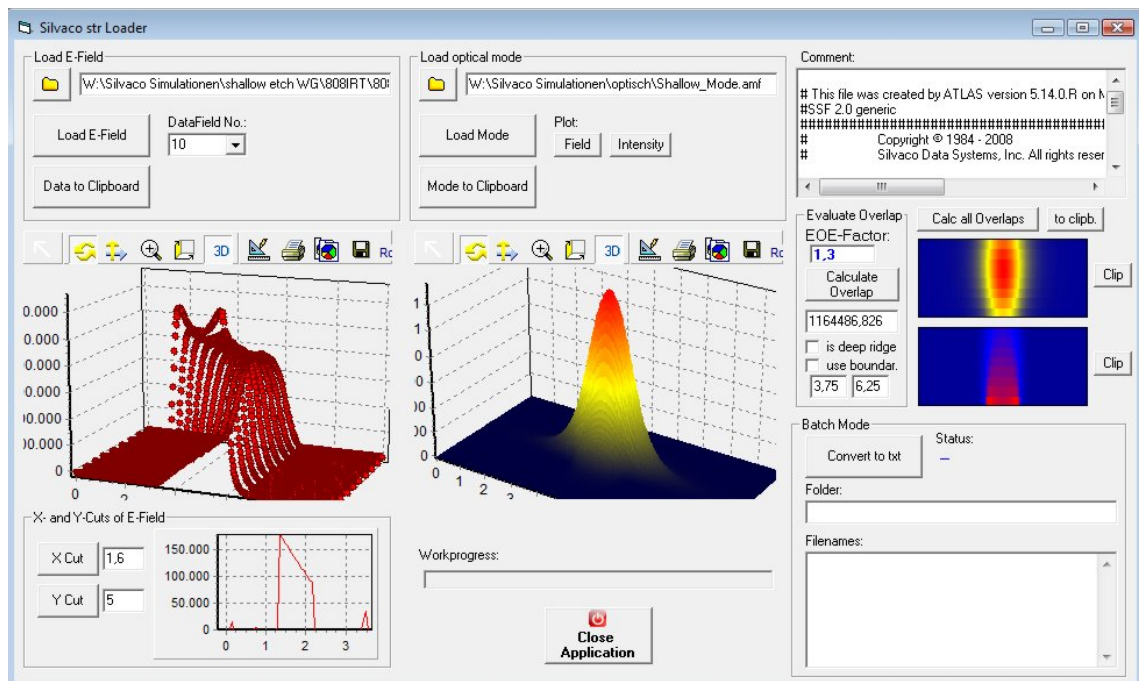
Fig. C.1: Graphical user interface of the electro-optic overlap calculator. The program loads electric field data from Silvaco *ATLAS* structure files and optical mode data from *FIMMWAVE* ASCII files. The mode data is linearly interpolated to the grid points from the electric field data.

electric field distribution data from Silvaco *ATLAS* structure files. The data is displayed to provide a visual feedback to the user. The next step is to load the optical mode profile of the waveguide geometry which is obtained from the simulations with *FIMMWAVE*. After loading the mode profile it is normalized to give a total mode power of one which is required for later calculation of the electro-optic overlap (cf. Equation (3.6)). In order to be able to calculate the overlap integral the optical mode data have to be linearly interpolated to the same x-y-grid used for the electric field data. The electric field is calculated using a grid size of 31.25-nm. The following step is to extract the electric field and mode data just from the electro-optic (eo) active core which is the multi quantum well region. After this data extraction the eo-core data is again displayed to provide visual feedback to the user before the eo overlap is computed and displayed. The software allows to set the electro-optic efficiency (EOE) factor (cf. Equation (3.6)) to account for nonlinear effects (QCSE) in the structure. The program features two batch modes. The first one allows to extract different quantities (e.g. electric field, doping concentration, potential etc.) from Silvaco *ATLAS* structure files. The second batch mode allows to calculate the eo-overlap from multiple electric field data files with the respective mode profile.

C.2 SimuLase data extractor

The output data from the commercial software package *SimuLase* (NLCSTR Inc.) is stored in so called gain databases which consist of a collection of standardized ASCII files. Separate output files are generated for each individual set of input parameters for the following quantities: conduction band energies, valence band energies, electron wavefunctions, hole wavefunctions, energy levels, absorption spectrum (TE and TM polarization), refractive index spectrum (TE and TM polarization), photoluminescence spectrum (TE and TM polarization). The simulations in Section 3.3.1 are performed for 7 different applied fields, 7 different broadening factors at only one carrier density. 8 different quantum well widths (7 nm - 14 nm) were evaluated for eleven material composition parameters y (0.7 to 0.9 with step 0.2) giving a total of 4312 simulations. To evaluate this large amount of data generated the 'data extractor' directly exports and evaluates the data from the gain databases to Microsoft Excel. The software was programmed in Visual Basic 6. The graphical user interface is shown in Figure C.2. The software features an advanced batch mode to evaluate multiple electric fields, carrier densities, broadening factors and alloy composition parameters in a single run. Selections can be made for the data that should be evaluated and exported.
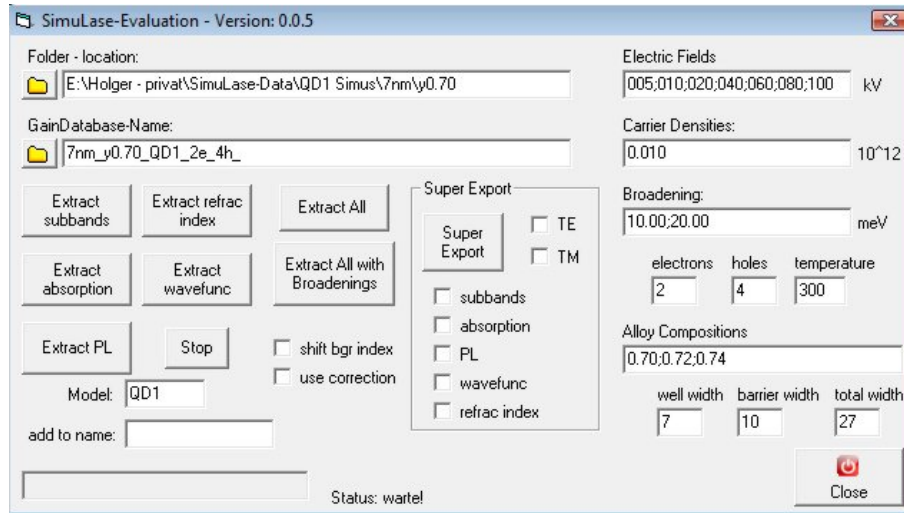
Fig. C.2: Graphical user interface of the *SimuLase Data extractor*. The tool loads the gain databases generated by *SimuLase* and evaluates and exports the data directly into Excel files.

C.3 DC matrix simulation and evaluation tool

The DC matrix simulation tool is a graphical user interface that allows to manipulate the 11 input parameters of the mathematical InP-based Mach-Zehnder modulator model developed in Section 4.3 and to calculate and display the resulting DC matrix and the respective cuts shown in Figure 4.5. The software was programmed in Visual Basic 6 and features a direct connection the SQL server database where all MZ modulator measurement data is stored. Experimental data can be loaded and displayed for direct comparison with the simulated DC intensity matrix. The mathematical functionality is provided by a compiled *MATLAB* COM-object which delivers the computed result in less than two seconds back to the main program. Seven cuts from the measured and simulated matrix are plotted on the bottom for better comparison and adaption of the fit. For each simulation run, the DC-matrix tool calculates and displays a difference matrix. It gives a quantitative and visual feedback on the quality of the fit parameters. A difference value of less than 7% means an adequate value set was found.
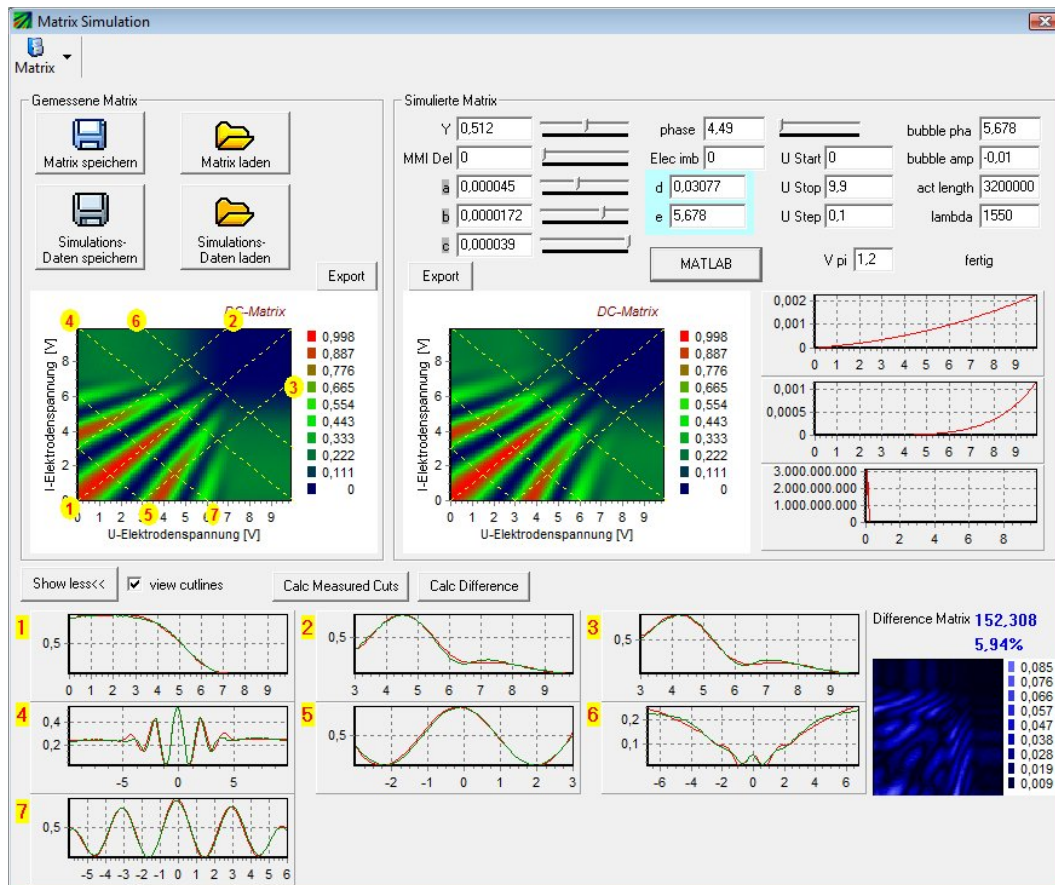
Fig. C.3: Graphical user interface of the DC matrix simulation tool. The program loads a measured DC matrix and allows to fit a simulated DC matrix by changing input parameters to the mathematical model. The seven cuts on the bottom allow visual control to find the best fitting parameters.

Acknowledgements

I am very grateful to Prof. Dieter Bimberg for giving me the opportunity to realize this thesis under his advise. He always found the best combination of keeping up a gentle pressure to ensure the progress of my thesis and being patient in times when other work was more important. I would also like to express my gratitude to Prof. Dieter Jäger for accepting the task of refereeing my thesis and to Prof. Eckehard Schöll for chairing the examination board.

The research for this thesis has been conducted while I was working at the Fraunhofer Institute for Telecommunications, Heinrich Hertz Institute (HHI) in Berlin. I am grateful to each and every one at HHI who supported me in doing the research for this thesis. First of all I'd like to thank the members of the modulator group. The past years have been interesting, informative, inquisitive, intense, incredible, indulgent, infinite, informal, ingenious, intelligible, intricate and much more. Thanks to the fab team for finally providing working IQM samples, the packaging group for the working module and the test equipment together with the people who helped me making the successful measurements. I would like to address special thanks to Herbert Venghaus und Ronald Kaiser for their thorough and critical proofreading of the manuscript of this thesis and giving valuable feedback. The readability has been greatly improved by your support.

I would like to thank Assoc. Prof. Jörg Hader for providing a fully functional demo version of *SimuLase*.

Last not least I have to say that I am deeply indebted to all my friends and my family. Without their support and patience in the past years the realization of this thesis would not have been possible.

Thanks to Rose DeWolf and Arthur Freemann, Paul Watzlawick, Manfred Spitzer, Fritz B. Simon and many more for unveiling the secrets of the human psyche.

List of Abbreviations

ASE . . . . Amplified spontaneous emission

BDC . . . . Background doping concentration

BER . . . . Bit error rate

BPM . . . . Beam propagation method

C-band . . . . Conventional band: 1528 nm to 1567 nm

CAD . . . . Computer aided design

DBPSK . . . . Differential binary phase shift keying

DC . . . . Direct current

DCF . . . . Dispersion-compensated fiber

DE . . . . Deep etch

DML . . . . Directly modulated laser

DP-QPSK . . . . dual-polarization quadrature phase shift keying

DPSK . . . . Differential phase shift keying

DQPSK . . . . Differential quadrature phase shift keying

DUT . . . . Device under test

DWDM . . . . Dense wavelength division multiplexing

ECL . . . . External Cavity Laser

EDFA . . . . Erbium-doped fibre amplifier

ER . . . . Extinction ratio

ESAG . . . . Enhanced selective area growth

ESD . . . . Electrostatic discharge

EVM . . . . Error vector magnitude

FEC . . . . Forward error correction

FF . . . . Filling factor

FKE . . . . Franz-Keldysh effect

FMM	Film mode matching
FOM	Figure of merit
FWHM	Full width at half maximum
GaAs	Gallium arsenide
GL	Guiding layer
GSG	Ground signal ground
InGaAlAs	Indium gallium aluminum arsenide
InGaAs	Indium gallium arsenide
InGaAsP	Indium gallium arsenide phosphide
InP	Indium phosphide
IQ	In-phase-Quadrature
IQM	In-phase-Quadrature modulator
IRT	Intrinsic region thickness
KKR	Kramers-Kronig relation
KKT	Kramers-Kronig transform
LCA	Lightwave component analyzer
LEO	Linear electro-optic effect
$LiNbO_3$	Lithium niobate
MCP	Material composition parameter
ME	Median etch
MER	Modulation error rate
MFD	Mode field diameter
MMI	Multimode interference coupler
MOCVD	Metall-organic chemical vapor deposition
MQW	Multi quantum well
MZM	Mach-Zehnder modulator
NDA	Non disclosure agreement
NRZ	Non return to zero
OCSA	Optical complex spectrum analyzer
OMA	Optical modulation analyzer
OOK	On off keying
PL	Photoluminescence
POI	Power overlap integral
PRBS	Pseudo-random bit sequence

PSK .... Phase shift keying

PSR .... P-contact sheet resistance

QAM .... Quadrature amplitude modulation

QCSE .... Quantum-Confined Stark effect

QEO .... Quadratic electro-optic effect

QPSK .... Quadrature phase shift keying

RF .... Radio frequency

RMS .... Root mean square

RZ .... Return to zero

SE .... Shallow etch

SMF .... Single-mode fiber

SMU .... Source measure unit

SNR .... Signal-to-noise ratio

TE .... Transverse electric

TEC .... Thermoelectric cooler

TM .... Transverse magnetic

VOA .... Variable optical attenuator

WDM .... Wavelength division multiplexing

WG .... Waveguide

WSE .... Wannier-Stark Effect

List of Symbols

α .... Absorption coefficient

c .... Vacuum velocity of light

C_L .... Loaded transmission line sheet capacitance

C_μ .... Unloaded transmission line sheet capacitance

χ .... Optical susceptibility

χ_b .... Background susceptibility

D .... Displacement vector

E .... Electric field

E_c .... Conduction band energy

E_g .... Bandgap energy

E_v .... Valence band energy

E_X .... Exciton binding energy

ϵ_0 .... Vacuum permittivity

ϵ_b .... Background dielectric constant

ϵ_{ij} .... Complex permittivity tensor

ϵ_r .... Dielectric constant

ϵ_{st} .... Static dielectric constant

f_{3dB} .... 3-dB frequency

f_{Bragg} .... Bragg frequency

G_{TWE} .... Electrode gap size

γ .... Harmonic oscillator damping factor

$\hbar$ .... Reduced Planck constant

k_B .... Boltzmann constant

K_{crit} .... Critical carrier density

K_{ijkl} .... Kerr coefficients

κ .... Extinction coefficient

L .... Active length

L_0 .... Loaded transmission line sheet inductance

L_μ .... Unloaded transmission line sheet inductance

λ .... Wavelength

$\bar{n}$ .... Complex refractive index

m_0 .... Free electron mass

M_b .... Momentum matrix element of a bulk semiconductor

m_e .... Electron mass

m_{hh} .... Heavy hole mass

m_{lh} .... Light hole mass

m_r .... Reduced mass

N .... Electron concentration

n_b .... Background refractive index

n_{gr} .... Optical group refractive index

n_{opt} .... Optical refractive index

n_μ .... Microwave refractive index

P .... Period length

P_{den} .... Polarization density

P_b .... Background polarization

P_{holes} .... Hole concentration

q .... Unit charge

$r_{ij,k}$ .... Pockels coefficients

R_y .... Exciton Rydberg energy

t .... Time

T .... Temperature

V .... Voltage

V_{bias} .... Bias voltage

V_π .... Half wave drive voltage

V_{pp} .... Peak-to-peak voltage

ω .... Angular frequency

W_{QW} .... Quantum well width

W_{TWE} .... Electrode width

Z_0 .... Loaded transmission line impedance

Z_μ .... Unloaded transmission line impedance

List of Publications

Parts of this thesis have been published:

H. N. Klein, H. Chen, D. Hoffmann, S. Staroske, A. G. Steffan and K.-O. Velthaus. *1.55 μm Mach-Zehnder Modulators on InP for Optical 40/80 Gbit/s Transmission Networks.* Proc. International Conference on Indium Phosphide and Related Materials, pages 171–173, 2006.

H. Chen, H. N. Klein, D. Hoffmann, K.-O. Velthaus, H. Venghaus. *Improvement Strategy towards 80 Gbit/s Low Drive Voltage InP based Mach-Zehnder Modulator.* Digest of the 4th Joint Symposium on Opto- and Microelectronic Devices and Circuits (SODC '06), Duisburg 2006.

Bibliography

[1] P. J. Winzer and R.-J. Essiambre. *Advanced Modulation Formats for High-Capacity Optical Transport Networks*. J. Lightw. Technol., 24(12):4711–4728, 2006.

[2] H. N. Klein, H. Chen, D. Hoffmann, S. Staroske, A. G. Steffan, and K.-O. Velthaus. *1.55µm Mach-Zehnder Modulators on InP for Optical 40/80 Gbit/s Transmission Networks*. In *Proc. International Conference on Indium Phosphide and Related Materials*, pages 171–173, 2006.

[3] K. Tsuzuki, T. Ishibashi, T. Ito, S. Oku, Y. Shibata, R. Iga, Y. Kondo, and Y. Tohmori. *40 Gbit/s n-i-n InP Mach-Zehnder modulator with a π voltage of 2.2 V*. Electron. Lett., 39(20):1464–1466, October 2003.

[4] L. Zehnder. *Ein neuer Interferenzrefraktor*. Zeitschrift für Instrumentenkunde, 11:275–285, 1891.

[5] L. Mach. *Über einen Interferenzrefraktor*. Zeitschrift für Instrumentenkunde, 12:89–93, 1892.

[6] B. E. A. Saleh and M. C. Teich. *Fundamentals of Photonics*. Wiley & Sons, 2007.

[7] R. G. Walker. *High-speed III-V semiconductor intensity modulators*. IEEE J. Quantum Electron., 27(3):654–667, March 1991.

[8] G. L. Li, T. G. B. Mason, and P. K. L. Yu. *Analysis of segmented traveling-wave optical modulators*. J. Lightw. Technol., 22(7):1789–1796, July 2004.

[9] D. M. Pozar. *Microwave Engineering*. John Wiley & Sons, 2005.

[10] V. K. Varadan, K. J. Vinoy, and K. A. Jose. *RF MEMS and Their Applications*. John Wiley & Sons, 2003.

[11] R. G. Walker. *Broadband (6 GHz) GaAs/AlGaAs electro-optic modulator with low drive power*. Appl. Phys. Lett., 54(17):1613–1615, 1989.

[12] J. Piprek. *Semiconductor Optoelectronic Devices*. Academic Press, 2003.

[13] V. Lucarini, J. J. Saarinen, K.-E. Peiponen, and E. M. Vartiainen. *Kramers-Kronig Relations in Optical Materials Research*. Springer, 2005.

[14] E. T. Kunkee, Chun-Ching Shih, QiSheng Chen, Chia-Jean Wang, and L. J. Lembo. *Electrorefractive Coupled Quantum Well Modulators: Model and Experimental Results*. IEEE J. Quantum Electron., 43(8):641–650, August 2007.

[15] S. Nojima. *Enhancement of excitonic electrorefraction by optimizing quantum well materials and structures*. Appl. Phys. Lett., 55:1868–1870, 1989.

[16] A. Alping and L. A. Coldren. *Electrorefraction in GaAs and InGaAsP and its application to phase modulators*. J. Appl. Phys., 61(7):2430–2433, 1987.

[17] J. E. Zucker, I. Bar-Joseph, G. Sucha, U. Koren, B. I. Miller, and D. S. Chemla. *Electrorefraction in GaInAs/InP multiple quantum well heterostructures*. Electron. Lett., 24(8):458–460, 1988.

[18] A. Bhatnagar, D. W. E. Allsopp, X. Chen, M. P. Earnshaw, and W. Batty. *Electrorefraction associated with Wannier-Stark localization in strongly coupled three-quantum-well structures*. IEEE J. Quantum Electron., 36(6):702–707, June 2000.

[19] S. L. Chuang. *Physics of Photonic Devices*. John Wiley & Sons, 2009.

[20] A. Ahland, D. Schulz, and E. Voges. *Efficient modeling of the optical properties of MQW modulators on InGaAsP with absorption edge merging*. IEEE J. Quantum Electron., 34(9):1597–1603, September 1998.

[21] J. Hader, J.V. Moloney, and S.W. Koch. *Microscopic theory of gain, absorption, and refractive index in semiconductor laser materials-influence of conduction-band non-parabolicity and Coulomb-induced intersubband coupling*. IEEE J. Quantum Electron., 35(12):1878–1886, 1999.

[22] B. R. Bennett, R. A. Soref, and J. A. Del Alamo. *Carrier-induced change in refractive index of InP, GaAs and InGaAsP*. IEEE J. Quantum Electron., 26(1):113–122, January 1990.

[23] J. G. Mendoza-Alvarez, L. A. Coldren, A. Alping, R. H. Yan, T. Hausken, K. Lee, and K. Pedrotti. *Analysis of depletion edge translation lightwave modulators*. J. Lightw. Technol., 6(6):793–808, June 1988.

[24] K. Ishida, H. Nakamura, H. Matsumura, T. Kadoi, and H. Inoue. *InGaAsP/InP optical switches using carrier induced refractive index change*. Appl. Phys. Lett., 50(3):141–142, 1987.

[25] A. M. Fox, D. A. B. Miller, G. Livescu, J. E. Cunningham, and W. Y. Jan. *Quantum well carrier sweep out: relation to electroabsorption and exciton saturation*. IEEE J. Quantum Electron., 27(10):2281–2295, October 1991.

[26] T. Ido, H. Sano, S. Tanaka, and H. Inoue. *Frequency-domain measurement of carrier escape times in MQW electro-absorption optical modulators*. IEEE Photon. Technol. Lett., 7(12):1421–1423, December 1995.

[27] S. Adachi. *Physical properties of III-V semiconductor compounds: InP, InAs, GaAs, GaP*. Wiley-Interscience, 1992.

[28] S. Adachi and K. Oe. *Linear electro-optic effects in zincblende-type semiconductors: Key properties of InGaAsP relevant to device design*. J. Appl. Phys., 56(1):74–80, 1984.

[29] S. Adachi and K. Oe. *Quadratic electro-optic (Kerr) effects in zincblende-type semiconductors: Key properties of InGaAsP relevant to device design*. J. Appl. Phys., 56(5):1499–1504, 1984.

[30] W. Franz. *Einfluß eines elektrischen Feldes auf eine Absorptionskante*. Z. Naturforschg., 13a:484–489, 1958.

[31] V. Keldysh. *The effect of a strong electric field on the optical properties of insulating crystals*. J. Exptl. Theoret. Phys (U.S.S.R.), 34:788–790, 1958.

[32] J. Callaway. *Optical Absorption in an Electric Field*. Phys. Rev., 130(2):549–553, April 1963.

[33] K. Tharmalingam. *Optical Absorption in the Presence of a Uniform Field*. Phys. Rev., 130(6):2204–2206, June 1963.

[34] J. D. Dow and D. Redfield. *Electroabsorption in Semiconductors: The Excitonic Absorption Edge*. Phys. Rev. B, 1(8):3358–3371, April 1970.

[35] P. Harrison. *Quantum Wells, Wires and Dots*. John Wiley & Sons, 2005.

[36] C. Y. Chao and S. L. Chuang. *Analytical and numerical solutions for a two-dimensional exciton in momentum space*. Phys. Rev. B, 43(8):6530–6543, March 1991.

[37] NLCSTR Inc. *http://www.nlcstr.com*, September 2009.

[38] C. Thirstrup. *Refractive index modulation based on excitonic effects in GaInAs-InP coupled asymmetric quantum wells*. IEEE J. Quantum Electron., 31(6):988–996, June 1995.

[39] N. Susa and T. Nakahara. *Enhancement of change in the refractive index in an asymmetric quantum well*. Appl. Phys. Lett., 60(20):2457–2459, 1992.

[40] Hao Feng, J. P. Pang, M. Sugiyama, K. Tada, and Y. Nakano. *Field-induced optical effect in a five-step asymmetric coupled quantum well with modified potential*. IEEE J. Quantum Electron., 34(7):1197–1208, July 1998.

[41] D. A. B. Miller, D. S. Chemla, T. C. Damen, A. C. Gossard, W. Wiegmann, T. H. Wood, and C. A. Burrus. *Band-Edge Electroabsorption in Quantum Well Structures: The Quantum-Confined Stark Effect*. Phys. Rev. Lett., 53(22):2173–2176, November 1984.

[42] G. Bastard, E. E. Mendez, L. L. Chang, and L. Esaki. *Variational calculations on a quantum well in an electric field*. Phys. Rev. B, 28(6):3241–3245, September 1983.

[43] J. A. Brum and G. Bastard. *Electric-field-induced dissociation of excitons in semiconductor quantum wells*. Phys. Rev. B, 31(6):3893–3898, March 1985.

[44] S. L. Chuang, S. Schmitt-Rink, D. A. B. Miller, and D. S. Chemla. *Exciton Green's-function approach to optical absorption in a quantum well with an applied electric field*. Phys. Rev. B, 43(2):1500–1509, January 1991.

[45] J. Bleuse, G. Bastard, and P. Voisin. *Electric-Field-Induced Localization and Oscillatory Electro-optical Properties of Semiconductor Superlattices*. Phys. Rev. Lett., 60(3):220–223, January 1988.

[46] P. Voisin, J. Bleuse, C. Bouche, S. Gaillard, C. Alibert, and A. Regreny. *Observation of the Wannier-Stark Quantization in a Semiconductor Superlattice*. Phys. Rev. Lett., 61(14):1639–1642, October 1988.

[47] E. Bigan, M. Allovon, M. Carre, C. Braud, A. Carenco, and P. Voisin. *Optimization of optical waveguide modulators based on Wannier-Stark localization: an experimental study*. IEEE J. Quantum Electron., 28(1):214–223, January 1992.

[48] N Susa. *Electric-field-induced refractive index changes in three-step asymmetric coupled quantum wells*. J. Appl. Phys., 73(12):8463–8470, 1993.

[49] M. P. Earnshaw, D. W. E. Allsopp, E. T. R. Chidley, and R. Grey. *Enhanced electrorefraction in symmetric narrow coupled quantum wells*. IEEE Photon. Technol. Lett., 12(6):627–629, June 2000.

[50] M. S. Whalen and J. Stone. *Index of refraction of n-type InP at 0.633- and 1.15-mu m wavelengths as a function of carrier concentration*. J. Appl. Phys., 53(6):4340–4343, 1982.

[51] H. C. Casey and P. L. Carter. *Variation of intervalence band absorption with hole concentration in p-type InP*. Appl. Phys. Lett., 44(1):82–83, January 1984.

[52] C. H. Henry, R. A. Logan, and K. A. Bertness. *Spectral dependence of the change in refractive index due to carrier injection in GaAs lasers*. J. Appl. Phys., 52(7):4457–4461, 1981.

[53] E. Burstein. *Anomalous Optical Absorption Limit in InSb*. Phys. Rev., 93(3):632–633, February 1954.

[54] T.S. Moss, G.J. Burrel, and B. Ellis. *Semiconductor Opto-Electronics*. Butterworth & Co. Ltd., 1973.

[55] S. Adachi. *Material parameters of $In_{1-x}Ga_xAs_yP_{1-y}$ and related binaries*. J. Appl. Phys., 53(12):8775–8792, 1982.

[56] P. A. Wolff. *Theory of the Band Structure of Very Degenerate Semiconductors*. Phys. Rev., 126(2):405–412, April 1962.

[57] R. Zengerle, O. Leminger, W. Weiershausen, K. Faltin, and B. Hubner. *Laterally tapered InP-InGaAsP waveguides for low-loss chip-to-fiber butt coupling: a comparison of different configurations*. IEEE Photon. Technol. Lett., 7(5):532–534, May 1995.

[58] G. Müller, B. Stegmüller, H. Westermeier, and G. Wenger. *Tapered InP/InGaAsP wave-guide structure for efficient fibre-chip coupling.* Electron. Lett., 27(20):1836–1838, September 26, 1991.

[59] L. Moerl, L. Ahlers, P. Albrecht, H. Engel, H. J. Hensel, H. P. Nolting, and F. Reier. *Efficient fiber-chip butt coupling using InGaAsP/InP waveguide tapers.* In *Conference on Optical Fiber Communication/International Conference on Integrated Optics and Optical Fiber Communication*, page ThK2. Optical Society of America, 1993.

[60] T.L. Koch, U. Koren, G. Eisenstein, M.G. Young, M. Oron, C.R. Giles, and B.I. Miller. *Tapered waveguide InGaAs/InGaAsP multiple-quantum-well lasers.* IEEE Photon. Technol. Lett., 2(2):88–90, February 1990.

[61] G. Wenger, L. Stoll, B. Weiss, M. Schienle, R. Muller-Nawrath, S. Eichinger, J. Muller, B. Acklin, and G. Muller. *Design and fabrication of monolithic optical spot size transformers (MOSTs) for highly efficient fiber-chip coupling.* J. Lightw. Technol., 12(10):1782–1790, October 1994.

[62] C.M. Weinert. *Design of fiber-matched uncladded rib waveguides on InP with polarization-independent mode matching loss of 1 dB.* IEEE Photon. Technol. Lett., 8(8):1049–1051, August 1996.

[63] Photon Design Ltd. *http://www.photond.com*, September 2009.

[64] A. S. Sudbo. *Numerically stable formulation of the transverse resonance method for vector mode-field calculations in dielectric waveguides.* IEEE Photon. Technol. Lett., 5(3):342–344, March 1993.

[65] S. Adachi. *Optical properties of $In_{1-x}Ga_xAs_yP_{1-y}$ alloys.* Phys. Rev. B, 39(17):12612–12621, June 1989.

[66] K. Okamoto. *Fundamentals of Optical Waveguides.* Academic Press, 2005.

[67] S. Dupont, A. Beaurain, P. Miska, M. Zegaoui, J.-P. Vilcot, H. W. Li, M. Constant, D. Decoster, and J. Chazelas. *Low-loss InGaAsP/InP submicron optical waveguides fabricated by ICP etching.* Electron. Lett., 40(14):865–866, July 8, 2004.

[68] J. W. Bae, W. Zhao, J. H. Jang, I. Adesida, A. Lepore, M. Kwakernaak, and J. H. Abeles. *Characterization of sidewall roughness of InP/InGaAsP etched using inductively cou-*

pled plasma for low loss optical waveguide applications. Journal of Vacuum Science & Technology B: Microelectronics and Nanometer Structures, 21(6):2888–2891, 2003.

[69] W. Zhao, J. W. Bae, I. Adesida, and J. H. Jang. *Effect of mask thickness on the nanoscale sidewall roughness and optical scattering losses of deep-etched InP/InGaAsP high mesa waveguides.* Journal of Vacuum Science & Technology B, 23(5):2041–2045, 2005.

[70] H. Klein. *Vergleichende Analyse elektrooptischer Effekte in Multi-Quantenfilm- und Bulk-Schichten zur Realisierung von InP-Mach-Zehnder-Modulatoren für 40Gbit/s.* Diplomarbeit, TU Berlin, 2004.

[71] K. G. Ravikumar, T. Aizawa, S. Suzaki, and R. Yamauchi. *Observation of polarization independent electric field effect in InGaAs/InP tensile strained quantum well and its proposal for optical switch.* Appl. Phys. Lett., 61(16):1904–1906, 1992.

[72] S. Nojima and K. Wakita. *Optimization of quantum well materials and structures for excitonic electroabsorption effects.* Appl. Phys. Lett., 53(20):1958–1960, November 1988.

[73] Silvaco Data Systems Inc. *http://www.silvaco.com/products/vwf/atlas/blaze/blaze_br.html*, December 2009.

[74] R. C. Alferness. *Waveguide Electrooptic Modulators.* IEEE Trans. Microwave Theory Tech., 30(8):1121–1137, August 1982.

[75] C. E. Shannon. *Communication in the Presence of Noise.* Proceedings of the IRE, 37(1):10–21, January 1949.

[76] M. Secondini. *Optical Equalization: System Modeling and Performance Evaluation.* J. Lightw. Technol., 24(11):4013–4021, November 2006.

[77] M. I. Hayee and Rami Haddad. *Enhancing spectral efficiency of binary NRZ optical networks with electronic signal processing.* J. Opt. Netw., 5(9):655–661, 2006.

[78] Ansoft Corporation. *http://www.ansoft.com/*, December 2009.

[79] H. Chen. *Development of an 80 Gbit/s InP-based Mach-Zehnder Modulator.* PhD thesis, TU Berlin, 2007.

[80] M. Rohde, C. Caspar, N. Heimes, M. Konitzer, E.-J. Bachus, and N. Hanik. *Robustness of DPSK direct detection transmission format in standard fibre WDM systems.* Electron. Lett., 36(17):1483–1484, August 17, 2000.

[81] R.A. Griffin and A.C. Carter. *Optical differential quadrature phase-shift key (oDQPSK) for high capacity optical transmission*. Proc. Optical Fiber Communications Conference OFC 2002, pages 367–368, March 2002.

[82] K.-P. Ho. *Phase-Modulated Optical Communication Systems*. Springer, 2005.

[83] E. Forestieri. *Optical Communication Theory and Techniques*. Springer, 2005.

[84] A. H. Gnauck and P. J. Winzer. *Optical phase-shift-keyed transmission*. J. Lightw. Technol., 23(1):115–130, January 2005.

[85] D. McGhan, M. O'Sullivan, M. Sotoodeh, A. Savchenko, C. Bontu, M. Belanger, and K. Roberts. *Electronic dispersion compensation*. In *Optical Fiber Communication Conference, 2006*, pages 15 pp.–, March 2006.

[86] R. Griffin, R. Johnstone, R. Walker, S. Wadsworth, A. Carter, and M. Wale. *Integrated DQPSK transmitter for dispersion-tolerant and dispersion-managed DWDM transmission*. In *Proc. Optical Fiber Communications Conference OFC 2003*, pages 770–771, March 23–28, 2003.

[87] R. A. Griffin. *Integrated DQPSK transmitters*. In *Proc. Optical Fiber Communications Conference OFC 2005*, volume 3, page 3pp., March 6–11, 2005.

[88] H. Yasaka, K. Tsuzuki, N. Kikuchi, E. Yamada, Y. Shibata, and T. Ishibashi. *High-speed InP-based Mach-Zehnder modulators for telecom applications*. In *Proc. IEEE Compound Semiconductor Integrated Circuit Symposium CSIC '05*, page 4pp., October 30–November 2, 2005.

[89] D. Varoutas, A. Arapogianni, D. Syvridis, and T. Sphicopoulos. *Electrical crosstalk analysis in OEIC modules*. In *(SPIE) Conference Series*, volume 3631, pages 44–54, April 1999.

[90] N. S. Lagali, M. R. Paiam, and R. I. MacDonald. *Theory of variable-ratio power splitters using multimode interference couplers*. IEEE Photon. Technol. Lett., 11(6):665–667, June 1999.

[91] The MathWorks Inc. *http://www.mathworks.com*, December 2009.

[92] S. Betti, G. De Marchis, and E. Iannone. *Coherent Optical Communications Systems*. Wiley & Sons, 1995.

[93] C. Wree, J. Leibrich, J. Eick, W. Rosenkranz, and D. Mohr. *Experimental investigation of receiver sensitivity of RZ-DQPSK modulation using balanced detection*. In *Proc. Optical Fiber Communications Conference OFC 2003*, pages 456–457, March 23–28, 2003.

[94] F. Dorgeuille and F. Devaux. *On the transmission performances and the chirp parameter of a multiple-quantum-well electroabsorption modulator*. IEEE J. Quantum Electron., 30(11):2565–2572, November 1994.

[95] D. van den Borne, G.D. Khoe, H. de Waardt, and E. Gottwald. *Bit pattern dependence in optical DQPSK modulation*. Electron. Lett., 43(22):–, 25 2007.

[96] M. McKinley, K. Remley, M. Myslinski, J. Kenney, D. Schreurs, and B. Nauwelaers. *EVM Calculation for Broadband Modulated Signals*. In *Proceedings of 64th ARFTG Conference*, pages 45–52, December 2004.

[97] R.A. Shafik, S. Rahman, R. Islam, and N.S. Ashraf. *On the error vector magnitude as a performance metric and comparative analysis*. In *2nd International Conference on Emerging Technologies, 2006*, pages 27 –31, November 2006.

[98] J.-F. Vinchant, J. A. Cavailles, M. Erman, P. Jarry, and M. Renaud. *InP/GaInAsP guided-wave phase modulators based on carrier-induced effects: theory and experiment*. J. Lightw. Technol., 10(1):63–70, January 1992.

[99] Agilent Technologies. *http://www.agilent.com/find/lca*, March 2010.

[100] APEX Technologies. *http://www.apex-t.com/ap2440complex.htm*, March 2010.

[101] D. E. Aspnes and A. A. Studna. *Dielectric functions and optical parameters of Si, Ge, GaP, GaAs, GaSb, InP, InAs, and InSb from 1.5 to 6.0 eV*. Phys. Rev. B, 27(2):985, January 1983.

[102] P. Chandra, L.A. Coldren, and K.E. Strege. *Refractive index data from $Ga_xIn_{1-x}As_yP_{1-y}$ films*. Electron. Lett., 17(1):6–7, 8 1981.

[103] S. Adachi. *Refractive indices of III–V compounds: Key properties of InGaAsP relevant to device design*. J. Appl. Phys., 53(8):5863–5869, 1982.

[104] R. E. Nahory, M. A. Pollack, W. D. Jr. Johnston, and R. L. Barns. *Band gap versus composition and demonstration of Vegard's law for $In_{1-x}Ga_xAs_yP_{1-y}$ lattice matched to InP*. Appl. Phys. Lett., 33(7):659–661, 1978.

[105] A. A. Ballman, A. M. Glass, R. E. Nahory, and H. Brown. *Double doped low etch pit density InP with reduced optical absorption*. Journal of Crystal Growth, 62(1):198 – 202, 1983.

[106] M. Bugajski and W. Lewandowski. *Concentration-dependent absorption and photoluminescence of n-type InP*. J. Appl. Phys., 57(2):521–530, 1985.

[107] F. R. Bacher, J. S. Blakemore, J. T. Ebner, and J. R. Arthur. *Optical-absorption coefficient of $In_{1-x}Ga_xAs/InP$*. Phys. Rev. B, 37(5):2551–2557, February 1988.